

---

# Synthesis and thermoelectric studies of Zintl phases in the systems Ba-Al-Sb, Ba-Ga-Sb, and Ba-In-Sb



TECHNISCHE  
UNIVERSITÄT  
DARMSTADT

Vom Fachbereich Chemie

der Technischen Universität Darmstadt

zur Erlangung des akademischen Grades eines

Doktor rerum naturalium (Dr. rer. nat.)

genehmigte

Dissertation

vorgelegt von

Manikanda Prabu Nagu, M.Sc.

aus Madurai, Indien

Referentin:	Prof. Dr. Barbara Albert
Korreferent:	Prof. Dr. Jörg J. Schneider
Tag der Einreichung:	04-09-2014
Tag der mündlichen Prüfung:	03-11-2014

Darmstadt 2014  
D17

---



The present work was performed under the supervision of Prof. Dr. Barbara Albert at the Eduard Zintl Institute of Inorganic and Physical Chemistry, Technische Universität Darmstadt from December 2009 to August 2014.

---

---

***Dedicated to my parents***

---

---

## Acknowledgments

---

I would like to extend my gratitude to Prof. Dr. Barbara Albert for providing this interesting research work for my PhD thesis. I thank for her guidance and supervision throughout this work with her immense knowledge and valuable feedback. Her motivation and enthusiasm helped to successfully complete the project. This thesis would not have been possible without her determination and constant support.

I thank Dr. G. Cordier for introducing this new research field to me. I thank Dr. K. Hofmann, Dr. C. Litterscheid, Ms. D. Nikolaus, Ms. R. Klemens, technicians and non-teaching staffs of Ak-Albert and of Eduard Zintl institute of inorganic and physical chemistry, TU Darmstadt. I specially thank all former and present group members of research group of Prof. B. Albert. I extend my gratitude especially to our thermoelectric project members and my officemates for their support, enthusiasm and timely help.

I would like to thank In-TEG project collaborators and the funding agencies that supported this work. I thank Prof. Juri Grin and his research group for the thermoelectric measurements of my samples. I sincerely thank Prof. S. Natarajan who was the inspiration and motivation for me throughout my carrier. I also thank the members of research group of Prof. S. Natarajan. I want to thank Dr. P. M. Sundaram for his support and also I thank all the teachers of my college and school.

Finally, I express my deepest gratitude to my parents, family members, relatives and friends for their love, moral support and encouragement that make my life happy and meaningful.

---

---

## Abstract

---

### Synthesis and thermoelectric studies of Zintl phases in the systems Ba-Al/Ga/In-Sb

Zintl phases have attracted interest due to their physical properties, electronic and crystal structures. In recent years ternary Zintl phases were being studied for their interesting thermoelectric properties. Though many Zintl phases are known, the compounds discussed in this work were not studied extensively before. This work emphasizes ternary Zintl phases containing barium and antimony.  $\text{Ba}_3\text{AlSb}_3$ ,  $\text{Ba}_3\text{GaSb}_3$ ,  $\text{Ba}_7\text{Ga}_4\text{Sb}_9$ ,  $\text{BaGa}_2\text{Sb}_2$ , and  $\text{Ba}_5\text{In}_2\text{Sb}_6$  have been investigated. In this work, ternary Zintl phases were prepared with optimized synthetic routes and characterized. DFT was used to calculate band gaps, according to which  $\text{Ba}_3\text{AlSb}_3$  and  $\text{Ba}_3\text{GaSb}_3$  are expected to be semiconductors and  $\text{Ba}_7\text{Ga}_4\text{Sb}_9$ ,  $\text{BaGa}_2\text{Sb}_2$  and  $\text{Ba}_5\text{In}_2\text{Sb}_6$  should be metallic.

Spark plasma sintering was used to compact the products of high-temperature reactions of the elements to make pellets for thermoelectric measurements.  $\text{Ba}_3\text{AlSb}_3$  exhibits high Seebeck coefficients ( $\alpha_{\text{max}} = 383 \mu\text{VK}^{-1}$  at 342 K), low electrical ( $\sigma_{\text{max}} = 18 \text{ Sm}^{-1}$  at 342 K) and thermal conductivities ( $K_{\text{min}} = 0.75 \text{ Wm}^{-1}\text{K}^{-1}$  at 342 K).  $\text{Ba}_3\text{GaSb}_3$  also shows high Seebeck coefficients, low electrical and thermal conductivities.  $ZT$  values of both compounds were found to be low due to very low electrical conductivities. To modify the properties doping was attempted using zinc, calcium and strontium as dopants. The products were analysed to identify the presence of dopants using energy dispersive X-ray spectroscopy and atomic absorption spectroscopy. As an example, the thermoelectric properties of  $\text{Ba}_3\text{Al}_{0.97}\text{Zn}_{0.03}\text{Sb}_3$  were studied. It shows modified properties and a higher figure of merit ( $ZT_{\text{max}} = 0.1081$  at 490 K) than the undoped  $\text{Ba}_3\text{AlSb}_3$ . The thermoelectric properties of  $\text{Ba}_7\text{Ga}_4\text{Sb}_9$  could not be studied due to lack of thermal stability.  $\text{BaGa}_2\text{Sb}_2$  was found to be stable in air. It shows high Seebeck coefficients, low electrical and thermal conductivities.  $\text{Ba}_5\text{In}_2\text{Sb}_6$  was found to be an  $n$ -type semiconductor.  $\text{Ba}_5\text{In}_2\text{Sb}_6$  exhibits low Seebeck

---

---

coefficients ( $\alpha_{\min} = -74 \mu\text{VK}^{-1}$  at 473 K), low electrical ( $\sigma_{\max} = 12,955 \text{ Sm}^{-1}$  at 683 K) and thermal conductivities ( $K_{\min} = 1.73 \text{ Wm}^{-1}\text{K}^{-1}$  at 520 K). The  $ZT$  values of  $\text{BaGa}_2\text{Sb}_2$  and  $\text{Ba}_5\text{In}_2\text{Sb}_6$  were also found to be low.

---

---

## Kurzzusammenfassung

---

### Synthese und thermoelektrische Untersuchungen von Zintl-Phasen in den Systemen Ba-Al/Ga/In-Sb

Zintl-Phasen sind interessant aufgrund ihrer physikalischen Eigenschaften, elektronischen Zustände und Kristallstrukturen. In den letzten Jahren sind ternäre Zintl-Phasen aufgrund ihrer interessanten thermoelektrischen Eigenschaften untersucht worden. Obwohl viele Zintl-Phasen bekannt sind, sind die Verbindungen, die in dieser Arbeit diskutiert werden, nicht gut untersucht worden. Im Rahmen dieser Arbeit standen ternäre Zintl-Phasen mit Barium und Antimon im Fokus.  $\text{Ba}_3\text{AlSb}_3$ ,  $\text{Ba}_3\text{GaSb}_3$ ,  $\text{Ba}_7\text{Ga}_4\text{Sb}_9$ ,  $\text{BaGa}_2\text{Sb}_2$  und  $\text{Ba}_5\text{In}_2\text{Sb}_6$  wurden untersucht. In dieser Arbeit wurden ternären Zintl-Phasen mit optimierten Synthesewegen hergestellt und charakterisiert. DFT-Rechnungen wurden verwendet, um Bandlücken zu bestimmen. Demnach wird für  $\text{Ba}_3\text{AlSb}_3$  und  $\text{Ba}_3\text{GaSb}_3$  halbleitendes wohingegen verhalten erwartet  $\text{Ba}_7\text{Ga}_4\text{Sb}_9$ ,  $\text{BaGa}_2\text{Sb}_2$  und  $\text{Ba}_5\text{In}_2\text{Sb}_6$  metallisch sein sollten.

Feldaktiviertes Sintern (Spark plasma sintering) wurde benutzt, um die Produkte der Hochtemperaturreaktionen der Elemente zu verdichten, um Presslinge für thermoelektrische Messungen zu erhalten.  $\text{Ba}_3\text{AlSb}_3$  zeigt einen hohen Seebeck-Koeffizienten ( $\alpha_{\text{max}} = 383 \mu\text{VK}^{-1}$  bei 342 K), niedrige elektrische Leitfähigkeit ( $\sigma_{\text{max}} = 18 \text{ Sm}^{-1}$  bei 342 K) und niedrige Wärmeleitfähigkeiten ( $K_{\text{min}} = 0,75 \text{ Wm}^{-1}\text{K}^{-1}$  bei 342 K).  $\text{Ba}_3\text{GaSb}_3$  zeigt ebenfalls einen hohen Seebeck-Koeffizienten, geringe elektrische Leitfähigkeit und geringe thermische Leitfähigkeit. Aufgrund der sehr niedrigen elektrischen Leitfähigkeiten wurden geringe ZT-Werte für beide Verbindungen erhalten. Um die Eigenschaften zu optimieren, wurden Dotierungen mit Zink, Calcium und Strontium durchgeführt. Energie-dispersive Röntgenspektroskopie und Atomabsorptionsspektroskopie wurde verwendet, um die Gegenwart von Dotierungsmitteln nachzuweisen. Als Beispiel wurden die thermoelektrischen Eigenschaften  $\text{Ba}_3\text{Al}_{0,97}\text{Zn}_{0,03}\text{Sb}_3$  untersucht. Es zeigt veränderten Eigenschaften und einen höheren Leistungszahl ( $ZT_{\text{max}} = 0.1081$  bei 490 K) als die undotierte Probe. Die thermoelektrischen Eigenschaften von  $\text{Ba}_7\text{Ga}_4\text{Sb}_9$  konnten wegen mangelnder

---

---

thermischer Stabilität nicht untersucht werden. BaGa<sub>2</sub>Sb<sub>2</sub> ist an Luft stabil. Es zeigt einen hohen Seebeck-Koeffizienten und geringe elektrische und thermische Leitfähigkeit. Ba<sub>5</sub>In<sub>2</sub>Sb<sub>6</sub> wurde als *n*-Typ-Halbleiter identifiziert. Es zeigt einen geringen Seebeck-Koeffizienten ( $\alpha_{\min} = -74 \mu\text{VK}^{-1}$  bei 473 K) und niedrige elektrische ( $\sigma_{\max} = 12.955 \text{ Sm}^{-1}$  bei 683 K) und niedrige Wärmeleitfähigkeit ( $K_{\min} = 1,73 \text{ Wm}^{-1}\text{K}^{-1}$  bei 520 K). Die *ZT*-Werte von BaGa<sub>2</sub>Sb<sub>2</sub> und Ba<sub>5</sub>In<sub>2</sub>Sb<sub>6</sub> sind gering.

---

---

---

## Contents

---

1 Introduction	1
2 Experimental techniques	4
2.1 Starting materials	4
2.2 Inert atmosphere techniques	4
2.3 Metal distillation setup	6
2.4 Preparatory techniques	7
2.5 Spark plasma sintering	10
3 Characterization techniques	12
3.1 Powder X-ray diffraction	12
3.2 Scanning electron microscopy and Energy dispersive X-ray spectroscopy	14
3.3 Atomic absorption spectroscopy	16
3.4 Thermal analysis	17
3.5 Density measurement	18
3.6 Thermoelectric property measurements	19
4 Literature/ State of the art	25
5 Density functional theory calculations	49
6 Ba <sub>3</sub> AlSb <sub>3</sub>	57
6.1 Synthesis, characterization and compaction	57
6.2 Thermoelectric studies	63
6.3 Doping studies	67
6.4 Discussion of results	77
7 Ba-Ga-Sb systems	79
7.1 Ba <sub>3</sub> GaSb <sub>3</sub>	79

---

---

7.1.1 Synthesis, characterization and compaction	79
7.1.2 Thermoelectric studies	88
7.1.3 Comparing properties of different samples	91
7.1.4 Doping studies	94
7.1.5 Discussion of results	101
7.2 Ba <sub>7</sub> Ga <sub>4</sub> Sb <sub>9</sub>	103
7.2.1 Synthesis, Characterization and compaction	103
7.2.2 Discussion of results	110
7.3 BaGa <sub>2</sub> Sb <sub>2</sub>	111
7.3.1 Synthesis, Characterization and compaction	111
7.3.2 Thermoelectric studies	119
7.3.3 Discussion of results	122
8 Ba <sub>5</sub> In <sub>2</sub> Sb <sub>6</sub>	124
8.1 Synthesis, Characterization and compaction	124
8.2 Thermoelectric studies	130
8.3 Discussion of results	134
9 Summary and outlook	135
10 References	137
11 List of figures	150
12 List of tables	157

---

---

---

## 1 Introduction

---

The modern world is in a serious demand for the generation of energy to fulfill its energy requirements. Energy can be obtained from diverse sources such as combustion of fossil fuels, hydropower stations, wind energy, solar power, tidal energy, nuclear energy etc. The combustion of fossil fuels leads to climate changes. The nuclear power plants operate with a high level of risk. Other options are seriously being investigated to improve their efficiency. Around 40 to 60 % of energy is being lost as thermal waste [1]. The conversion of heat into electricity can reduce this loss by utilizing the waste heat and also avoid excess production of energy. Thermoelectric materials are quite useful for this purpose [2, 3].

Applications of thermoelectric materials are wide such as waste heat recovery, refrigeration, usage in auto mobiles, space probes, temperature sensors and so on [4]. Applications of thermoelectric materials can still be extended to many other useful fields. They help to protect the environment since these materials reduce the amount of combustion of fossil fuels in energy production and also the usage of chlorofluorocarbons (CFCs) in refrigeration which cause ozone depletion. When thermoelectric materials are used to convert the waste heat from exhaust, fuel efficiency can be improved. More over the thermoelectric generators are solid state devices. Those are silent, scalable, and reliable to fit as right candidates for small distributed energy production [5]. There are many kinds of materials under investigation for their usage in thermoelectric conversion. Zintl phases, intermetallic compounds, nano structured compounds, Zinc antimonides, oxides, half heusler compounds, clathrates, skutterudites etc. are the materials of interest [6-14]. Among these, several Zintl phases are promising thermoelectric materials due to their complex crystal structures, interesting electronic, chemical and physical properties [15, 16]. They are well known compounds but less studied for thermoelectric applications.

Zintl phases are a special class of intermetallic compounds which are formed by anionic networks and electropositive cations [15]. Zintl phases usually obey the octet rule. Mostly, these phases are valence balanced according to the Zintl-Klemm or Zintl-

---

---

Klemm-Busmann concept (still there are exceptions) [17-20]. Zintl phases are intermediate compounds between metallic and ionic compounds [21]. They exhibit bond lengths which are intermediate between metallic and ionic counterparts. Zintl phases usually exhibit higher melting points than their elemental counterparts. They require high heat of formation. They are more brittle compared to the metals and exhibit salt like properties. These unique properties make them different from other kinds of intermetallic compounds. The anionic networks are covalent and the cationic part is ionic in nature. The covalent anionic structure can adopt different topologies such as zero dimensional isolated ions, dimers, polyatomic anions. They can also form one-, two- and three-dimensional chains, planes and nets. They are named as Zintl phases after the German chemist Eduard Zintl. Laves first used the term Zintl phases in 1941.

Zintl phases are often poor conductors or semiconductors. This indicates the existence of band gaps in Zintl phases. Band gaps of semiconductors can be less than 2.0 eV according to Nesper [21] or 2.5 eV according to Pearson [22]. These compounds usually exhibit diamagnetic behavior. There are exceptions with paramagnetic behavior but they do not show temperature independent paramagnetism [23]. Traditional Zintl phases are those formed by the combination of alkali or alkaline earth metals with post transition elements. Transition metal Zintl phases were also prepared and studied [24-26].

The Zintl border [15] is the vertical line that separates group 13 and group 14 elements in the periodic table. Generally the elements to the left of this line form insoluble solids and the elements right to this form soluble products in non-aqueous solvents. Al, Cu, Ag and Au are normal metals. They are soft, ductile and exhibit Pauli paramagnetism. They form closed packed structures and exhibit decreasing electrical conductivity with increasing temperature. On the other hand the nonmetals (Si, Ge and  $\alpha$ -Sn) are brittle, diamagnetic and exhibit increasing electrical conductivity with increasing temperature. The elements close to the Zintl border exhibit intermediate properties between metals and nonmetals. Combinations of all these elements with main group or rare earth elements yield Zintl phases. Understanding the behavior,

---

reactivity and relationship between structure and composition of the elements around the Zintl border helps to study the properties of their corresponding Zintl products.

High mobility and low effective mass are commonly found in covalent structures. Low mobility and high effective mass are frequently found in ionic materials. Zintl phases with both ionic and covalent bonding can bridge these two extremes. An efficient thermoelectric material is expected to have an electronic structure that can enhance the mobility by acting as electron-crystal and phonon inhibiting structure that can act as phonon-glass. Covalent networks of Zintl phases can help to enhance the electrical conduction and at the same time the complex structures can lead to the scattering of phonons which reduces lattice thermal conduction. This phenomenon is called electron-crystal phonon-glass behavior. There is a clear relationship between geometry and electronic structure of Zintl phases. Combination of different bond types can lead to the formation of multiple structural units in the crystal structure. Due to this kind of bonding nature and electronic properties, Zintl phases emerge as suitable candidates for [1, 6] thermoelectric studies. In this work a special group of ternary Zintl compounds, 'Barium-tri- (Aluminum/ Gallium/ Indium)-antimonides' was studied. Density functional theory calculations were employed to study their band structure. Their synthetic procedures have been optimized to prepare products with as little as possible side-phases. The powders were characterized by different characterization techniques. Mono-phasic Zintl compounds obtained were compacted and their thermoelectric properties were studied.

---

---

## 2 Experimental techniques

---

### 2.1 Starting materials

All starting materials for this work are commercially available and listed in table 2.1. Air sensitive reactants were stored in the argon filled glove box. All manipulations were done inside the glove box with moisture and oxygen levels below 1 ppm. The oxides layers at the surfaces were removed by scalpel. Alkaline earth metals were distilled using a metal distillation setup that is described in the section 2.3. The synthesis methods are discussed later.

Table 2.1 Starting materials used in this work.

Element	Manufacturer	Form	Purity (%)
Ca	<i>Aldrich</i>	Pieces	99.0
Sr	<i>Alfaaesar</i>	Pieces	99.0
Ba	<i>Chempur</i>	Rod	99.3
Al	<i>Acros organics</i>	Shot (2-10 mm)	99.5
Ga	<i>Degussa</i>	Pieces	99.99
In	<i>Fluka AG</i>	Rod	99.99
Sb	<i>Chempur</i>	Shot (1-3 mm)	99.999
Bi	<i>Chempur</i>	Pieces	99.5
Zn	<i>Chempur</i>	Pieces	99.9

### 2.2 Inert atmosphere techniques

Some of the starting materials (alkaline earth metals) and the resulting products are sensitive to air and moisture. The preparation requires an inert atmosphere to protect the sample from oxidation or decomposition. Inert atmosphere techniques play a key role in handling Zintl phases, preparing samples for powder X-ray diffraction etc. In this section the protective techniques are discussed. The Schlenk line set up contains a dual manifold which consists of many parts such as vacuum pump, gas lines, cold trap, vacuum glass line, drying towers etc. One manifold is connected to the vacuum pump and the other manifold is connected to the purified argon gas line. Argon gas is purified by passing through four different towers respectively silica gel, potassium

hydroxide, molecular sieves (*mesh size 3*) and phosphorous pentoxide. Then the gas passes through the furnace with titanium that is heated to 973 K. The whole process removes moisture, oxygen, other gases and impurities from argon. The maximum evacuation  $3 \times 10^{-3}$  mbar can be achieved in this set up that can be followed using the manometer. Fig 2.1 shows the schematic of the inert gas line or Schlenk line [27, 28]. This set up is useful to handle air sensitive materials.

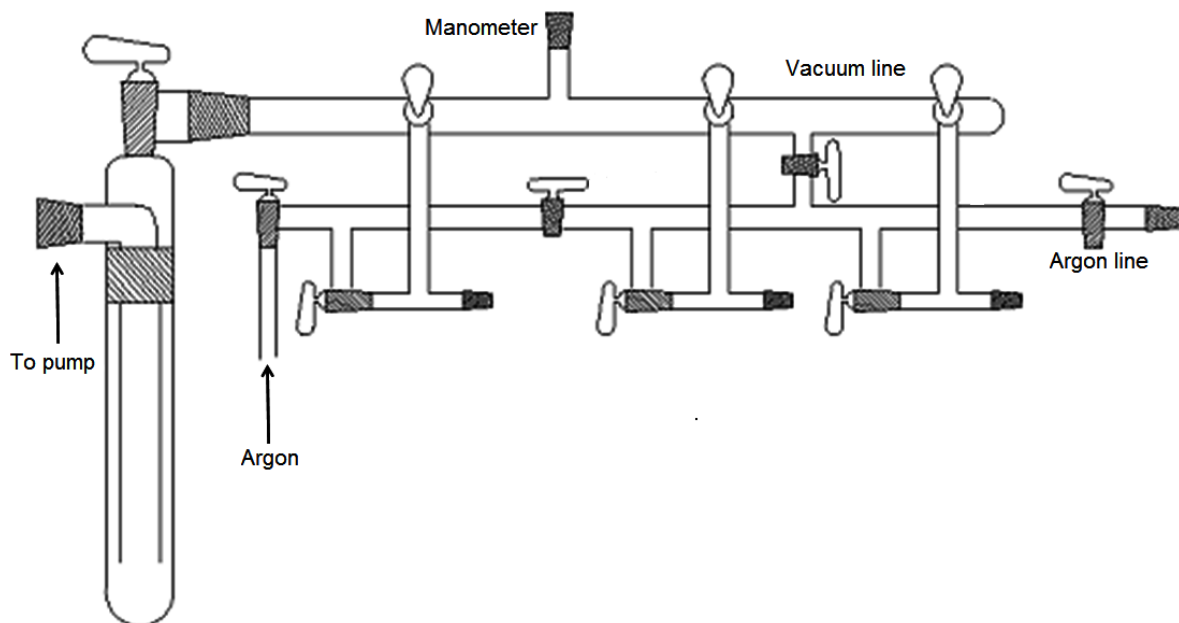


Fig. 2.1 Schlenk or vacuum line set up to handle air sensitive materials [27].

A glove box (*M.Braun*) was used for all kind of manipulations for materials that were air or moisture sensitive and required the inert atmosphere. Schlenk or vacuum lines cannot offer all possibilities to handle air sensitive materials. The argon filled glove box has moisture and water levels below 1 ppm. The quality of the argon atmosphere can be monitored using a gas analyzer. The gloves at the sides of the box are used to place the hands and perform tasks inside the glove box. The big and small airtight evacuation chambers allow the transport of materials inside and outside the glove box. While transporting, these chambers were evacuated and filled with argon gas. The same procedure was repeated for three times. Alkaline earth metals and the Zintl compounds were always kept inside the glove box to avoid contact with air.

## 2.3 Metal distillation setup

Due to their high reactivity, alkaline earth metals form many products like oxides, hydroxides etc. Though they are kept under argon atmosphere the surface may be covered by a thin layer of oxide impurities. To remove the impurities and purify the metal, the distillation setup shown in fig. 2.2 can be used [27, 29]. This set up consists of a cylindrical steel apparatus in which there is a tantalum container at the bottom. The top portion is cooled by the stream of cold water and also with the help of a fan. This is connected to a liquid nitrogen cold trap, further connected to the vacuum pump and also to the Schlenk line. The metal pieces are loaded in the tantalum container and the cylindrical apparatus is sealed under argon atmosphere. This part is connected to the distillation setup. First, the whole setup was evacuated using a diffusion pump (*BOC Edwards*).

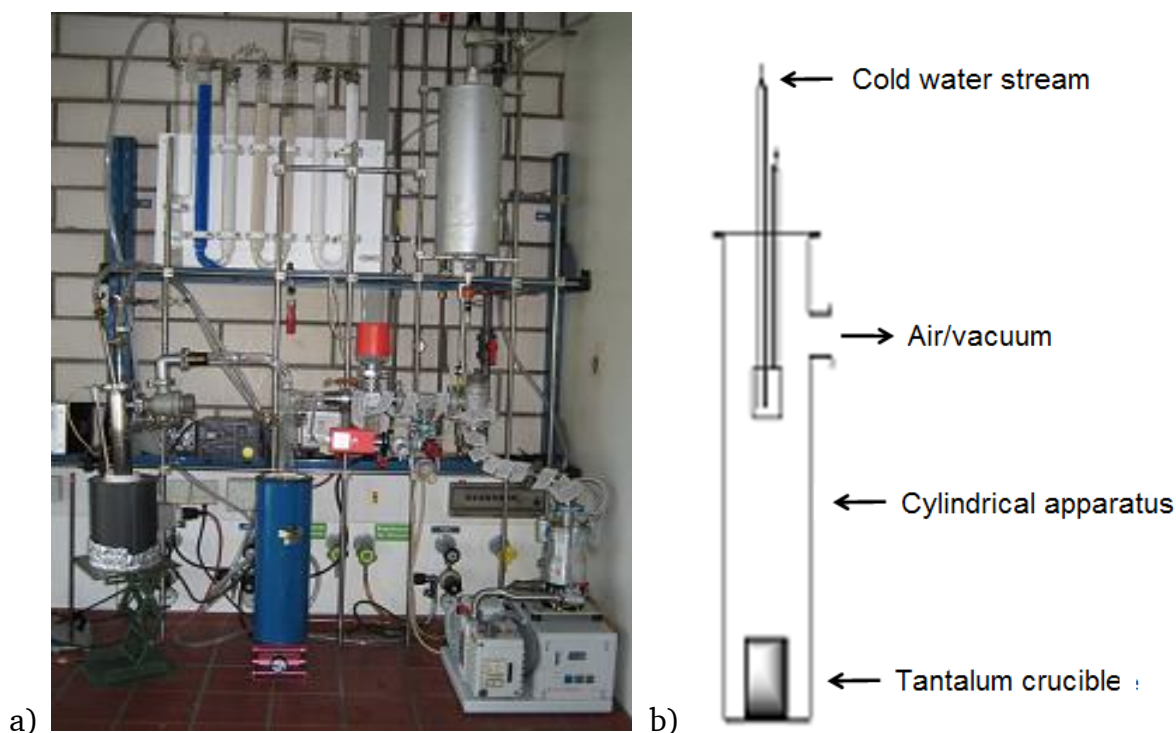


Fig. 2.2 a) Metal distillation setup b) cylindrical steel apparatus [27].

The pressure is maintained in the range of  $3 \times 10^{-4}$  to  $3 \times 10^{-6}$  mbar. The steel apparatus is slowly heated using a furnace at the bottom with the heating rate of 5 K/minute to 1073 K and after 10 to 12 hours it is cooled down to room temperature with the same rate. The metal pieces in the tantalum container will be recrystallized

---

at the cold top portion of the vessel. Later, the sealed cylindrical vessel can be taken inside the glove box and opened to obtain the distilled pure metal.

## 2.4 Preparatory techniques

The Zintl compounds were prepared using solid state synthetic routes such as heating in quartz ampoules, arc melting, induction heating etc. In this section the details of the synthesis procedures are discussed.

To heat the starting materials in quartz ampoules clean tantalum tubes were sealed at one end and then taken inside the glove box. Tantalum tubes were cleaned by sonication in petroleum ether for one hour. The required amounts of reactants were loaded in the tantalum tube. Those were closed either with a tantalum lid or squeezed to close the opening. The tube was transferred to an arc melting device (discussed later) and sealed under the reduced pressure of argon. These tantalum containers were inserted into quartz tubes that were already sealed at one end. They were connected to the vacuum line and flame sealed under vacuum. Fig. 2.3 shows the quartz ampoule [30] prepared for further heating.



Fig. 2.3 Evacuated quartz ampoule with sealed tantalum container.

The arc melting device [31] is shown in the fig. 2.4. It was used to seal the tantalum containers or to directly melt the starting materials in a copper crucible. This setup consists of different parts such as stainless steel stand, welding electric rectifier (*Fronius, Transtig 1600*), connecting cables, melting chamber etc [27]. This device is connected to the vacuum line in order to evacuate and fill argon gas in the airtight melting chamber. The melting chamber is made up of a brass base attached to a copper crucible to melt the reactants and it is connected to a water cooled copper

block with a concavity in the center to melt and seal the metal containers. This part is covered by a quartz tube and further by an air tight glass chamber which is connected to the vacuum line. A tungsten electrode is used to melt the samples. The melting chamber can be evacuated to  $3 \times 10^{-3}$  mbar pressure. The process of evacuation and purging argon will be repeated for three to five times before melting. Using the foot pedal the amount of current supplied can be controlled. The maximum attainable current is 160 A. Depending on the nature of materials and thickness the amount of current supplied can be changed.

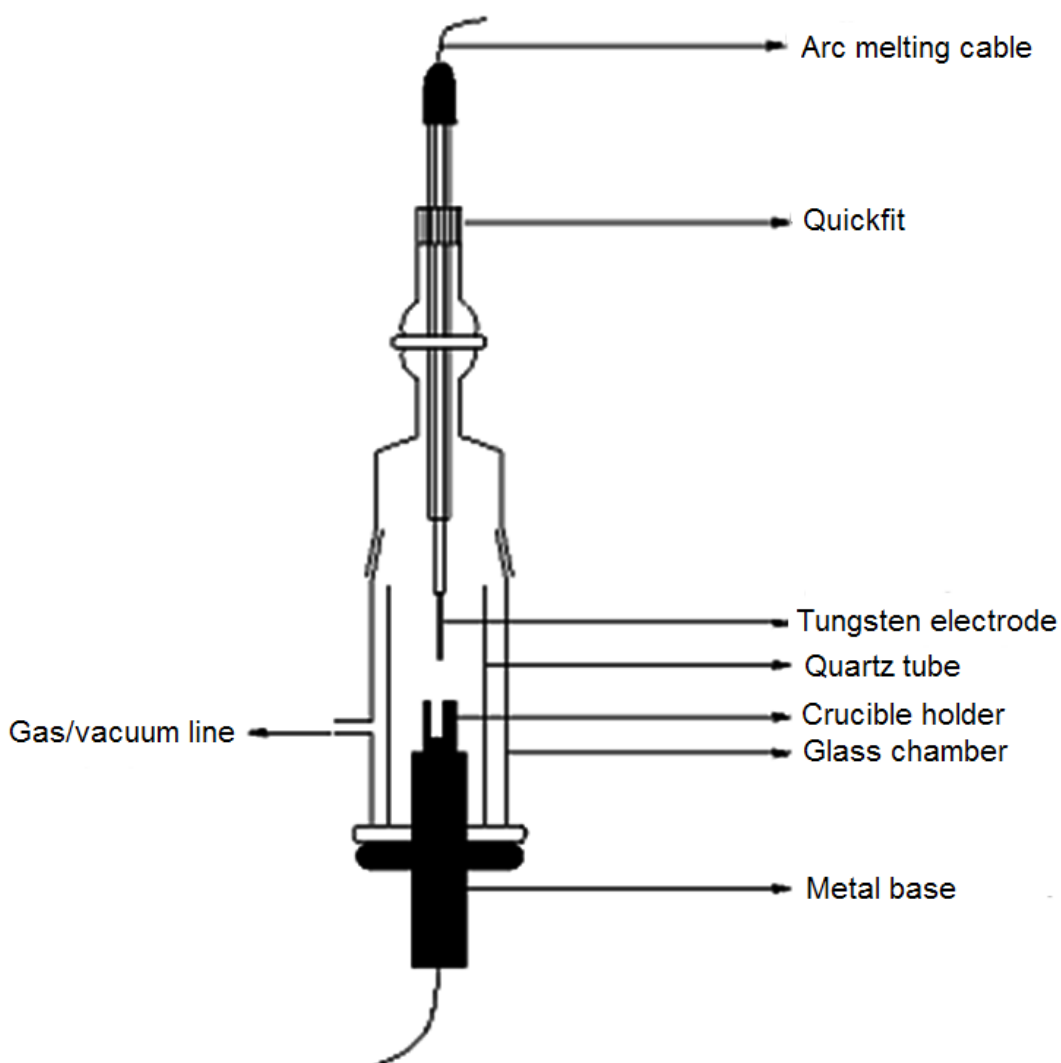


Fig. 2.4 Schematic of arc melting device [27].

Thermal treatments were carried out using tubular, computer controlled furnaces (Carbolite). The samples or the reactants were loaded in sealed tantalum containers covered by evacuated quartz tubes. These ampoules were placed in the aluminum

---

oxide tube in the furnaces to carry out the reactions [27]. The maximum attainable temperature of these furnaces is 1473 K. It is also possible to carry out the reactions under vacuum or reduced pressure of argon since some of these aluminum oxide tubes can be connected to the gas line. Temperature of the furnace can be measured using platinum-rhodium/platinum thermocouple. The characteristics of the ovens are SiC tubes with an interior diameter of 45 mm, a tube length of 500 mm and a length of uniform temperature zone of 50 mm.

Reactions above 1473 K were performed using high frequency induction furnaces [29, 32]. Fig. 2.5 shows the schematic of the induction furnace with high frequency generator (*AXIO 10/450 und Truheat HF 5010*). It consists of a variety of parts that are given below. The sample can be put in a tantalum or carbon container and placed on top of the sample holder inside the quartz reactor. The reactor is connected to the vacuum line for evacuation or purging argon. Under reduced pressure of argon or in vacuum the samples can be heated. This method offers quick heating and quick or controlled cooling. The maximum temperature attainable is 2673 K when BN crucibles are employed.

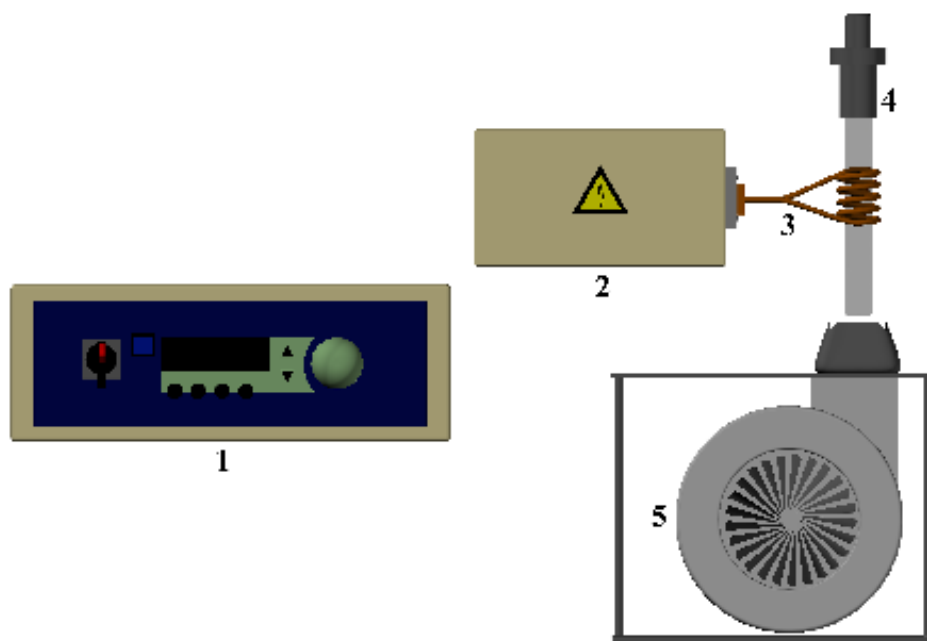


Fig. 2.5 Schematic of high frequency induction furnace. (1-High frequency generator, 2-moderator, 3-induction coil, 4-quartz reactor, 5-fan) [29].

---

## 2.5 Spark plasma sintering

Spark plasma sintering (SPS) is a well-known technique to densify powders. It utilizes uniaxial force and pulsed direct electric current under low atmospheric pressure. This method offers various advantages such as accurate control of sintering energy and high sintering speed etc. [33]. The schematic diagram of a SPS device is shown in fig. 2.6 which consists of many parts such as sintering chamber, atmosphere controls, vacuum exhaust units, SPS controller, DC generator, thermocouple, graphite dies and punches etc [34, 35]. The sample is loaded in the graphite die and placed in between the punches. A thermocouple is fixed into the dye that is closer to the sample. The chamber is evacuated and then a heating program can be executed followed by sintering. In this method the heating power is distributed over the volume of powder sample homogeneously. SPS offers improved sintering behavior compared to ordinary hot-pressing method with less grain growth, minimum decomposition and efficient use of heat input. The instruments *SPS – 211 Lx, Dr. Sinter – LAB*, FUJI (Technische Universität Darmstadt) which is shown in fig. 2.7 and *SPS – 515 ET, Dr. Sinter – LAB*, FUJI (Max Planck Institute for Chemical Physics of Solids, Dresden), were used to densify the samples. If needed the compacted samples were cut according to the required dimension using an automatic saw (*BUEHLER, ISOMET 11-1180* lows peed saw) inside the glove box. Samples with the dimension of 14 x 3 x 3 mm were used for Seebeck and resistivity measurements (sec. 8.2) and for other measurements compacted samples with the dimension of 8 x 1.5 x 1.5 mm (sec. 6.2, 7.1.2, 7.3.2) or 10 x 2 mm (sec. 7.2.2) were used. The theoretical densities were used to calculate the mass of the powdered samples that were used for densification.

$$m = \pi r^2 h d$$

m is the total mass of the sample for sintering, r is the radius of the die, h is the thickness of the compacted sample and d is the density of the compound.

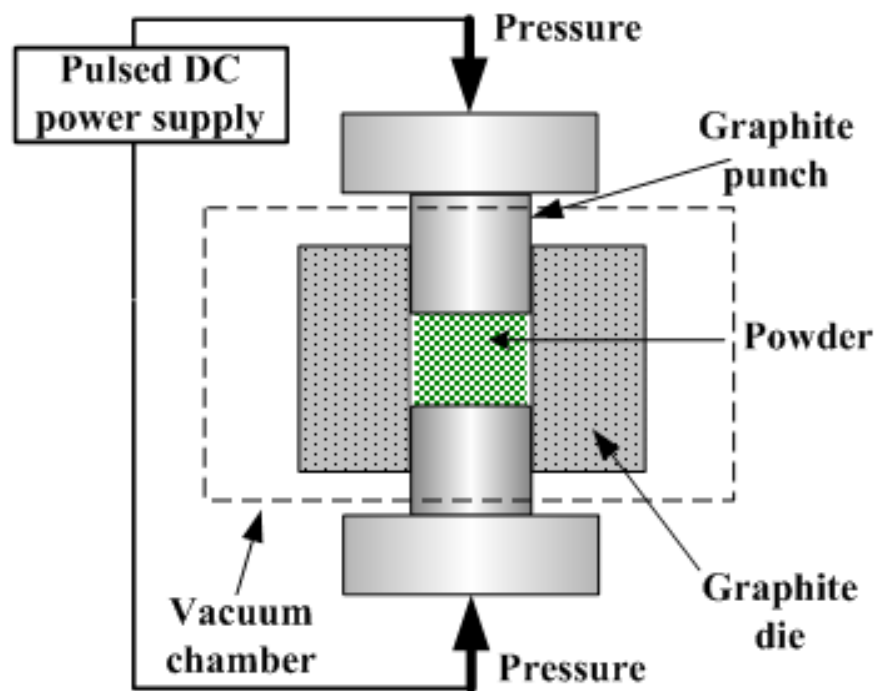


Fig. 2.6 Schematic representation of spark plasma sintering [34].

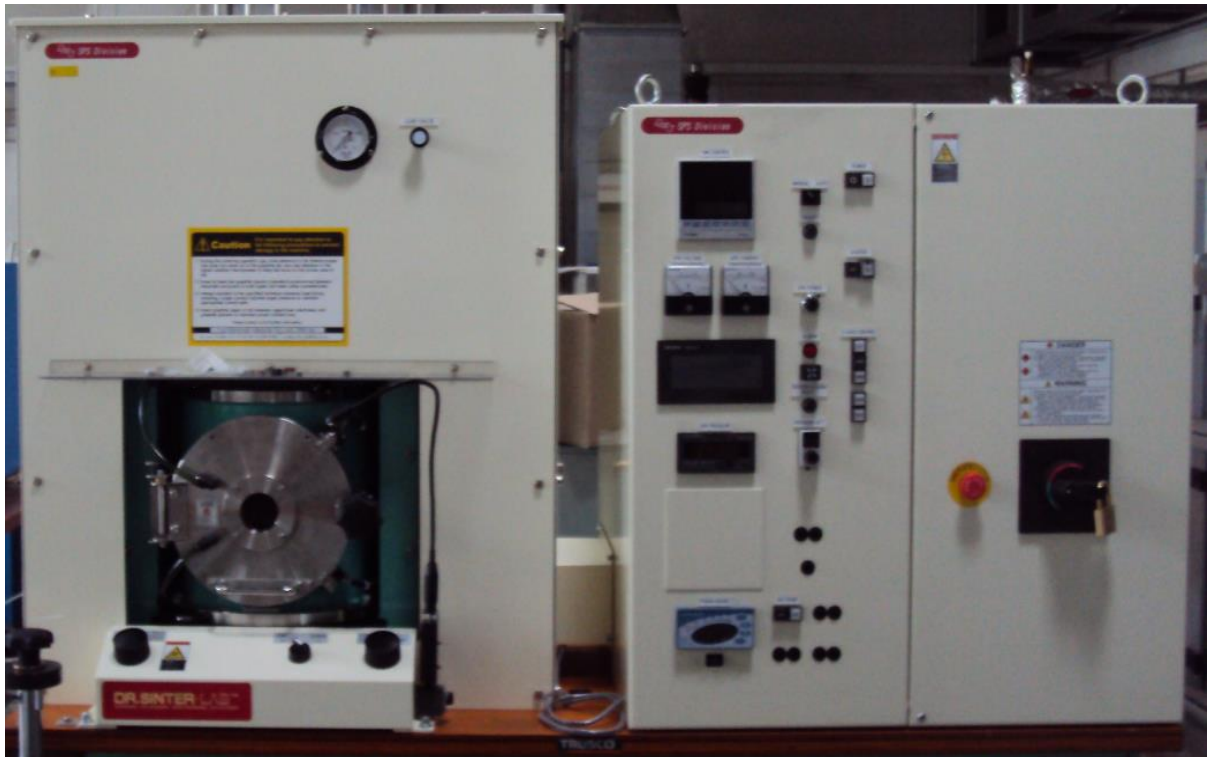


Fig. 2.7 SPS – 211 Lx, Dr. Sinter LAB, FUJI electronics (Japan) used for spark plasma sintering.

---

## 3 Characterization techniques

---

### 3.1 Powder X-ray diffraction

Primary characterization of all prepared samples was done using powder X-ray diffraction as it is one of the most important characterization tools in solid state chemistry. This method gives details about the composition of the crystalline sample. The powder diffraction pattern gives information about diffraction angles and the corresponding intensities. The number of reflections and the intensities are affected by different factors such as crystal class, lattice type, unit cell parameter, symmetry, type of atoms present in the unit cell and their distribution. The Bragg's law gives the relationship between diffraction angle and  $d$  spacing (distance between pairs of adjacent lattice planes) [40-42].

$$n \lambda = 2 d \sin \theta$$

All crystalline samples have unique powder X-ray diffraction patterns in terms of peak positions and intensities of the observed reflections. Thus, for the finger print characterization of crystalline materials powder X-ray diffraction is widely used. Room temperature powder X-ray diffraction measurements were carried out using a *STOE STADI P* diffractometer operated at 50 kV and 40 mA (monochromatized  $\text{Cu } K\alpha_1$  radiation,  $\lambda = 1.5406 \text{ \AA}$ , transmission mode). Fig. 3.1 shows the diffractometer with a curved germanium (111) monochromator [43]. Tape (*Scotch magic 3M*) was used to place the finely ground powder sample in the diffractometer for the measurement. This is useful for compounds that are stable in air. Polyimide ( $d = 7.5 \mu\text{m}$ , *Chemplex*) films were used to measure samples which are sensitive to air and moisture. Sample is taken between two polyimide films and the edges were sealed by the vacuum grease (*Lithelen, Leybold*) to protect the sample from air. Alternatively, air sensitive samples can be measured using sealed glass capillaries as shown in fig. 3.1. A position sensitive detector in Debye-Scherrer geometry was used. In this method, the use of Cu radiation led to problems due to the very high absorption of samples containing elements like antimony.

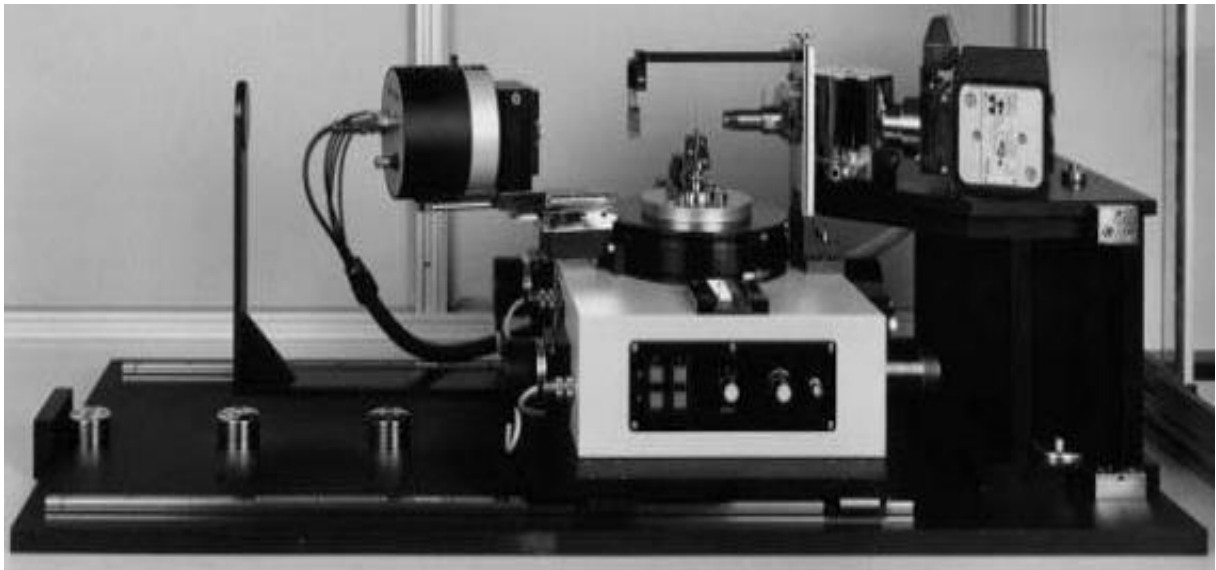


Fig. 3.1 *STOE STADI P* diffractometer [43].

High temperature X-ray diffraction measurements were carried out in a *STOE STADI P* diffractometer operated at 50 kV and 40 mA which was equipped with a heating furnace (monochromatized  $\text{Mo } K\alpha$  radiation,  $\lambda = 0.70930 \text{ \AA}$ ) [44].



Fig. 3.2 Heating furnace used in HTXRD measurements [44].

The samples were filled in quartz capillaries that were sealed with tar and placed in the heating furnace. Samples were heated from room temperature to a specific

---

temperature as programmed. After every step of heating or cooling, the temperature was retained and the diffraction measurement was carried out. The maximum attainable temperature is 1168 K. These measurements are useful to study the thermal stability of the compound, phase transitions etc. Fig. 3.2 shows the heating furnace that was used to carry out the high temperature powder X-ray diffraction measurements.

To analyze the powder X-ray diagrams, the Rietveld method was applied. This method was devised by Hugo Rietveld in the year 1966 for the characterization of crystalline materials [45, 46]. Rietveld refinement offers a method to analyze powder patterns using known structure models. This refinement uses a least squares approach to refine a structure model that leads to a calculated diffractogram. Using the Rietveld method a quantitative phase analysis can also be done. The program *TOPAS* [47] was used to carry out the refinements for the powder X-ray diffraction patterns.

### 3.2 Scanning electron microscopy and Energy dispersive X-ray spectroscopy

Scanning electron microscopy can be used to study the surface topography of the sample. Fig. 3.3 shows the schematic diagram of the scanning electron microscope [48]. A beam of electrons is emitted by the electron gun where the electrons are accelerated to high energies between 1 to 30 KeV. A tungsten electrode serves as the electron gun in this instrument [49]. The condenser lenses focus the beam and allow passing through the scan coils and other lenses. This scans over a rectangular area of the sample surface in a raster fashion. The interaction of electron beam with the sample produces secondary, backscattered and auger electrons, X-rays etc. These are collected by various detectors in the specimen chamber. All these signals can be fed to a monitor that is rastered in synchronization with the electron beam and the images are produced. SEM and EDS measurements were performed using *Joel JSEM-6400* (EDAX) equipped with *APOLLO X* silicon drift detector with resolution  $< 131$  eV and surface  $10 \text{ mm}^2$  (operating pressure  $< 10^{-6}$  mbar). This technique is useful for high magnification (up to 1,000,000x) with an ultimate resolution of  $1 \mu\text{m}$  which is much higher than an ordinary optical microscope [50]. SEM allows nondestructive

evaluation of the sample as the sample can be recovered after the analysis. Sample preparation is very simple as it requires placing the sample in the stub or sample holder.

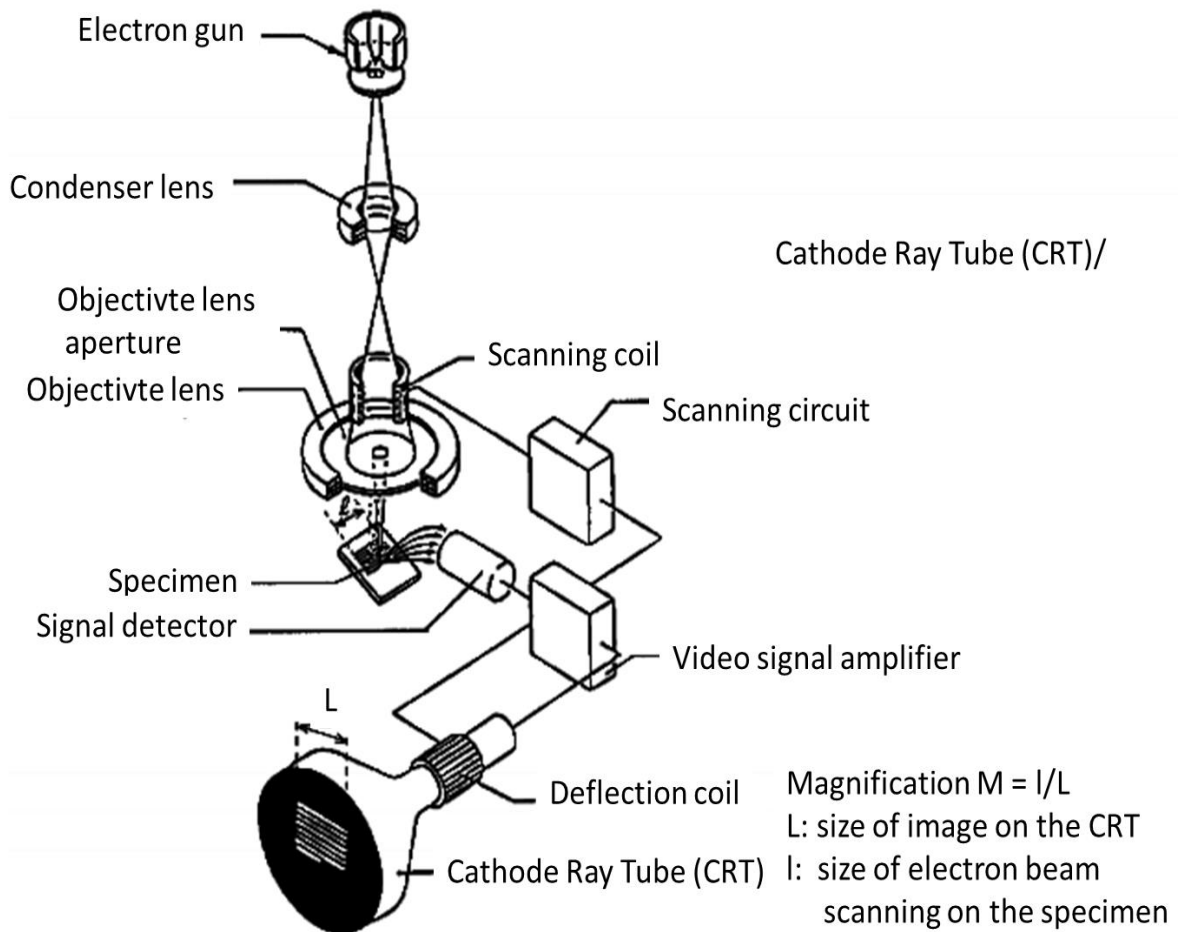


Fig. 3.3 Schematic diagram of SEM [48].

When a sample is bombarded with a focus beam of electrons the emitted X-rays can be measured to identify the chemical composition. These X-rays are detected using an energy dispersive spectrometer (EDS) attached to the SEM [51, 52]. EDS instruments include a sensitive X-ray detector, a cooling liquid nitrogen dewar and a software to collect and analyze energy spectra. A schematic diagram is shown in fig. 3.4. The incident electron beam provides energy to eject electrons from the K shell. Then, an electron from L shell jumps to the K shell and emits characteristic X-rays which can be detected by EDS detector. This helps to identify the elements and the intensities can be compared with the calibration intensities to determine their abundance in the

sample. Thus, EDS can provide a rapid qualitative and semi-quantitative analysis. The same method is useful to identify impurities and to study the homogeneous nature of the sample.

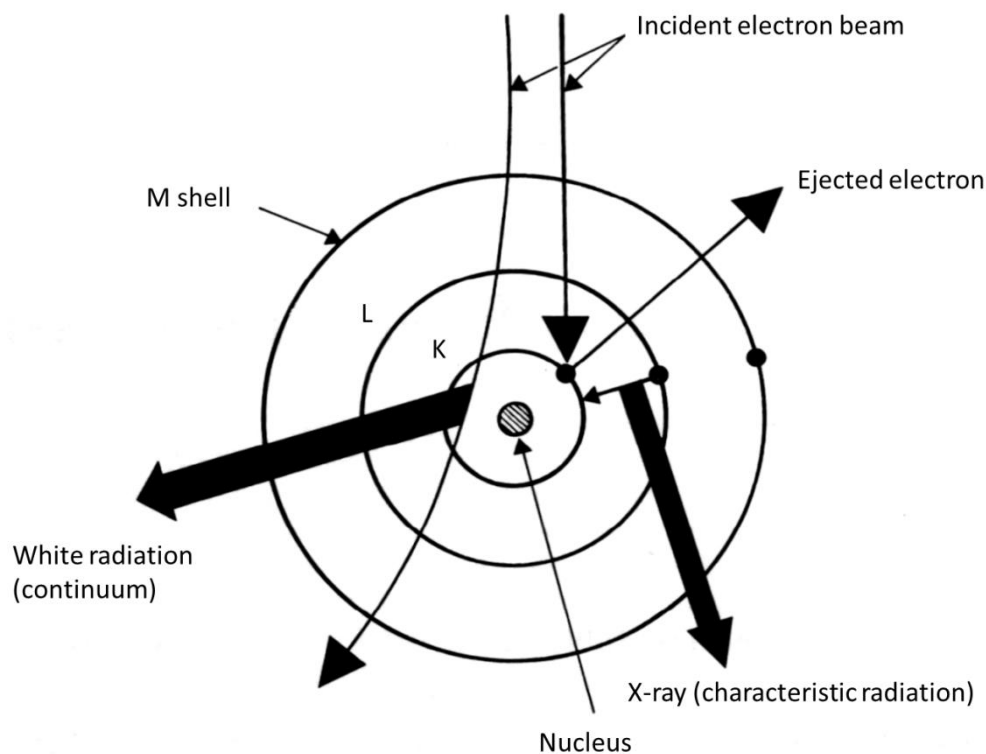


Fig. 3.4 Schematic diagram of Energy Dispersive Spectroscopy [53].

### 3.3 Atomic absorption spectroscopy

Atomic absorption spectroscopy is useful to determine the concentration of any element present in the sample [54]. This method is useful to find the elements in extremely lower concentrations (ppm) as it can measure down to parts per billion in given samples. This method can determine over 70 elements. *H 2799 PERKINELMER, AAnalyst 300* instrument was used to determine the concentration of selected analytes in this work. A schematic view of atomic absorption spectroscopy is given in fig. 3.5 which consists of a light source, atomizer, and sample cell along with flame or furnace heating facility, monochromator, detector and display. The common light source of atomic absorption spectroscopy utilizes a hollow cathode lamp which is made up of a tungsten anode and cathode is made of the element to be determined. The sample is vaporized by flame or electrical heating and the concentration of analyte will be determined in the gaseous state. The emitted electromagnetic radiation passes

through the ground state atoms (in gaseous state) and excites them as they absorb energy from the radiation. Absorbance can be related to the concentration according to Lambert -Beer law.

$$A = \varepsilon c l$$

$A$  is the absorbance,  $\varepsilon$  is the molar absorption,  $c$  is the concentration and  $l$  is the path length. Measurement of standard samples help to determine the concentration of the analyte in the sample solution.

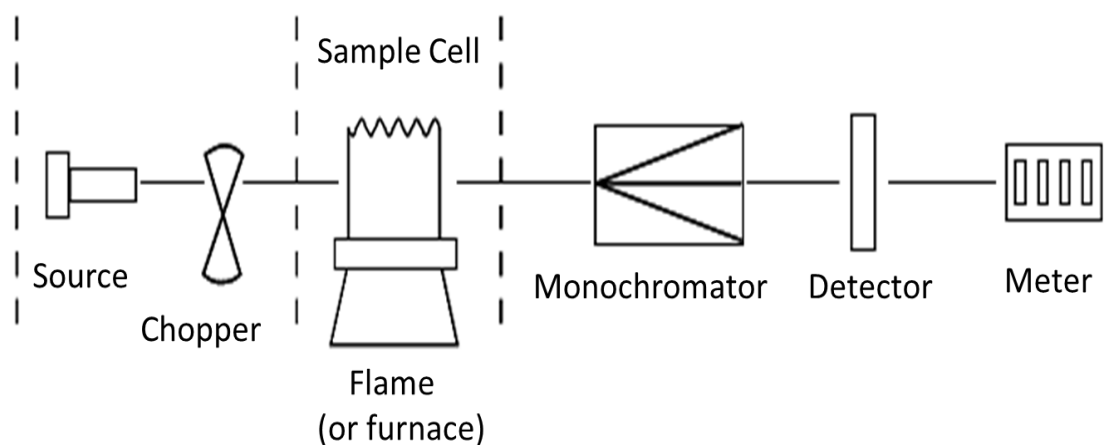


Fig. 3.5 Schematic of atomic absorption spectroscopy [54].

### 3.4 Thermal analysis

The thermal stability of the samples was studied using differential thermal analysis (DTA) and thermogravimetry (TG) [44, 51]. Samples and reference materials were placed in the instrument *NETZSCH STA 449 C* (Max Planck Institute for Chemical Physics of Solids, Dresden) or *NETZSCH STA 409 EP* (Technische Universität Darmstadt) thermal analyzer. 20 mg of sample was used for each measurements. Alumina powder was used as the reference material. To measure air sensitive samples a *NETZSCH STA 449 C* instrument was used where niobium crucibles with lids were used. To measure the air stable compounds a *NETZSCH STA 409 EP* instrument was used with alumina crucibles. In a DTA measurement, the temperature difference between the sample and the reference material is monitored during heating and the heat either emitted or absorbed explains the exothermic or endothermic events. Using this method the reaction temperatures, melting point or decomposition point can be determined. The DTA curve can also give details of the transformations such as

---

crystallization, sublimation, glass transition etc. TG gives details about the weight loss or gain due to various changes such as oxidation, dehydration, decomposition etc. TG explains the thermal stability of the sample. The combination of DTA and TG is connected to a program controlled furnace and the measurements can be done under argon atmosphere. Samples were heated with a specific heating rate (10 K/min) and then cooled down to room temperature with the same rate.

### 3.5 Density measurement

The densities of the compacted samples were determined using an *AccuPyc II 1340* gas pycnometer, the schematic of which is shown in the fig. 3.6. This works with the gas expansion principle. Helium is employed for this purpose. There are two chambers with volumes  $V_1$  and  $V_2$ . By filling them with helium gas the volumes can be determined. The pressures  $P_1$  and  $P_2$  are related to the volumes as follows,

$$P_1 (V_1 + V_2) = P_2 V_1$$

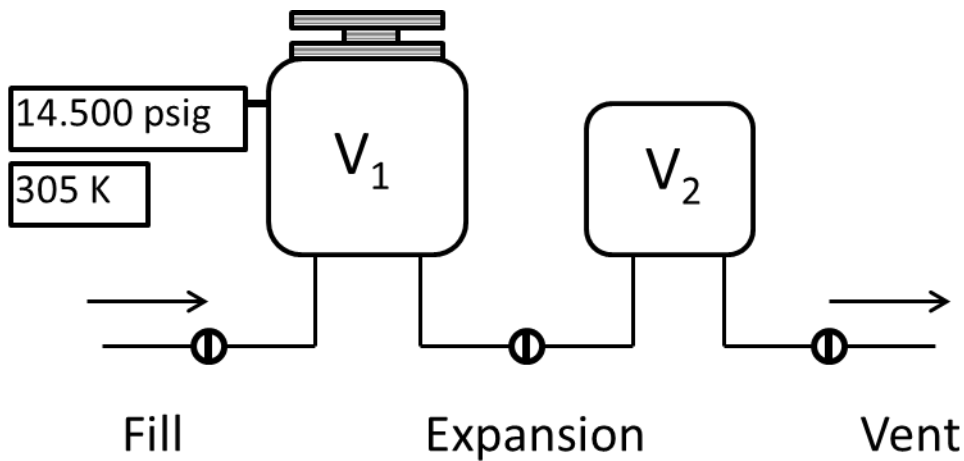
$$\frac{P_1}{P_2} = \frac{V_1 + V_2}{V_1}$$

When the sample with volume  $V_s$  is placed in the first chamber as seen in fig. 3.6. b,

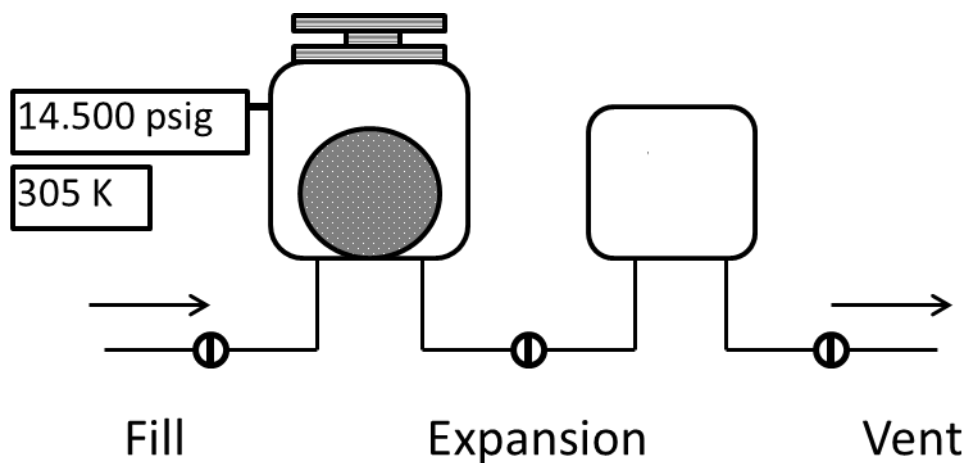
$$\frac{P_1}{P_2} = \frac{(V_1 - V_s) + V_2}{(V_1 - V_s)}$$

$$V_s = V_1 - \frac{V_2}{\left(\frac{P_1}{P_2}\right) - 1}$$

Thus the volume of the sample is calculated and divided from the mass of the sample to determine the density. The measurements were repeated for ten times and the average value was taken as density of the sample.



a)



b)

Fig. 3.6. Schematic of gas pycnometer used for density measurements that work with helium. a) chambers filled by helium b) chambers with sample and helium [55].

### 3.6 Measurement of thermoelectric properties

To study the thermoelectric efficiency of any material, it is important to understand the thermoelectric effect and the figure of merit ( $ZT$ ). Investigations of properties which influence  $ZT$  are the Seebeck coefficient, the electrical conductivity and the thermal conductivity. Details are discussed in this section. When there is a temperature gradient, the conversion of temperature difference into electricity is known as thermoelectric effect and also the thermoelectric effect can be described as the conversion of electricity to temperature difference. When there is a temperature gradient, the thermoelectric device can create voltage between two sides of the device. Alternatively, it can produce a temperature difference when voltage is supplied [56]. Fig. 3.7 shows the schematic representation of a thermoelectric generator with hot and cold ends.

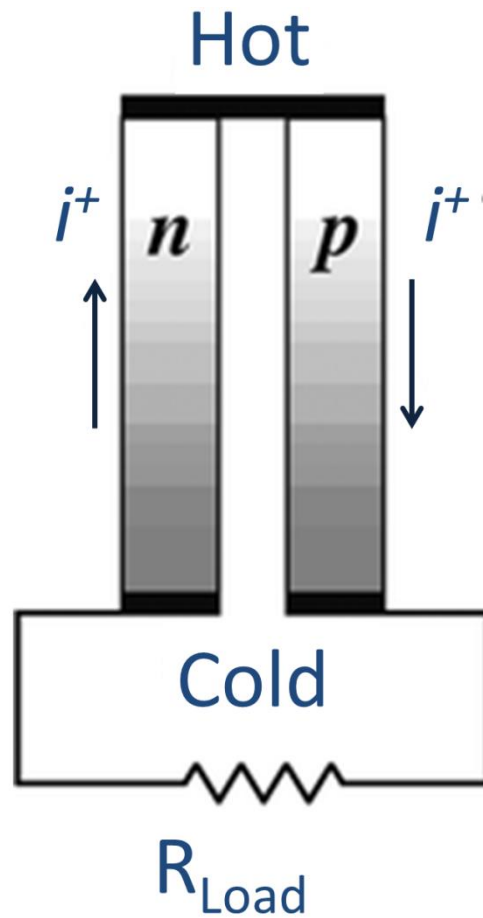


Fig. 3.7 Schematic of a thermoelectric generator with hot and cold ends [6].

The thermoelectric effect includes three major effects comprehensively such as Seebeck effect, Peltier effect and Thomson effect [57]. In 1821, the German physicist Thomas Johann Seebeck discovered the Seebeck effect. When there is a closed loop of two different metals and they meet at two different ends with a temperature difference between the junctions, a compass needle can be deflected. This was called as thermomagnetic effect in the beginning. Later, it was observed that this effect creates an electric current and magnetic field, so the current produced was called as thermoelectric current. The Seebeck coefficient can be simply defined as,

$$\alpha = \Delta V / \Delta T$$

$\alpha$  is the Seebeck coefficient (thermopower),  $\Delta V$  is the voltage difference and  $\Delta T$  is the temperature difference. In general, Seebeck coefficients can vary as a function of temperature and strongly depend on carrier concentration and thus the composition

---

of the material, so doping can seriously affect the Seebeck coefficient [38, 59]. Positive values of the Seebeck coefficient indicate  $p$ -type conduction and negative values of Seebeck coefficient indicate  $n$ -type conduction. Seebeck coefficients may range in value from  $-100 \mu\text{V/K}$  to  $+1000 \mu\text{V/K}$ . Higher values lead to better performance in general, but to achieve efficiency the optimum values must be found.

The thermoelectric efficiency of any material can be described as dimensionless figure of merit value which is always mentioned as  $ZT$ . Values close to 1 or above 1 indicate good thermoelectric efficiency.

$$ZT = \frac{\alpha^2 \sigma T}{\kappa}$$

$\sigma$  is the electrical conductivity and  $\kappa$  is the thermal conductivity.  $\alpha^2 \sigma$  is referred as power factor. To achieve high figures of merit, the Seebeck coefficient should be high and that can be found in low carrier concentration insulators or semiconductors. Electric conductivity should also be high and that can be found in high carrier concentration metals. But the thermal conductivity must be as low as possible as in the case of insulators. To obtain a large Seebeck value, the system should possess a single type of charge carriers. Carrier concentration is an important parameter that influences the transport properties. Higher carrier concentration leads to high electrical conductivity because of more number of charge carriers. The following equation [16] gives the relationship between Seebeck and other properties,

$$\alpha = \frac{8 \pi^2 K_B^2 m^* T}{3 e h^2} \left( \frac{\pi}{3n} \right)^{\frac{2}{3}}$$

where  $n$  is the carrier concentration and  $m^*$  is the effective mass of the carrier. The electrical resistivity ( $\rho$ ) or the inverse of electrical conductivity can be related to  $n$  along with the carrier mobility  $\mu$ :

$$\sigma = \left( \frac{1}{\rho} \right) = n e \mu$$

The effective mass ( $m^*$ ) is another important factor that determines thermoelectric efficiency. A large effective mass leads to higher Seebeck values but this lowers the electrical conductivity. Large mass reduces the electrical mobility ( $\mu$ ) as the charge

---

carriers move with a slow velocity which leads to the reduction in conductivity. The relationship between effective mass and mobility is difficult to understand. This can be influenced by many other factors such as anisotropy, scattering, electronic structure etc. When there are flat, narrow bands with high density of states at the Fermi surface, the effective mass can be increased. The carrier mobility [16] can be described by the following equation,

$$\mu = \frac{\zeta e}{m_i^*}$$

$\zeta$  is the time between scattering events. The mobility can be reduced by many scattering sources such as crystal defects, ionized impurities, extended defects, grain boundaries, lattice vibrations, distorted spin states etc.

Thus, measurements of Seebeck coefficient and electrical conductivity help to study the compound's thermoelectric behavior and to calculate the overall figure of merit. High temperature Seebeck and resistivity measurements were carried out using the instrument *LSR-3*, *Linseis*, Technische Universität Darmstadt [29, 110] that is shown in fig. 3.8. Some of the samples were measured using another setup, *ZEM-3*, *Ulvac-Riko*, Max Planck Institute for Chemical Physics of Solids, Dresden for which disks of densified samples with 8 mm diameter and 2 mm thickness were used. The samples were vertically positioned between two electrodes and then two thermocouples were connected to the side of the samples. This device utilizes platinum-rhodium/platinum thermocouples. The chamber is closed with a quartz cover that allows evacuating and purging argon. The furnace surrounding this part heats the sample to the specific temperature. The heater at the bottom of the lower electrode creates a temperature gradient. The two touching thermocouples measure the accurate temperatures  $T1$  and  $T2$ . Seebeck coefficients and resistivities were measured as the functions of temperature.



Fig. 3.8 Seebeck/resistivity measurement with a *Linseis LSR-3* instrument [110].

Thermal conductivity is another property that affects the overall figure of merit to a great extent. It is a sum of electronic (electrons and holes transporting heat) and lattice thermal (phonons travelling through the lattice) conductivities [1]. The electronic thermal conductivity can be derived from Wiedemann-Franz law,

$$\kappa = L \sigma T = n e \mu L T$$

$$\kappa = \kappa_e + \kappa_l$$

$L$  is the Lorenz factor ( $2.4 \times 10^{-8} \text{ J}^2 \text{ K}^{-2} \text{ C}^{-2}$ ). Glass is the material which shows one of the lowest thermal conductivities. In glass thermal transport is not generally considered as phonon transport through the lattice but it is considered as a random walk of energy through the lattice. The thermal conductivity of glass is known as  $\kappa_{\min}$  [88]. But glass is not a good thermoelectric material due to the lack of electronic conductivity. An efficient thermoelectric material should possess a crystal structure that can support the transport of charge and enhance the electrical conductivity and that is also capable of scattering the phonons without affecting electrical conductivity. This unusual property is well known as electron crystal-phonon glass behavior [4]. Such a behavior might be a compromise between a high Seebeck (or high electrical conductivity) and a low thermal conductivity. Many thermoelectric materials are doped with elements which are isovalent, so that the crystal and the electronic

---

structures are preserved. At the same time a mass contrast scatters phonons and the thermal conductivity drops significantly. The relationship between thermal conductivity and carrier concentration should always be analyzed because the balance between these two properties determines the overall figure of merit  $ZT$ .

The thermal diffusivity ( $a$ ) and heat capacity ( $C_p$ ) were measured using a laser flash apparatus (*Netzsch LFA 457*, Max Planck Institute for Chemical Physics of Solids, Dresden, or *Linseis LFA 1000*, Technische Universität Darmstadt) that is shown in the fig. 3.9. The thermal conductivity was then calculated using the following equation,

$$\kappa = a C_p \rho_v$$

$\rho_v$  is the density of the compacted sample. A disk like sample with diameter of 10 mm was used for the measurements in *Linseis LFA 1000*. Samples with 8 mm diameter were used for the measurements in *Netzsch LFA 457*. The compacted sample was placed inside the sample holder and positioned in the laser flash unit. The chamber was closed and the measurements were carried out under the argon atmosphere.



Fig. 3.9 Thermal conductivity/thermal diffusivity measurement with a *Linseis LFA 1000* instrument [110].

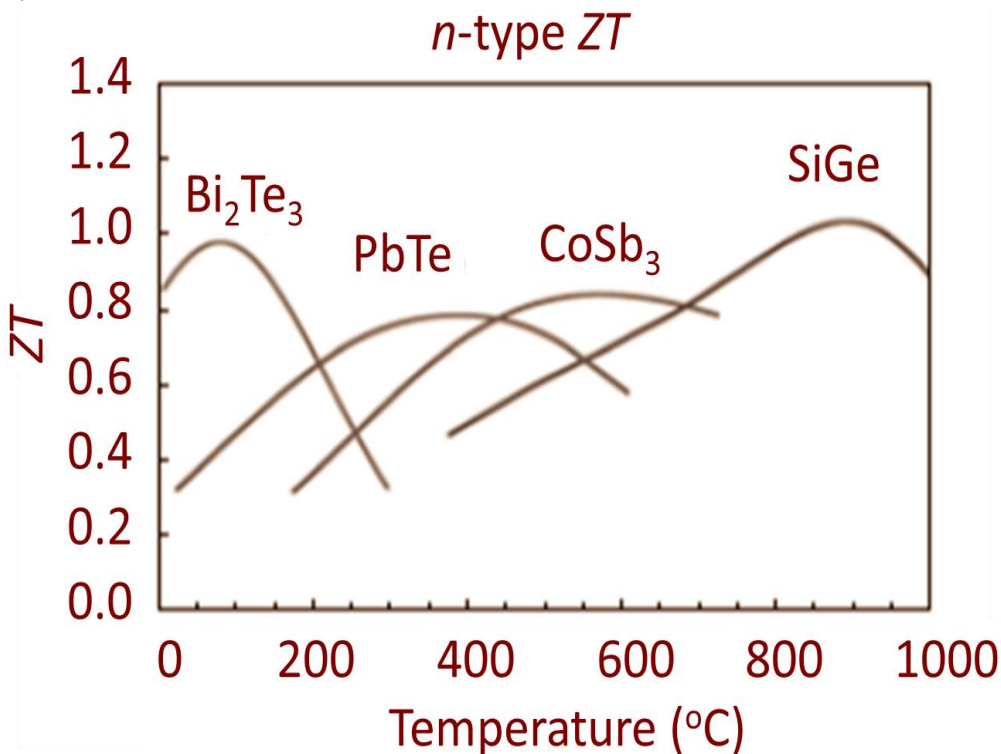
---

## 4 Literature/ State of the art

---

Zintl phases are well-known compounds in solid state chemistry but less studied than other classes of solids like oxides. Some of them exhibit interesting thermoelectric properties. Achieving high figures of merit is important to produce an efficient thermoelectric material and it is possible with neither metals nor insulators. It is only possible with semiconductors to bring a balance between Seebeck coefficients and thermal conductivity. Usually semiconductors or heavily doped semiconductors are showing relatively high values of the figure of merit. Improving the electronic and thermal properties can enhance the figure of merit [60-63]. For example,  $\text{Bi}_2\text{Te}_3$  (*n*-type) and  $\text{Sb}_2\text{Te}_3$  (*p*-type) alloys are the widely used thermoelectric materials [64-67]. Especially  $\text{Bi}_2\text{Te}_3$  is used for the refrigeration and heat recovery near the room temperature (up to 200 °C). These materials have high values of the figure of merit [68-75]. Fig. 4.1. a and b show different *n*- and *p*-type materials with high figure of merit values.

a)



b)

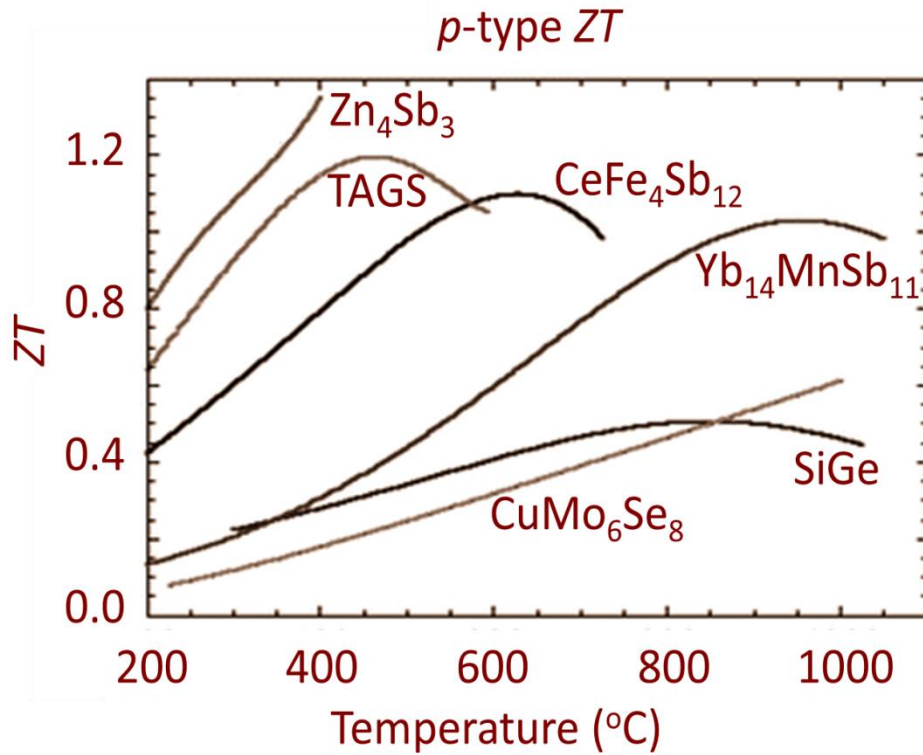


Fig. 4.1. (a)  $ZT$  of  $n$ -type materials (b)  $ZT$  values of  $p$ -type materials [1, 6].

The carrier concentration of  $Sb_2Te_3$  and  $Bi_2Se_3$  can be finely tuned and also the lattice thermal conductivity can be reduced by means of doping.  $(Sb_{0.8}Bi_{0.2})_2Te_3$  is the most studied  $p$ -type phase and  $Bi_2(Te_{0.8}Se_{0.2})_3$  is the one with  $n$ -type conductivity.  $ZT$  values of these materials vary from 0.8 to 1.1. Some of the highest  $ZT$  values of commercial thermoelectric materials and those developed or produced by NASA (National Aeronautics and Space Administration, USA) are given in fig. 4.1. a and b for both  $n$ -type and  $p$ -type materials.

Semimetals do not often show good thermoelectric properties due to the coexistence of both type of charge carriers (electrons and holes or  $n$ -type and  $p$ -type conduction) [76]. Cation vacancies or anion vacancies can bring a change in their properties. Cation vacancies usually do not change the number of states in the valence band but they can change the number of electrons added to the system [77-79]. In the case of  $PbTe$ , the tellurium content can be changed by controlling the  $Te$  vapor pressure [80]. Carrier concentration can also be modified by means of doping. For example, the high temperature thermoelectric material  $Si_{0.8}Ge_{0.2}$  can of course be doped with any

element which has one electron less than Si or Ge like boron or more like phosphorus. These changes can render the material *p*-type or *n*-type conduction. Zintl compounds like  $\text{Yb}_{14}\text{AlSb}_{11}$  were studied where  $\text{Mn}^{2+}$  substituted  $\text{Al}^{3+}$  to increase the *p*-type conduction of this compound [77].

Materials with carrier concentration in the range of  $10^{19}$ - $10^{21}$  carriers/ $\text{cm}^3$  are considered to be having the optimum values. These values are often shown by heavily doped semiconductors. For example,  $\text{Ba}_8\text{Ga}_{16-x}\text{Ge}_{30+x}$  was used to investigate the relationship between the carrier concentration and the electronic properties [16]. The effect of carrier concentration on figure of merit values were also taken into account [16]. Fig. 3.9. shows the effect of carrier concentration on Seebeck coefficients, electrical conductivity, thermal conductivity and figure of merit in  $\text{Ba}_8\text{Ga}_{16-x}\text{Ge}_{30+x}$ . According to fig. 4.2,  $10^{19}$ - $10^{21}$   $\text{cm}^3$  is the optimum range to achieve high figure of merit values [16].

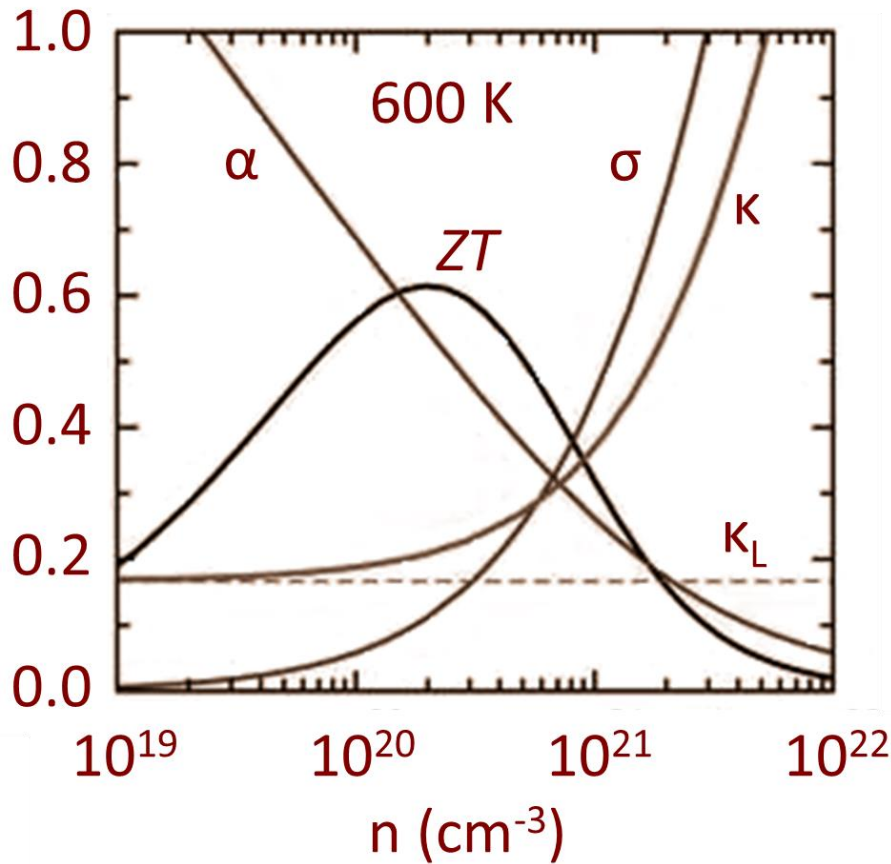


Fig. 4.2 Effect of carrier concentration on thermoelectric properties and  $ZT$  for  $\text{Ba}_8\text{Ga}_{16-x}\text{Ge}_{30+x}$  [16].

---

Electronic structure and band structure calculations are also very important to understand the behavior of the thermoelectric materials. Often narrow band gap semiconductors were proved to be the right choices. Many good thermoelectric compounds have their Fermi level near the edge of the band gap.

When the difference in electronegativity is small, the chances of having low effective mass and high mobility are higher for binary semiconductors such as IrSb<sub>3</sub> which has the effective mass  $\mu = 1320 \text{ cm}^2/\text{Vs}$ ,  $(m^*/m_e) = 0.17$  at 300 K. At the same time low mobility and high effective mass can be found for ionic materials, an example being Fe<sub>x</sub>Cr<sub>3-x</sub>Se<sub>4</sub> which has  $\mu = 0.1 \text{ cm}^2/\text{Vs}$ ,  $(m^*/m_e) = 4$  at 300 K [71, 81, 82]. Doping can alter the carrier effective mass as in the case of PbTe. Tl doped PbTe shows higher hole effective mass than the Na doped PbTe samples [60]. Although the effective mass increase leads to the reduction in mobility, overall thermoelectric efficiency could be improved. Other examples for this observation are Ba<sub>8</sub>M<sub>y</sub>Ga<sub>x</sub>Ge<sub>46-x-y</sub>, Ba<sub>8</sub>Cu<sub>x</sub>Ga<sub>16-3x</sub>Ge<sub>30+2x</sub> and Ba<sub>8</sub>Ga<sub>x</sub>Ge<sub>46-x</sub> [83-87].

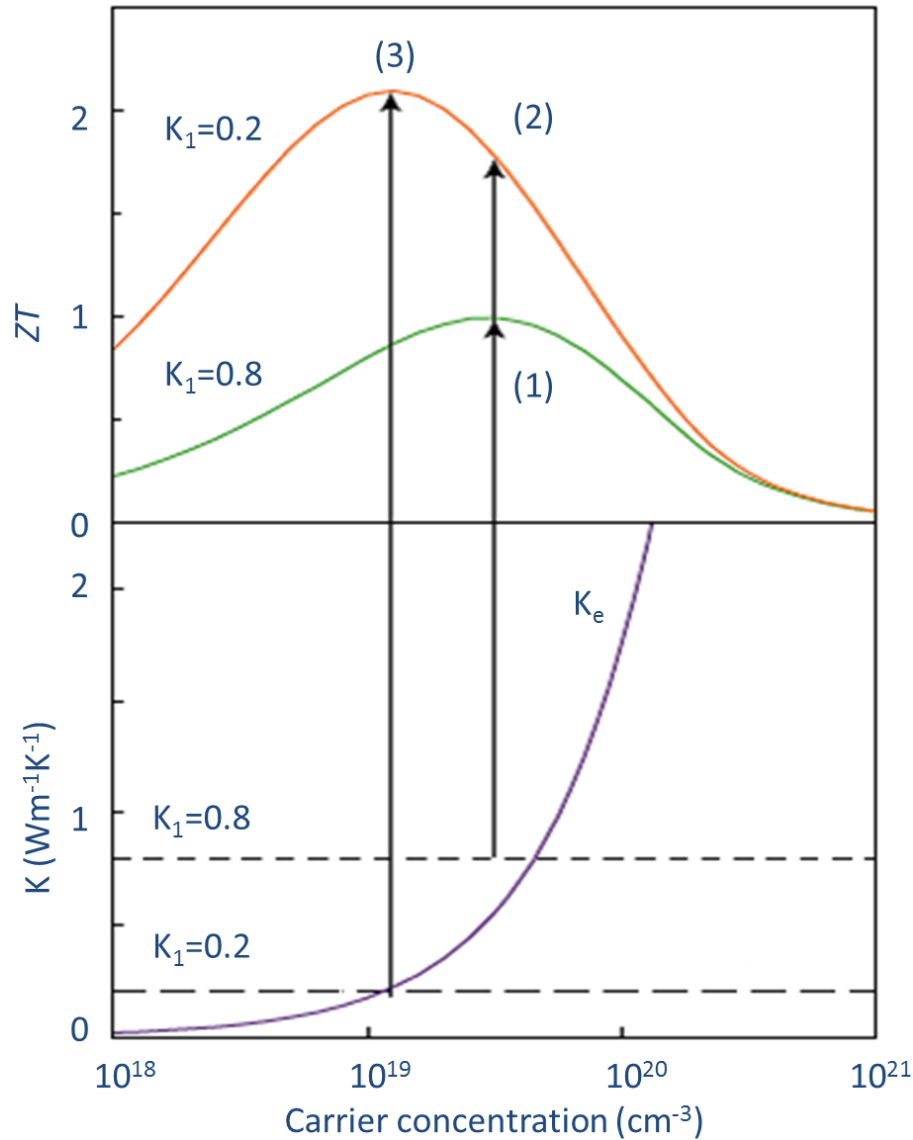


Fig. 4.3 Relationship between thermal conductivity and carrier concentration in enhancing  $ZT$  [1].

Fig. 4.3 explains how  $ZT$  is enhanced when thermal conductivity is reduced for the model system  $\text{Bi}_2\text{Te}_3$  [89]. At point (1)  $ZT$  is less with higher thermal conductivity  $K_1 = 0.8 \text{ W m}^{-1} \text{ K}^{-1}$  and at point (2),  $ZT$  increases two fold when thermal conductivity drops to  $0.2 \text{ W m}^{-1} \text{ K}^{-1}$ . Point (3) shows the maximum  $ZT$  and the optimum values of carrier concentration. Point defects can help to reduce thermal conductivity since they create local strain or mass contrast, so phonons can easily be scattered. For example in  $\text{La}_{3-x}\text{Te}_4$  and in some clathrates these vacancies lead to the scattering of phonons thereby reducing thermal conductivities. In cage-like compounds like clathrates and skutterudites there can be rattling atoms [90-93]. These atoms are able

to decrease thermal conductivity by scattering the phonons with their rattling motion within a cage. Diffraction techniques [94] can give evidence for this from the large atomic displacement parameters. Unit cells which are large in size can confine phonons in a small fraction of the vibrational states and so reduce the thermal conductivity. Large and complex unit cells can also reduce lattice thermal conductivity. The complex structure leads to the change of the band gap. Altering the effective mass can enhance the possibilities to find a better material. Near room temperature, thallium based materials like  $\text{Ag}_9\text{TlTe}_5$  and  $\text{Tl}_9\text{BiTe}_6$  show very low thermal conductivity values that are close to  $0.23 \text{ W m}^{-1} \text{ K}^{-1}$  [58, 69, 95-102]. Fig. 4.4 shows the various thermoelectric materials exhibiting very low thermal conductivities.

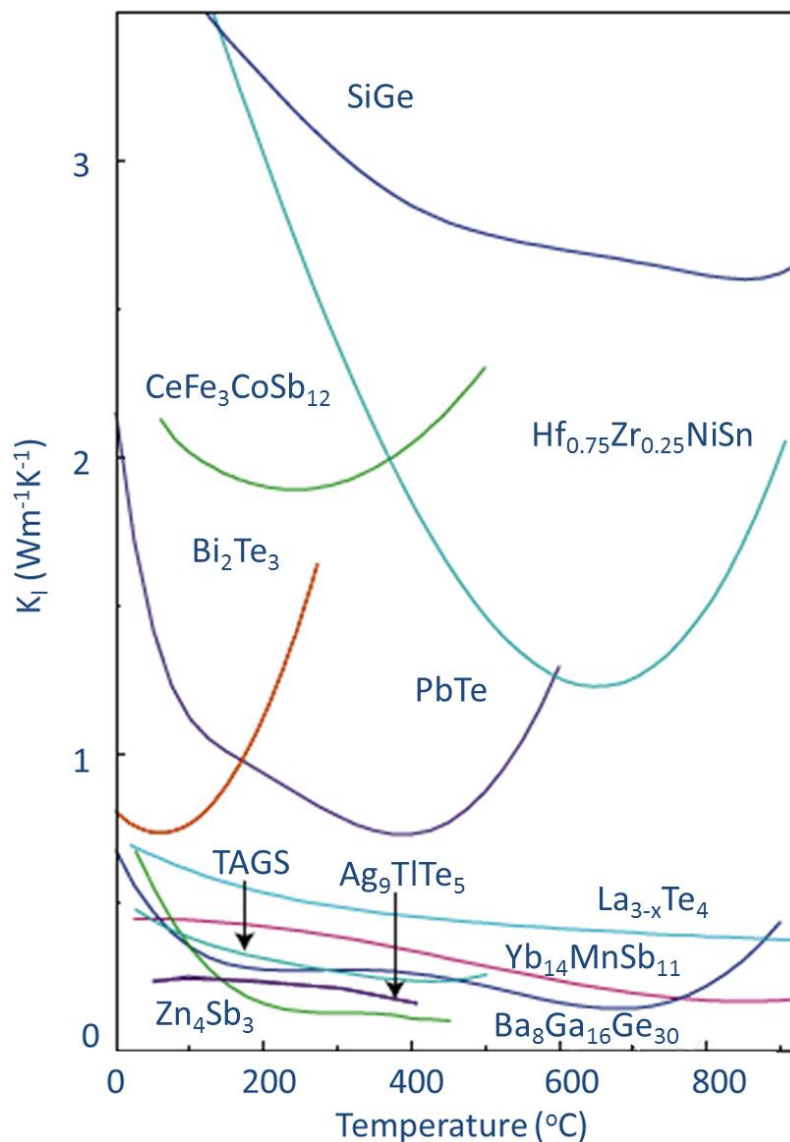


Fig. 4.4 Low thermal conductivities found in various thermoelectric materials [1].

When the unit cells of Zintl phases are large and their crystal structures are complex then the lattice thermal conductivities are found to be low in many systems [16, 76, 77, 103]. Fig. 4.5 shows the lattice thermal conductivities of variety of antimonides with respect to their unit cell volumes where the dashed line indicates the inverse dependence on primitive cell volume [1, 76, 78, 103-109]. It is clear from fig. 4.5 that the lattice thermal conductivity decreases with increasing unit cell volume. Similar observations are found in other complex compounds with large unit cells. On the other hand, the Zintl compounds with small unit cells can also show low thermal conductivities when there are other scattering mechanisms such as alloy scattering.

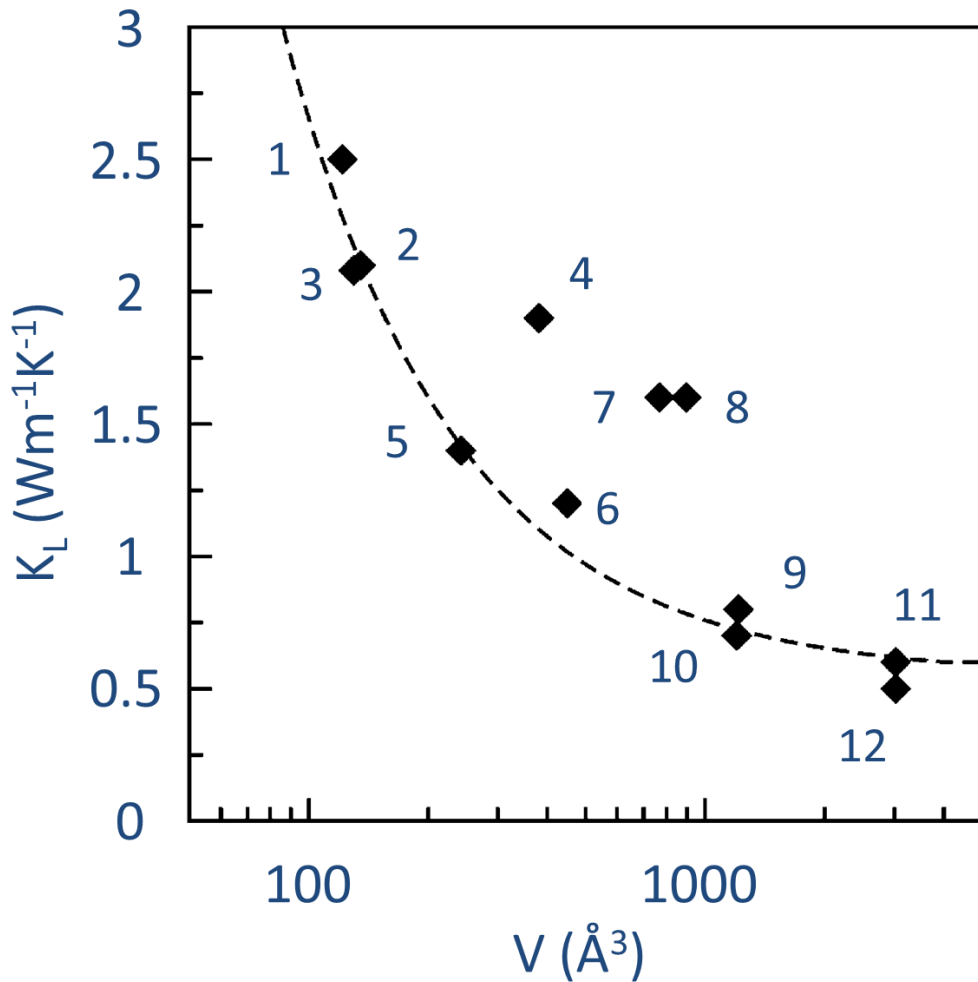


Fig. 4.5 Lattice thermal conductivities of a variety of Zintl antimonides at 300 K. (1-LiZnSb, 2-SrZn<sub>2</sub>Sb<sub>2</sub>, 3-Mg<sub>3</sub>Sb<sub>2</sub>, 4-CeFe<sub>4</sub>Sb<sub>12</sub>, 5-BaZn<sub>2</sub>Sb<sub>2</sub>, 6-SrZnSb<sub>2</sub>, 7-Yb<sub>5</sub>In<sub>2</sub>Sb<sub>6</sub>, 8-Ba<sub>4</sub>In<sub>8</sub>Sb<sub>16</sub>, 9-Yb<sub>11</sub>Sb<sub>10</sub>, 10-Yb<sub>11</sub>GaSb<sub>9</sub>, 11-Yb<sub>14</sub>AlSb<sub>11</sub>, 12-Yb<sub>14</sub>MnSb<sub>11</sub>) [16].

Thus, Zintl phases exhibit interesting thermoelectric properties such as the other well-known thermoelectric compounds. The preparation and thermoelectric study of ternary Zintl phases is expected to be interesting and useful to achieve efficient thermoelectric materials for the future. Recently, Zintl phases from the  $A_3MPn_3$  family of compounds such as  $Ca_3AlSb_3$  and  $Sr_3AlSb_3$  were reported in the literature and their thermoelectric properties were studied [123, 125]. They exhibit high figure of merit values ( $ZT$ ) when they are doped.  $Ca_3AlSb_3$  exhibits  $ZT$  of 0.8 around 1050 K and  $Sr_3AlSb_3$  exhibits  $ZT$  of 0.3 around 600 K when they were doped with Zn at the sites of aluminum. Aluminum sites can also be doped by Mn [123, 124], and alkaline earth metals [136] and the antimony sites can be doped for further studies too. In this work Ba-Al-Sb, Ba-Ga-Sb, Ba-In-Sb phases have been studied.  $Ba_3AlSb_3$  is one of the well-known Zintl compounds of the  $A_3MPn_3$  family (A = Alkaline earth metals, M = Triels, Pn = Pnictogens). The structure of  $Ba_3AlSb_3$  was reported by Cordier et al. in 1982 [111]. The structure of  $Ba_3AlSb_3$  was determined from single crystals but a method to produce monophasic powder sample was not known. According to literature [111] stoichiometric amounts of elements were loaded under argon atmosphere in a corundum container which was then sealed by a quartz tube after evacuation. This assembly was heated for 12 hours to reach 770 K. After few hours it was heated to 1200 K for 20 minutes. Then, it was cooled down to 900 K in 12 hours and later quenched in water. An air sensitive product with metallic grey color was found that contained  $Ba_3AlSb_3$  along with other side phases.  $Ba_3AlSb_3$  crystallizes in the orthorhombic crystal system with space group  $Cmce$  (no. 64). Table 4.1 and 4.2 give the crystallographic data of this compound.

Table 4.1 Crystallographic data of  $Ba_3AlSb_3$  [111].

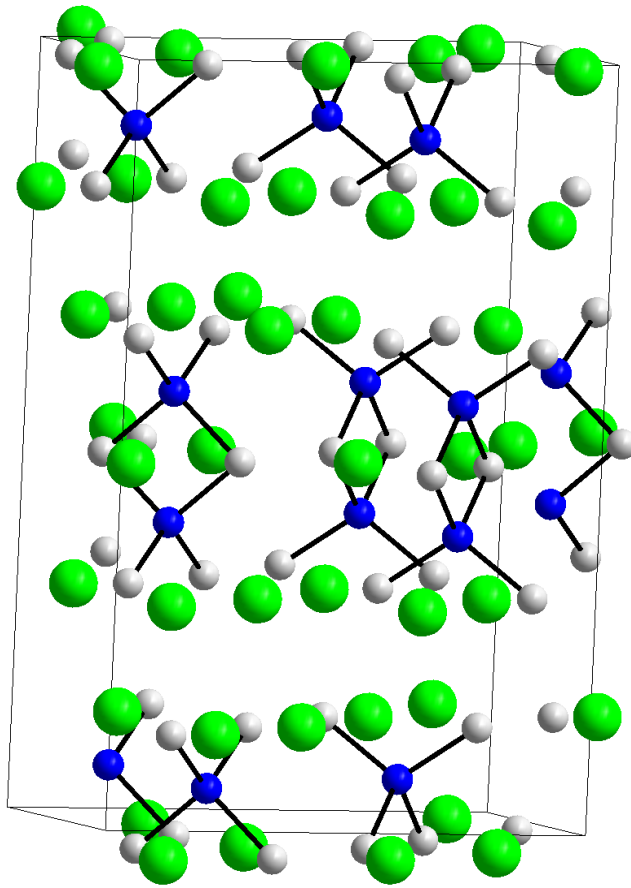
Molecular formula	$Ba_3AlSb_3$
Molecular weight (g/mol)	803.41
Crystal system	Orthorhombic
Space group	$Cmce$ (No. 64)
$a$ (Å)	21.133 (10)

$b$ (Å)	7.194 (5)
$c$ (Å)	14.069 (8)
Volume (Å <sup>3</sup> )	2138.9
$Z$	8
Density (g/cm <sup>3</sup> )	4.998

Table 4.2 Atomic coordinates and Wyckoff positions of Ba<sub>3</sub>AlSb<sub>3</sub> [111].

Atom	Wyck.	$x/a$	$y/b$	$z/c$
Ba1	8 <i>f</i>	0	0.1846(1)	0.6484(1)
Ba2	16 <i>g</i>	0.3256(1)	0.1940(1)	0.1293(1)
Sb1	8 <i>f</i>	0	0.7049(2)	0.6010(1)
Sb2	16 <i>g</i>	0.3412(1)	0.7000(2)	0.1198(1)
Al1	8 <i>d</i>	0.9150(4)	0	0

a)



b)

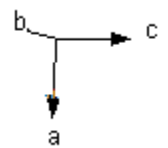
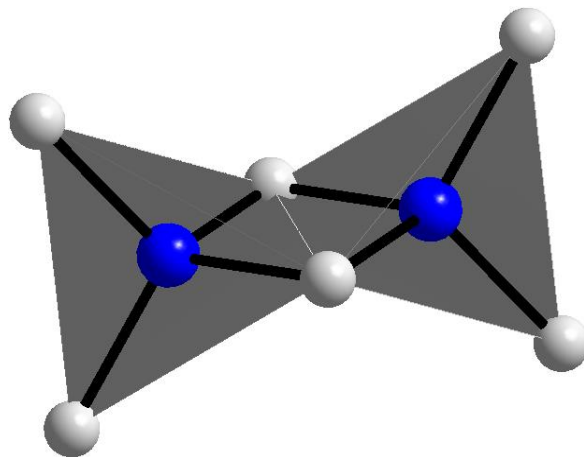


Fig. 4.6 a) Unit cell of  $\text{Ba}_3\text{AlSb}_3$  b) Dimer  $(\text{Al}_2\text{Sb}_6)^{12-}$ , Barium atoms are green, aluminum atoms are blue and antimony atoms are grey in color [111].

Fig. 4.6. a, shows the unit cell structure of  $Ba_3AlSb_3$ . The aluminum atoms are connected to four antimony atoms and form tetrahedra. Two 'AlSb<sub>4</sub>' tetrahedra are connected by sharing an edge and thereby they form a dimer which is shown in fig. 4.6. b. Barium cations balance the charges. According to the Zintl concept aluminum atoms with four neighbors carry a single negative charge ( $Al^-$ ), the edge sharing antimony atoms carry a single negative charge ( $Sb^-$ ) and the four terminal antimony atoms (single bonded) carry two negative charges ( $Sb^{2-}$ ). The anionic dimer can be described as  $(Al_2Sb_6)^{12-}$ . Six barium ions compensate the charges. Thus,  $Ba_3AlSb_3$  can be described as  $[3 Ba^{2+} Ga^{1-} Sb^{1-} 2 Sb^{2-}]$  according to the Zintl formalism.

Further compounds of  $A_3MPn_3$  type were investigated before in the field of Zintl chemistry (A = Alkaline earth metals, M = Triels, Pn = Pnictogens).  $Sr_3GaSb_3$  was studied in literature and found to be showing high values of the figure of merit when doped with zinc at the sites of gallium [129]. This compound exhibits figure of merit of 0.9 around 1000 K.  $Ba_3GaSb_3$  is one of the well-known Zintl compounds. Its structure was reported by Cordier et al. in 1985 [112]. This compound is isostructural to  $Ba_3AlSb_3$ . According to the literature the crystals were obtained by loading the required elements in corundum containers under argon atmosphere which were then sealed in a quartz tube. This assembly was heated to 1270 K with a heating rate of 100 K/hour. After seven days the reaction mixture was cooled down to room temperature with a cooling rate of 50 K/hour. The air sensitive, metallic grey product contained  $Ba_3GaSb_3$  crystals along with side phases. Table 4.3 and 4.4 give the crystallographic data of  $Ba_3GaSb_3$ .

Table 4.3 Crystallographic data of  $Ba_3GaSb_3$  [112].

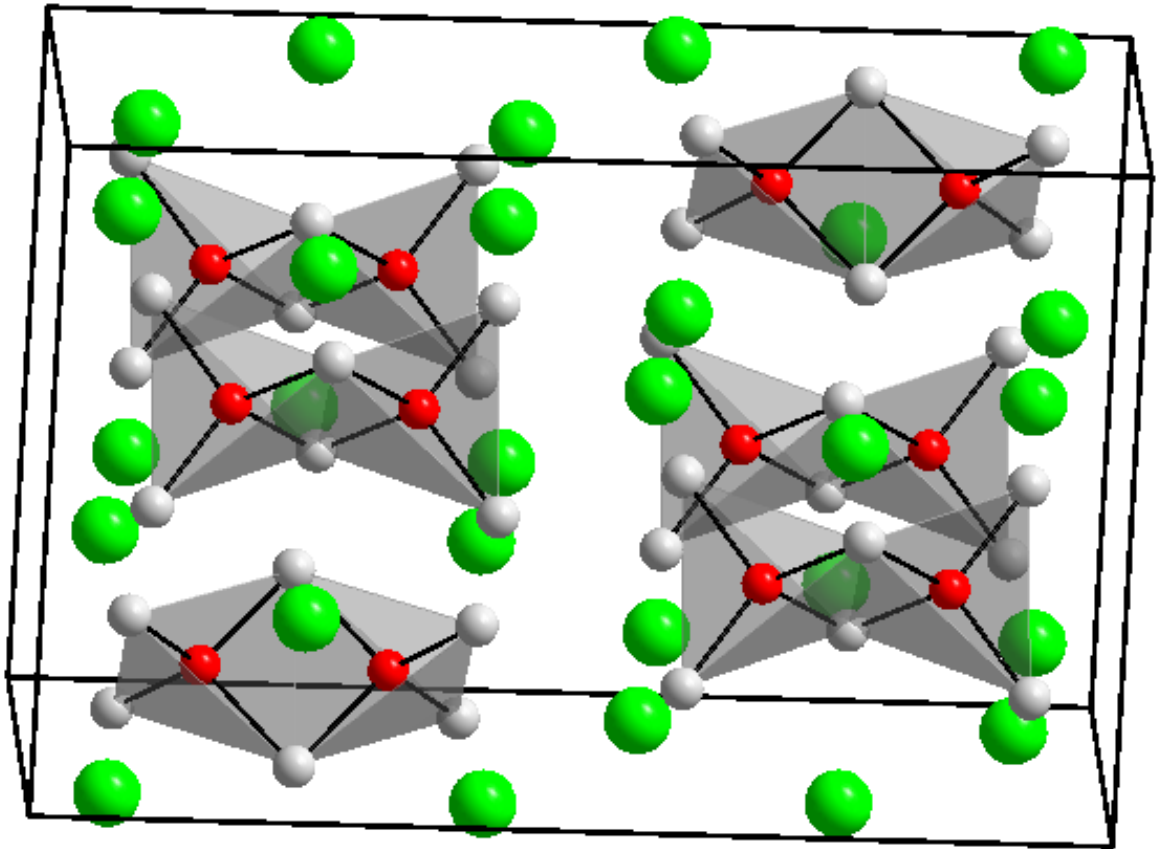
Molecular formula	$Ba_3GaSb_3$
Molecular weight (g/mol)	845.35
Crystal system	Orthorhombic
Space group	<i>Pnma</i> (No.62)
<i>a</i> (Å)	14.118 (5)

$b$ (Å)	21.177 (7)
$c$ (Å)	7.128 (3)
Volume (Å <sup>3</sup> )	2130.0
$Z$	8
Density (g/cm <sup>3</sup> )	5.28

Table 4.4 Atomic coordinates and Wyckoff positions of Ba<sub>3</sub>GaSb<sub>3</sub> [112].

Atom	Wyck.	$x/a$	$y/b$	$z/c$
Ba1	8 <i>d</i>	0.0095(1)	0.4235(1)	0.7716(2)
Ba2	8 <i>d</i>	0.7371(1)	0.4236(1)	0.1943(2)
Ba3	4 <i>c</i>	0.7346(2)	0.25	0.8022(3)
Ba4	4 <i>c</i>	0.0168(2)	0.25	0.1754(3)
Ga1	8 <i>d</i>	0.8739(2)	0.1632(1)	0.4848(4)
Sb1	4 <i>c</i>	0.7678(2)	0.25	0.2904(4)
Sb2	4 <i>c</i>	0.9810(2)	0.25	0.6806(4)
Sb3	8 <i>d</i>	0.5135(1)	0.9097(1)	0.7691(3)
Sb4	8 <i>d</i>	0.2587(1)	0.0895(1)	0.8012(3)

a)



b)

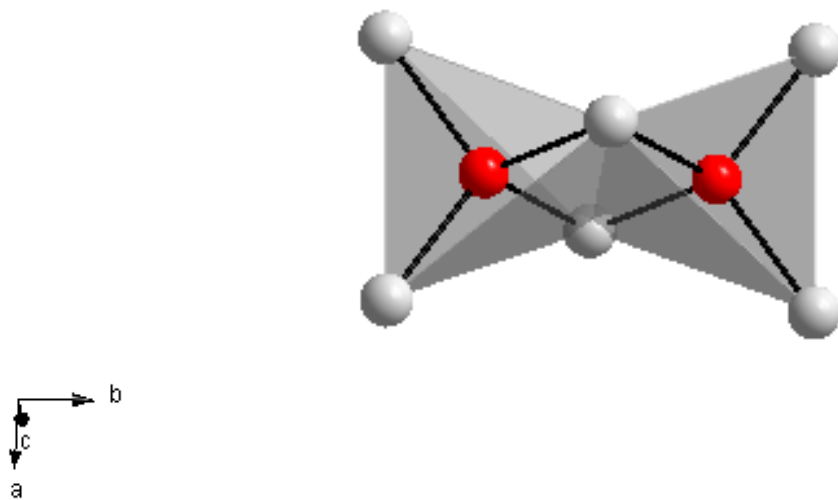


Fig. 4.7 (a) Unit cell of  $\text{Ba}_3\text{GaSb}_3$ , (b)  $(\text{Ga}_2\text{Sb}_6)^{12-}$  dimer formed by Ga and Sb atoms (Ba atoms are green, Ga atoms are red and Sb atoms are grey) [112].

---

$\text{Ba}_3\text{GaSb}_3$  crystallizes in the orthorhombic system with space group  $Pnma$  (No. 62) [112]. Among the  $\text{A}_3\text{MPn}_3$ -type compounds two structural patterns ( $\text{Ca}_3\text{InP}_3$ -type and  $\text{Ba}_3\text{AlSb}_3$ -type) are widely known.  $\text{Ca}_3\text{AlSb}_3$  for example exhibits  $\text{Ca}_3\text{InP}_3$ -type structure where the aluminum atoms are connected to four antimony atoms to form a tetrahedron. These tetrahedra are further connected to each other by sharing a corner and form an infinite chain. Calcium ( $\text{Ca}^{2+}$ ) ions balance the charge. But  $\text{Ba}_3\text{GaSb}_3$  exhibits a  $\text{Ba}_3\text{AlSb}_3$ -type structure. In  $\text{Ba}_3\text{GaSb}_3$  the gallium atom is also connected to four antimony atoms to form a tetrahedron ( $\text{GaSb}_4$ ). But the two tetrahedra share a common edge and thereby they form a dimer. The  $\text{Ga}_2\text{Sb}_6^{12-}$  unit is the basic building block of the structure. The structure of the dimer is shown in fig. 4.7. b and the three-dimensional arrangement of  $\text{Ba}_3\text{GaSb}_3$  is shown in fig. 4.7. a. Barium atoms provide electrons to the polymeric anionic network to form bonds. The dimer unit acts as the anionic part of the structure. The gallium ions can form four bonds like group 14 elements. Gallium is assumed to carry a negative formal charge ( $\text{Ga}^-$ ). Antimony atoms that are located at the common edges form two bonds like group 16 elements and so they are assumed to carry one negative formal charge ( $\text{Sb}^-$ ). Antimony atoms in the terminal positions are forming a single bond like halogens, so they carry two negative charges ( $\text{Sb}^{2-}$ ). In total the anionic network carries twelve negative charges that are compensated by six  $\text{Ba}^{2+}$  ions. According to the Zintl formalism this compound can be denoted as  $[\text{3 Ba}^{2+} \text{ Ga}^{1-} \text{ Sb}^{1-} \text{ 2 Sb}^{2-}]$ .

$\text{Ba}_7\text{Ga}_4\text{Sb}_9$  is a unique compound that is not in accordance with the Zintl concept. The formal charge of the anionic network is not equal to -14 though seven barium atoms donate 14 electrons to the anionic structure.  $\text{Ba}_7\text{Ga}_4\text{Sb}_9$  was reported by Cordier et al. in 1986 [113]. This compound crystallizes in the orthorhombic system with space group  $Pmmn$  (No. 59). Stoichiometric amounts of the elements were loaded in a corundum tube and heated to 1270 K with the heating rate of 100 K/hour. Then the reaction vessel was cooled down to room temperature with a cooling rate of 50 K/hour. This method yielded a metallic, dark product that contained  $\text{Ba}_7\text{Ga}_4\text{Sb}_9$ . The compound was found to be air and moisture sensitive. Table 4.5 and 4.6 give the crystallographic data of this compound.

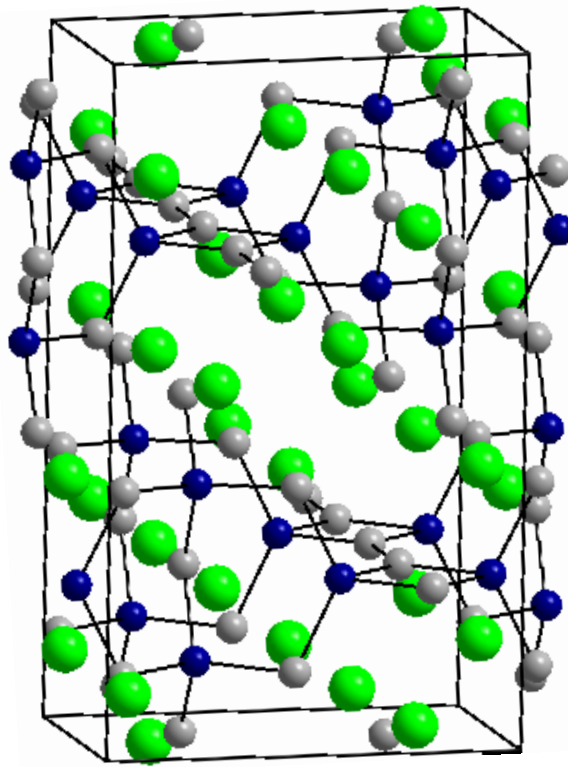
Table 4.5 Crystallographic data of Ba<sub>7</sub>Ga<sub>4</sub>Sb<sub>9</sub> [113].

Molecular formula	Ba <sub>7</sub> Ga <sub>4</sub> Sb <sub>9</sub>
Molecular weight (g/mol)	2329.17
Crystal system	Orthorhombic
Space group	<i>Pmmn</i> (No.59)
<i>a</i> (Å)	18.024 (7)
<i>b</i> (Å)	10.861 (4)
<i>c</i> (Å)	7.100 (3)
Volume (Å <sup>3</sup> )	1389
<i>Z</i>	2
Density (g/cm <sup>3</sup> )	5.58

Table 4.6 Atomic coordinates and Wyckoff positions of Ba<sub>7</sub>Ga<sub>4</sub>Sb<sub>9</sub> [113].

Atom	Wyck.	<i>x/a</i>	<i>y/b</i>	<i>z/c</i>
Ba1	4f	0.0374(1)	0.25	0.0406(1)
Ba2	8g	0.1258(1)	0.4796(1)	0.5438(1)
Ba3	2b	0.25	0.75	0.9207(3)
Ga1	4f	0.8772(1)	0.25	0.7420(4)
Ga2	4e	0.25	0.0684(3)	0.0587(4)
Sb1	8g	0.1175(1)	0.9589(1)	0.0449(2)
Sb2	4f	0.5074(1)	0.25	0.5197(2)
Sb3	2a	0.25	0.25	0.7910(4)
Sb4	2a	0.25	0.25	0.3268(5)
Sb5	2b	0.25	0.75	0.4541(3)

a)



b)

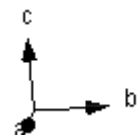
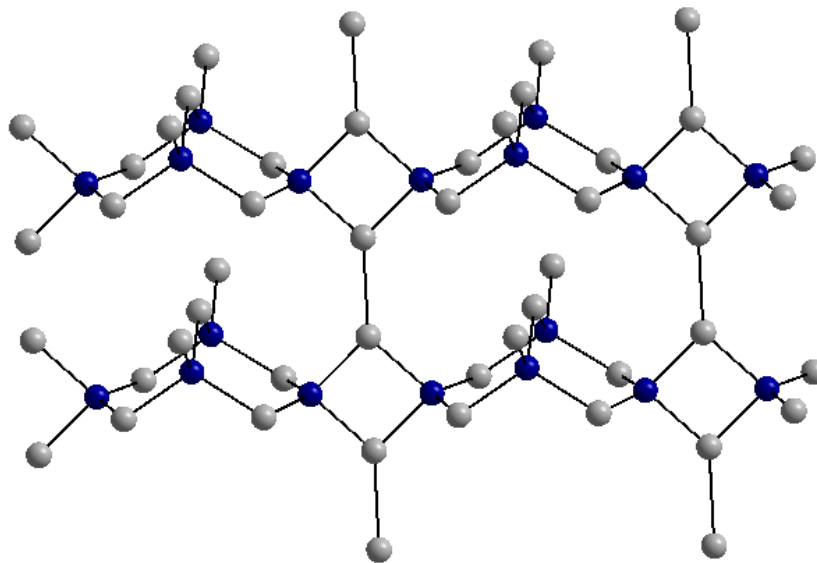


Fig. 4.8 (a) Unit cell of  $\text{Ba}_7\text{Ga}_4\text{Sb}_9$ , (b) Ga-Sb anionic network. (Ba atoms are green, Ga atoms are blue and Sb atoms are grey) [113].

---

Each gallium atom is tetrahedrally surrounded by four antimony atoms.  $\text{Ga}_4\text{Sb}_4$  rings are formed by connecting four of these tetrahedral units. The shape of the ring allows two of the trans-disposed gallium atoms to share another corner. The antimony atom that is located at this corner connects the  $\text{Ga}_2\text{Sb}_2$  fragments to form a bridged bicyclic structure ( $\text{Ga}_4\text{Sb}_5$ ). This structure is analogous to bicyclo [3.3.1] nonane [140]. All gallium atoms are four-fold coordinated in this structure. The antimony atoms located in the ring and the antimony atoms at the bridging position are two foldly coordinated. Every bicyclic ring contains four terminal antimony atoms that are not involved in bridging. The terminal antimony atoms are connecting two bicyclic rings together and help to form a chain like structure with four-membered and bicyclic rings. The chains are further connected by the same antimony atoms that lead to the formation of two-dimensional layers which are shown in the fig. 4.8. b. The three-dimensional structure of  $\text{Ba}_7\text{Ga}_4\text{Sb}_9$  is formed by a stacking of Ga-Sb layers which is shown in fig. 4.8. a. The barium atoms donate electrons and also act as space fillers by occupying octahedral and trigonal-prismatic voids between the layers.

According to the Zintl formalism the four-coordinated gallium atoms are assigned to a single negative charge (-1). Each single-coordinated antimony atom is assigned to two negative charges (-2). Two-coordinated antimony atoms are assigned to single negative charges (-1). But there is a problem regarding the calculation of charges for the antimony atoms that connect Ga-Sb chains and form the layered structure. The distance between two antimony atoms of two chains is 3.296 Å. A Sb-Sb bond distance within the layers of the elemental antimony structure is 2.91 Å, but the Sb-Sb distance between the layers is found to be 3.36 Å. Thus, the Sb-Sb distance in  $\text{Ba}_7\text{Ga}_4\text{Sb}_9$  is found to be longer than some of the bond lengths observed in the elemental structure. This observation leads to two different ways of calculating the formal charges (1) considering the Sb-Sb bond between the layers (2) ignoring Sb-Sb bond between the layers. The formal charge is expected to be -14 to compensate the charge of seven barium cations (+14). When the bond is considered then these antimony atoms can be assigned a formal charge zero as they are three-coordinated. Then the total formal charge of the anionic part is -13 which would be one electron less. If the bond is not considered then these antimony atoms are two foldly coordinated, thus their formal charge can be assigned to be -1. This consideration

leads to the formal charge of -15 for the anionic part which is one electron rich. Either method is not in accordance to the Zintl concept.

Among the  $AM_2Pn_2$ -type compounds  $BaGa_2Sb_2$  is a well-known Zintl compound. It is stable in air.  $BaGa_2Sb_2$  reacts vigorously with water. This compound was reported by M. G. Kanatzidis et al. in 2001 [114]. Other  $AM_2Pn_2$  type compounds such as  $BaGa_2P_2$  and  $BaGa_2As_2$  were also synthesized and reported to be semiconductors. But their thermoelectric properties were not studied in detail [134]. Another compound,  $BaMn_2Sb_2$  was prepared and doped with zinc at the manganese sites. The thermoelectric properties were studied [135]. The power factor of  $BaMn_2Sb_2$  improves with increasing amount of dopant and the maximum value was found to be  $0.063 \mu W C m^{-1} K^{-2}$  around 473 K ( $BaMn_{1.3}Zn_{0.7}Sb_2$ ). According to literature,  $BaGa_2Sb_2$  was synthesized at 1223 K for two days using graphite containers [114]. When the reaction mixture was cooled down to room temperature rod shaped black color single crystals of  $BaGa_2Sb_2$  were found in the graphite container. This method yielded a single phase product. Table 4.7 and 4.8 give the crystallographic data of this compound.

Table 4.7 Crystallographic data of  $BaGa_2Sb_2$  [114].

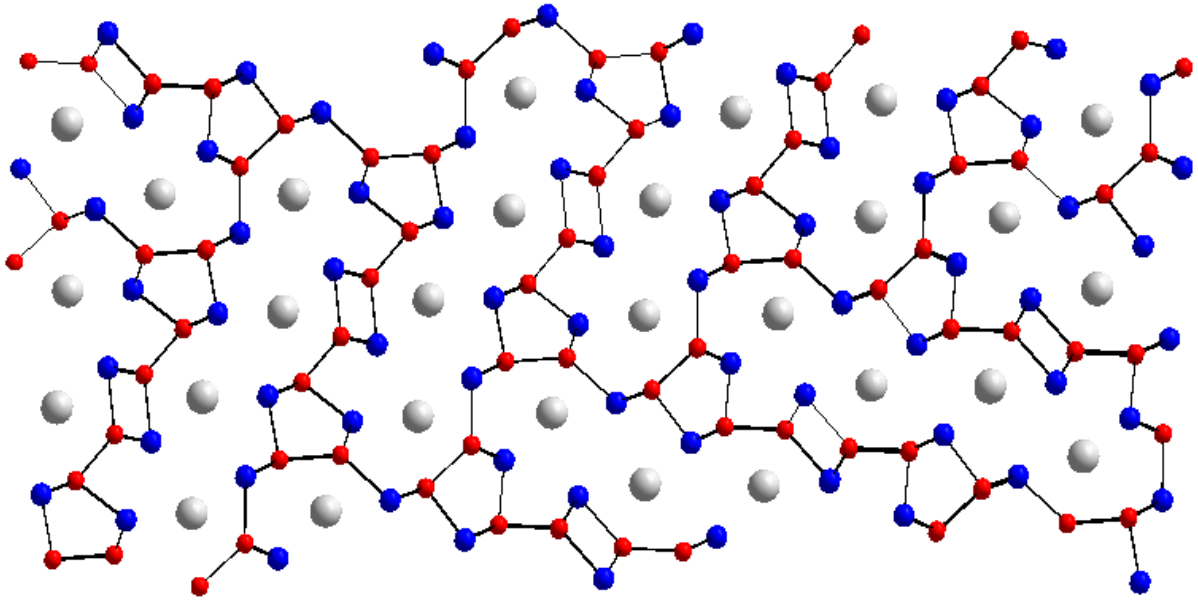
Molecular formula	$BaGa_2Sb_2$
Molecular weight (g/mol)	517.56
Crystal system	Orthorhombic
Space group	<i>Pnma</i> (No.62)
a (Å)	25.454 (5)
b (Å)	4.4421 (9)
c (Å)	10.273 (2)
Volume (Å <sup>3</sup> )	1161.6
Z	8

Density (g/cm <sup>3</sup> )	5.95
------------------------------	------

Table 4.8 Atomic coordinates and Wyckoff positions of BaGa<sub>2</sub>Sb<sub>2</sub> [114].

Atom	Wyck.	$x/a$	$y/b$	$z/c$
Ba1	4c	0.20740(2)	0.25	0.54985(6)
Ba2	4c	0.03933(2)	-0.25	0.77953(6)
Sb1	4c	0.32920(3)	0.25	0.80072(7)
Sb2	4c	0.18564(3)	-0.25	0.81204(7)
Sb3	4c	0.07792(3)	0.25	0.02635(6)
Sb4	4c	0.07039(3)	0.25	0.51953(7)
Ga1	4c	0.31866(4)	-0.25	0.46562(11)
Ga2	4c	0.42116(4)	0.25	0.67683(11)
Ga3	4c	0.28567(4)	-0.25	0.70152(10)
Ga4	4c	0.46495(4)	0.25	0.89714(11)

a)



b)

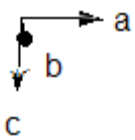
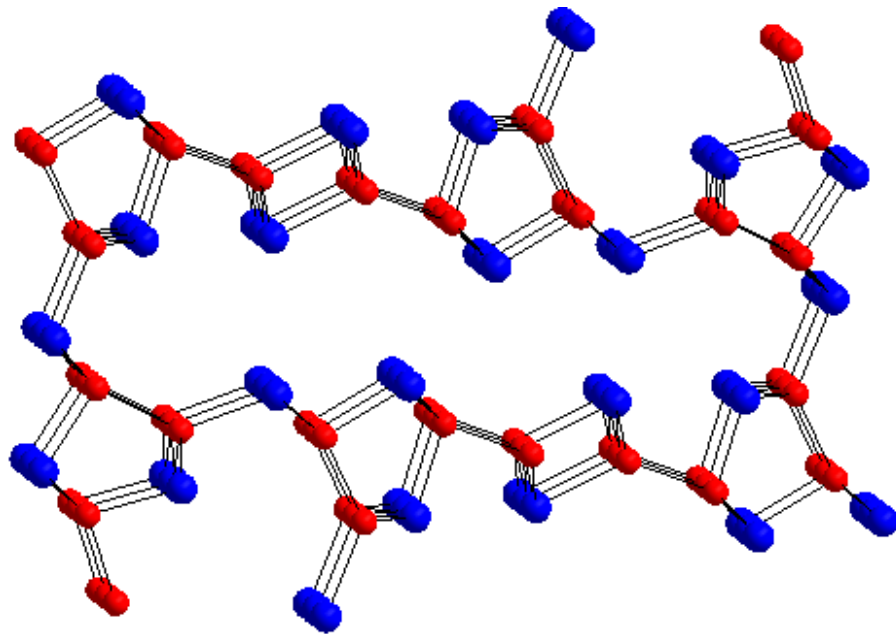


Fig. 4.9 a) Structure of BaGa<sub>2</sub>Sb<sub>2</sub> b) Structure of [Ga<sub>2</sub>Sb<sub>2</sub>]<sup>2-</sup> framework. (Ba atoms are grey, Ga atoms are red and Sb atoms are blue) [114].

---

BaGa<sub>2</sub>Sb<sub>2</sub> exhibits a unique structure type. This structure consists of 26-membered rings made of gallium and antimony atoms. [Ga<sub>2</sub>Sb<sub>6/3</sub>]<sup>2-</sup> units are the basic building blocks of the structure that is shown in fig. 4.9. b. In these units six antimony atoms are connected to the Ga-Ga dimers and represent an ethane-like conformation [Sb<sub>3</sub>Ga-GaSb<sub>3</sub>]. These antimony atoms are shared to form four-membered and five-membered rings and are further connected by Ga-Ga and Ga-Sb bonds. The 26-membered rings lead to the formation of tunnels in the structure that run along the [010] direction. Barium cations reside in the tunnels. Fig. 4.9. a shows the tunnel-like formations and the residing Ba<sup>2+</sup> cations. There are two crystallographically different barium atoms in the tunnels that are surrounded by six antimony atoms and five gallium atoms. The coordination sphere of Ba (1) was found to be a bicapped trigonal prism along with five gallium and six antimony atoms and Ba (2) was found to be in a monocapped trigonal prismatic coordination sphere. The basic building units [Ga<sub>2</sub>Sb<sub>2</sub>]<sup>2-</sup> can be compared to the one-electron reduction product of GaSb. This extra electron can reduce the formal oxidation state of gallium from +3 to +2. Ga<sup>2+</sup> exhibits a strong tendency to form Ga-Ga bonds that lead to the formation of the tunnel-like structures. [Ga<sub>2</sub>Sb<sub>2</sub>]<sup>2-</sup> unit is isoelectronic to GaS which also exhibits Ga-Ga bonds.

Not many barium-indium-antimony compounds are known, an exception being Ba<sub>7</sub>In<sub>8</sub>Sb<sub>8</sub> which was reported by S. Bobev et al. in 2010 [116]. Ca<sub>5</sub>M<sub>2</sub>Sb<sub>6</sub> (M =Al, Ga, In) compounds were studied recently which exhibit high Seebeck coefficients and low thermal conductivity values [131]. Ba<sub>5</sub>In<sub>2</sub>Sb<sub>6</sub> was reported by Cordier et al. in 1988 [115]. To synthesize Ba<sub>5</sub>In<sub>2</sub>Sb<sub>6</sub>, stoichiometric amounts of the elements were loaded in a corundum tube and heated to 1270K under reduced pressure of argon with a heating rate of 100 K/hour. At this temperature the reaction vessel was heated for 1 hour and then cooled down to room temperature with a cooling rate of 50 K/hour. The crystal structure of this compound was described [115]. Table 4.9 and 4.10 give the crystallographic data of this compound.

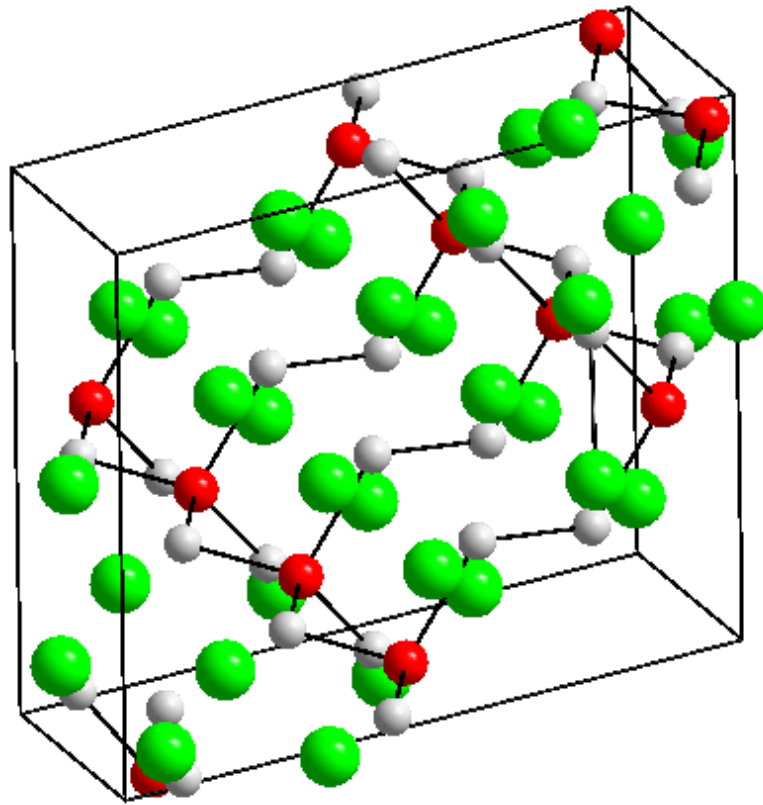
Table 4.9 Crystallographic data of Ba<sub>5</sub>In<sub>2</sub>Sb<sub>6</sub> [115].

Molecular formula	Ba <sub>5</sub> In <sub>2</sub> Sb <sub>6</sub>
Molecular weight (g/mol)	1644.76
Crystal system	Orthorhombic
Space group	<i>Pbam</i> (No.55)
<i>a</i> (Å)	15.307 (6)
<i>b</i> (Å)	13.358 (5)
<i>c</i> (Å)	4.686 (2)
Volume (Å <sup>3</sup> )	978.6
<i>Z</i>	2
Density (g/cm <sup>3</sup> )	5.59

Table 4.10 Atomic coordinates and Wyckoff positions of Ba<sub>5</sub>In<sub>2</sub>Sb<sub>6</sub> [115].

Atom	Wyck.	<i>x/a</i>	<i>y/b</i>	<i>z/c</i>
Ba1	4 <i>h</i>	0.4828(1)	0.6727(1)	0.5
Ba2	4 <i>h</i>	0.2523(1)	0.4129(1)	0.5
Ba3	2 <i>d</i>	0	0.5	0.5
In1	4 <i>g</i>	0.2888(2)	0.6741(2)	0
Sb1	4 <i>g</i>	0.4030(1)	0.8429(2)	0
Sb2	4 <i>h</i>	0.1832(1)	0.6626(2)	0.5
Sb3	4 <i>g</i>	0.4075(1)	0.4861(2)	0

a)



b)

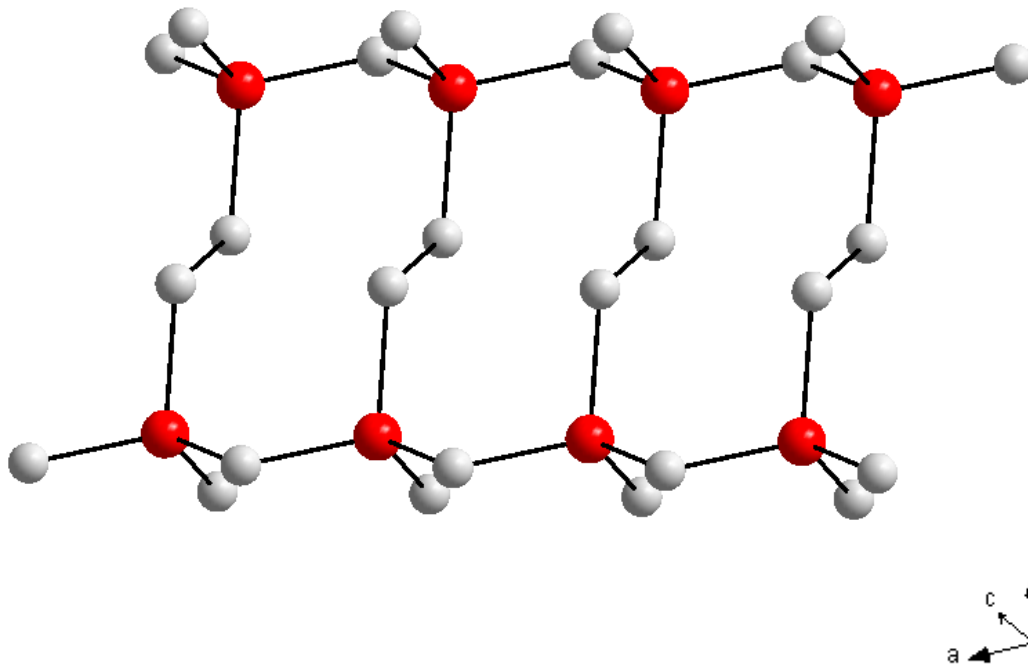


Fig. 4.10 a) Unit cell of  $\text{Ba}_5\text{In}_2\text{Sb}_6$  b) Structure of the  $[\text{In}_2\text{Sb}_6]^{10-}$  network. (Ba atoms are green, In atoms are red and Sb atoms are grey) [115].

---

An indium atom is connected to four antimony atoms to form a tetrahedron. The indium atoms are connected by In-Sb-In bonds and thus form a one-dimensional chain-like structure. These chains are further connected by Sb-Sb bonds to form a layer. Fig. 4.10. a shows the three-dimensional structure of  $\text{Ba}_5\text{In}_2\text{Sb}_6$  and fig. 4.10. b shows the indium-antimony network. This is the anionic network of the structure. The barium atoms donate electrons to compensate the charges. Ba(2) and Ba(3) are in octahedral environment with six antimony atoms each, Ba(1) is in a trigonal prismatic environment and faces another antimony atom, resulting in seven-fold coordination. In the basic building block of the compound there are two indium atoms with four bonds. These indium atoms carry a single negative charge ( $\text{In}^-$ ). There are four antimony atoms with two bonds that carry single negative charges ( $\text{Sb}^-$ ). The antimony atoms at the terminal positions are assumed to carry two negative charges ( $\text{Sb}^{2-}$ ) as they form only one bond [115]. According to the Zintl formalism this compound can be written as  $5 \text{Ba}^{2+} [2 \text{In}^- 4 \text{Sb}^- 2 \text{Sb}^{2-}]$ .

---

## 5 Density functional theory calculations

---

Density functional theory (DFT) is a successful and well-known quantum mechanical approach to matter. This method is useful to calculate electrical, magnetic and structural properties of materials [36, 37]. Wave functions ( $\psi$ ) are the basic functions in quantum mechanics which can be calculated from Schrodinger's equation. But the Schrodinger's equation becomes too complex to be carried out for the calculation of many body systems. So, the usage of this in calculating energy of a system was difficult until E. Fermi and L. H. Thomas explained that the energy of a system can be expressed as a function of the total electron density. Later J. C. Slater used this concept and developed the Hartree-Fock-Slater method which is regarded as a predecessor theory of density functional theory. Then P. Hohenberg and W. Kohn in 1960s demonstrated their theorem that states the electronic density of a system can define the ground state energy of a nondegenerate electronic system and their corresponding electronic properties. According to the Hohenberg-Kohn theorem [36] the total energy functional of a system with potential  $v(r)$ , particle density  $n(r)$ , density ( $n$ ), Coulomb ( $\hat{U}$ ) and kinetic energy operator ( $\hat{T}$ ), functionals for potential ( $V[n]$ ) and internal energy ( $F[n]$ ) can be written as,

$$E_v[n] = \min_{\Psi \rightarrow n} \langle \Psi | \hat{T} + \hat{U} | \Psi \rangle + \int d^3r n(r)v(r) =: F[n] + V[n]$$

Thus the existence of a functional relating energy of the system and the electron density was confirmed by the Hohenberg-Kohn theorem. But it does not explain the form of the functional. Later W. Kohn and L. Sham developed the Kohn-Sham formalism that considers atomic orbital formalism. This can solve the Hohenberg-Kohn theorem more precisely because the difficulty in representing kinetic energy of the system was overcome by splitting kinetic energy term into two parts: the first part can be calculated precisely considering electrons as non-interacting particles and the second part accounts for the electron-electron interactions. According to the Kohn-Sham formalism [37] the ground state electronic energy of a system can be expressed as,

$$E[\rho] = -\frac{1}{2} \sum_{i=1}^n \int \Psi_i^*(r_1) \nabla_i^2 \Psi_i(r_1) dr_1 - \sum_{x=1}^N \int \frac{Z_x}{r_{xi}} \rho(r_1) dr_1 + \frac{1}{2} \iint \frac{\rho(r_1)\rho(r_2)}{r_{12}} dr_1 dr_2 + E^{XC}[\rho]$$

$E[\rho]$  is the electronic energy,  $n$  is the number of electrons,  $\rho(r)$  is the total electron density in space  $r$ ,  $N$  is the number of nuclei,  $\Psi_i$  ( $i = 1, 2, \dots, n$ ) are the Kohn-Sham orbitals. The first term represents the kinetic energy of the non-interacting electrons. The second term represents the nuclear-electron interactions. The third term represents Coulombic repulsions. The fourth term represents the correction in kinetic energy which is known as exchange-correlation term. To represent the exchange-correlation term approximation methods are necessary among which local density approximation (LDA) is most efficient. The assumption of this method is that the exchange-correlation energy at any point in space is a function of the electron density at that point in space. The exchange–correlation term can be split into two parts, an exchange term ( $E^X$ ) and the correlation term ( $E^C$ ) and can be given as

$$E^{XC}[\rho] = E^X[\rho] + E^C[\rho]$$

The exchange functional can be represented as,

$$E^X[\rho] = -2^{1/3} C_x \int (\rho_\alpha^{4/3} + \rho_\beta^{4/3}) dr$$

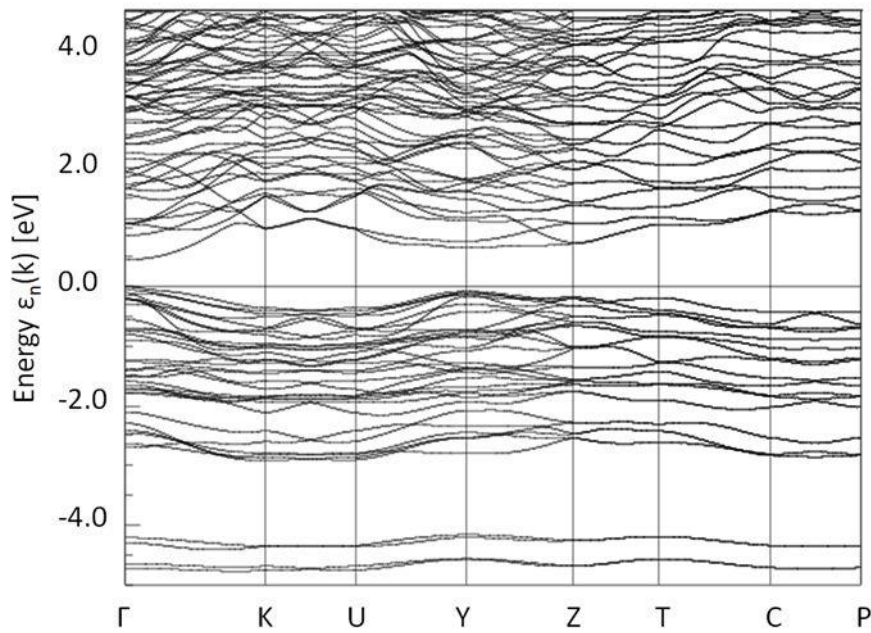
Where  $C_x$  is given by

$$C_x = -\frac{3}{4} \left(\frac{3}{\pi}\right)^{1/3}$$

Where  $\alpha$  and  $\beta$  represent spin up and spin down densities. The correlation energy term  $E^C$  cannot be obtained separately from the exchange energy. This can be obtained using an appropriate interpolation formula. This approximation method is simple and accurate. Thus density functional theory serves as an important tool to calculate energy of the system. The program FPLO-7 [38, 39] was used to perform the density functional theory calculations. In this work density functional theory was used to calculate the band gaps and band structures of Zintl phases.

Density functional theory calculations were performed to understand the electronic structure of  $\text{Ba}_3\text{AlSb}_3$ . The band gap was evaluated. Fig. 5.1. a shows the band structure of  $\text{Ba}_3\text{AlSb}_3$  and fig. 5.1. b shows the density of states.

(a)



(b)

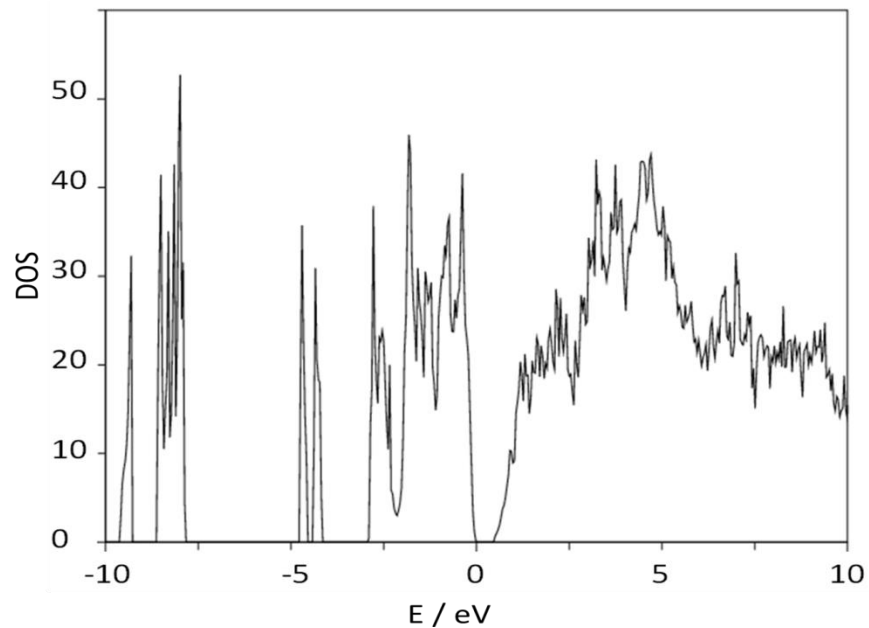
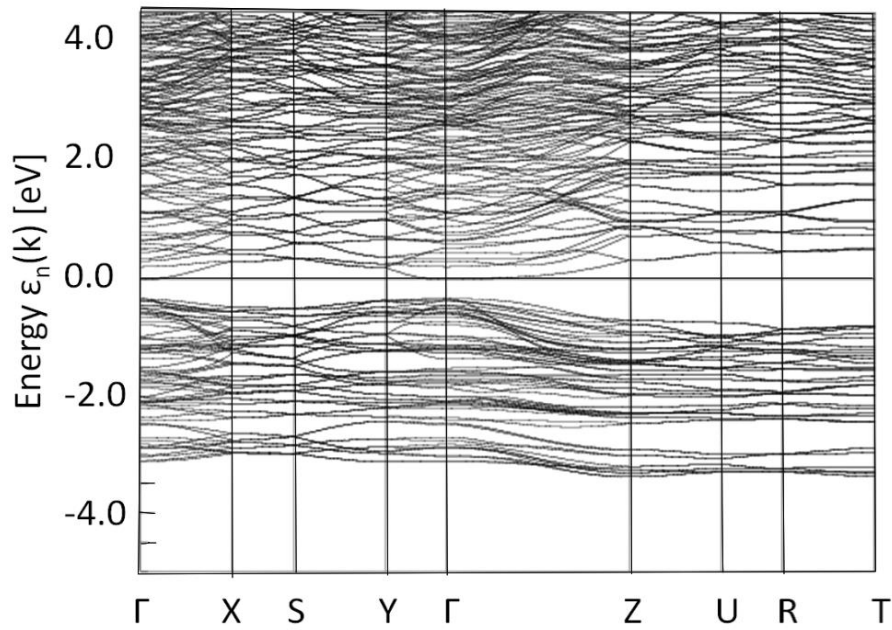


Fig. 5.1 a) Band structure of Ba<sub>3</sub>AlSb<sub>3</sub> compound b) Density of states (DOS).

Lattice parameters and atomic positions given by Cordier et al. were used as input for the calculations [111]. Fig. 5.1. a and fig. 5.1. b show no overlap between valence and conduction bands of Ba<sub>3</sub>AlSb<sub>3</sub>. The band gap of this compound according to the calculations was estimated to be 0.5 eV. Thus, Ba<sub>3</sub>AlSb<sub>3</sub> being a narrow band gap semiconductor can be considered as a suitable candidate for thermoelectric studies.

(a)



(b)

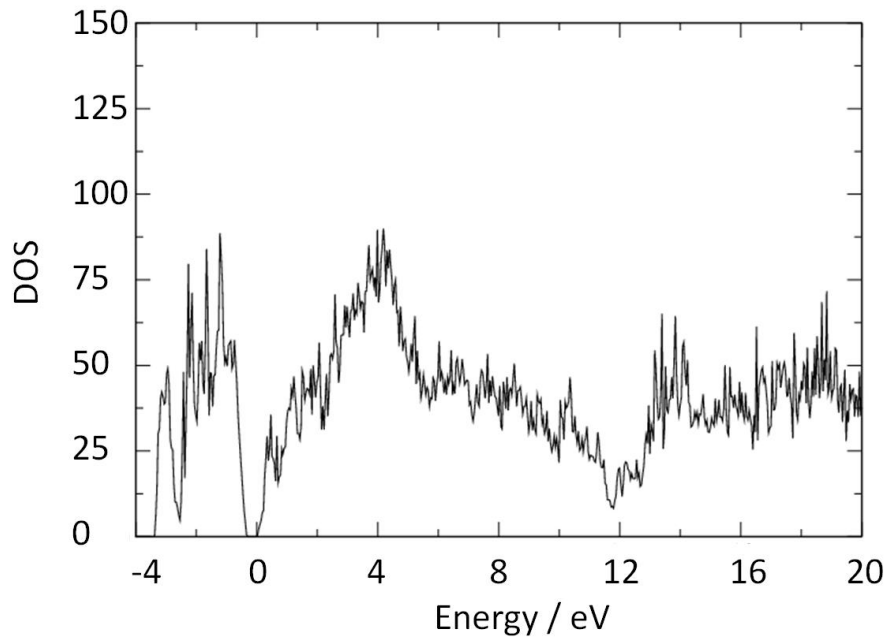
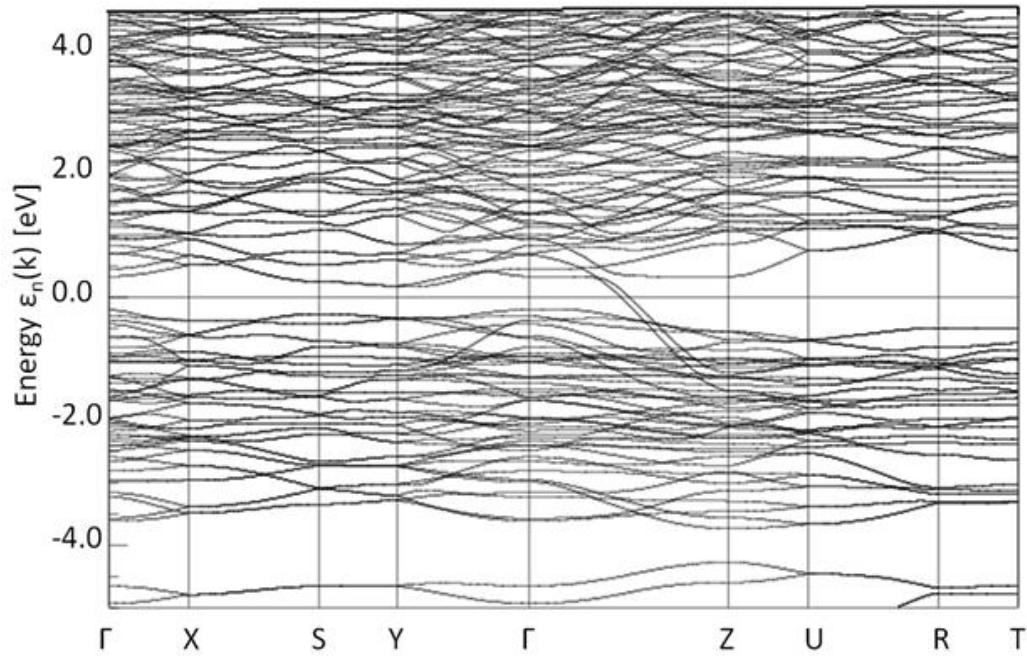


Fig. 5.2 (a) Band structure of Ba<sub>3</sub>GaSb<sub>3</sub>. (b) Density of states.

Density functional theory (DFT) calculations were performed for Ba<sub>3</sub>GaSb<sub>3</sub> to determine the band gap and density of states. Fig. 5.2. a and fig. 5.2. b show the band structure and density of states respectively. The structure given by Cordier et al. [112] was used as input for the calculations. Fig. 5.2. a and b show the band gap between valence and conduction bands. The band gap of Ba<sub>3</sub>GaSb<sub>3</sub> was estimated to be 0.3 eV.

$\text{Ba}_3\text{GaSb}_3$  was identified as a narrow band gap semiconductor, so studying its thermoelectric properties should be interesting.

a)



b)

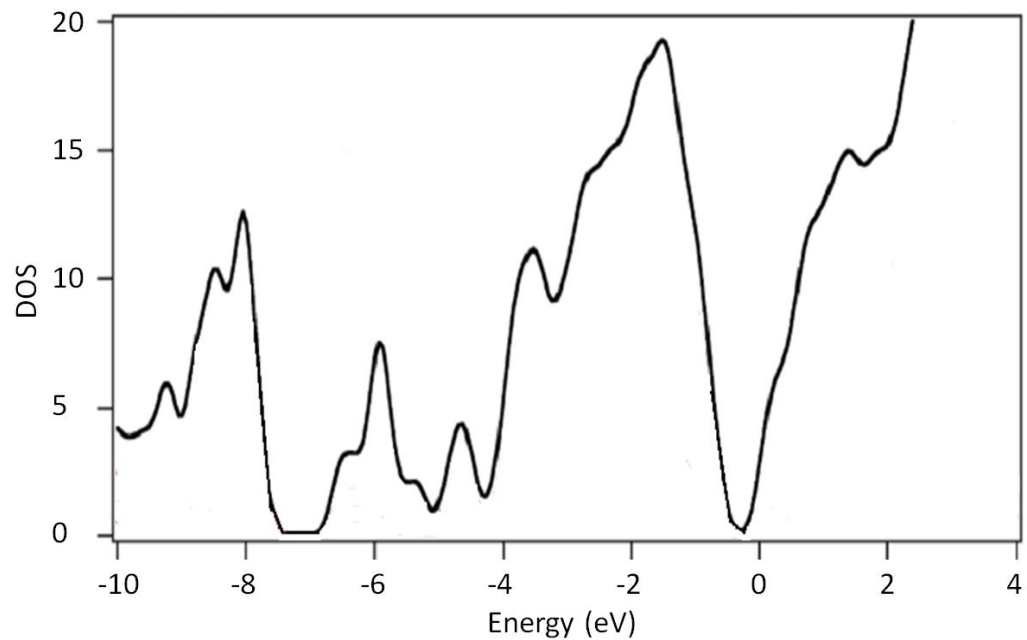


Fig. 5.3 a) Band structure of  $\text{Ba}_7\text{Ga}_4\text{Sb}_9$  b) density of states from literature [141].

Band gap and density of states for the Zintl compound  $\text{Ba}_7\text{Ga}_4\text{Sb}_9$  were calculated in the same way it was carried out by E. Canadell et al. [141] and the results were same. Band gap and density of states from literature are given in fig. 5.3. a and fig. 5.3. b [141]. The experimental lattice constants and atom positions given by Cordier et al. [113] were used as input for the calculations. A band gap does not exist for this compound according to the band structure calculations as the valence and conduction bands are overlapping with each other.  $\text{Ba}_7\text{Ga}_4\text{Sb}_9$  is expected to exhibit metallic properties rather than semiconducting properties.

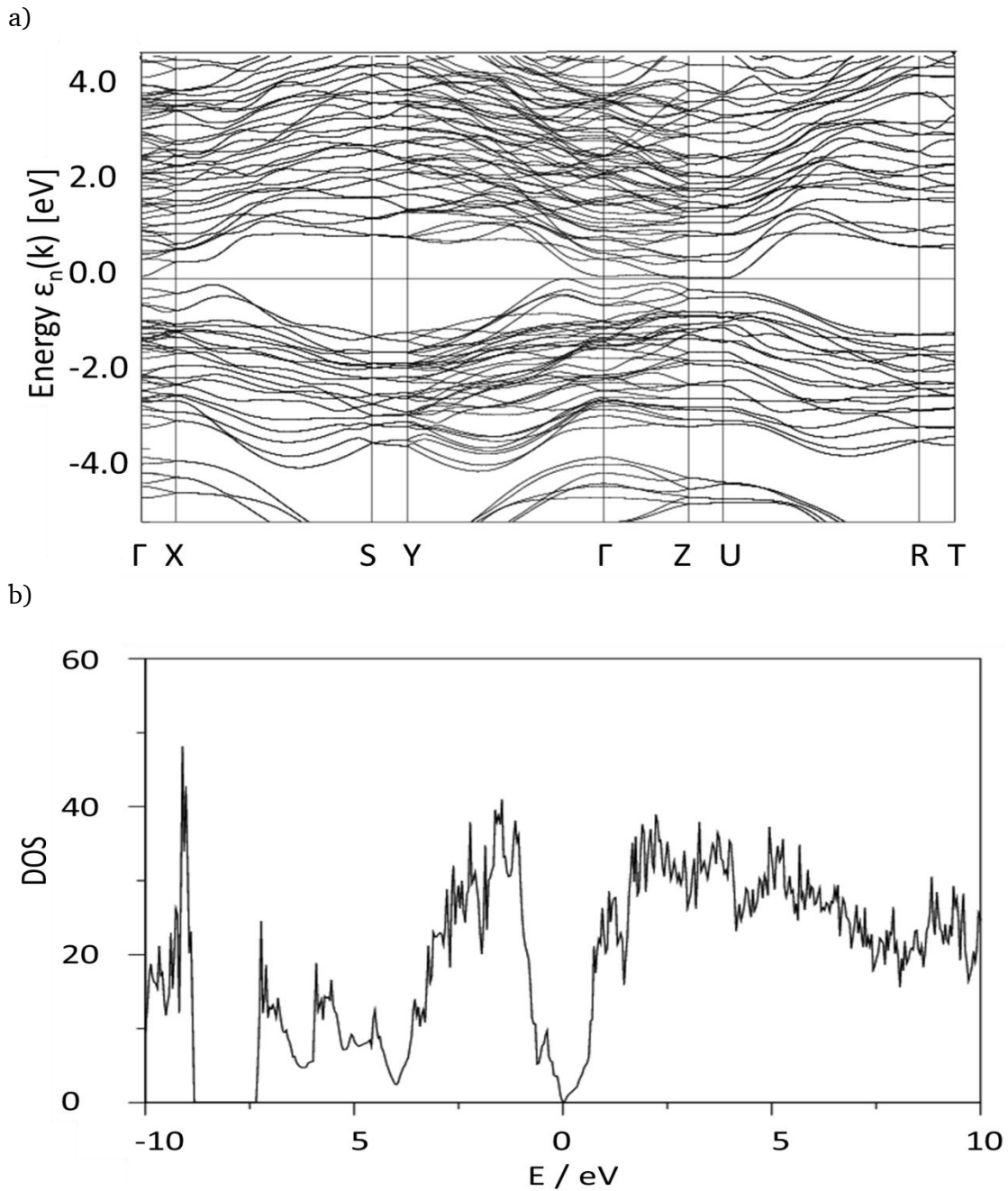


Fig. 5.4 a) Band structure of  $\text{BaGa}_2\text{Sb}_2$  compound b) Density of states (DOS).

---

Fig. 5.4. a shows the band structure of  $\text{BaGa}_2\text{Sb}_2$  and Fig. 5.4. b shows the density of states. The lattice constants and atom positions given by M. G. Kanatzidis et al. [114] were taken as inputs for the density functional theory calculations for the electronic structure of  $\text{BaGa}_2\text{Sb}_2$ . In the literature, the extended-Hückel formalism was used to calculate the electronic structure that suggests semiconducting behavior. The figures (fig. 5.4. a and b) do not show the existence of the band gap. The valence and conduction bands are very close to each other and touching the Fermi level. According to literature this compound is a narrow band gap semiconductor as shown by the infra-red absorption spectrum of a polycrystalline sample of  $\text{BaGa}_2\text{Sb}_2$  from which the band gap was calculated to be 0.35 eV [114].

Density functional theory calculations were performed for  $\text{Ba}_5\text{In}_2\text{Sb}_6$  and the band structure was determined. The crystallographic information reported by Cordier et al. [115] was used as input for the density functional theory calculations. Fig. 5.5. a shows the band structure of  $\text{Ba}_5\text{In}_2\text{Sb}_6$  and fig. 5.5. b shows the density of states. A band gap does not open for this compound according to the calculations as the valence and conduction bands are overlapping with each other.  $\text{Ba}_5\text{In}_2\text{Sb}_6$  is expected to exhibit metallic properties rather than semiconducting properties. Since the carrier concentration is expected to be higher than in other phases, this system was investigated further despite the fact that it was calculated to be metallic. In the case of additional defects in the crystal structure, different properties can be expected.

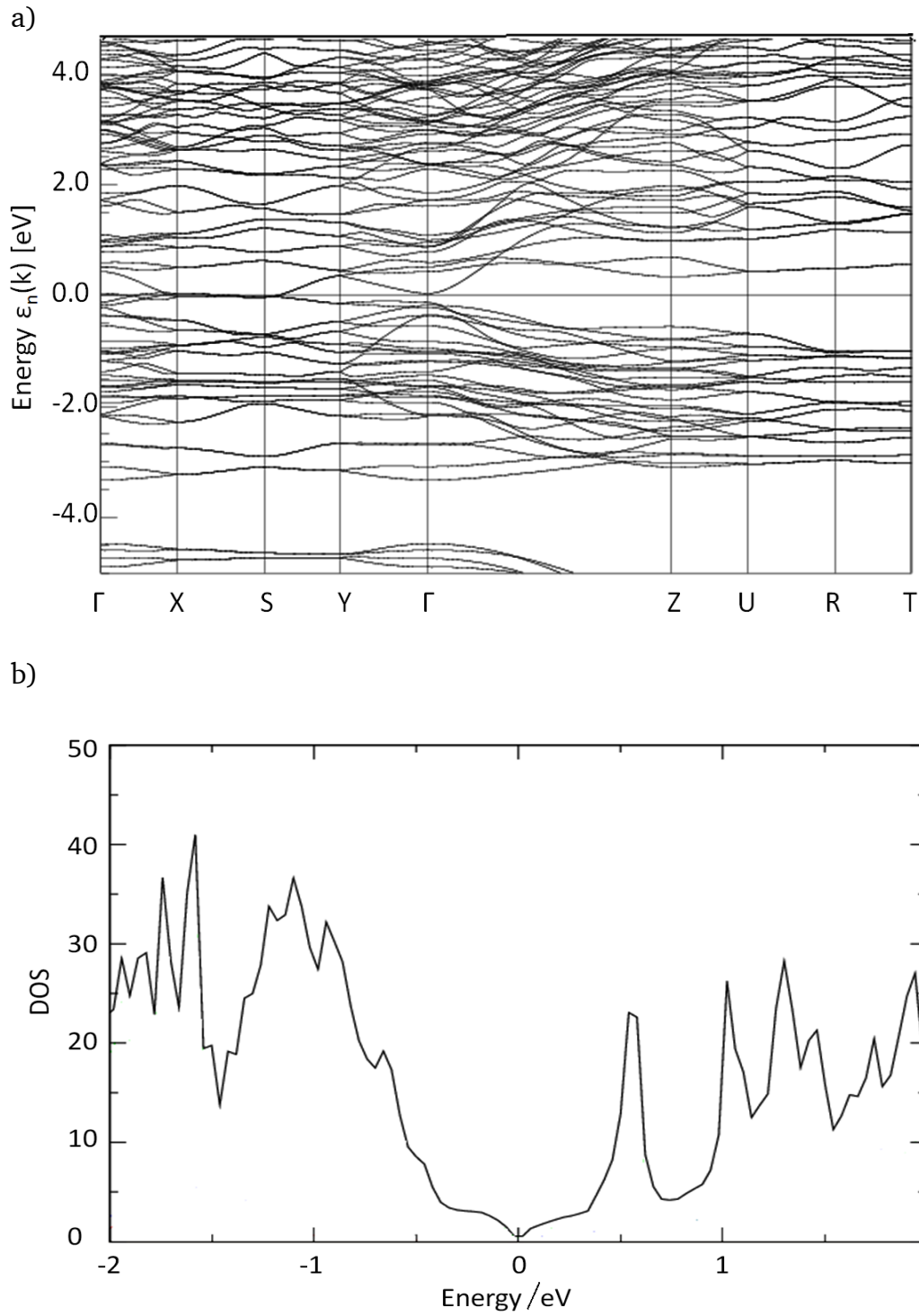


Fig. 5.5 a) Band structure of  $\text{Ba}_5\text{In}_2\text{Sb}_6$  b) Density of states (DOS).

---

---

## 6 Ba<sub>3</sub>AlSb<sub>3</sub>

---

### 6.1 Synthesis, characterization and compaction

The synthetic procedure described in literature [111] was optimized to obtain monophasic and crystalline products. Stoichiometric amounts of Ba (0.5122 g, 3.7 mmol, Chempur, 99.3%), Al (0.0335 g, 1.2 mmol, Acros organics, 99.99%) and Sb (0.4541 g, 3.7 mmol, Chempur, Sb-Shots, 1-3 mm, 99.999%) were used as purchased without further purification, loaded into tantalum containers and sealed in quartz ampoules. The samples were heated to 1123 K for three days, cooling and heating rates were 60 K/hour. The resulting products were found to be air-sensitive and reacted vigorously with water. They were grey in color with metallic luster.

Powder samples of Ba<sub>3</sub>AlSb<sub>3</sub> with high phase-purity (96 %) were prepared. The powder X-ray diffraction technique was used to analyze the products. The sample was ground in a mortar under argon atmosphere. The measurements were done from 15 – 70° 2 $\theta$  using Cu K $\alpha$  radiation with  $\lambda = 1.5406 \text{ \AA}$ . Using the program *TOPAS*, Rietveld refinements of the lattice parameters and the phase fractions were carried out to determine the phase-purity of Ba<sub>3</sub>AlSb<sub>3</sub>. The calculated powder diagram was compared to the measured powder X-ray diagram of Ba<sub>3</sub>AlSb<sub>3</sub> (fig. 6.1). Ba<sub>11</sub>Sb<sub>10</sub> was identified as the secondary phase in this product (1-4%). The X-ray pattern matches very well with the calculated powder pattern of Ba<sub>3</sub>AlSb<sub>3</sub>. The difference curve does not show any significant peaks except the reflections from Ba<sub>11</sub>Sb<sub>10</sub>. The inset shows the magnified area (2  $\theta = 26 - 40^\circ$ ) where the impurity reflections were marked by the asterisk symbols. The calculated and experimental lattice parameters of Ba<sub>3</sub>AlSb<sub>3</sub>, the refinement residuals and the goodness of fit (*GOF*) are given in table 6.1. Reaction times longer than three days led to Ba<sub>2</sub>Sb<sub>3</sub> as additional by-product. At elevated temperatures (above 1273 K) other binary phases were observed as impurities. Though a binary phase diagram is not available in literature for the binary barium-antimony system there are many known binary phases apart from Ba<sub>11</sub>Sb<sub>10</sub> such as BaSb<sub>3</sub>, Ba<sub>5</sub>Sb<sub>4</sub>, Ba<sub>2</sub>Sb, BaSb<sub>2</sub>, Ba<sub>5</sub>Sb<sub>3</sub>, and Ba<sub>2</sub>Sb<sub>3</sub> [117-122]. These binary phases are observed at higher temperatures, so exclusion of impurity phases makes it necessary to precisely control the temperature and duration.

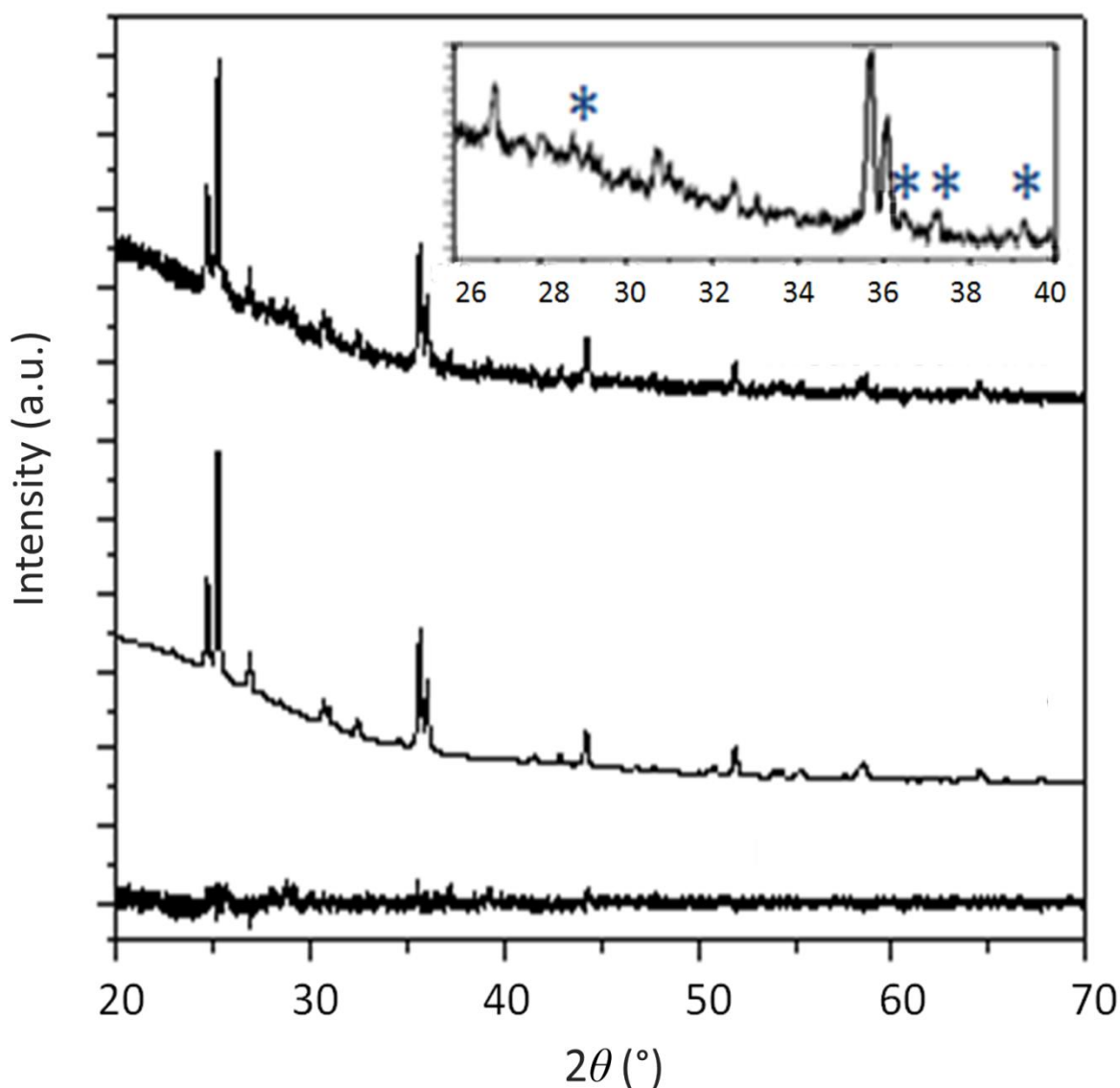


Fig. 6.1 Experimental (top), calculated powder X-ray diffraction (middle) diagrams of Ba<sub>3</sub>AlSb<sub>3</sub> and difference curve (bottom) [inset shows the magnified area ( $2\theta = 26 - 40^\circ$ ) where the asterisk symbols indicate the impurity peaks].

Using other synthesis methods like the arc melting technique did not lead to the desired product. Binary phases like Ba<sub>5</sub>Sb<sub>3</sub>, Ba<sub>2</sub>Sb<sub>3</sub> etc. were identified as side-products in large amounts.

Table 6.1 Lattice parameters of Ba<sub>3</sub>AlSb<sub>3</sub> from Rietveld refinement based on the structure model from literature [111].

	<i>a</i>	<i>b</i>	<i>c</i>
Literature	21.133 (10) Å	7.194 (5) Å	14.069 (8) Å
This work	21.137 (3) Å	7.196 (5) Å	14.080 (2) Å
$R_{\text{exp.}}$ : 4.42	$R_{\text{wp.}}$ : 4.76	$R_{\text{p.}}$ : 3.59	$GOF$ : 1.08

High-temperature powder X-ray diffraction studies were carried out for Ba<sub>3</sub>AlSb<sub>3</sub> in order to investigate the thermal stability of the compound. A finely ground powder sample was filled into a quartz capillary. The end of the capillary was sealed using tar. The sample was heated from room temperature to 1073 K. Powder X-ray diffraction patterns were recorded in steps of 100 K. Fig. 6.2 shows the powder X-ray patterns of Ba<sub>3</sub>AlSb<sub>3</sub> at all measured temperatures. There are no changes in the powder patterns of the sample in the temperature range of 323 K to 1073 K. The sample was found to be stable upon cooling. Fig. 6.2 makes it evident that there are no phase transitions up to 1073 K.

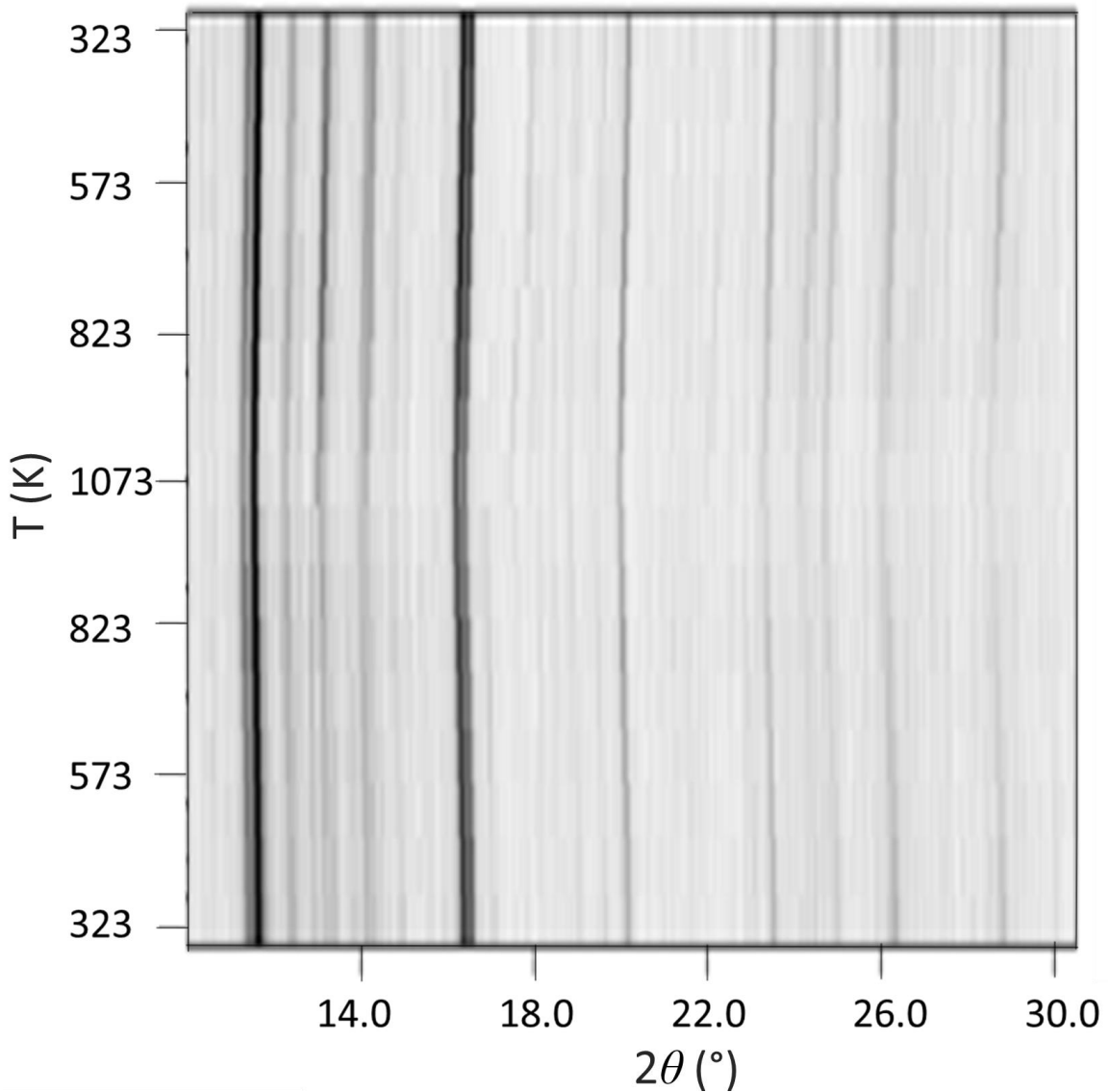


Fig. 6.2 High-temperature powder X-ray diffraction (bottom: heating from 323 to 1073 K, top: cooling from 1073 to 323 K).

The powder X-ray diffraction patterns at different temperatures were fitted using the Rietveld method. Lattice parameters were calculated and the variation with temperature was studied. Fig. 6.3 gives the variation of lattice parameters with temperature. Lattice parameters increase continuously with the temperature. Due to thermal expansion, the unit cell volume increases with temperature. The relationship between unit cell volume and temperature is shown in the fig. 6.3. d. As seen in the diagrams the lattice parameters are comparable for heating and cooling cycles.

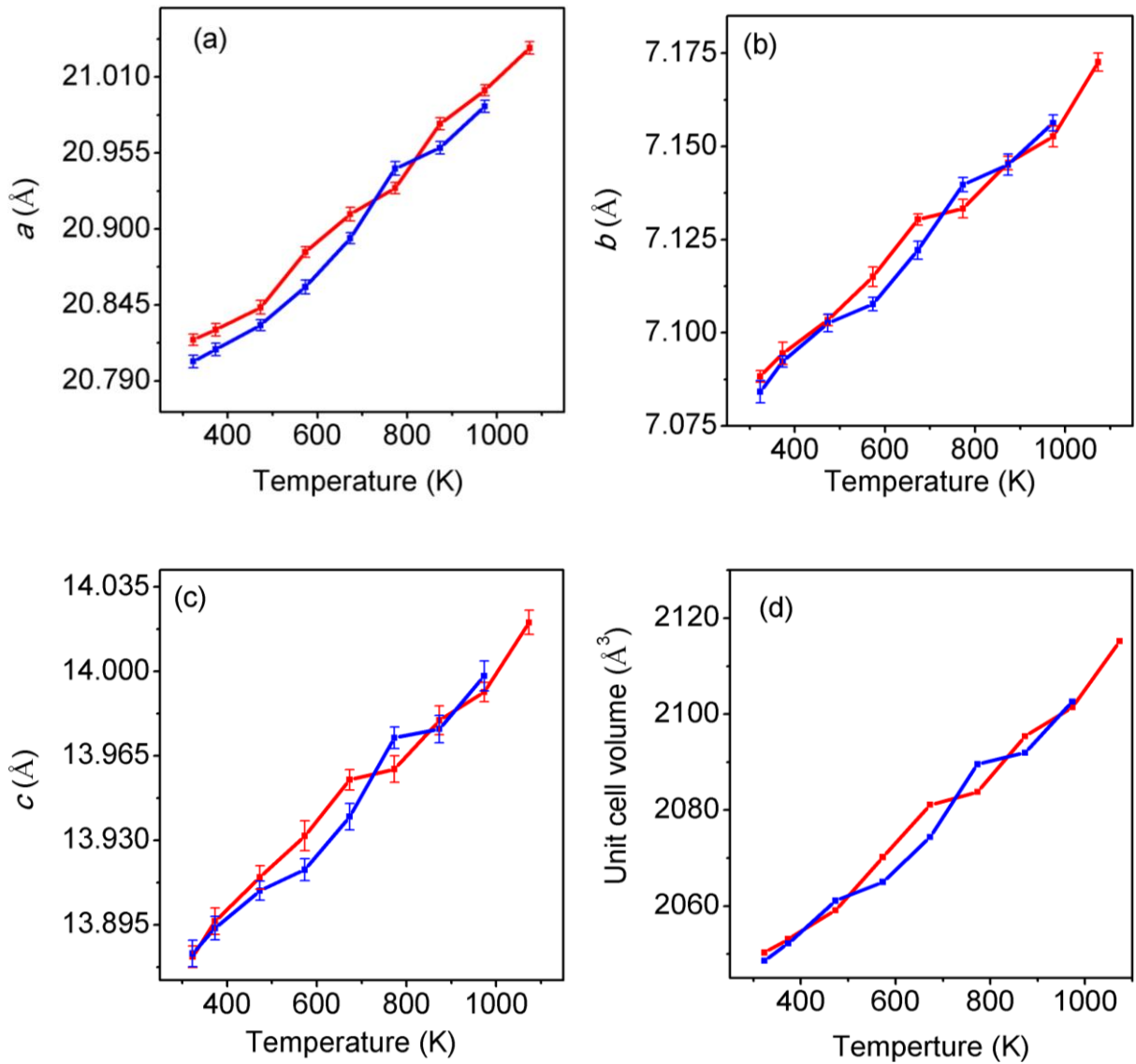


Fig. 6.3. a, b, c: Lattice parameters  $a$ ,  $b$ ,  $c$  (Å) with temperature [Red lines indicate heating cycle (323 K to 1073 K) and blue lines indicate cooling cycle (1073 K to 323 K)]. Fig. 6.3. d Unit cell volume as a function of temperature (standard deviations were too small to be visible).

Ba<sub>3</sub>AlSb<sub>3</sub> was compacted by the spark plasma sintering technique (Max Planck Institute for Chemical Physics of Solids, Dresden). The sample was finely powdered and then loaded in a graphite die. The inner diameter of the graphite die was 8 mm. Carbon foils were used to surround and protect the sample. The sample was heated to 923 K with the heating rate of 25 K/min. In vacuum under uniaxial pressure of 100 MPa the sample was sintered for about 20 minutes and then cooled down to room

temperature. A small portion was taken from the compacted sample for powder X-ray diffraction measurements.

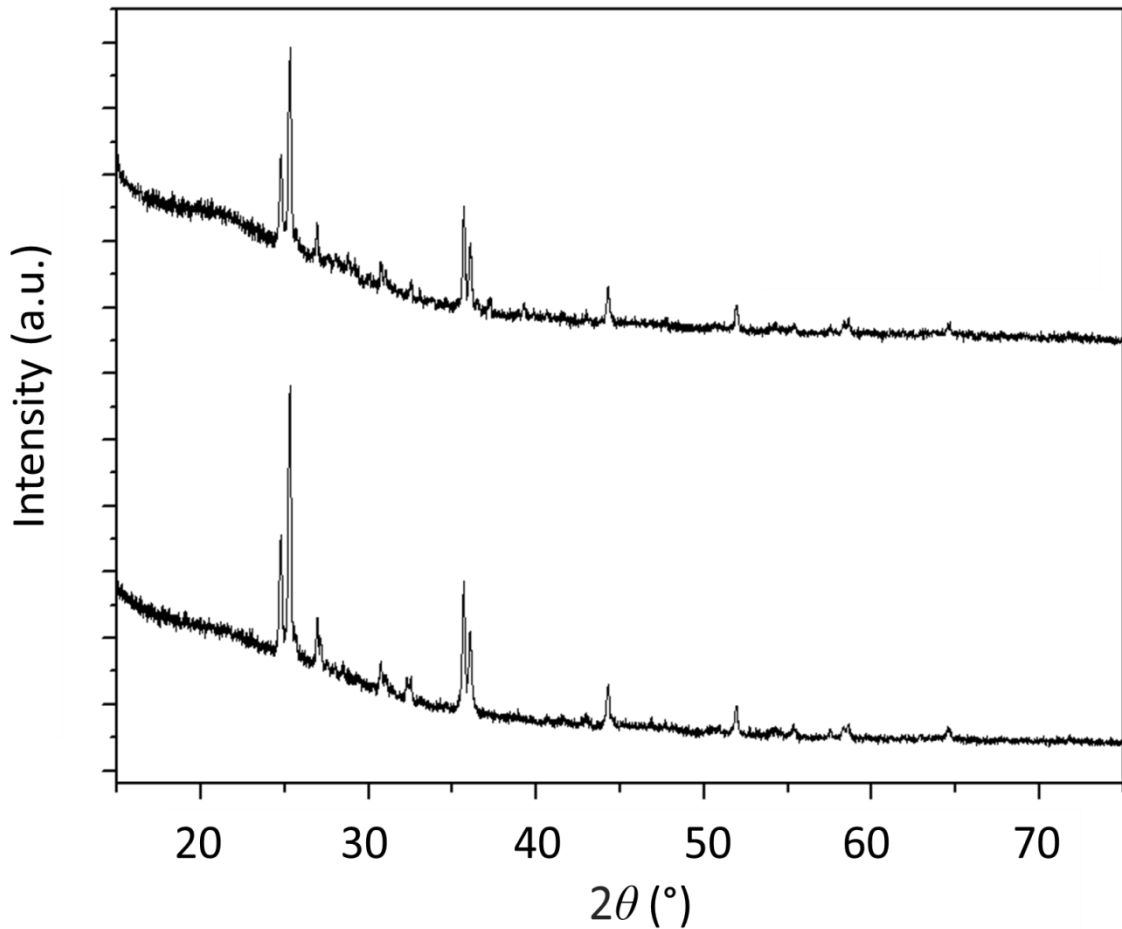


Fig. 6.4 Powder X-ray diffraction patterns of Ba<sub>3</sub>AlSb<sub>3</sub> before (bottom) and after SPS (top).

Powder diffraction patterns of the product before and after compacting are given in fig. 6.4. Both diffraction patterns are identical and neither impurity peaks nor phase transitions were observed. Ba<sub>3</sub>AlSb<sub>3</sub> is stable under SPS conditions and did not undergo any changes during the sintering process. The compacted sample was 95 % dense compared to the theoretical density (4.998 g/cm<sup>3</sup>) which was determined by the geometrical method.

Fig. 6.5 shows the scanning electron microscopy images of Ba<sub>3</sub>AlSb<sub>3</sub>. Small pieces of Ba<sub>3</sub>AlSb<sub>3</sub> were picked from the synthesized product and placed in the sample holder in the glove box. Then, the sample was quickly transferred to the instrument. Fig. 6.5. a shows the surface of Ba<sub>3</sub>AlSb<sub>3</sub> at higher resolution (20 μm) and fig. 6.5. b shows the image with low resolution where the red circles indicate the spots of EDS

measurements. Energy dispersive spectroscopy was carried out to analyze the homogeneity of  $\text{Ba}_3\text{AlSb}_3$ . The atomic percentages are close to the theoretical values, as shown in table 6.2. These measurements prove the homogeneous nature of the sample. No traces of tantalum were found in the sample.

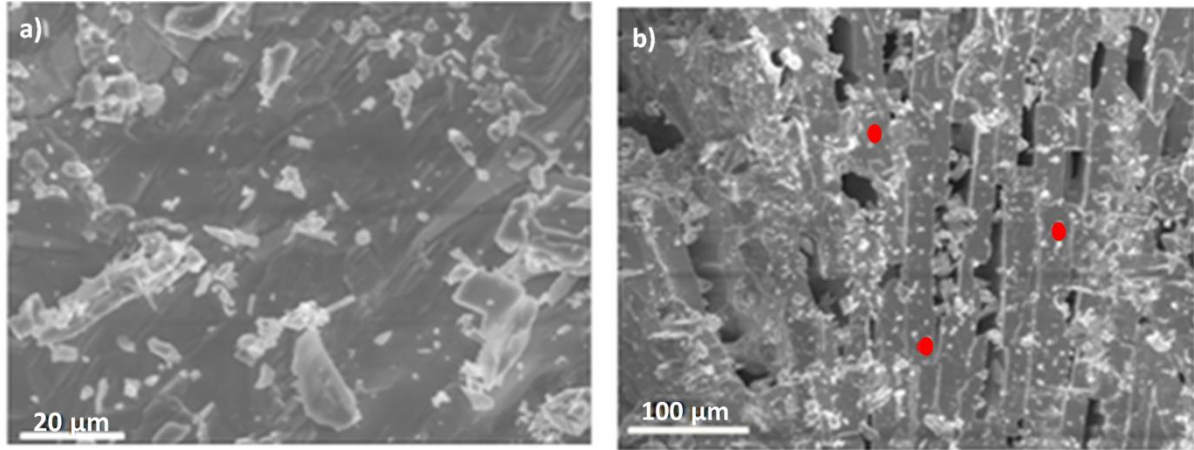


Fig. 6.5 SEM images of  $\text{Ba}_3\text{AlSb}_3$  (in fig. 6.5.b red circles indicate the spots where EDS measurements have been done).

Table 6.2 Atomic percentages of all elements in  $\text{Ba}_3\text{AlSb}_3$  determined using EDS.

	Ba (%)	Al (%)	Sb (%)
Spot 1	42.9	14.15	42.95
Spot 2	43.09	14.69	42.22
Spot 3	42.28	14.04	43.68
Average	42.75	14.29	43.28
Theoretical values	42.86	14.28	42.86

## 6.2 Thermoelectric studies

The thermoelectric properties of  $\text{Ba}_3\text{AlSb}_3$  were measured at the Max Planck Institute for Chemical Physics of Solids, Dresden. Seebeck coefficients were measured from 75 K to 350 K and are shown in fig. 6.6. a. The values increase continuously along with the temperature up to 350 K. Around, 100 K  $\text{Ba}_3\text{AlSb}_3$  shows a Seebeck coefficient of  $55.7 \mu\text{VK}^{-1}$ . It is a *p*-type material that reaches a Seebeck coefficient as high as 383

---

$\mu\text{VK}^{-1}$  around 342 K.  $\text{Ba}_3\text{AlSb}_3$  was expected to exhibit semiconducting behavior according to the DFT calculations. Electrical conductivity measurements support this prediction. The electrical conductivities increase with temperature due to the thermally activated charge carriers which is typical of a semiconductor. Fig. 6.6. b shows the electrical conductivity curve with increasing temperature. The sample was measured from 100 K up to 350 K. Up to 225 K, there are no significant changes in the electrical conductivities and so the curve is almost a straight line. After 225 K the electrical conductivity starts to increase. Around 342 K, the electrical conductivity reaches its maximum of  $18 \text{ Sm}^{-1}$ .

The thermal conductivity was measured from almost 0 K to 350 K (fig. 6.6. c). It increases between 0 K and 19 K where it reaches a maximum of  $3.8 \text{ Wm}^{-1}\text{K}^{-1}$ , then it drops slowly with increasing temperature. When the temperature is close to 350 K the thermal conductivity reaches a value as low as  $0.75 \text{ Wm}^{-1}\text{K}^{-1}$ . The values of the figure of merit are calculated and shown in fig. 6.6. d. Above 250 K,  $ZT$  starts to rise slowly and reaches 0.0012 near 350 K. Due to the poor electrical conductivity observed below 250 K, the figure of merit is close to zero in this region. High Seebeck coefficients and low thermal conductivities of  $\text{Ba}_3\text{AlSb}_3$  lead to higher  $ZT$  values at high temperatures. But due to the very low electrical conductivities  $ZT$  values are not as high as expected.

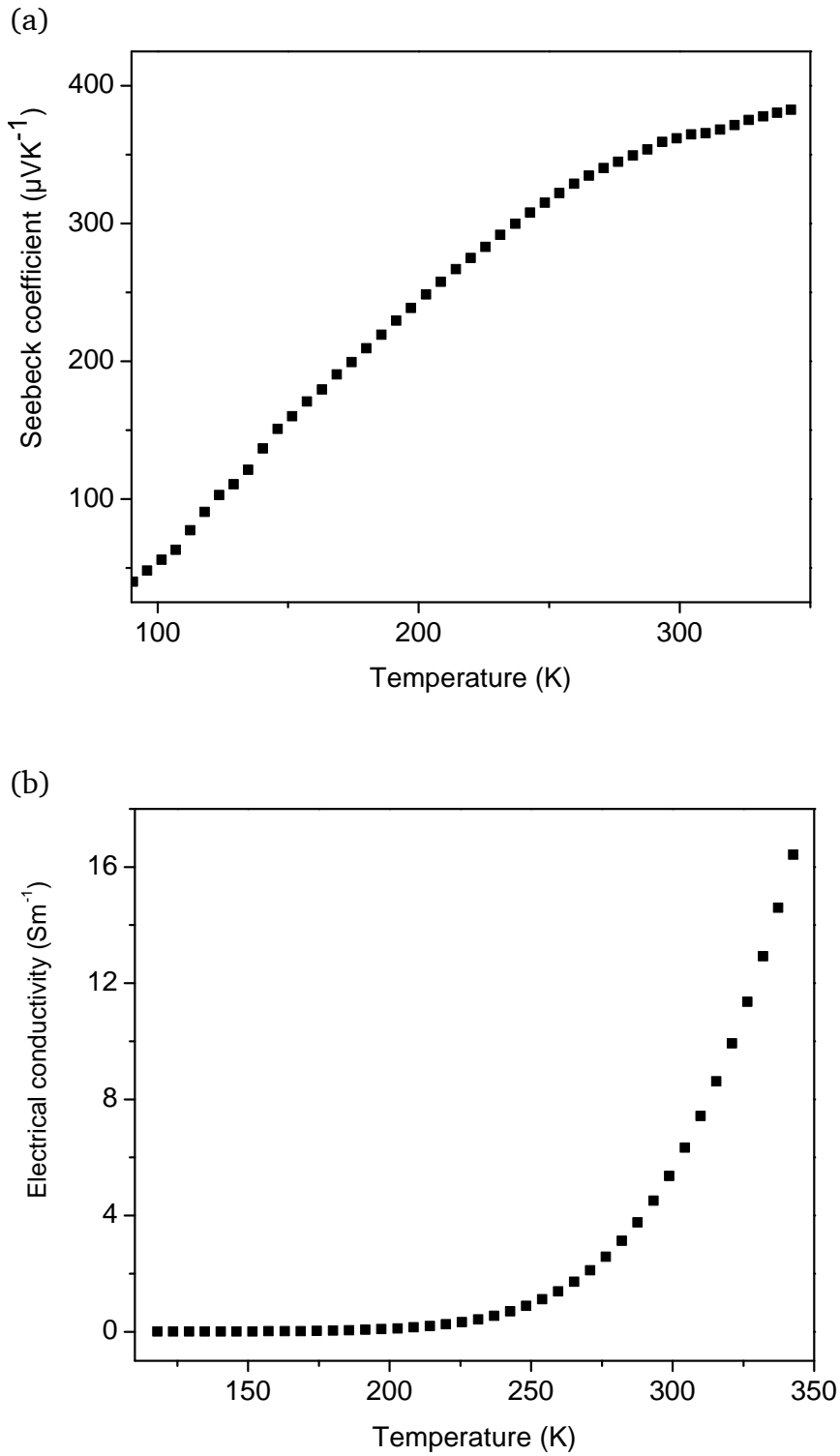


Fig. 6.6. (a) Seebeck coefficients of  $\text{Ba}_3\text{AlSb}_3$  as a function of temperature, (b) Electrical conductivity of  $\text{Ba}_3\text{AlSb}_3$  as a function of temperature.

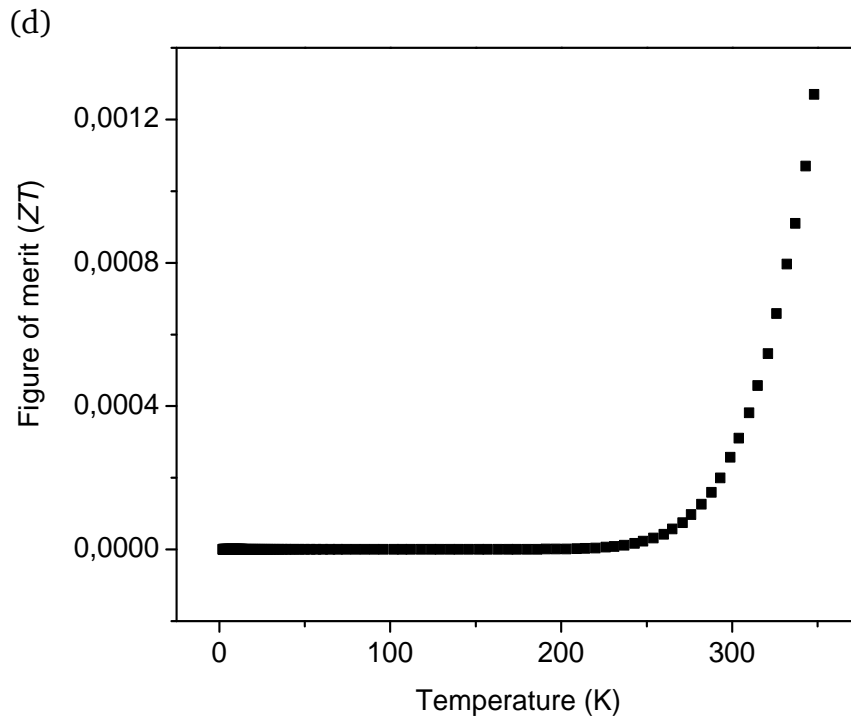
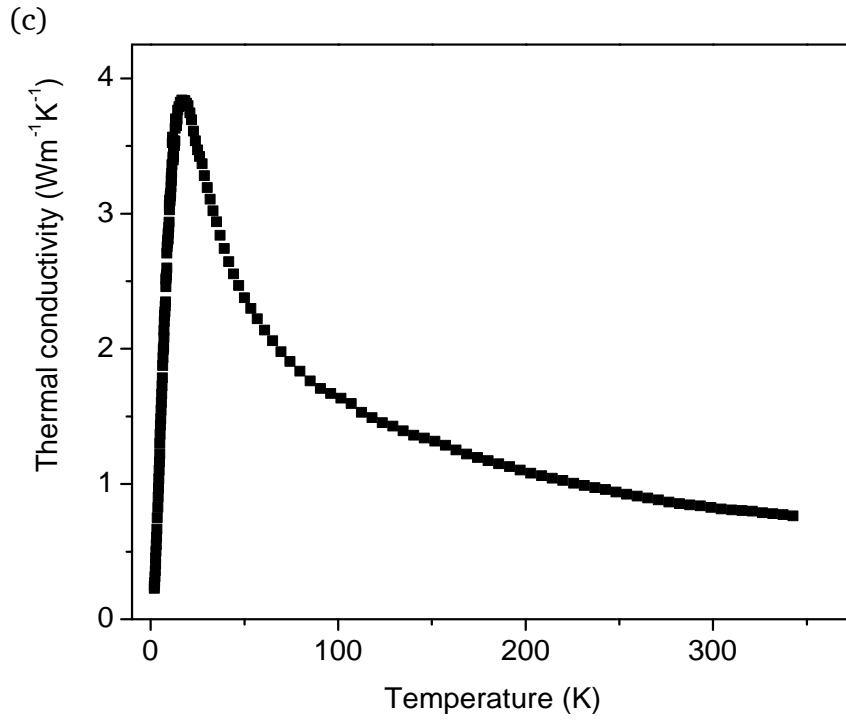


Fig. 6.6 (c) Thermal conductivity of  $\text{Ba}_3\text{AlSb}_3$  as a function of temperature, (d) Figure of merit ( $ZT$ ) of  $\text{Ba}_3\text{AlSb}_3$  as a function of temperature.

### 6.3 Doping studies

$\text{Ba}_3\text{AlSb}_3$  could be doped in different ways in order to improve the transport and physical properties. There are three possible sites for doping. Here,  $\text{Ba}_3\text{AlSb}_3$  was doped in two different ways.

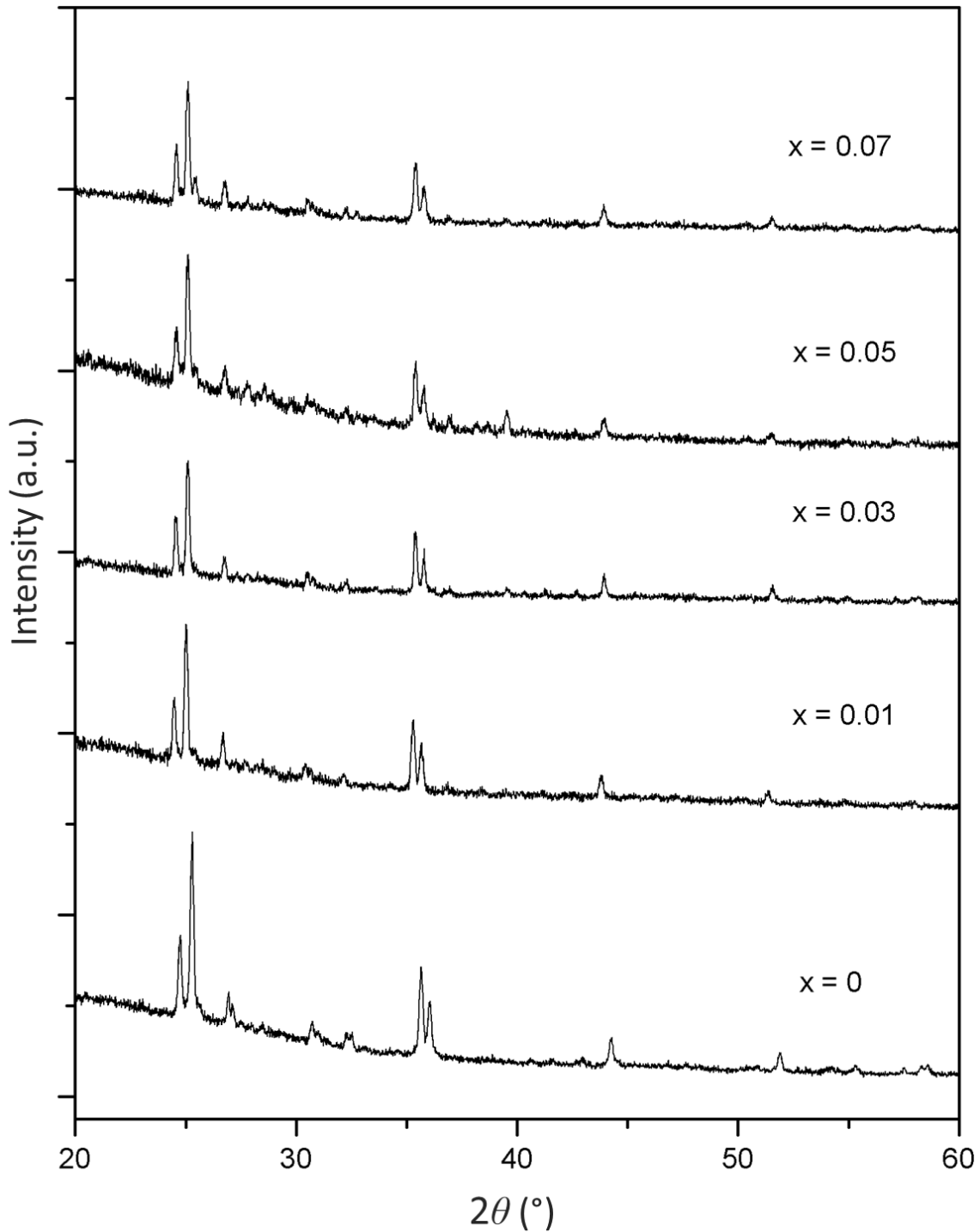


Fig. 6.7 Powder X-ray diffraction patterns of doped and undoped  $\text{Ba}_3\text{Al}_{1-x}\text{Zn}_x\text{Sb}_3$ .

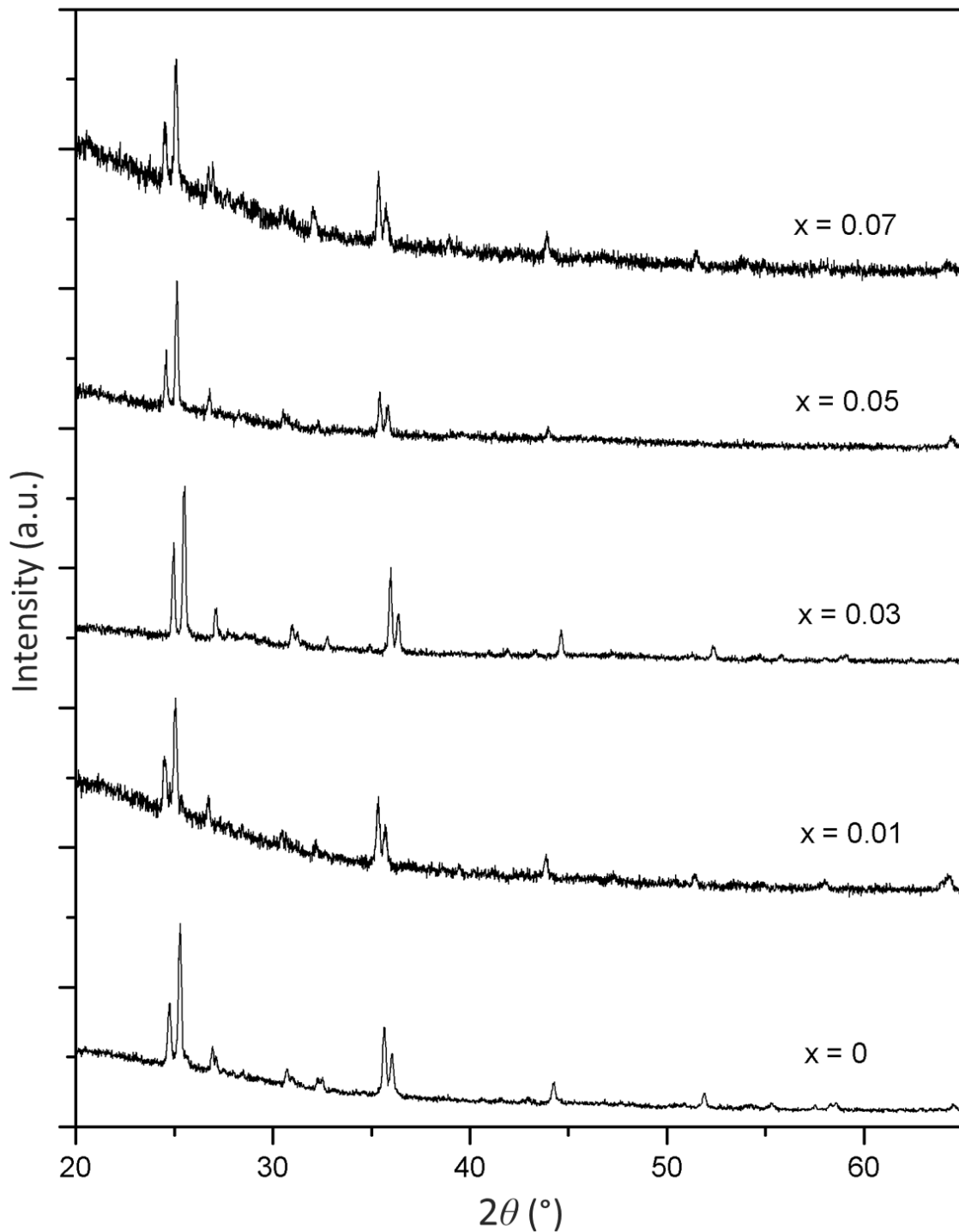


Fig. 6.8 Powder X-ray diffraction patterns of doped and undoped  $\text{Ba}_{3-x}\text{Ca}_x\text{AlSb}_3$ .

Aluminum atoms were substituted by zinc atoms in different ratios. Synthetic procedures were the same as explained in sec. 6.1 except for the substitution of zinc in specific quantities. It was attempted to prepare doped samples according to the following stoichiometry; 1)  $\text{Ba}_3\text{Al}_{0.99}\text{Zn}_{0.01}\text{Sb}_3$  (Ba = 0.5120 g, 3.73 mmol, Al = 0.0332 g, 1.23 mmol, Zn = 0.0008 g, 0.01 mmol, Sb = 0.4540 g, 3.73 mmol) 2)

---

$\text{Ba}_3\text{Al}_{0.97}\text{Zn}_{0.03}\text{Sb}_3$  (Ba = 0.5116 g, 3.72 mmol, Al = 0.0325 g, 1.20 mmol, Zn = 0.0024 g, 0.04 mmol, Sb = 0.4535 g, 3.72 mmol) 3)  $\text{Ba}_3\text{Al}_{0.95}\text{Zn}_{0.05}\text{Sb}_3$  (Ba = 0.5111 g, 3.72 mmol, Al = 0.0318 g, 1.18 mmol, Zn = 0.0041 g, 0.06 mmol, Sb = 0.4531 g, 3.72 mmol) 4)  $\text{Ba}_3\text{Al}_{0.93}\text{Zn}_{0.07}\text{Sb}_3$  (Ba = 0.5107 g, 3.71 mmol, Al = 0.0311 g, 1.15 mmol, Zn = 0.0057 g, 0.09 mmol, Sb = 0.4526 g, 3.71 mmol).

Powder X-ray diffraction measurements were carried out for all of the doped samples. Fig. 6.7 shows the powder X-ray diffraction patterns of undoped and doped  $\text{Ba}_3\text{Al}_{1-x}\text{Zn}_x\text{Sb}_3$ . The diffraction patterns of undoped and doped samples are almost identical except some very small reflections between 25-35°. These peaks arise due to the presence of side phases such as  $\text{Ba}_{11}\text{Sb}_{10}$  or any other binary phases as discussed in sec. 6.1. In the sample with 7 % doping a small peak appears next to the high intense peak and when the dopant concentration is more than 10 % additional impurities appear in the sample. Fig. 6.8 shows the powder X-ray diffraction patterns of undoped and doped  $\text{Ba}_{3-x}\text{Ca}_x\text{AlSb}_3$ . It was attempted to substitute barium with calcium atoms in different proportions (1%, 3%, 5%, 7%) to prepare the following samples; 1)  $\text{Ba}_{2.97}\text{Ca}_{0.03}\text{AlSb}_3$  (Ba = 0.5090 g, 3.71 mmol, Ca = 0.0015 g, 0.04 mmol, Al = 0.0336 g, 1.24 mmol, Sb = 0.4558 g, 3.74 mmol) 2)  $\text{Ba}_{2.91}\text{Ca}_{0.09}\text{AlSb}_3$  (Ba = 0.5024 g, 3.65 mmol, Ca = 0.0046 g, 0.11 mmol, Al = 0.0339 g, 1.26 mmol, Sb = 0.4592 g, 3.77 mmol) 3)  $\text{Ba}_{2.85}\text{Ca}_{0.15}\text{AlSb}_3$  (Ba = 0.4959 g, 3.61 mmol, Ca = 0.0076 g, 0.19 mmol, Al = 0.0342 g, 1.27 mmol, Sb = 0.4625 g, 3.80 mmol) 4)  $\text{Ba}_{2.79}\text{Ca}_{0.21}\text{AlSb}_3$  (Ba = 0.4888 g, 3.55 mmol, Ca = 0.0108 g, 0.27 mmol, Al = 0.0344 g, 1.28 mmol, Sb = 0.4660 g, 3.83 mmol). The powder diffraction patterns of undoped and doped samples are almost identical. These observations indicate that doping of  $\text{Ba}_3\text{AlSb}_3$  was successful and there are no extra impurities produced during the preparation.

Scanning electron microscopic studies were carried out for selected doped samples to study their morphology. Fig. 6.9 (a, b, c, d) shows the SEM images of the doped samples  $\text{Ba}_3\text{Al}_{0.99}\text{Zn}_{0.01}\text{Sb}_3$ ,  $\text{Ba}_3\text{Al}_{0.97}\text{Zn}_{0.03}\text{Sb}_3$ ,  $\text{Ba}_3\text{Al}_{0.95}\text{Zn}_{0.05}\text{Sb}_3$ ,  $\text{Ba}_3\text{Al}_{0.93}\text{Zn}_{0.07}\text{Sb}_3$  respectively. Doped samples have similar particle sizes like the undoped  $\text{Ba}_3\text{AlSb}_3$ . They are in the order of micrometers.

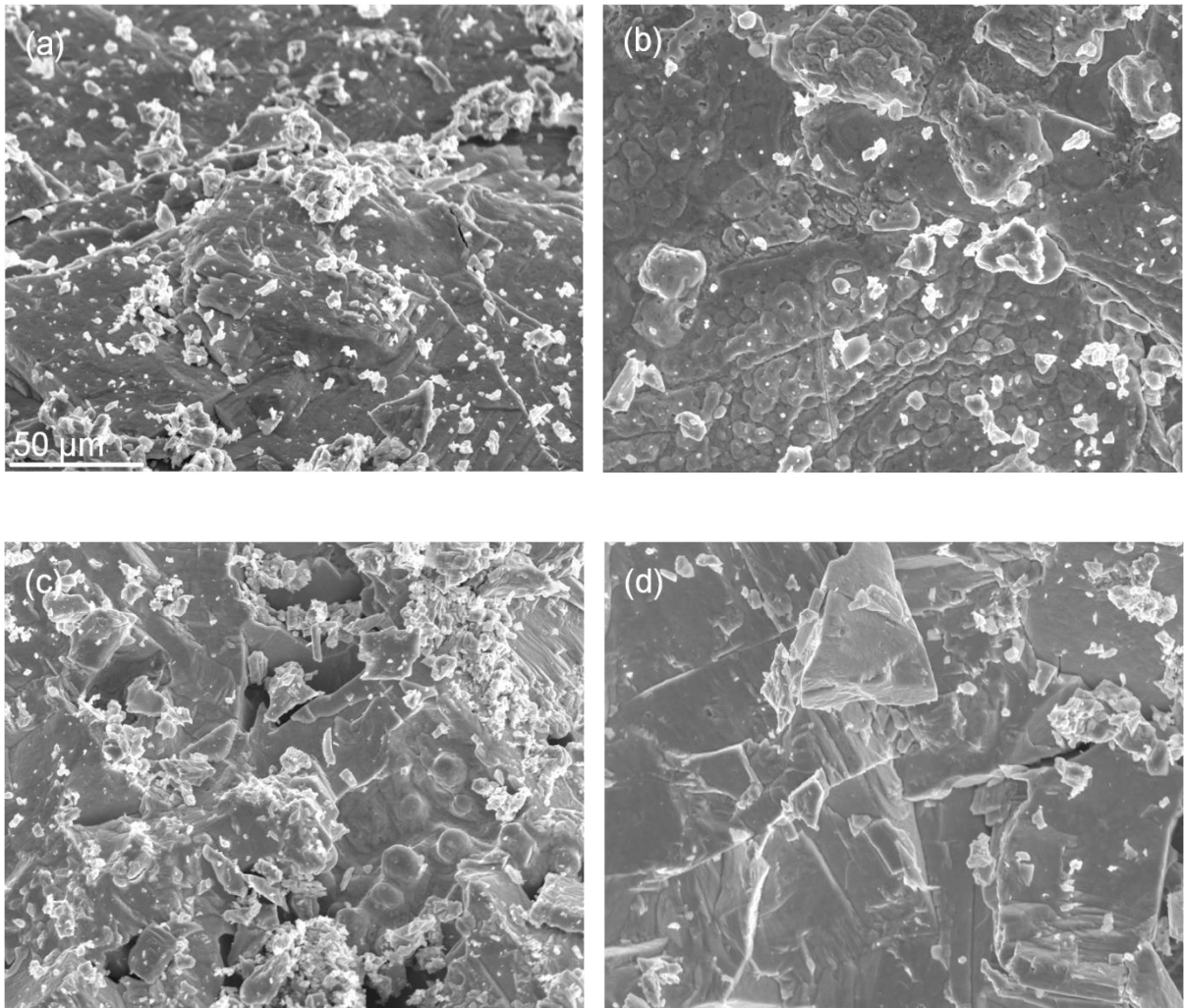


Fig. 6.9 SEM images of  $\text{Ba}_3\text{Al}_{1-x}\text{Zn}_x\text{Sb}_3$  a)  $x = 1\%$ , b)  $x = 3\%$ , c)  $x = 5\%$ , d)  $x = 7\%$ .

EDS measurements were carried out for  $\text{Ba}_3\text{Al}_{1-x}\text{Zn}_x\text{Sb}_3$ , but the zinc content could not be identified due to the low concentration of zinc in the sample. The samples were found to be homogeneous and there were no traces of the container material (tantalum). To identify the zinc present in the doped samples atomic absorption spectroscopy was carried out. Samples were taken in required amounts to make a 100 ml solution in dil. HCl (1:10). The weights were taken in a way that the mass of zinc in the solution would be 2.5 mg. Then using atomic absorption spectroscopy the zinc content in the doped samples was analyzed. Qualitative analysis was performed and zinc was identified to be present in all of the doped samples. Since the absorbance of the standard solutions of zinc (0.5 mg/l, 1 mg/l, 1.5 mg/l) was not correct and so the standard curve was not obtained as a straight line due to the instrumental errors the quantitative analysis was unsuccessful. The observations prove the presence of zinc in the samples though the amount of zinc could not be determined. Fig. 6.10 shows the

SEM images of the doped samples of  $Ba_{3-x}Ca_xAlSb_3$ . EDS measurements were carried out for all of the doped samples. The samples were found to be homogeneous and free from container material. Except for  $Ba_{2.97}Ca_{0.03}GaSb_3$ , the calcium content of the doped samples could be determined by EDS measurements. The obtained values are given in table 6.3. Fig. 6.11 shows the images of EDS mapping of  $Ba_{2.79}Ca_{0.21}AlSb_3$ .

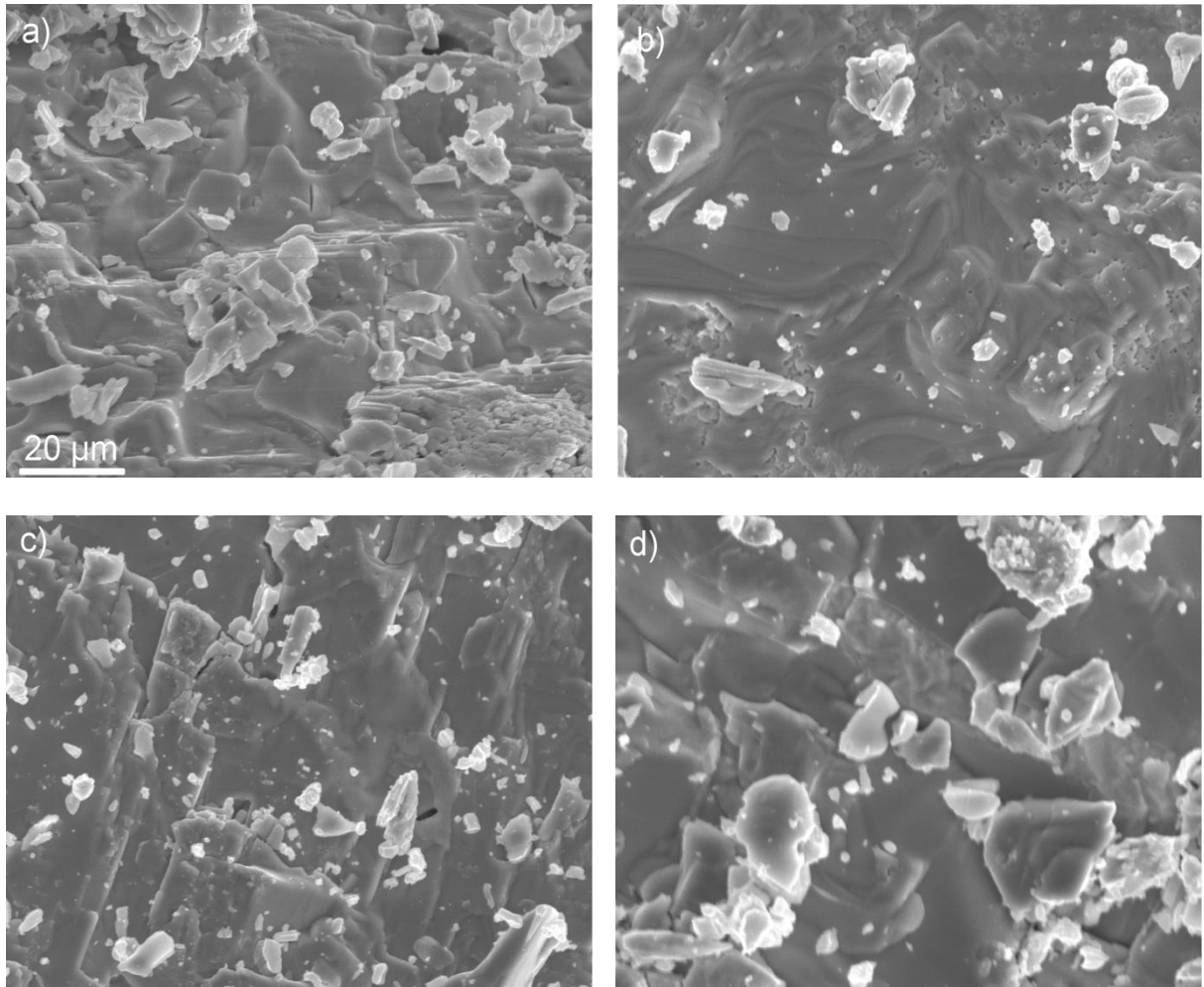
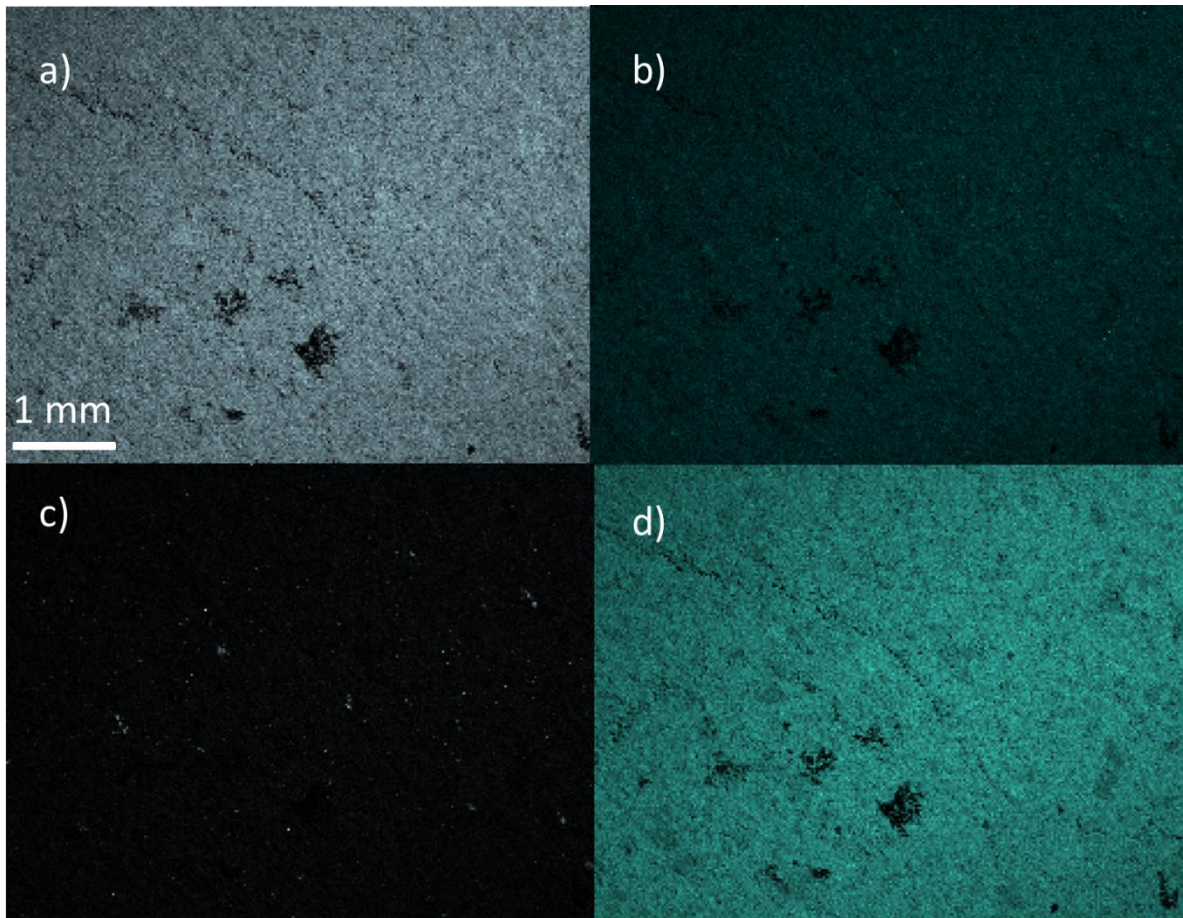


Fig. 6.10 SEM images of  $Ba_{3-x}Ca_xAlSb_3$  a)  $x = 1\%$ , b)  $x = 3\%$ , c)  $x = 5\%$ , d)  $x = 7\%$ .

Table 6.3 Average atomic percentages of doped samples of  $Ba_{3-x}Ca_xAlSb_3$ .

Formula	Ba (%)	Ca (%)	Al (%)	Sb (%)
$Ba_{2.97}Ca_{0.03}GaSb_3$ –Theory	42.43	0.43	14.28	42.86
	40.76	0	13.83	45.41

Measured				
$\text{Ba}_{2.91}\text{Ca}_{0.09}\text{GaSb}_3$ –Theory	41.57	1.29	14.28	42.86
Measured	43.53	2.01	13.71	40.75
$\text{Ba}_{2.85}\text{Ca}_{0.15}\text{GaSb}_3$ –Theory	40.71	2.15	14.28	42.86
Measured	41.63	2.87	15.08	40.42
$\text{Ba}_{2.79}\text{Ca}_{0.21}\text{GaSb}_3$ –Theory	39.85	3.01	14.28	42.86
Measured	41.46	3.97	15.56	39.01



---

Fig. 6.11 EDS mapping of  $Ba_{2.79}Ca_{0.21}AlSb_3$ . a) grey particles are barium ( $Ba_L$ ), b) shiny green particles are calcium ( $Ca_K$ ), c) shiny white particles are aluminum ( $Al_K$ ), d) green particles are antimony ( $Sb_L$ ), dark spots are the damaged portions and small holes in the surface.

The concentration of dopants affects the lattice parameters and that can be calculated from the powder diffraction data [126]. According to Vegard's law, the unit cell parameters vary linearly with composition for a continuous substitution where the atoms or ions are randomly distributed [127, 128]. The simple expression of Vegard's law for binary system A-B is,

$$a = (a^{\circ})_A (1-X) + (a^{\circ})_B (X)$$

where,  $X = X_B$  (mole fraction of component B),  $(a^{\circ})_A$  and  $(a^{\circ})_B$  are the lattice parameters of pure components A and B respectively. The lattice parameters of  $Ba_3Al_{1-x}Zn_xSb_3$  and  $Ba_{3-x}Ca_xAlSb_3$  were refined and plotted against the dopant concentrations (fig. 6.12 and 6.13). For  $Ba_3Al_{1-x}Zn_xSb_3$ , the lattice constant  $b$  decreases linearly with increasing zinc concentration which implies the doping of zinc was successful. The increment in the dopant concentration increases the lattice parameter  $b$  for  $Ba_{3-x}Ca_xAlSb_3$  which is shown in fig. 6.13. In both cases similar observations were found for  $a$  and  $c$ . For  $Ba_{3-x}Ca_xAlSb_3$ , the variation of  $b$  with changing calcium content was not observed as a straight line. Since the samples doped with zinc follow Vegard' law, doping seems to be possible in principle. This compound may possibly be doped with other elements to change the transport and physical properties.

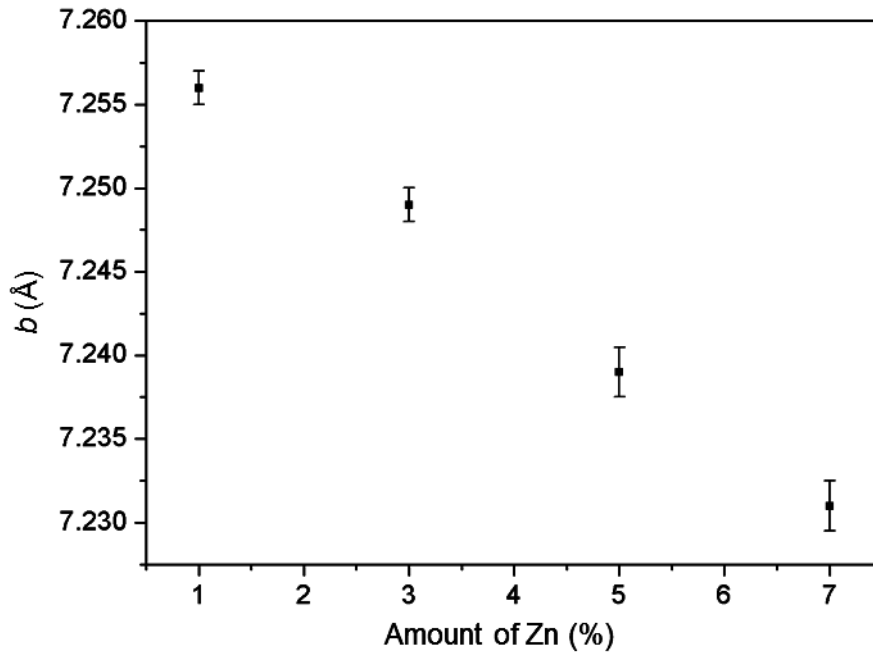


Fig. 6.12 Variation in lattice parameter  $b$  (Å) as a function of dopant concentration (Zn) in  $\text{Ba}_3\text{Al}_{1-x}\text{Zn}_x\text{Sb}_3$ .

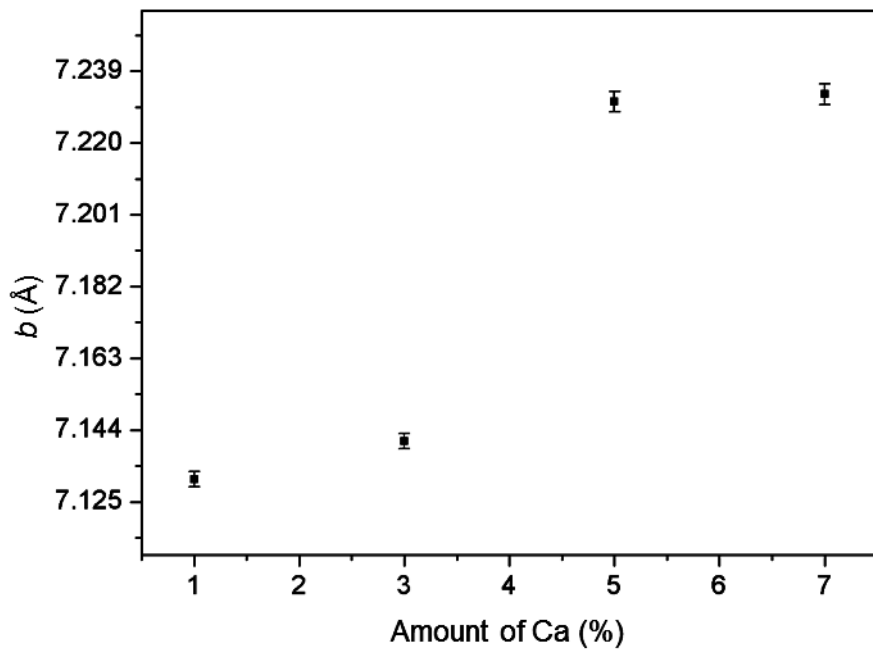
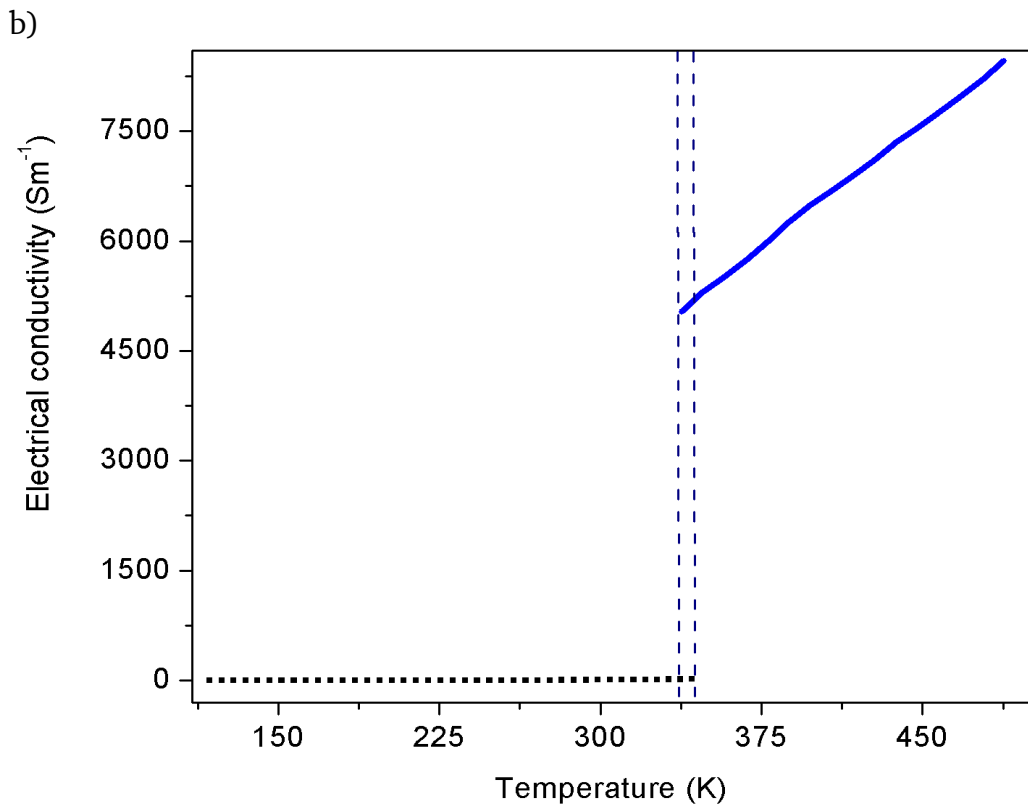
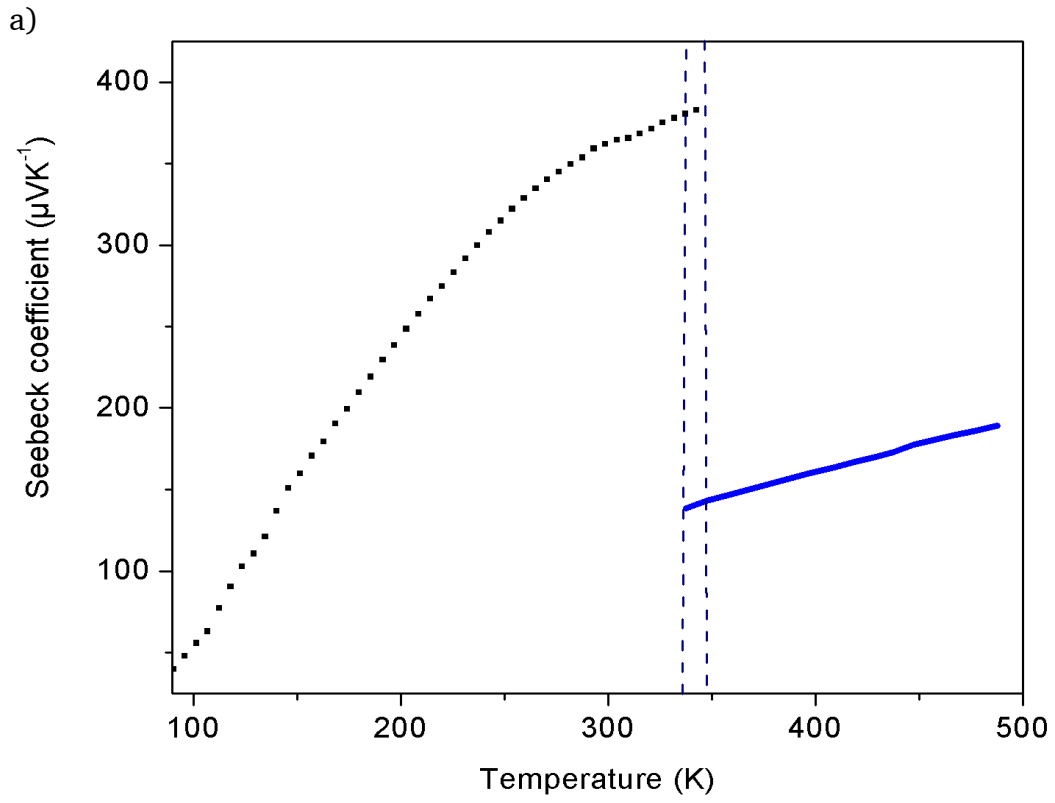


Fig. 6.13 Variation in lattice parameter  $b$  (Å) as a function of dopant concentration (Ca) in  $\text{Ba}_{3-x}\text{Ca}_x\text{AlSb}_3$ .

The thermoelectric properties of  $\text{Ba}_3\text{Al}_{0.97}\text{Zn}_{0.03}\text{Sb}_3$  were measured at high temperatures (330-490 K). Fig. 6.14 allows to compare the thermoelectric properties of  $\text{Ba}_3\text{Al}_{0.97}\text{Zn}_{0.03}\text{Sb}_3$  and undoped  $\text{Ba}_3\text{AlSb}_3$ . Dashed lines indicate the temperature

---

region (330-345 K) that is common in both samples. Seebeck coefficients of  $\text{Ba}_3\text{Al}_{0.97}\text{Zn}_{0.03}\text{Sb}_3$  are lower compared to the undoped  $\text{Ba}_3\text{AlSb}_3$  between 330-345 K but increase with temperature.  $\text{Ba}_3\text{Al}_{0.97}\text{Zn}_{0.03}\text{Sb}_3$  exhibits a maximum Seebeck coefficient of  $189 \mu\text{VK}^{-1}$  at 490 K. Electrical conductivities of  $\text{Ba}_3\text{Al}_{0.97}\text{Zn}_{0.03}\text{Sb}_3$  increase from 330 K and the electrical conductivities are higher than the undoped  $\text{Ba}_3\text{AlSb}_3$  between 330-345 K.  $\text{Ba}_3\text{Al}_{0.97}\text{Zn}_{0.03}\text{Sb}_3$  exhibits a maximum electrical conductivity of  $8450 \text{ Sm}^{-1}$  at 490 K. Thermal conductivities of  $\text{Ba}_3\text{Al}_{0.97}\text{Zn}_{0.03}\text{Sb}_3$ , are close to  $1.35 \text{ Wm}^{-1}\text{K}^{-1}$ .  $ZT$  values of  $\text{Ba}_3\text{Al}_{0.97}\text{Zn}_{0.03}\text{Sb}_3$  increase with increasing temperature. The maximum value observed is 0.1081 at 490 K. Enhancement in  $ZT$  values and differences in all of the thermoelectric properties are observed in the temperature range between 330-345 K. These observations indicate that presence of zinc changes the thermoelectric properties of  $\text{Ba}_3\text{AlSb}_3$ .



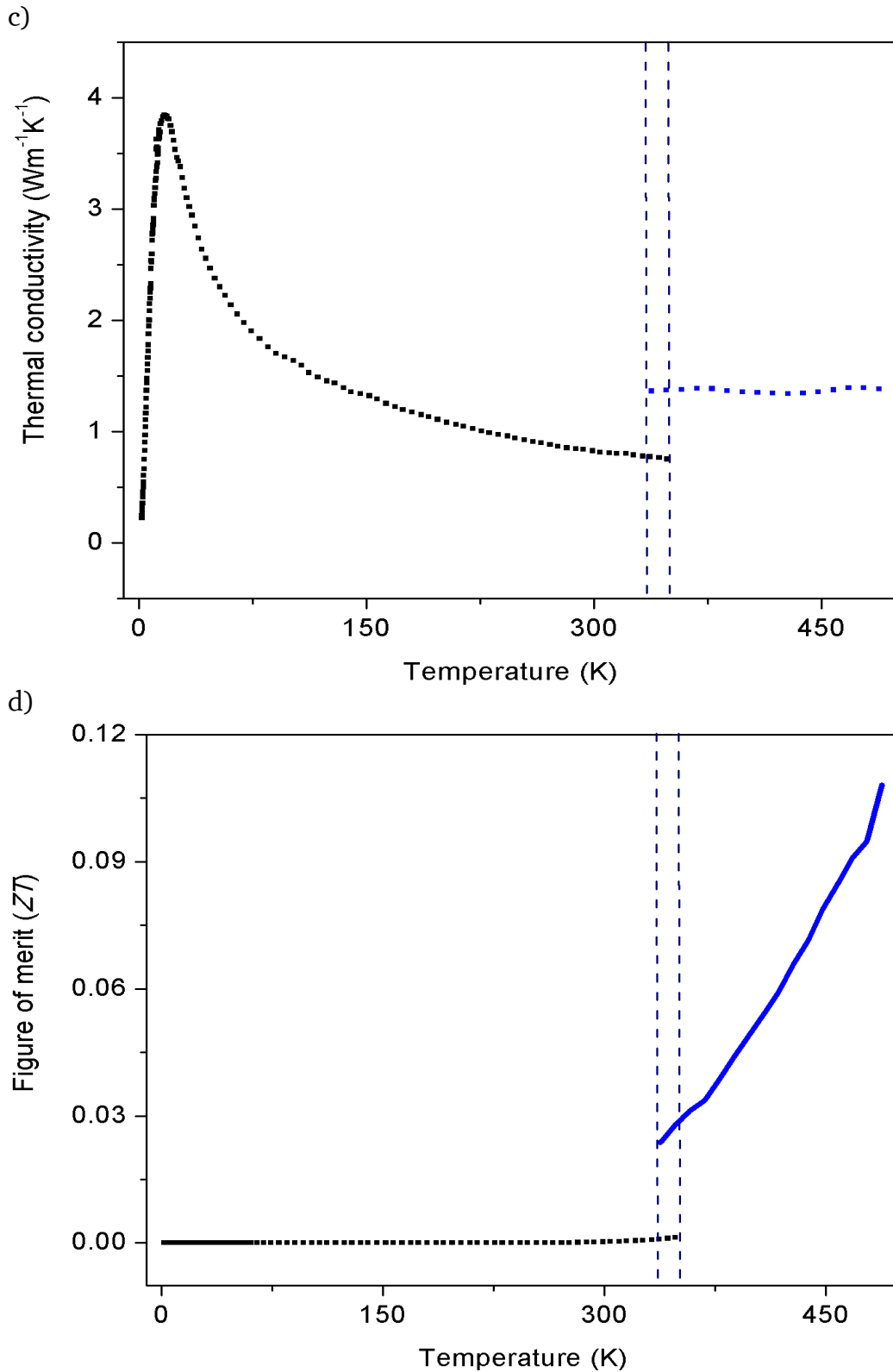


Fig. 6.14 (a) Seebeck coefficient as a function of temperature, (b) Electrical conductivity as a function of temperature, (c) Thermal conductivity as a function of temperature, (d) Figure of merit ( $ZT$ ) as a function of temperature of  $\text{Ba}_3\text{Al}_{0.97}\text{Zn}_{0.03}\text{Sb}_3$  (blue) in comparison to undoped  $\text{Ba}_3\text{AlSb}_3$  (black), blue dashed lines indicate, common temperature region (330-345 K) in both measurements.

---

## 6.4 Discussion of the results

$\text{Ba}_3\text{AlSb}_3$  was successfully synthesized as a main product using solid state reactions.  $\text{Ba}_{11}\text{Sb}_{10}$  appears as the side phase in very little quantity similarly to what has been observed in the literature for  $\text{Sr}_3\text{GaSb}_3$  where  $\text{Sr}_2\text{Sb}_3$  (1-3 %) was found as a secondary phase [129].  $\text{Ba}_3\text{AlSb}_3$  was predicted to be a narrow band gap semiconductor with a band gap of 0.5 eV using density functional theory calculations. Other Zintl phases such as  $\text{Ca}_5\text{Al}_2\text{Sb}_6$  and  $\text{Yb}_{14}\text{AlSb}_{11}$  are also semiconductors [77, 130] with similar band gaps (0.5 eV).  $\text{Ba}_3\text{AlSb}_3$  was found to be stable up to 1073 K. This compound was successfully compacted using the spark plasma sintering technique. The compacted sample was 95 % dense compared to the theoretical density.  $\text{Ba}_3\text{AlSb}_3$  exhibits high Seebeck coefficients. The observed maximum is  $383 \mu\text{VK}^{-1}$  at 342 K which can be compared with the Seebeck coefficients of other  $\text{A}_3\text{MSb}_3$  type compounds such as  $\text{Ca}_3\text{AlSb}_3$  and  $\text{Sr}_3\text{GaSb}_3$ .  $\text{Ca}_3\text{AlSb}_3$  [123] shows a high Seebeck value ( $> 400 \mu\text{VK}^{-1}$ ) around 650 K and  $\text{Sr}_3\text{GaSb}_3$  [129] shows its maximum Seebeck coefficient of  $340 \mu\text{VK}^{-1}$  at 700 K. Like the Seebeck coefficients the thermal conductivities of  $\text{Ba}_3\text{AlSb}_3$  ( $k_{\text{min}} = 0.75 \text{ Wm}^{-1}\text{K}^{-1}$ ) are also comparable to the other Zintl compounds known to exhibit high values of the figure of merit. Apart from  $\text{A}_3\text{MSb}_3$  type compounds some of the  $\text{A}_5\text{M}_2\text{Sb}_6$  compounds such as  $\text{Ca}_5\text{Al}_2\text{Sb}_6$ ,  $\text{Ca}_5\text{Ga}_2\text{Sb}_6$  and  $\text{Ca}_5\text{In}_2\text{Sb}_6$  are also known to exhibit thermal conductivities close to  $1 \text{ Wm}^{-1}\text{K}^{-1}$  in the temperature range of 300-1000 K [130, 131].

Due to low values of electrical conductivity the overall figure of merit is not as high as expected. This can be possibly due to the lack in carrier concentration or inefficiency to activate charge carriers across the band gap. Studying and modifying carrier concentration and other properties can yield an efficient thermoelectric material. Doping studies can help to improve the properties in future as doping can change the band structure and thus the electronic properties of the compound. Doping can also modify the carrier concentration and improve the overall figure of merit. In this aspect  $\text{Ba}_3\text{AlSb}_3$  was doped with zinc and calcium and then characterized. Zinc was attempted to substitute in the sites of aluminum and calcium was attempted to substitute in the sites of barium. As an example,  $\text{Ba}_3\text{Al}_{0.97}\text{Zn}_{0.03}\text{Sb}_3$  was compacted and the thermoelectric properties (330-490 K) were studied. This compound shows different properties and values of the figure of merit compared to undoped  $\text{Ba}_3\text{AlSb}_3$

---

which was investigated in the temperature range of 330-345 K. Seebeck coefficients are lower than the undoped  $\text{Ba}_3\text{AlSb}_3$  in this temperature region. Electrical conductivities and values of the figure of merit of  $\text{Ba}_3\text{Al}_{0.97}\text{Zn}_{0.03}\text{Sb}_3$  are found to be higher than those of undoped  $\text{Ba}_3\text{AlSb}_3$  between 330-345 K. A maximum figure of merit value of 0.1081 was observed around 490 K for  $\text{Ba}_3\text{Al}_{0.97}\text{Zn}_{0.03}\text{Sb}_3$ . Thus, doping experiments help to change the thermoelectric properties. Further studies in future can help to understand more about this system and to improve the properties.

---

---

## 7 Ba-Ga-Sb systems

---

---

### 7.1 Ba<sub>3</sub>GaSb<sub>3</sub>

---

#### 7.1.1 Synthesis, characterization and compaction

Ba<sub>3</sub>GaSb<sub>3</sub> was prepared as an almost single-phase sample. Ba (0.4864 g, 3.54 mmol, chempur, 99.3%), Ga (0.0823 g, 1.18 mmol, Degussa, 99.99%) and Sb (0.4313 g, 3.54 mmol, Chempur, Sb-shots, 1-3 mm, 99.999%) pieces with the stoichiometric ratio of 3 : 1 : 3 were loaded into a tantalum container. All manipulations were done under argon atmosphere using a glove box with oxygen and moisture levels below one. This sealed container was further inserted into a quartz tube and eventually evacuated and flame sealed to prepare the ampoule for heating. The assembly was then heated in a tubular furnace to 1173 K for three days with a heating rate of 90 K/h and a cooling rate of 60 K/h. Reaction conditions are similar to the preparation of Ba<sub>3</sub>AlSb<sub>3</sub> except for the higher reaction temperature. Ba<sub>3</sub>GaSb<sub>3</sub> was produced with a very high yield and the method was found to be reproducible. The resulting product is metallic grey in color with luster and consists of crystals, lumps and small pieces. The product was found to be air-sensitive.

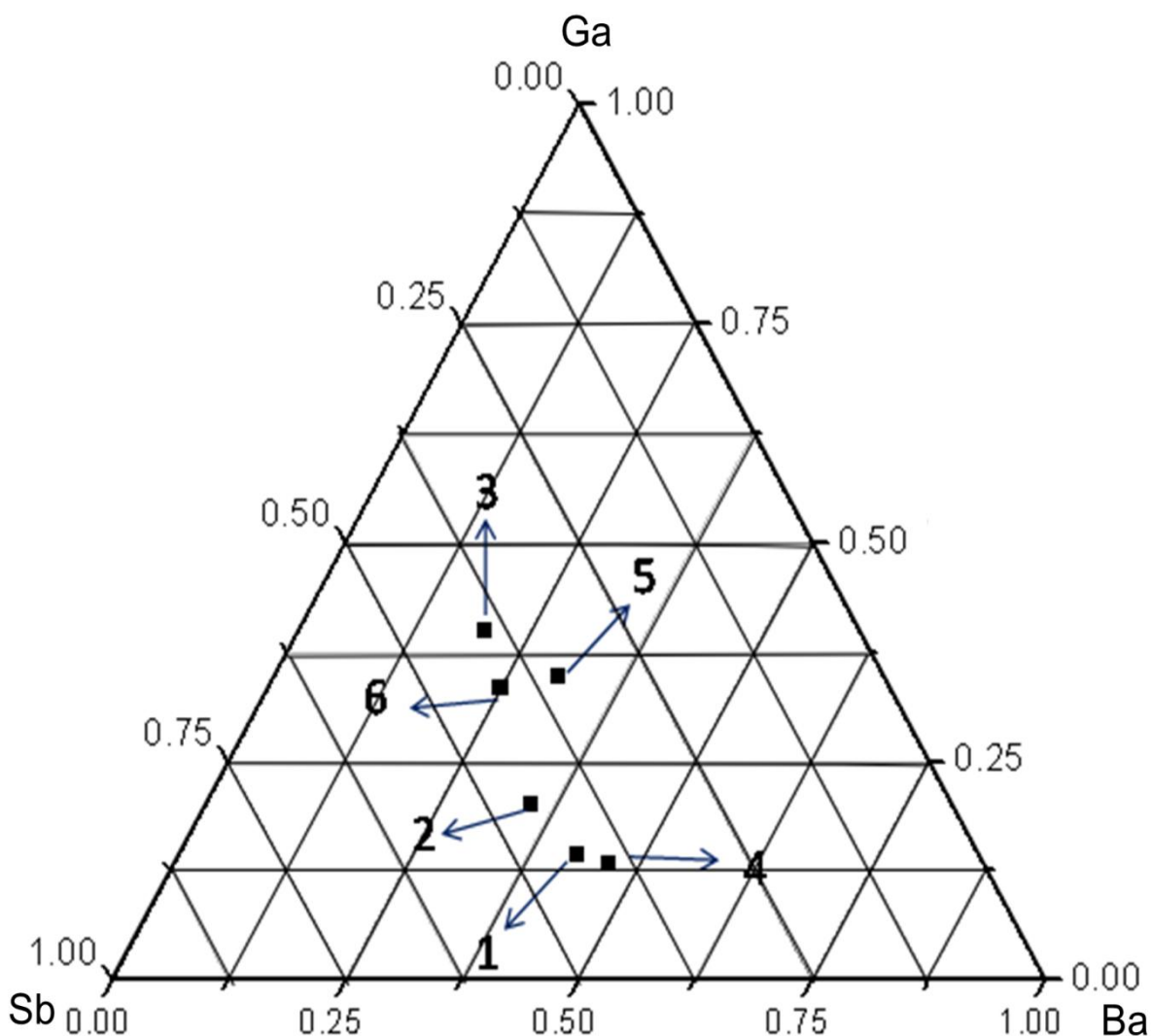


Fig. 7.1.1 Ternary phase diagram of well-known Ba-Ga-Sb compounds (1 =  $\text{Ba}_3\text{GaSb}_3$ , 2 =  $\text{Ba}_7\text{Ga}_4\text{Sb}_9$ , 3 =  $\text{BaGa}_2\text{Sb}_2$ , 4 =  $\text{Ba}_7\text{Ga}_2\text{Sb}_6$ , 5 =  $\text{Ba}_7\text{Ga}_8\text{Sb}_8$ , 6 =  $\text{Ba}_3\text{Ga}_4\text{Sb}_5$ ) [112-114, 116, 132-133].

A secondary phase  $\text{Ba}_7\text{Ga}_4\text{Sb}_9$  appears in very small quantities as an impurity. Any increase in the reaction temperature or longer duration of the reaction led to the formation of a mixture of these two phases. At higher temperatures binary impurity phases such as  $\text{Ba}_2\text{Sb}_3$  or  $\text{Ba}_5\text{Sb}_3$  were found [120, 122]. Sometimes additional tantalum phases were identified when the duration of reaction was longer than seven days at temperatures above 1273 K. Only precise control over temperature and time can yield the almost phase-pure product. The projection of the ternary phase diagram that is shown in fig. 7.1.1 shows the well-known Ba-Ga-Sb Zintl phases that can

appear as side phases during the preparation of  $\text{Ba}_3\text{GaSb}_3$ .  $\text{Ba}_7\text{Ga}_4\text{Sb}_9$  exists very close to  $\text{Ba}_3\text{GaSb}_3$  in the ternary diagram. Another example is  $\text{Ba}_7\text{Ga}_2\text{Sb}_6$  which is a dimer of  $\text{Ba}_3\text{GaSb}_3$  with one extra barium atom. Synthetic procedures using other methods did not yield the expected product.

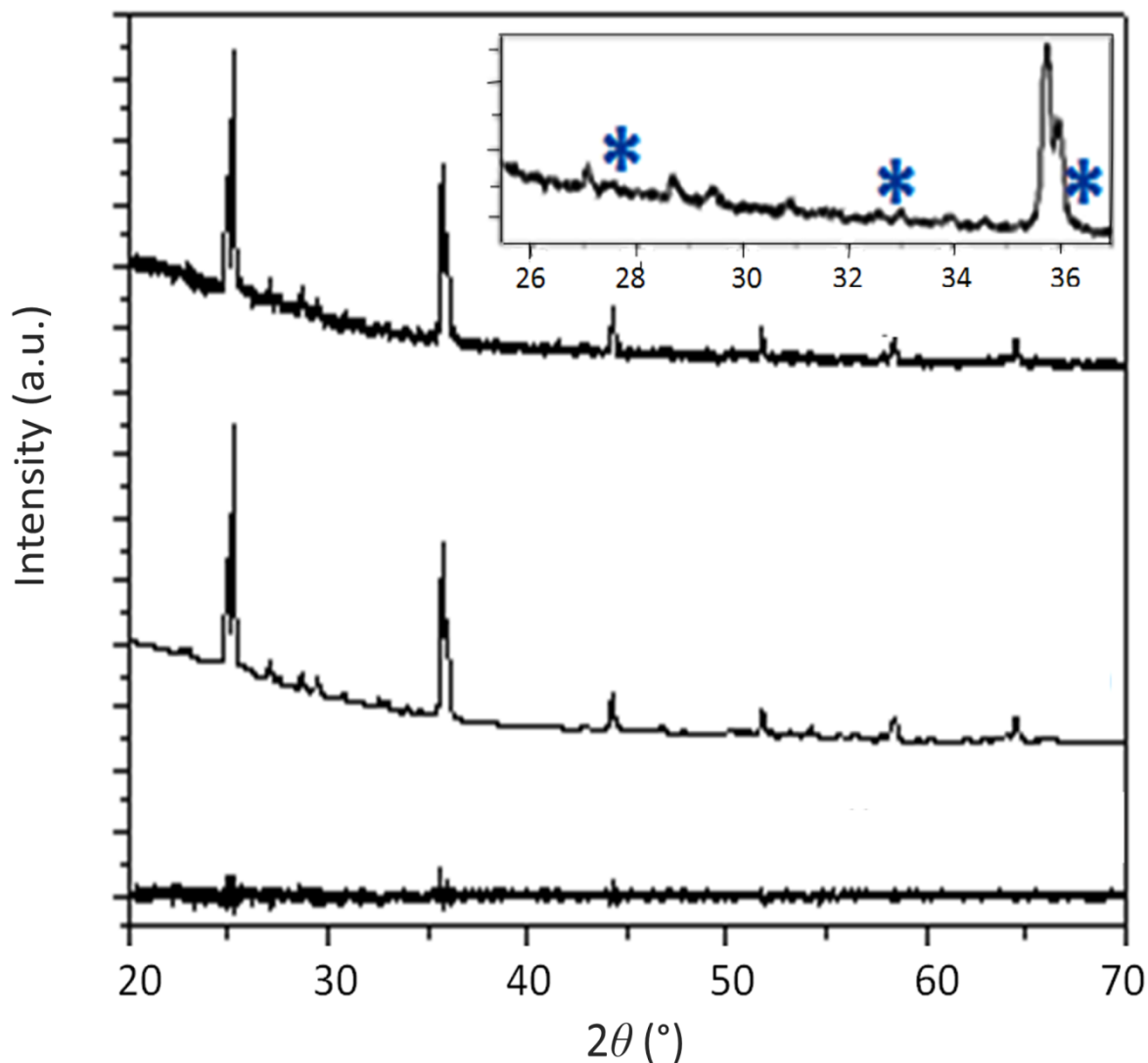


Fig. 7.1.2 Measured powder XRD (top), calculated powder XRD (middle) and difference curve (bottom) of  $\text{Ba}_3\text{GaSb}_3$  [The inset shows the marked reflections from the secondary phase].

Powder X-ray diffraction patterns were analyzed to evaluate the purity of the products. Samples for powder X-ray diffraction measurements were prepared as explained in sec. 3.1. Using the program *TOPAS* the powder X-ray patterns were fitted. This revealed that the sample was more than 98 % pure related to  $\text{Ba}_3\text{GaSb}_3$ .

Traces of Ba<sub>7</sub>Ga<sub>4</sub>Sb<sub>9</sub> appear as an impurity in a very small scale (1-2%). Fig. 7.1.2 shows the measured powder X-ray pattern of Ba<sub>3</sub>GaSb<sub>3</sub>, the calculated powder X-ray pattern and the difference curve. The inset shows the magnified area ( $2\theta$  range 26 - 38<sup>o</sup>) where the impurity reflections are marked by asterisk symbols. The calculated powder X-ray pattern matches very well to the measured powder X-ray pattern of the sample. The difference curve shows no significant peaks. Only the lattice parameters were refined. Experimental and literature lattice parameters are given in table 7.1.1.

Table 7.1.1 Lattice parameters of Ba<sub>3</sub>GaSb<sub>3</sub> calculated from Rietveld refinement based on the structure model from literature [112].

	<i>a</i>	<i>b</i>	<i>c</i>
Literature	14.118 (5) Å	21.177(7) Å	7.128(3) Å
This work	14.116 (1) Å	21.164 (9) Å	7.141 (3) Å
<i>R</i> <sub>exp.</sub> : 4.55	<i>R</i> <sub>wp.</sub> : 4.72	<i>R</i> <sub>p.</sub> : 3.62	<i>GOF</i> : 1.04

High-temperature powder X-ray diffraction measurements were carried out to investigate the thermal stability and phase transitions at higher temperatures for Ba<sub>3</sub>GaSb<sub>3</sub>. The sample for high temperature powder X-ray diffraction measurement was prepared by the method that was explained in sec. 3.1. The sample was heated from room temperature to 1168 K and then cooled down to room temperature. Powder X-ray diffraction measurements were carried out at every 100 K difference (increase or reduction). The sample did not show any changes. From fig. 7.1.3 it is evident that there are no phase transitions observed in the X-ray diffraction patterns in the temperature range investigated. The sample was found to be stable during heating and cooling cycles. This compound can be a suitable candidate for applications over a wide temperature range.

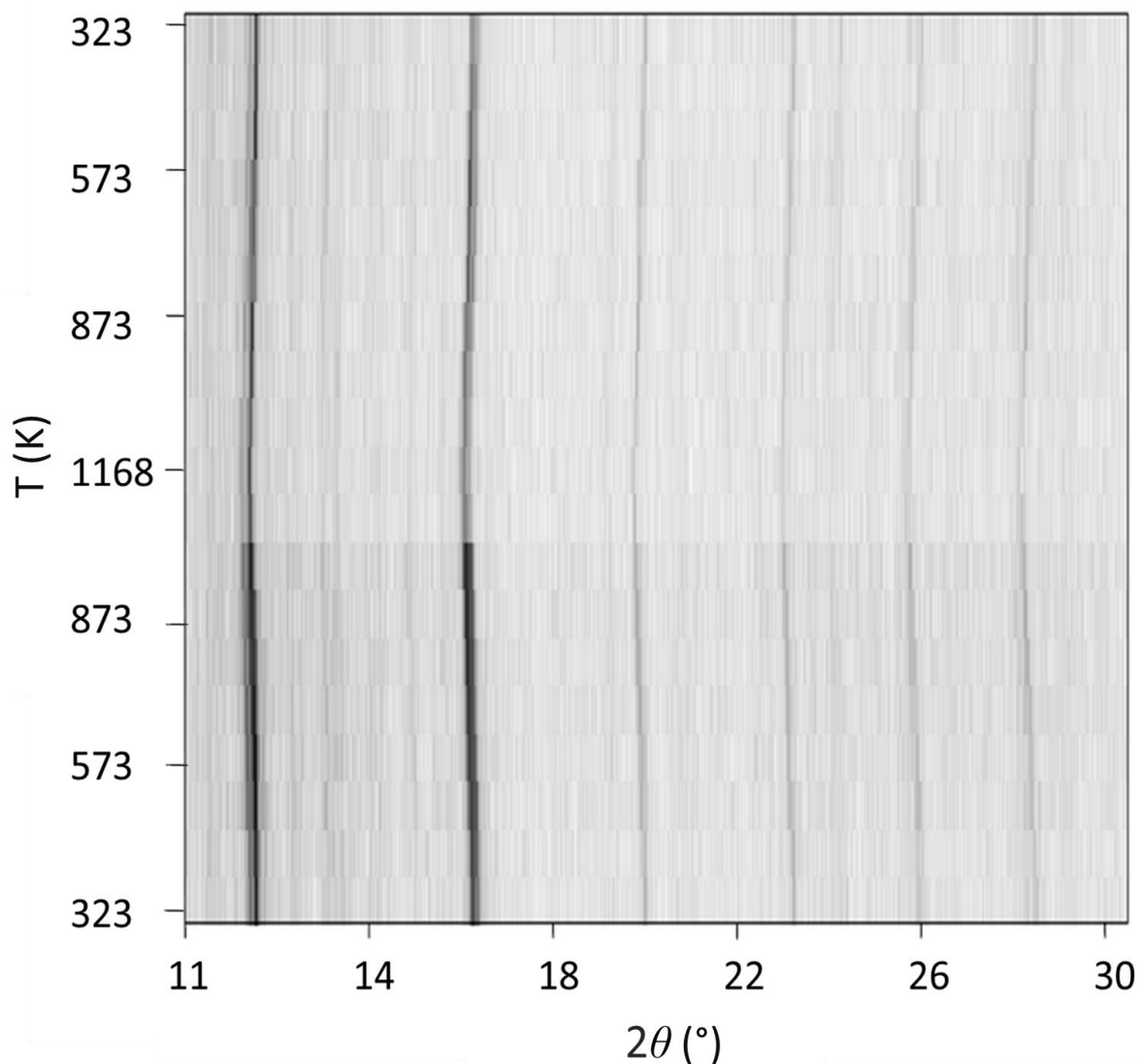


Fig. 7.1.3 High-temperature powder XRD of  $\text{Ba}_3\text{GaSb}_3$  (Lower part: heating from 323 K to 1168 K; and upper part: cooling from 1168 K to 323 K).

Using the program *TOPAS*, the powder X-ray diffraction patterns collected at different temperatures were fitted. The lattice parameters were refined. Fig. 7.1.4 shows the relationship between the lattice parameters and the temperature. They increase with increasing temperature. Lattice parameters are given in fig. 7.1.4. a, b, c where red lines indicate heating cycles and the blue lines indicate cooling cycles. As seen in the diagram the lattice parameters are comparable in heating and cooling cycles. Fig. 7.1.4.d shows the relationship between unit cell volume and temperature. The unit cell volumes increase with increasing temperature due to thermal expansion.

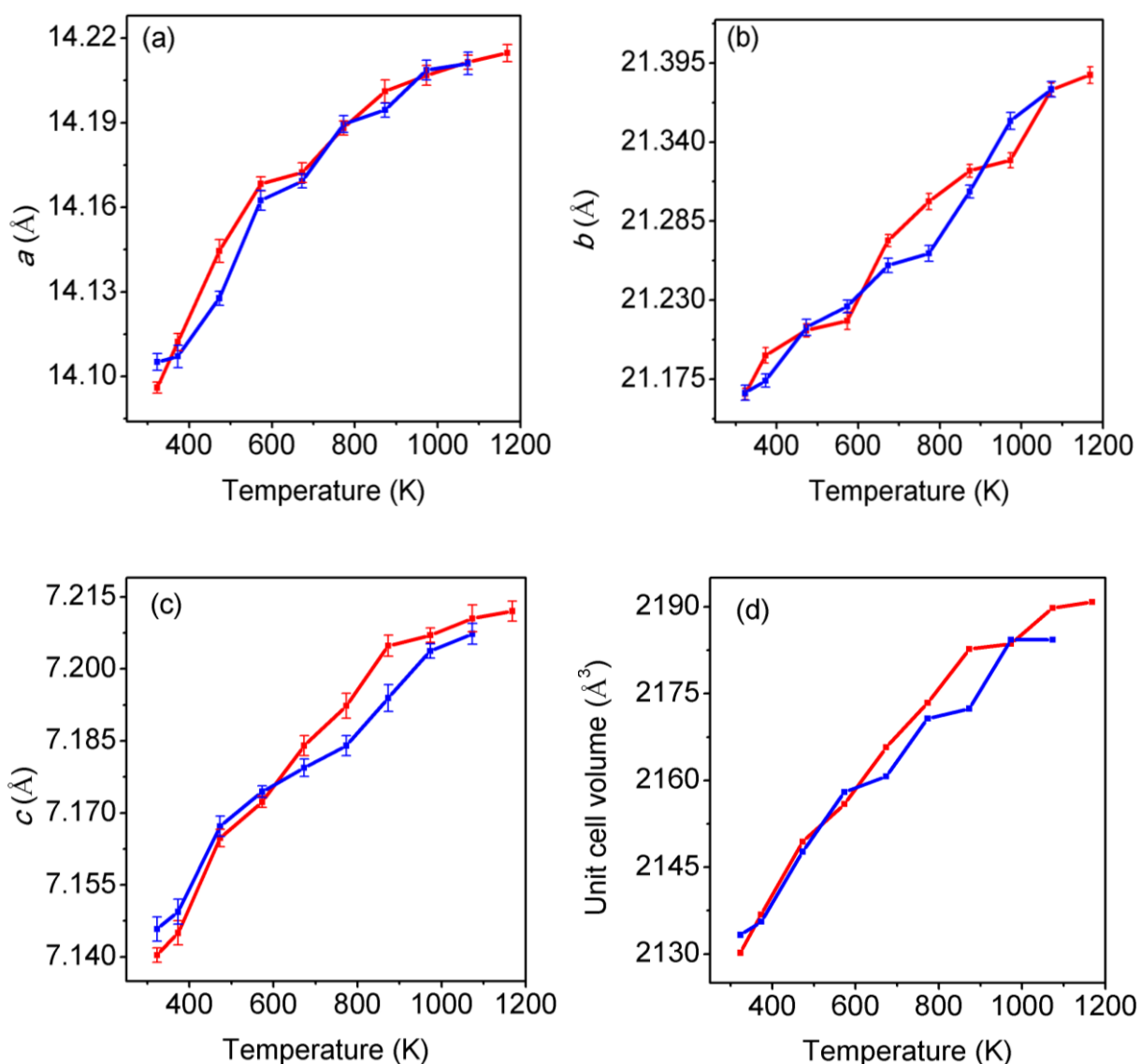


Fig. 7.1.4. a, b, c: Changes of lattice parameters (Å) with temperature (red lines indicate heating from 323 K to 1168 K and blue lines indicate cooling from 1168 K to 323 K). Fig. 5.1.6. d Unit cell volume as a function of temperature (standard deviations were too small to be visible).

Differential thermal analysis and thermal gravimetric studies were carried out (Max Planck Institute for Chemical Physics of Solids, Dresden) to investigate the thermal stability, melting point, possible phase transitions etc. Fig. 7.1.5 shows the differential thermal analysis and thermal gravimetry traces of Ba<sub>3</sub>GaSb<sub>3</sub>. 23 mg of sample were placed in a niobium container that was closed with a lid and then the measurements were carried out under argon atmosphere. The sample was heated from room

---

temperature up to 1173 K with a heating rate of 10 K/min. Then it was cooled down to room temperature with the same rate.

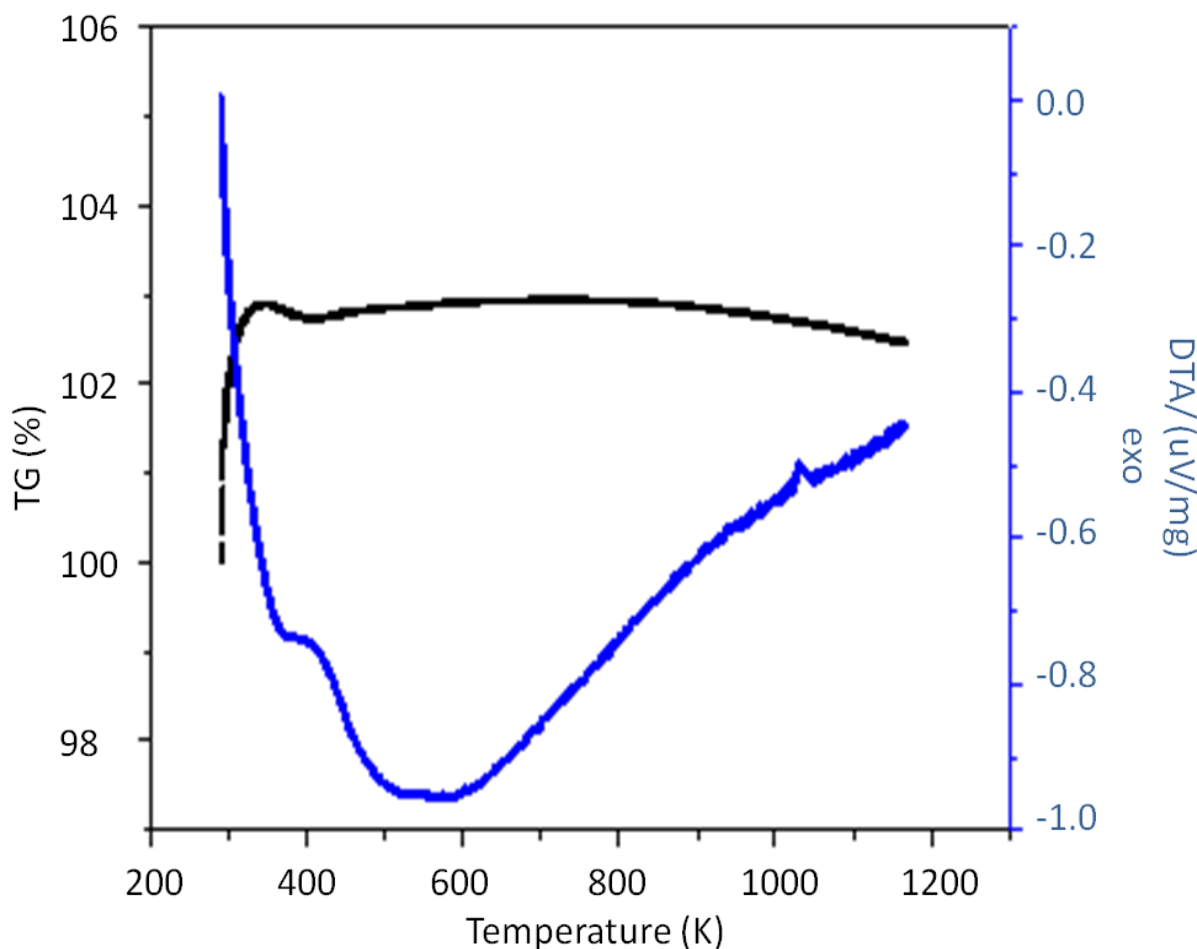


Fig. 7.1.5 Differential thermal analysis and thermal gravimetry measurements of  $\text{Ba}_3\text{GaSb}_3$ .

$\text{Ba}_3\text{GaSb}_3$  was found to be stable throughout the measurement. There are no sharp peaks observed in the differential thermal analysis except for a small peak that appears around 1033 K. The thermal gravimetric measurement showed no changes in the pattern, so the compound is thermally stable up to 1173 K. These results can be compared with high-temperature powder X-ray diffraction measurements. There are no indications for any phase transition or loss of material during heating in the sample.

A finely ground powder of  $\text{Ba}_3\text{GaSb}_3$  was compacted by spark plasma sintering (Max Planck Institute for Chemical Physics of Solids, Dresden). The finely ground powder was compacted at 923 K with an uniaxial pressure of 100 MPa. The heating and

cooling rates were 25 K/min. The sample was sintered for 20 minutes. The compacted sample was used for all of the physical property measurements. After spark plasma sintering the sample was analyzed by powder X-ray diffraction, SEM and EDS to confirm that the sample had not undergone any changes. The powder X-ray diffraction pattern of the compacted sample was identical to the starting material which is shown in fig. 7.1.6. The compacted sample was 95 % dense compared to the theoretical value ( $5.28 \text{ g/cm}^3$ ) from X-ray diffraction.

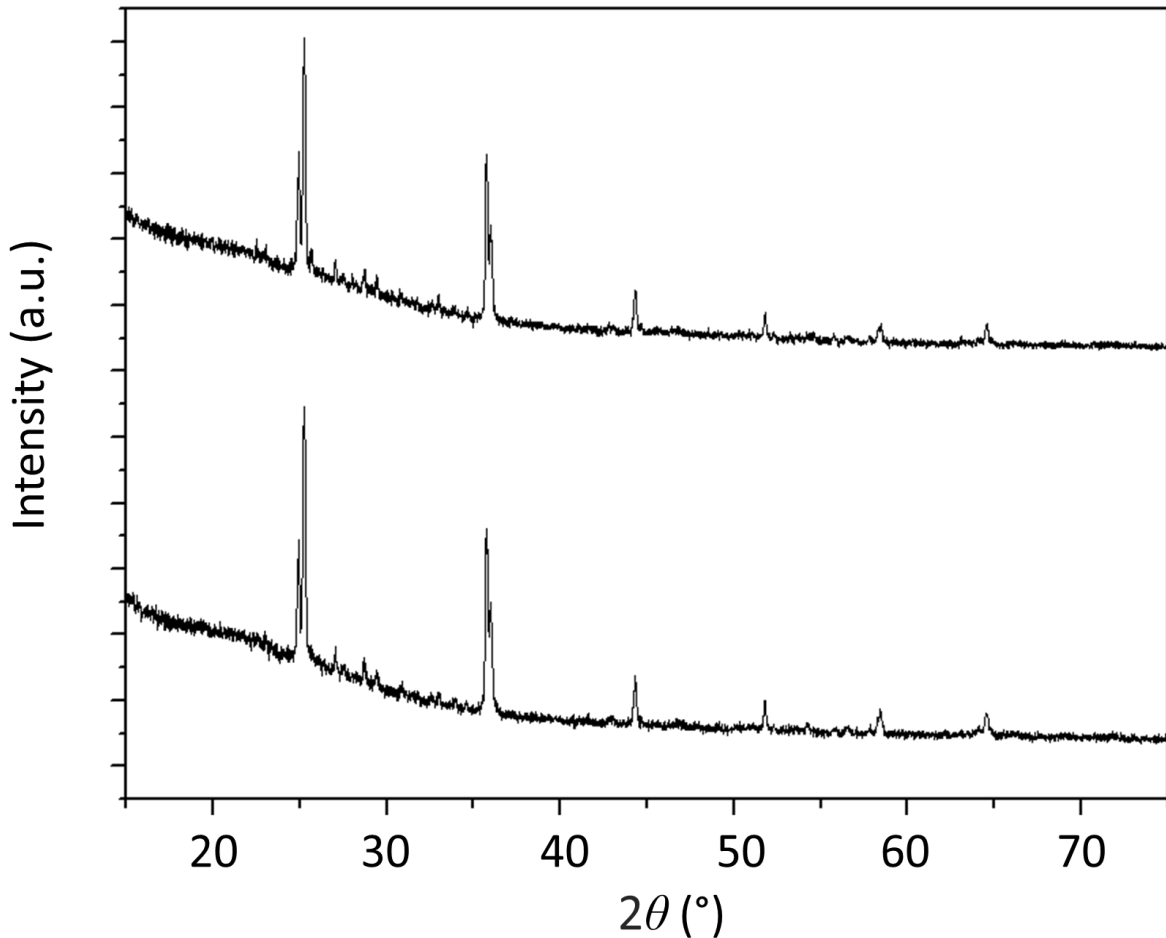


Fig. 7.1.6 Powder X-ray diffraction patterns of  $\text{Ba}_3\text{GaSb}_3$  before (bottom) and after sintering (top).

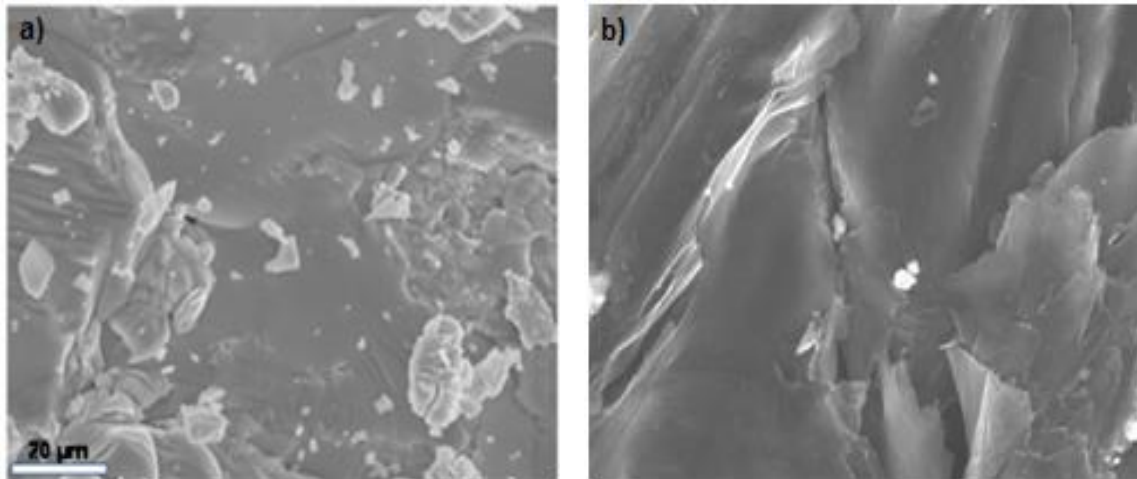


Fig. 7.1.7 SEM images of  $Ba_3GaSb_3$  a) as synthesized b) SEM image after spark plasma sintering.

Scanning electron microscopy images of  $Ba_3GaSb_3$  before and after spark plasma sintering are shown in fig. 7.1.7. Energy dispersive spectroscopy was used to measure the composition of  $Ba_3GaSb_3$ .

Table 7.1.2 Atomic percentages of all elements in  $Ba_3GaSb_3$  determined using EDS.

	Ba (%)	Ga (%)	Sb (%)
Spot 1	42.16	13.92	43.92
Spot 2	43.79	14.57	41.64
Spot 3	42.98	15.13	41.89
Average	42.98	14.54	42.48
Theoretical values	42.86	14.28	42.86

In three different spots the measurements were carried out and the measured atomic percentages are close to the theoretical values (table 7.1.2). From these measurements, the sample was found to be homogeneous. Another interesting observation is that there are no traces of tantalum in the sample. This shows that there were no reactions between the container and the reactants.

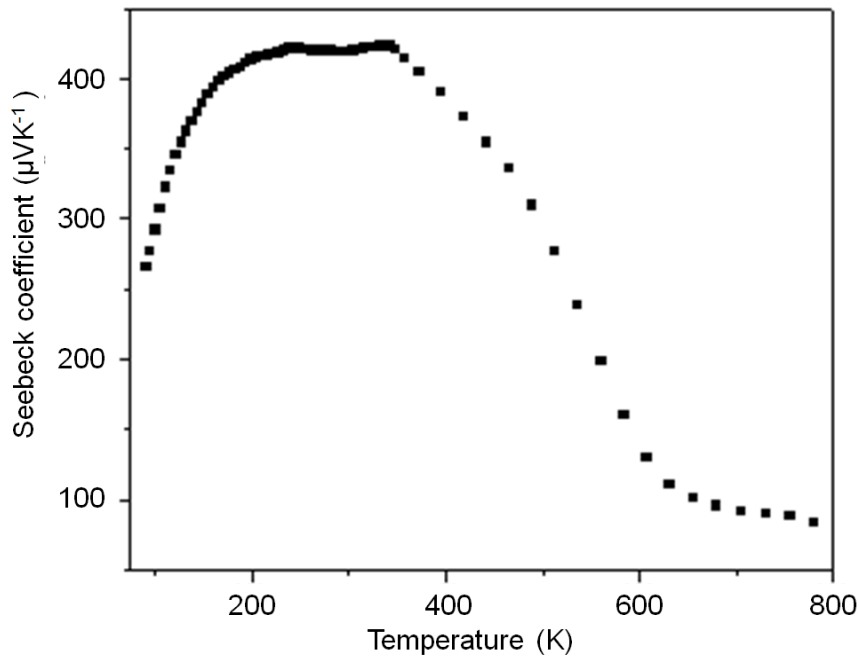
---

### 7.1.2 Thermoelectric studies

Thermoelectric properties were measured using the sintered sample (Max Planck Institute for Chemical Physics of Solids, Dresden). Fig. 7.1.8. a shows the Seebeck values of  $\text{Ba}_3\text{GaSb}_3$  with increasing temperature.  $\text{Ba}_3\text{GaSb}_3$  exhibits high Seebeck values. Seebeck coefficients were measured from 70 K up to 800 K. It reaches a maximum of  $425 \mu\text{VK}^{-1}$  around 340 K. Between 340 K and 380 K there were no significant changes in the Seebeck coefficients. After 380 K the Seebeck coefficients start to decrease. The electrical conductivities were measured from 70 K up to 800 K.  $\text{Ba}_3\text{GaSb}_3$  exhibits semiconducting behavior as the electrical conductivity values are increasing with temperature which is typical of a semiconductor. According to DFT calculations the band gap of this compound was estimated to be 0.3 eV. Fig. 7.1.8. b shows the electrical conductivity curve with increasing temperature. At low temperatures (below 200 K) the electrical conductivity appears to be very close to zero. Above 200 K the electrical conductivities start to increase slowly. Electrical conductivity values reach a maximum of  $2050 \text{ Sm}^{-1}$  around 800 K.

Thermal conductivities were measured from almost 0 K up to 750 K (fig. 7.1.8. c). Close to 0 K the thermal conductivity increases sharply and reach a maximum value of  $8.6 \text{ Wm}^{-1}\text{K}^{-1}$  at 12 K. Then, the thermal conductivities drop quickly up to 100 K, after that the values decrease slowly. Around 340 K a minimum value of  $0.75 \text{ Wm}^{-1}\text{K}^{-1}$  is reached. Above room temperature thermal conductivity values are close to  $1 \text{ Wm}^{-1}\text{K}^{-1}$ . Thus,  $\text{Ba}_3\text{GaSb}_3$  can be considered as an interesting thermoelectric material at room temperature. The values of the figure of merit are close to zero between 70 K and 225 K since the electrical conductivity values are very close to zero in this temperature range. Above this temperature,  $ZT$  values start to increase slowly and reach a maximum of 0.035 around 500 K. After this point, they decrease and the values become 0.01. Even though  $\text{Ba}_3\text{GaSb}_3$  exhibits high Seebeck coefficients and low thermal conductivities, the overall  $ZT$  values are not as high as expected due to the lack of electrical conductivity.

(a)



(b)

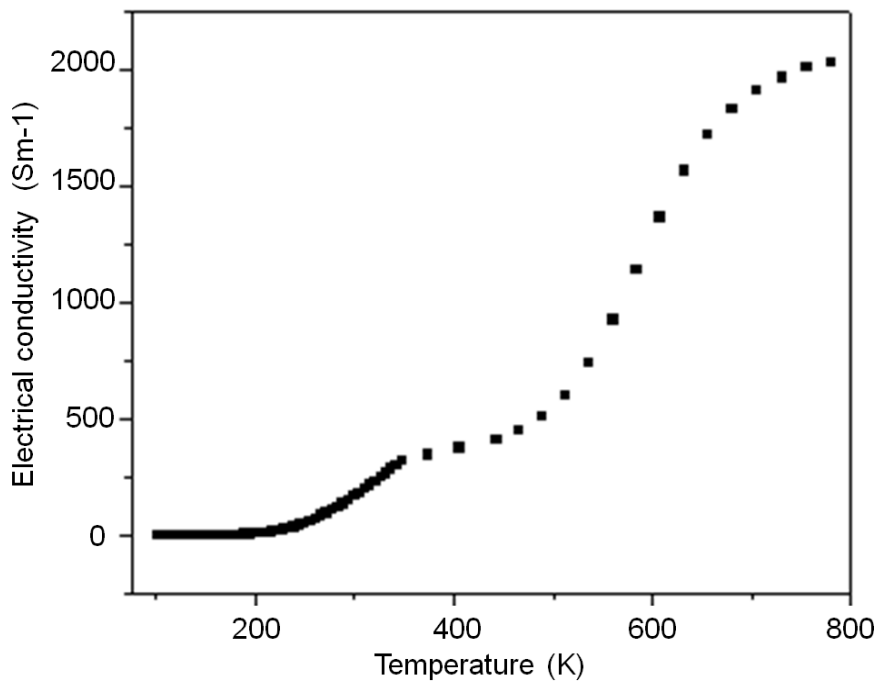


Fig. 7.1.8 (a) Seebeck coefficient of  $\text{Ba}_3\text{GaSb}_3$  as a function of temperature (b) Electrical conductivity of  $\text{Ba}_3\text{GaSb}_3$  as a function of temperature.

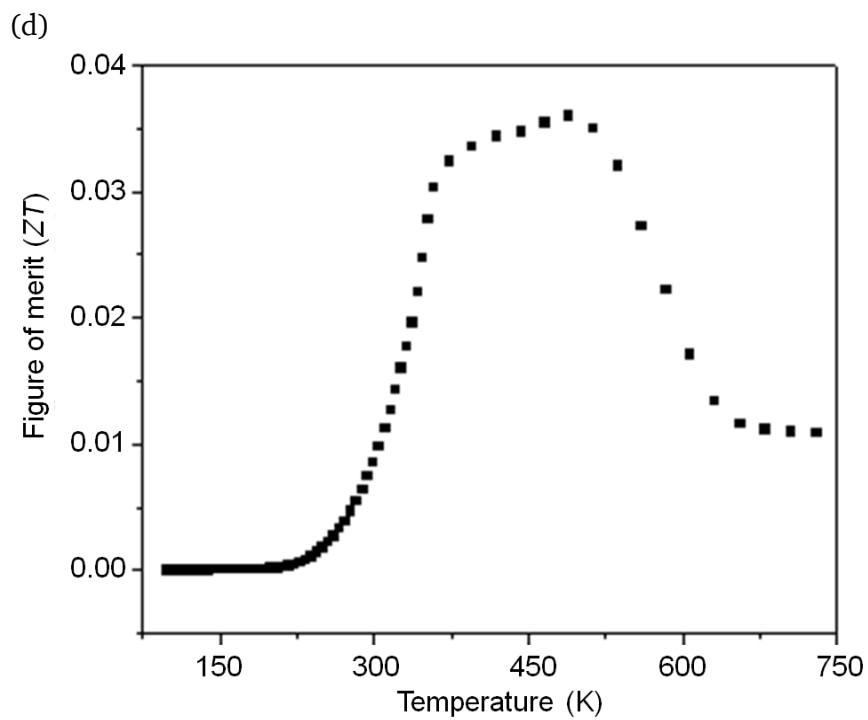
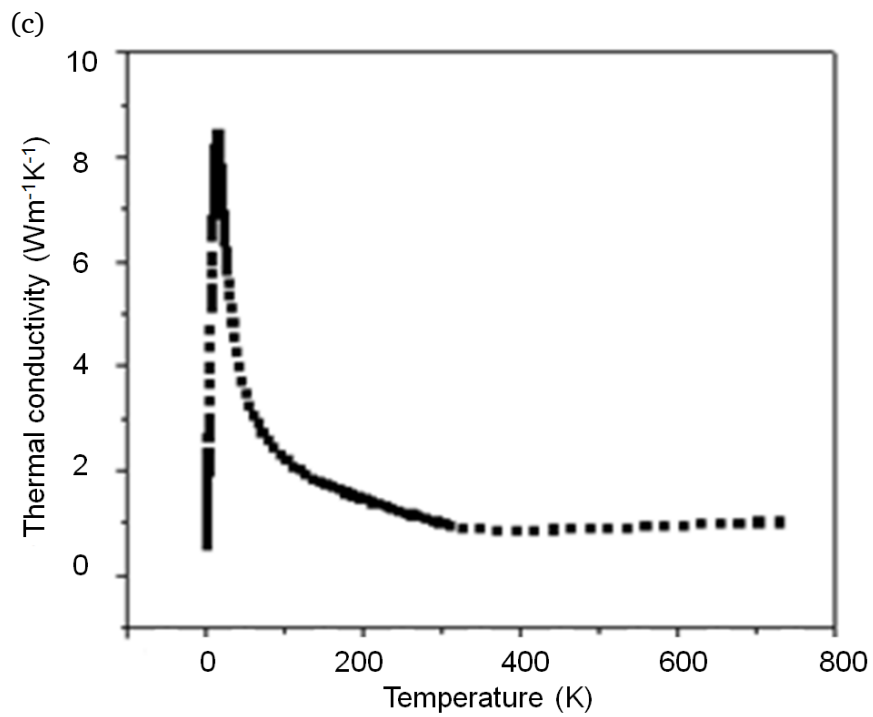


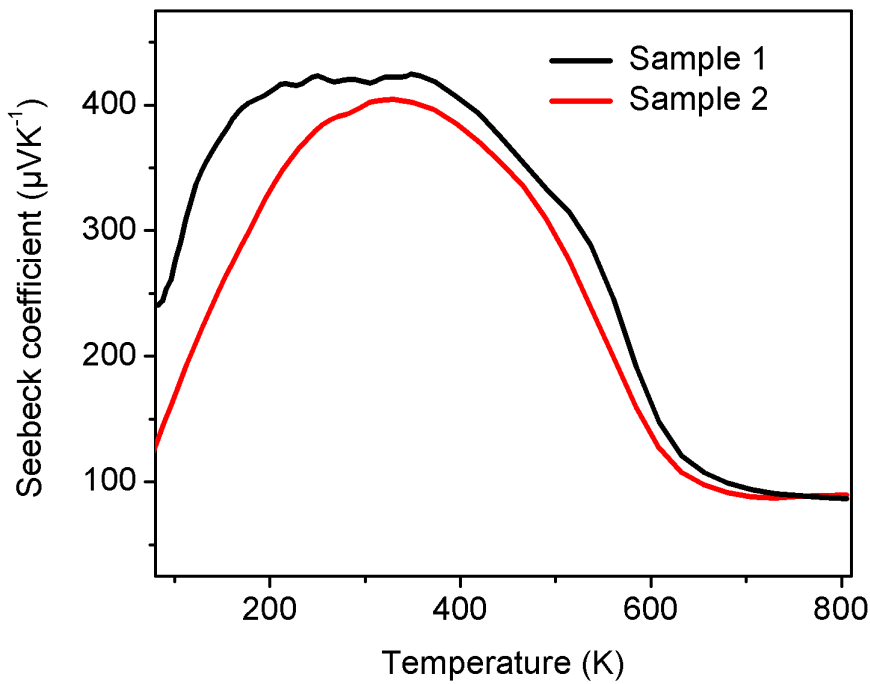
Fig. 7.1.8 (c) Thermal conductivity of  $\text{Ba}_3\text{GaSb}_3$  as a function of temperature (d) Figure of merit ( $ZT$ ) of  $\text{Ba}_3\text{GaSb}_3$  as a function of temperature.

---

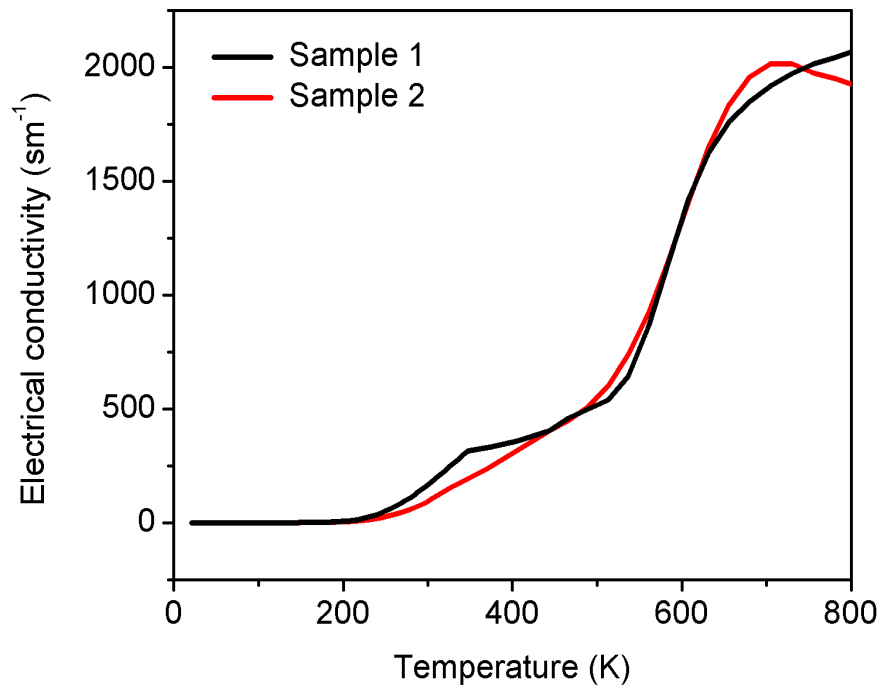
### 7.1.3 Comparing properties of different samples

Since it was difficult to prepare  $\text{Ba}_3\text{GaSb}_3$  as a monophasic product, initially a sample with 10% of  $\text{Ba}_7\text{Ga}_4\text{Sb}_9$  as side product was used for the investigations. It was synthesized at  $1173 \pm 20$  K as described in sec.7.1.1 (sample 2). Later it became feasible to precisely control the synthesis temperature ( $1173 \pm 10$  K) and the compound was obtained with very little impurity (sample 1). The sample containing 10 % impurities was used to study the influence of side phases on thermoelectric properties. Fig. 7.1.9 shows the comparison of the two samples of different amount of side phases.

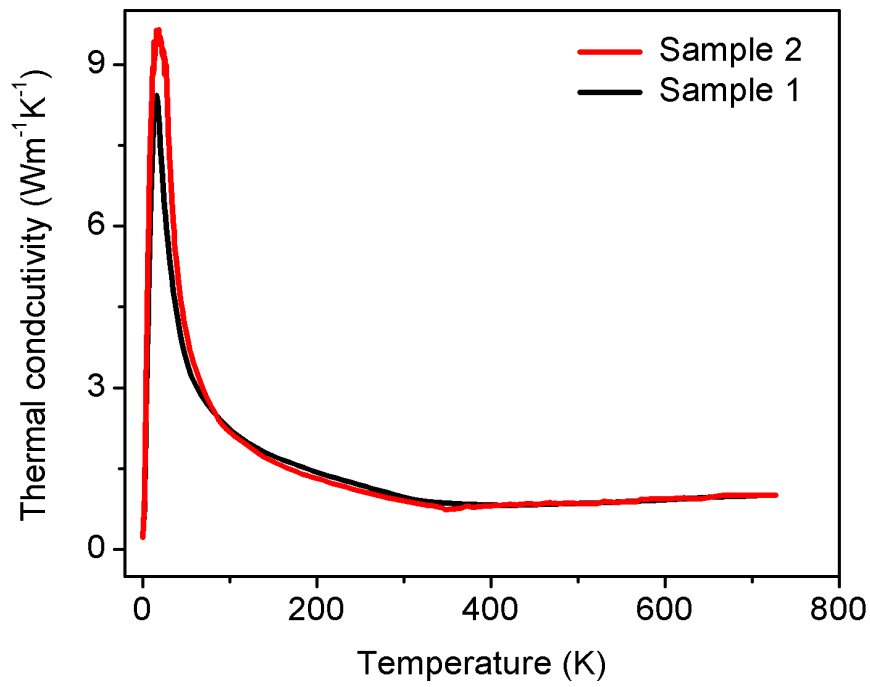
a)



b)



c)



d)

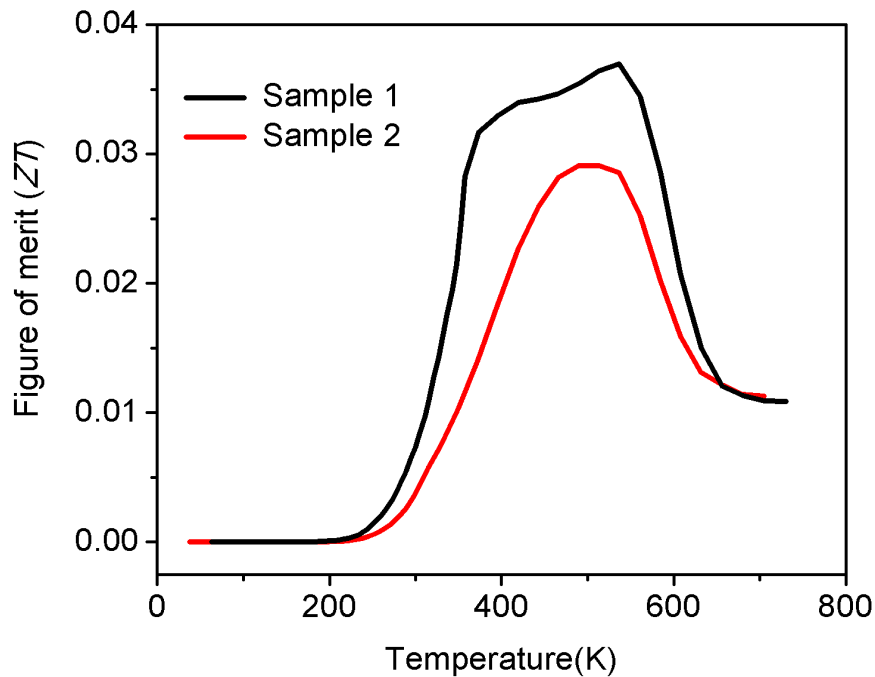


Fig.7.1.9 Thermoelectric properties of samples of  $Ba_3GaSb_3$  with different compositions, sample 1 (black line) has 1-2 % side phases and sample 2 (red line) has 10 % side phases. a) comparison of Seebeck coefficients, b) comparison of electrical conductivities, c) comparison of thermal conductivities, d) comparison of figure of merit values.

Seebeck coefficients were found to be higher in sample 1 compared to sample 2 as shown in fig. 7.1.9. a. But the curve of Seebeck coefficients of sample 2 followed the same trend of sample 1. Sample 2 exhibited a maximum Seebeck coefficient of  $403 \mu V K^{-1}$  around 330 K. Electrical conductivities were similar in both samples although there were small difference in the temperatures ranges of 240-410 K and 640-800 K. Sample 2 exhibited a maximum electrical conductivity of  $2011 S m^{-1}$  around 732 K. Thermal conductivities were also similar except for a small difference in the maximum value. Sample 2 exhibited a maximum value of  $9.5 W m^{-1} K^{-1}$  around 15 K. Values of the figure of merit were also found to be similar below 200 K. At higher temperatures sample 2 showed slightly lower  $ZT$  values and a maximum of 0.03 around 500 K. Overall, the trends were similar in both samples. Seebeck coefficients were different, but electrical and thermal conductivities were similar. These observations show that there are no serious changes in the thermoelectric properties of these two samples though impurity compositions were different. Also, it is observable that the sample with higher purity exhibited better Seebeck coefficients and figures of merit.

### 7.1.4 Doping studies

As discussed earlier doping is the key strategy to improve the thermoelectric properties of Zintl compounds. In this section, the characterization of doped samples of  $\text{Ba}_3\text{GaSb}_3$  is discussed.

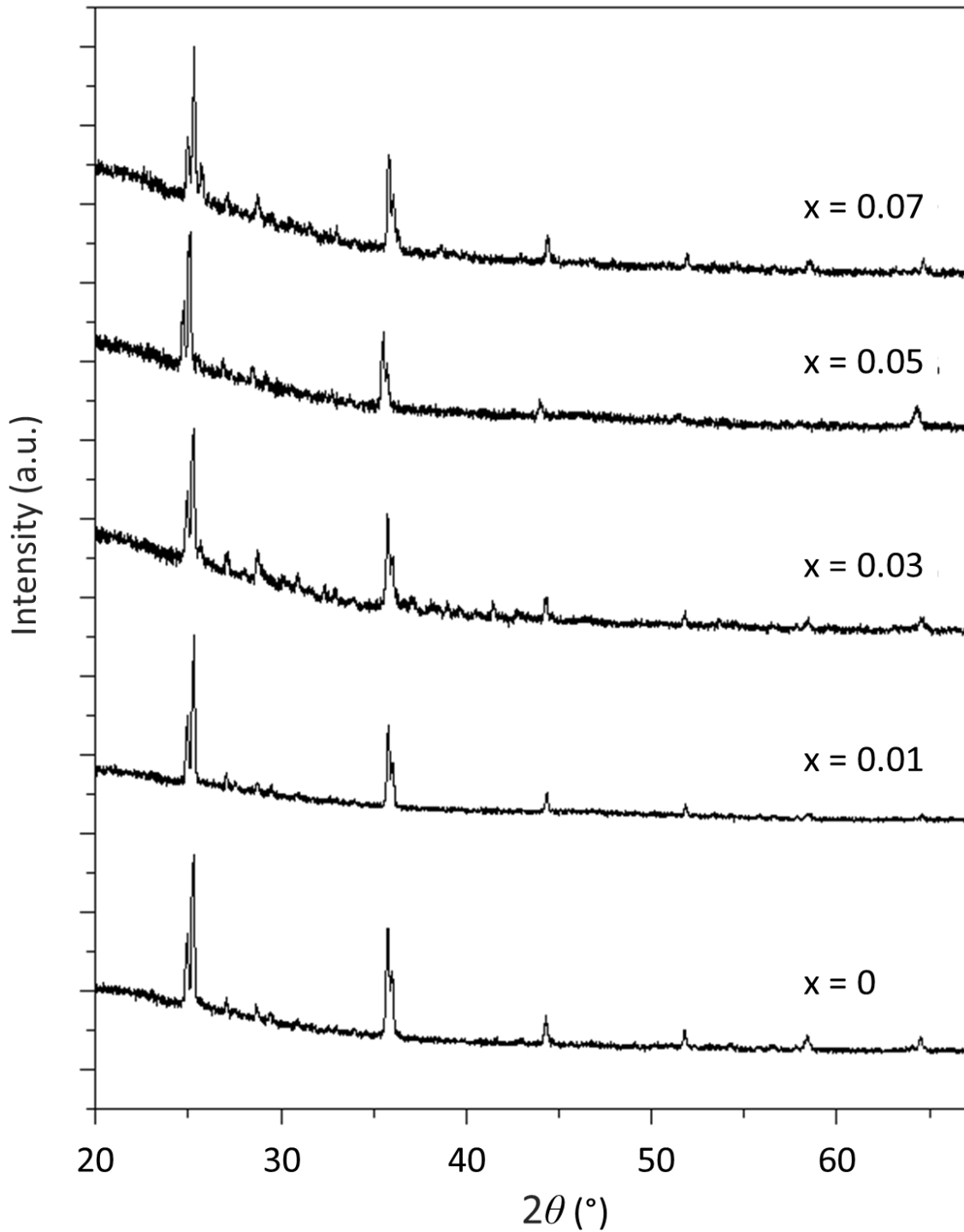


Fig. 7.1.10 Powder X-ray diffraction patterns of doped and undoped  $\text{Ba}_3\text{Ga}_{1-x}\text{Zn}_x\text{Sb}_3$ .

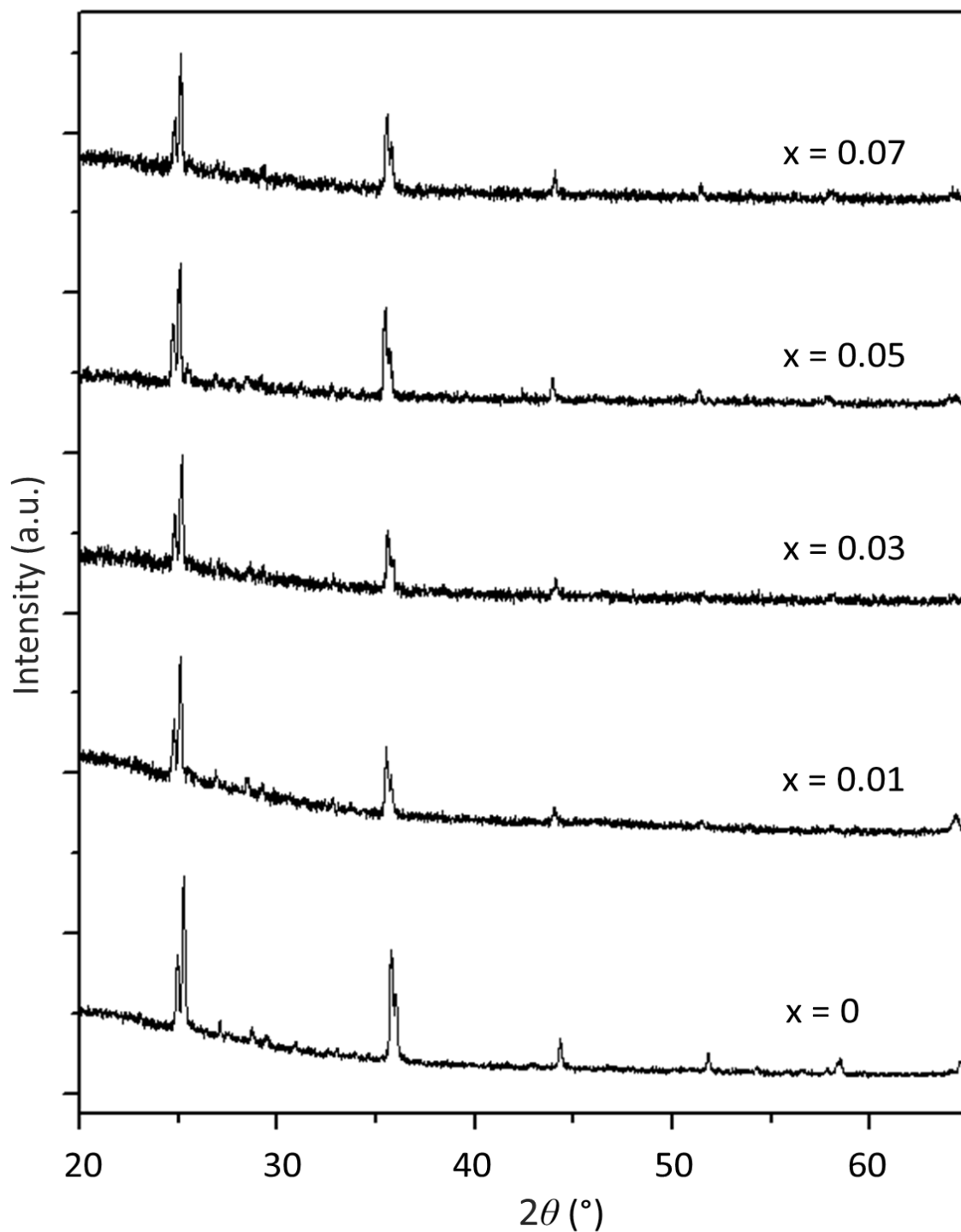


Fig. 7.1.11 Powder X-ray diffraction patterns of doped and undoped  $\text{Ba}_{3-x}\text{Sr}_x\text{GaSb}_3$ .

$\text{Ba}_3\text{GaSb}_3$  is isostructural to  $\text{Ba}_3\text{AlSb}_3$  and thus it can be expected to be doped in similar ways. It was attempted to substitute gallium with zinc and barium with strontium. Doped samples were prepared as explained in sec. 7.1.1 with 1%, 3%, 5%, 7% zinc to yield following samples; 1)  $\text{Ba}_3\text{Ga}_{0.99}\text{Zn}_{0.01}\text{Sb}_3$  (Ba = 0.4865 g, 3.54 mmol, Ga = 0.0815 g, 1.16 mmol, Zn = 0.0008 g, 0.01 mmol, Sb = 0.4313 g, 3.54 mmol) 2)  $\text{Ba}_3\text{Ga}_{0.97}\text{Zn}_{0.03}\text{Sb}_3$  (Ba = 0.4865 g, 3.54 mmol, Ga = 0.0799 g, 1.14 mmol, Zn =

0.0023 g, 0.03 mmol, Sb = 0.4313 g, 3.54 mmol) 3)  $\text{Ba}_3\text{Ga}_{0.95}\text{Zn}_{0.05}\text{Sb}_3$  (Ba = 0.4866 g, 3.54 mmol, Ga = 0.0782 g, 1.12 mmol, Zn = 0.40 g, 0.06 mmol, Sb = 0.4314 g, 3.54 mmol) 4)  $\text{Ba}_3\text{Ga}_{0.93}\text{Zn}_{0.07}\text{Sb}_3$  (Ba = 0.4866 g, 3.54 mmol, Ga = 0.0766 g, 1.09 mmol, Zn = 0.0054 g, 0.08 mmol, Sb = 0.4314 g, 3.54 mmol). In the same way, strontium was attempted to substitute barium to yield the following samples; 1)  $\text{Ba}_{2.97}\text{Sr}_{0.03}\text{GaSb}_3$  (Ba = 0.4824 g, 3.51 mmol, Sr = 0.0031 g, 0.03 mmol, Ga = 0.0825 g, 1.18 mmol, Sb = 0.4320 g, 3.54 mmol) 2)  $\text{Ba}_{2.91}\text{Sr}_{0.09}\text{GaSb}_3$  (Ba = 0.4743 g, 3.45 mmol, Sr = 0.0094 g, 0.10 mmol, Ga = 0.0828 g, 1.18 mmol, Sb = 0.4335 g, 3.55 mmol) 3)  $\text{Ba}_{2.85}\text{Sr}_{0.15}\text{GaSb}_3$  (Ba = 0.4662 g, 3.39 mmol, Sr = 0.0156 g, 0.17 mmol, Ga = 0.0831 g, 1.19 mmol, Sb = 0.4351 g, 3.57 mmol) 4)  $\text{Ba}_{2.79}\text{Sr}_{0.21}\text{GaSb}_3$  (Ba = 0.4608 g, 3.35 mmol, Sr = 0.0221 g, 0.25 mmol, Ga = 0.0835 g, 1.19 mmol, Sb = 0.4345 g, 3.57 mmol). The doped samples were found to be as air-sensitive as the undoped compounds.

Fig. 7.1.10 shows the powder X-ray diffraction patterns of the doped and undoped samples of  $\text{Ba}_3\text{Ga}_{1-x}\text{Zn}_x\text{Sb}_3$ . The powder diffraction patterns of doped and undoped samples are identical. In the sample with 7 % doping a small impurity peak appears next to the high-intense peak which was also present in the case of  $\text{Ba}_3\text{AlSb}_3$ . When the dopant concentration exceeds 10 %, some of the side phases start to appear in the sample. Fig. 7.1.11 shows the powder X-ray diffraction patterns of the doped and undoped  $\text{Ba}_{3-x}\text{Sr}_x\text{GaSb}_3$ . The powder diffraction patterns are identical for  $\text{Ba}_{3-x}\text{Sr}_x\text{GaSb}_3$  and that implies that the doping did not lead to the formation of any side phases.

Scanning electron microscopic images of  $\text{Ba}_3\text{Ga}_{1-x}\text{Zn}_x\text{Sb}_3$  are shown in fig. 7.1.12. Fig. 7.1.12. a, b, c, d show the images of the samples doped with Zn 1 %, 3 %, 5 %, 7 % respectively. Fig. 7.1.13 shows the scanning electron microscopic images of  $\text{Ba}_{3-x}\text{Sr}_x\text{GaSb}_3$ . The sizes of the particles are in the order of micrometers.

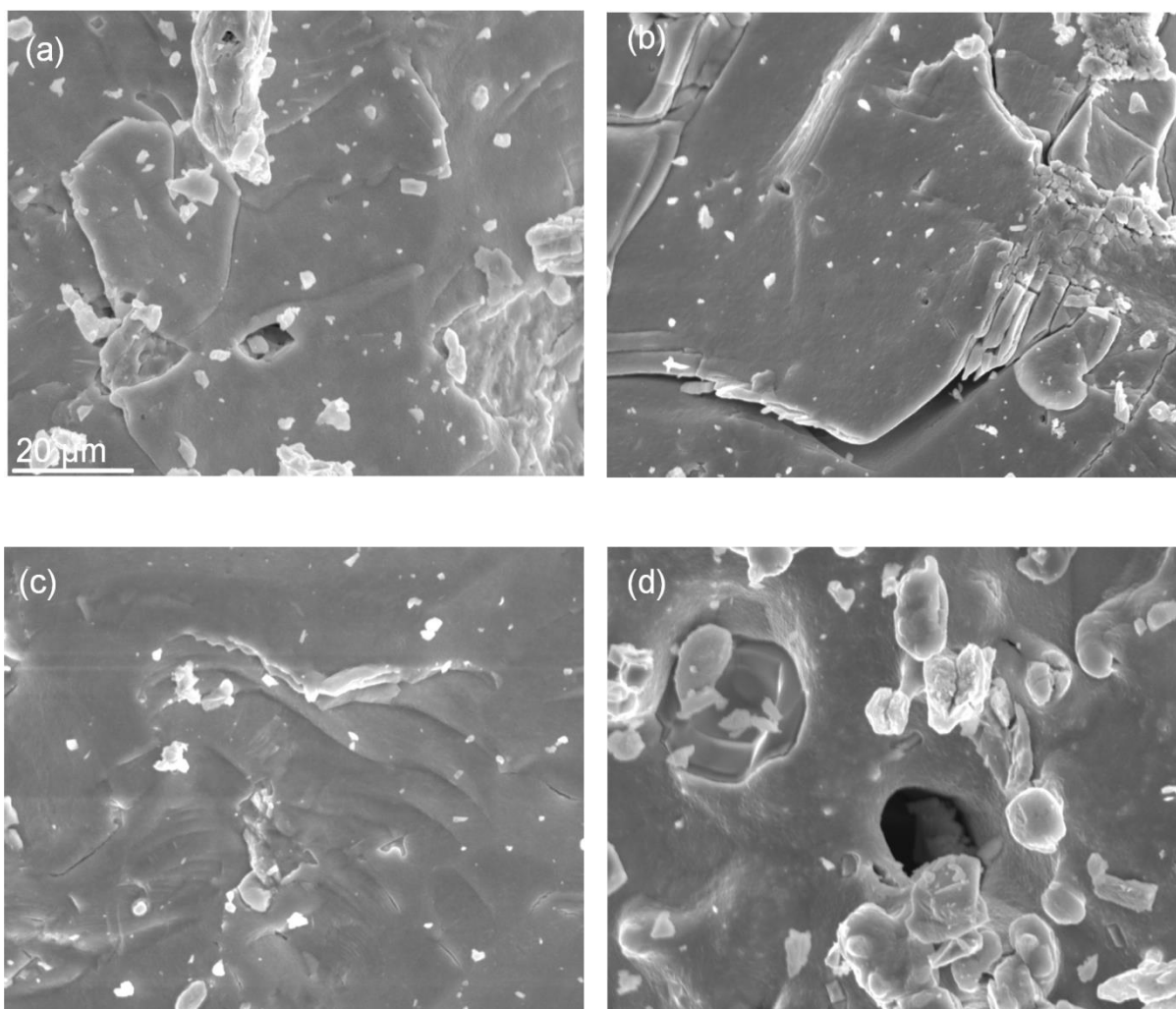


Fig. 7.1.12 SEM images of  $\text{Ba}_3\text{Ga}_{1-x}\text{Zn}_x\text{Sb}_3$ , a)  $x = 1\%$ , b)  $x = 3\%$ , c)  $x = 5\%$ , d)  $x = 7\%$ .

EDS measurements were carried out for  $\text{Ba}_3\text{Ga}_{1-x}\text{Zn}_x\text{Sb}_3$ , but Zn could not be identified. To study the dopant concentration atomic absorption spectroscopy was used. An amount of sample that led to 2.5 mg of zinc in 100 ml aqueous solution was weighed. The doped samples were dissolved in diluted HCl (1:10) for further analysis. Qualitative analysis was performed which proved the presence of zinc in all of the samples. As explained in sec. 6.3 the quantitative analysis was not successful.

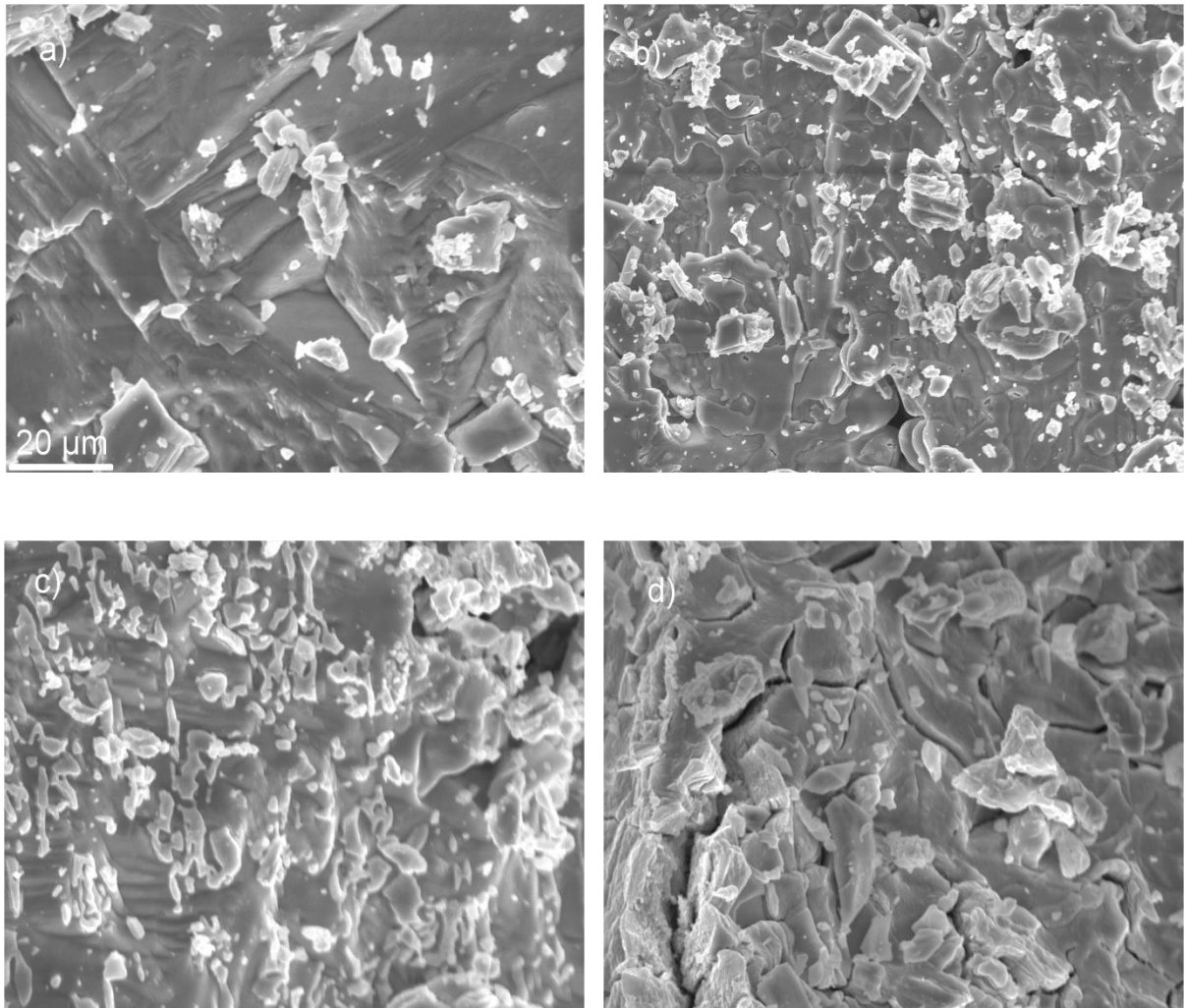


Fig. 7.1.13 SEM images of  $\text{Ba}_{3-x}\text{Sr}_x\text{GaSb}_3$ , a)  $x = 1 \%$ , b)  $x = 3 \%$ , c)  $x = 5 \%$ , d)  $x = 7 \%$ .

EDS measurements of  $\text{Ba}_{3-x}\text{Sr}_x\text{GaSb}_3$  allowed it to identify the strontium content in the doped samples except for  $\text{Ba}_{2.97}\text{Sr}_{0.03}\text{GaSb}_3$  due to the low concentration of strontium. The obtained atomic percentages are given in table 7.1.3. The samples were found to be homogeneous and there were no traces of container material (tantalum) in any of the doped samples. Images of EDS mapping are shown in fig.7.1.14. From the results obtained it is clear that when the dopant concentration is above 1.25 %, EDS allows it to detect the element (dopant) in the samples. For concentrations lower than that calcium was not detectable.

Table 7.1.3 Average atomic percentages of  $\text{Ba}_{3-x}\text{Sr}_x\text{GaSb}_3$ .

Formula	Ba (%)	Sr (%)	Ga (%)	Sb (%)
$\text{Ba}_{2.97}\text{Sr}_{0.03}\text{GaSb}_3$ –Theory	42.43	0.43	14.28	42.86
Measured	41.29	0	13.96	44.75
$\text{Ba}_{2.91}\text{Sr}_{0.09}\text{GaSb}_3$ –Theory	41.57	1.29	14.28	42.86
Measured	38.51	2.05	15.74	43.71
$\text{Ba}_{2.85}\text{Sr}_{0.15}\text{GaSb}_3$ –Theory	40.71	2.15	14.28	42.86
Measured	39.14	2.92	13.49	44.45
$\text{Ba}_{2.79}\text{Sr}_{0.21}\text{GaSb}_3$ –Theory	39.85	3.01	14.28	42.86
Measured	40.67	3.55	15.76	40.02

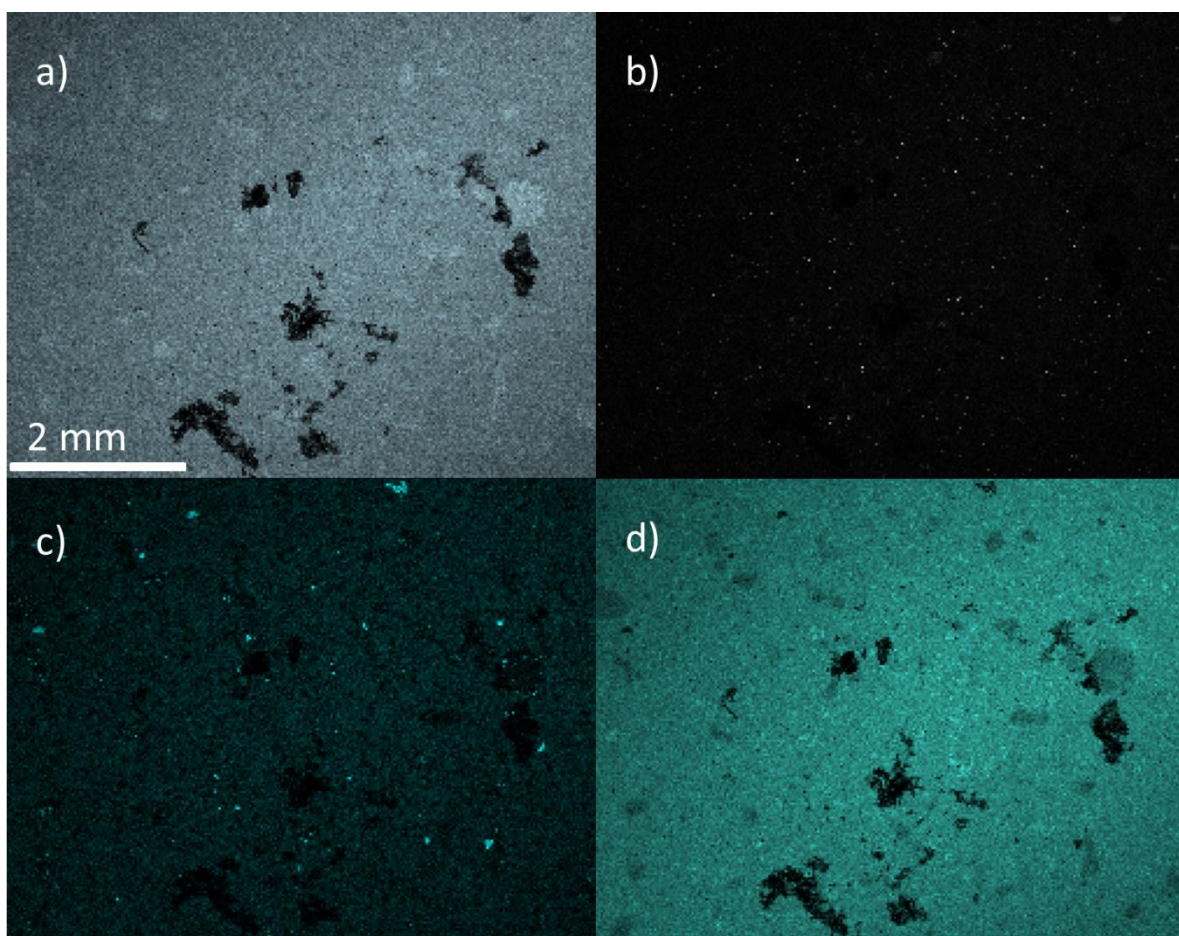


Fig. 7.1.14 EDS mapping of  $\text{Ba}_{2.79}\text{Sr}_{0.21}\text{GaSb}_3$ . a) grey particles are barium ( $\text{Ba}_L$ ), b) shiny white particles are strontium ( $\text{Sr}_L$ ), c) shiny greenish particles are gallium ( $\text{Ga}_K$ ), d) green particles are antimony ( $\text{Sb}_L$ ), dark spots are the damaged portions and small holes in the surface.

According to Vegard's law the dopant concentration affects the lattice parameters, so a linear variation of the lattice parameters with Zn content should be observed [127, 128]. Fig. 7.1.15 shows the relationship between the concentration of zinc and the lattice parameters  $b$  of  $\text{Ba}_3\text{Ga}_{1-x}\text{Zn}_x\text{Sb}_3$ . The lattice parameters increase with the increasing Zn concentration. Fig. 7.1.16 shows the relationship between the lattice parameters  $b$  and the dopant concentration of Sr in  $\text{Ba}_{3-x}\text{Sr}_x\text{GaSb}_3$ . The lattice parameters decrease with increasing dopant concentration. In both cases similar observations were found for  $a$  and  $c$ . For  $\text{Ba}_3\text{Ga}_{1-x}\text{Zn}_x\text{Sb}_3$ , the sample that should contain zinc seems to be below the Vegard's line which may indicate a lower doping level than attempted. For  $\text{Ba}_{3-x}\text{Sr}_x\text{GaSb}_3$  the variation of  $b$  with changing strontium content is observed as a straight line. These studies show that it is possible to dope  $\text{Ba}_3\text{GaSb}_3$  with zinc and strontium. Doping can be done without producing side phases.

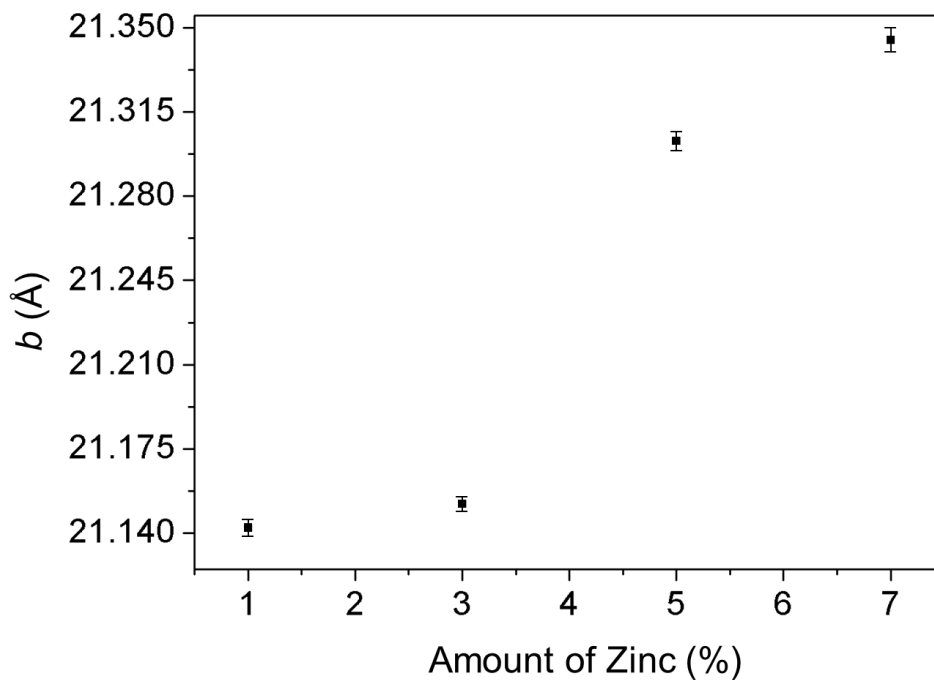


Fig. 7.1.15 Variation in lattice parameter  $b$  (Å) as a function of dopant concentration (Zn) in  $\text{Ba}_3\text{Ga}_{1-x}\text{Zn}_x\text{Sb}_3$ .

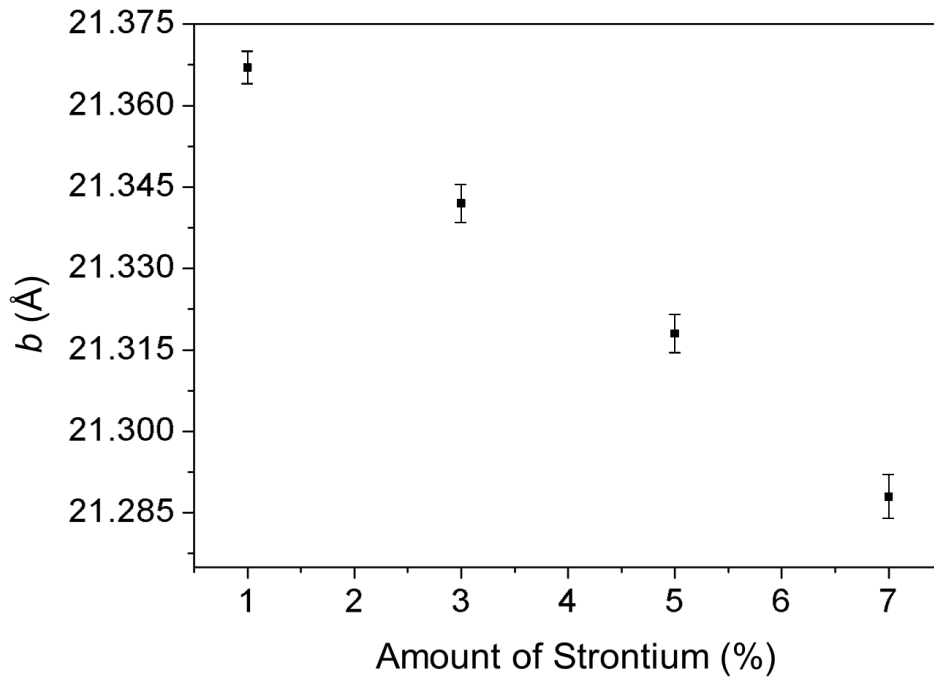


Fig. 7.1.16 Variation in lattice parameter  $b$  (Å) as a function of dopant concentration (Sr) in  $\text{Ba}_{3-x}\text{Sr}_x\text{GaSb}_3$ .

### 7.1.5 Discussion of results

$\text{Ba}_3\text{GaSb}_3$  was synthesized successfully as an almost monophasic sample. Traces of  $\text{Ba}_7\text{Ga}_4\text{Sb}_9$  appear as an impurity.  $\text{Ba}_3\text{GaSb}_3$  is a narrow band gap semiconductor with a band gap of 0.3 eV according to the DFT calculations. Among the  $\text{A}_3\text{MSb}_3$ -type compounds  $\text{Ca}_3\text{AlSb}_3$  [123] shows a band gap similar to  $\text{Ba}_3\text{GaSb}_3$ .  $\text{Sr}_3\text{GaSb}_3$  [129] exhibits a slightly larger band gap (0.75 eV).  $\text{Ba}_3\text{GaSb}_3$  is thermally stable up to 1168 K. It was compacted using SPS and the compacted sample was found to be 95 % dense. Thermoelectric properties of  $\text{Ba}_3\text{GaSb}_3$  were studied.  $\text{Ba}_3\text{GaSb}_3$  exhibits very high Seebeck coefficients and the maximum was found to be  $425 \mu\text{VK}^{-1}$  around 340 K. The isostructural compound  $\text{Ba}_3\text{AlSb}_3$  also exhibits high Seebeck coefficients (max =  $383 \mu\text{VK}^{-1}$  around 342 K).  $\text{Ba}_3\text{GaSb}_3$  exhibits very low thermal conductivity (min =  $0.75 \text{ Wm}^{-1}\text{K}^{-1}$ ). Other  $\text{A}_3\text{MSb}_3$ -type compounds such as  $\text{Ca}_3\text{AlSb}_3$  [123] and  $\text{Ba}_3\text{AlSb}_3$  also show low thermal conductivities like  $\text{Ba}_3\text{GaSb}_3$ . According to the literature [129] undoped  $\text{Sr}_3\text{GaSb}_3$  shows a minimum thermal conductivity of  $0.6 \text{ Wm}^{-1}\text{K}^{-1}$ . For  $\text{Ba}_3\text{GaSb}_3$  the amount of side phases in the system was shown not to affect the properties significantly. Seebeck coefficients, electrical conductivities, thermal conductivities and the values of the figure of merit were comparable for two samples

---

investigated. The values of the figure of merit were low in either sample due to the very low electrical conductivities. This behavior was comparable to that of  $\text{Ba}_3\text{AlSb}_3$ . A reason may be the poor carrier concentration or the insufficient activation of charge carriers across the valence and conduction bands. Modifying the band structure and band gap of this compound can enhance the electrical properties. Doping is the suitable method to achieve this.  $\text{Ba}_3\text{GaSb}_3$  was doped with zinc and strontium and characterized. Zinc was possibly substituted in the sites of aluminum and strontium was possibly substituted in the sites of barium.

---

---

## 7.2 Ba<sub>7</sub>Ga<sub>4</sub>Sb<sub>9</sub>

---

### 7.2.1 Synthesis, characterization and compaction

Stoichiometric amounts of Ba (0.2056 g, 1.49 mmol, Chempur, 99.3%), Ga (0.0597 g, 0.86 mmol, Degussa, 99.99%) and Sb (0.2346 g, 1.93 mmol, Chempur, Sb-Shots, 1-3 mm, 99.999%) were taken as purchased without any further purification. The elements were weighed inside the argon filled glove box with oxygen and moisture levels below 1 ppm and then quickly transferred to the arc melting device that was connected to the vacuum line. The sample was melted using 20 A current under reduced pressure of argon. After melting the sample was cooled quickly using running water stream. The process was repeated to make sure all of the reactants were melted properly and the reaction was complete. To avoid the loss of antimony by evaporation, the time of heating had to be controlled precisely. This method yields a monophasic sample of Ba<sub>7</sub>Ga<sub>4</sub>Sb<sub>9</sub>. The product was found to be air and moisture-sensitive. When the reactants were pelletized before melting, the sample obtained contained unidentified impurities and binary phases of Ba-Sb. Preparation in tantalum containers and programmed heating procedures were not successful to prepare monophasic products of Ba<sub>7</sub>Ga<sub>4</sub>Sb<sub>9</sub>. Often Ba<sub>3</sub>GaSb<sub>3</sub> was observed as a side phase.

The samples prepared using arc melting were analyzed by powder X-ray diffraction. Fig. 7.2.1 shows the measured and calculated powder X-ray diffraction patterns of Ba<sub>7</sub>Ga<sub>4</sub>Sb<sub>9</sub> along with the difference curve. The calculated and measured powder patterns were found to be identical and there were no impurities found. The structure model from literature [113] was used for the fitting procedure and only the lattice parameters were refined freely. Table 7.2.1 shows the refinement results.

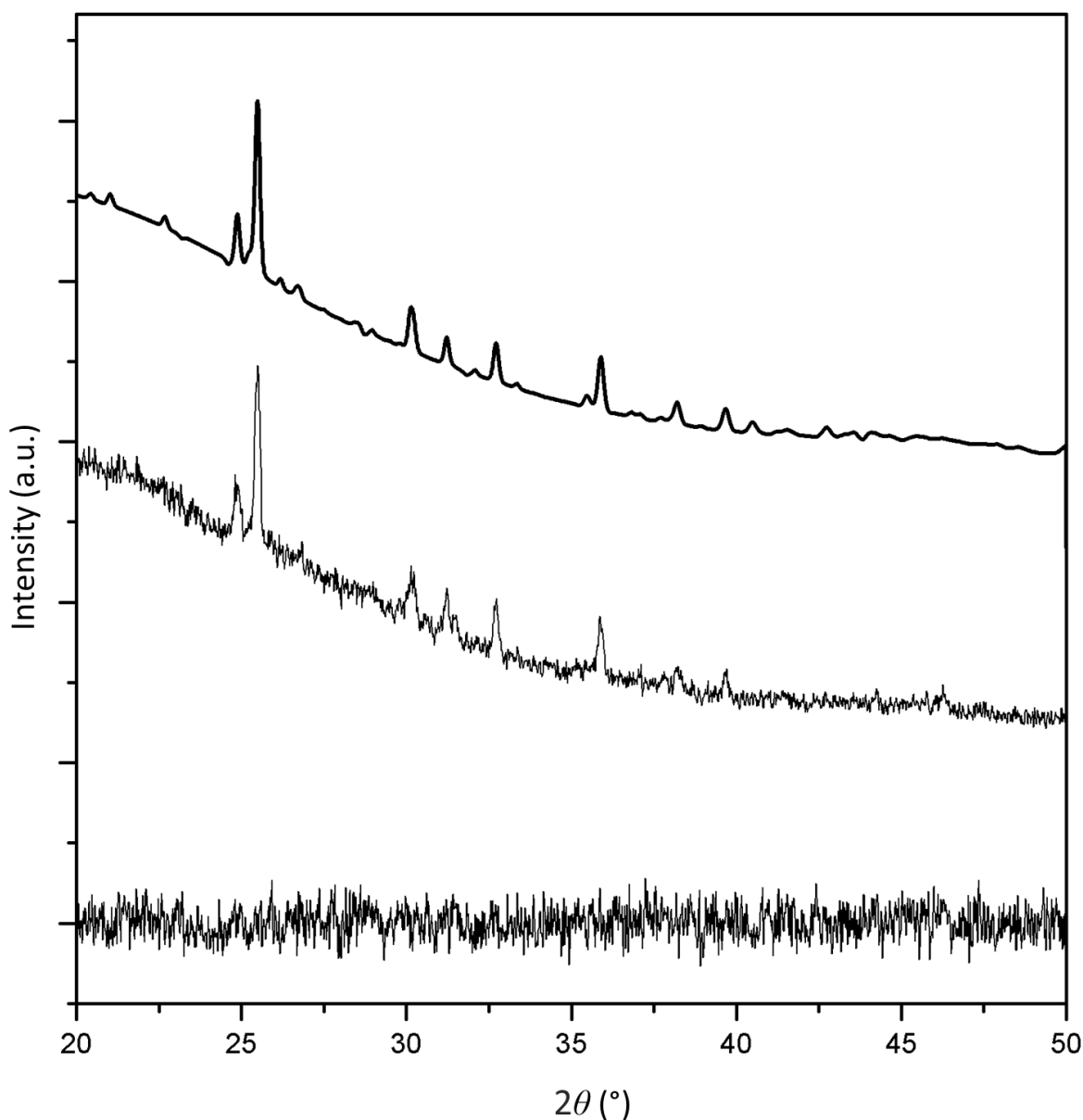


Fig.7.2.1 Measured (middle) and calculated (top) powder X-ray diffraction diagrams of  $\text{Ba}_7\text{Ga}_4\text{Sb}_9$  along with difference curve (bottom).

Table 7.2.1 Lattice parameters of  $\text{Ba}_7\text{Ga}_4\text{Sb}_9$  from Rietveld refinement based on the structure model from literature [113].

	$a$	$b$	$c$
Literature	18.024 (7) Å	10.861 (4) Å	7.100 (3) Å
This work	18.030 (2) Å	10.864 (6) Å	7.113 (2) Å
$R_{\text{exp.}}$ : 5.58	$R_{\text{wp.}}$ : 5.83	$R_{\text{p.}}$ : 4.35	$GOF$ : 1.04

High temperature powder X-ray diffraction measurements were carried out from room temperature to 1023 K. Fig. 7.2.2 shows the powder X-ray diffraction patterns at different temperatures with step size 100 K. There are no changes in the patterns up to 523 K. Above this temperature the sample changes its structure twice. The resulting products could not be identified. Above 923 K an amorphous product was found and the sample remained amorphous upon cooling to room temperature.

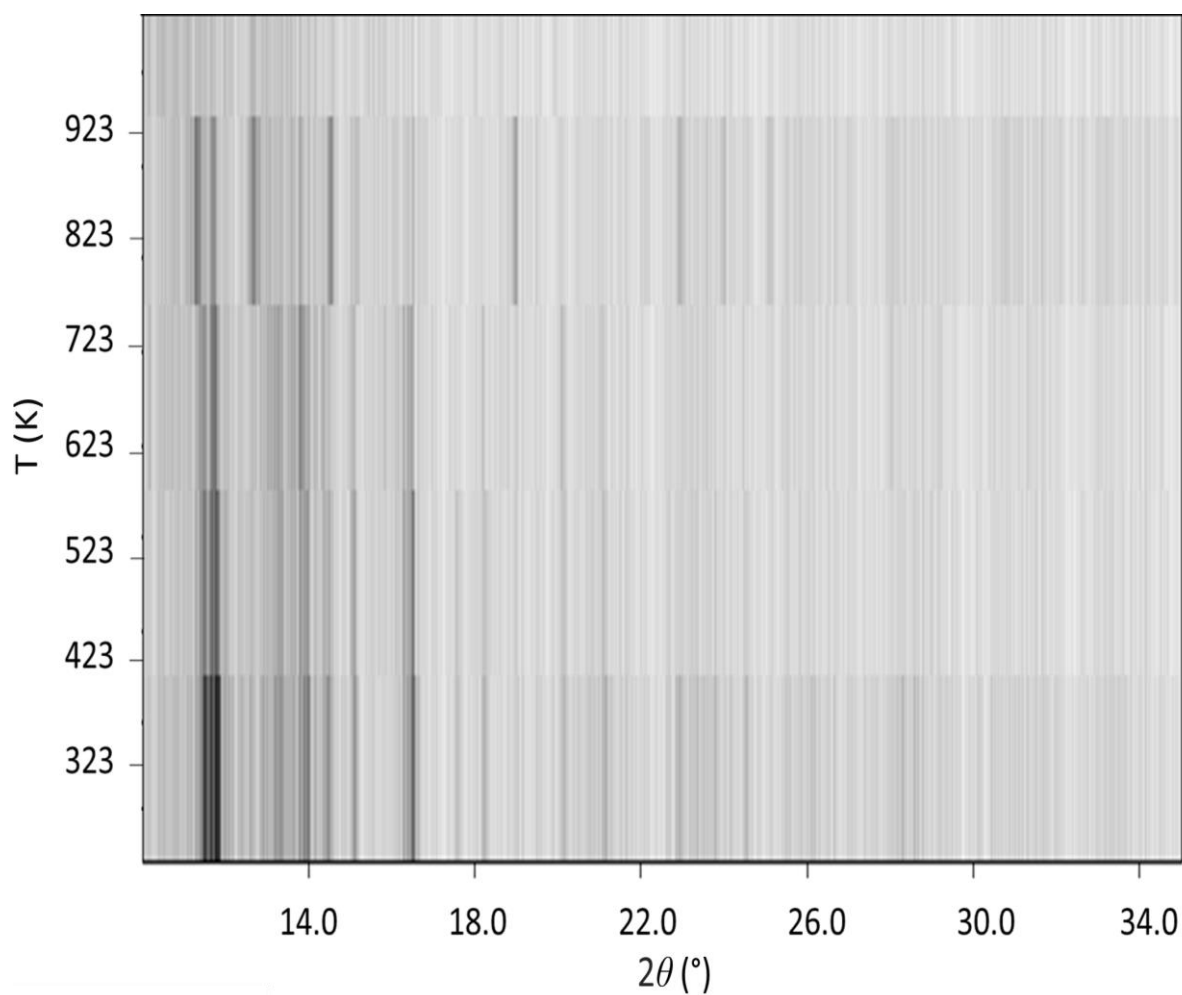


Fig. 7.2.2 High-temperature X-ray diffraction measurement for Ba<sub>7</sub>Ga<sub>4</sub>Sb<sub>9</sub>.

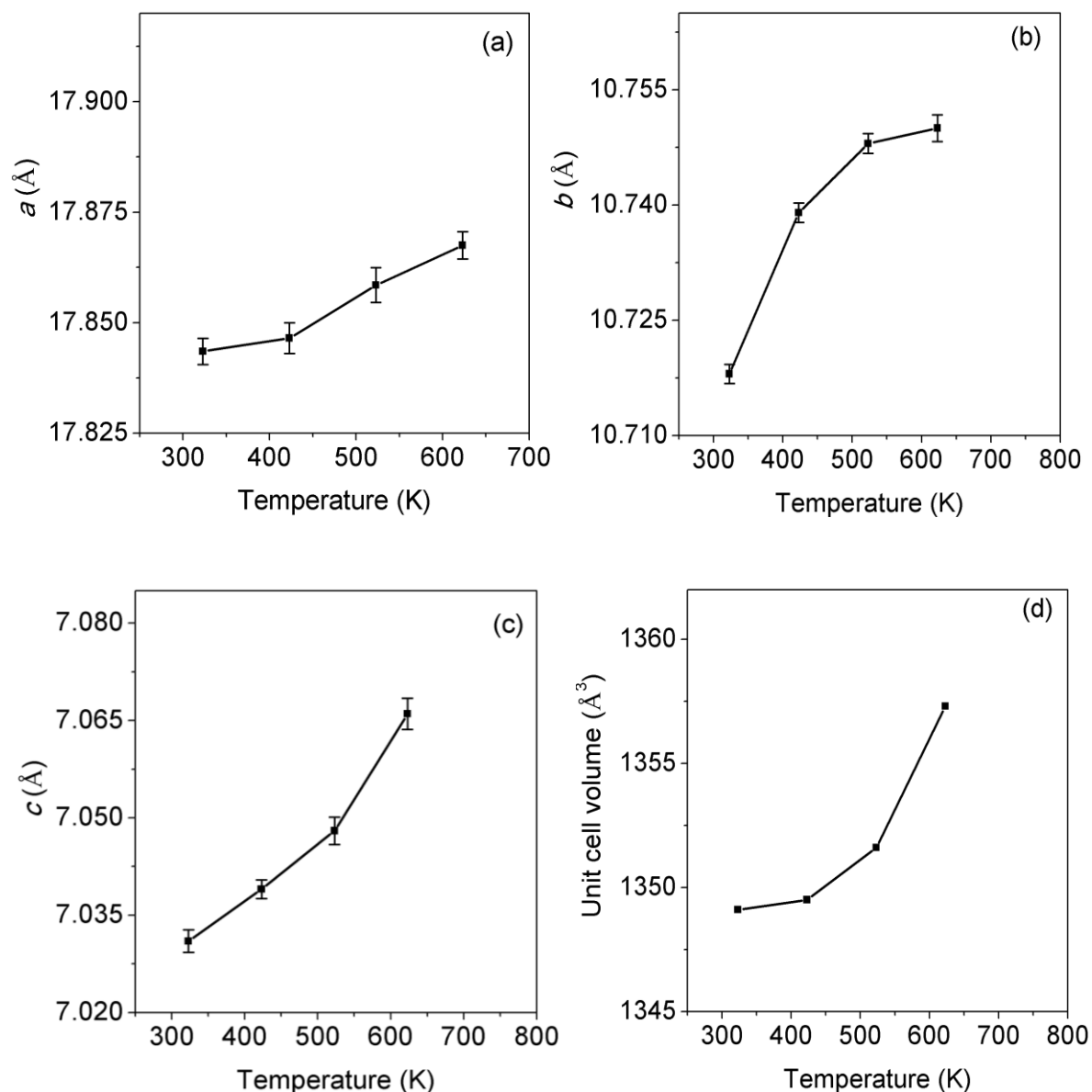


Fig. 7.2.3. a, b, c: Lattice parameters as function of temperature. Fig. 7.2.3. d Unit cell volume as function of temperature (standard deviations were smaller than the symbols).

Since the compound was prepared by arc melting at high temperatures it changes its structure when heated to temperatures above 523 K. It is probably stable at high temperatures and metastable at room temperature. The lattice parameters were refined and plotted against temperature found to be increasing with temperature up to 623 K (fig. 7.2.3 a, b, c). Fig. 7.2.3. d shows the changes of the unit cell volume with temperature. Above 623 K the lattice parameters show several anomalies that have to be investigated in more detail in future. The unit cell volume increases with temperature due to thermal expansion.

---

Fig. 7.2.4 shows scanning electron microscopy images of  $\text{Ba}_7\text{Ga}_4\text{Sb}_9$ . Red circles indicate the spots where EDS measurements were carried out to measure the atomic percentages of barium, gallium and antimony in  $\text{Ba}_7\text{Ga}_4\text{Sb}_9$ . The measurements were done in three different spots to ensure the homogenous nature of the sample. The calculated atomic percentages of the elements are close to the theoretical values which indicate the homogeneous nature of the sample (table 7.2.2). The measurements show a small lack in antimony and this could be because of the evaporation of antimony during the melting process of the reactants in the electric arc. Signals for tantalum were not observed anywhere in the sample, so there seems to be no reaction between the container material and reactants.

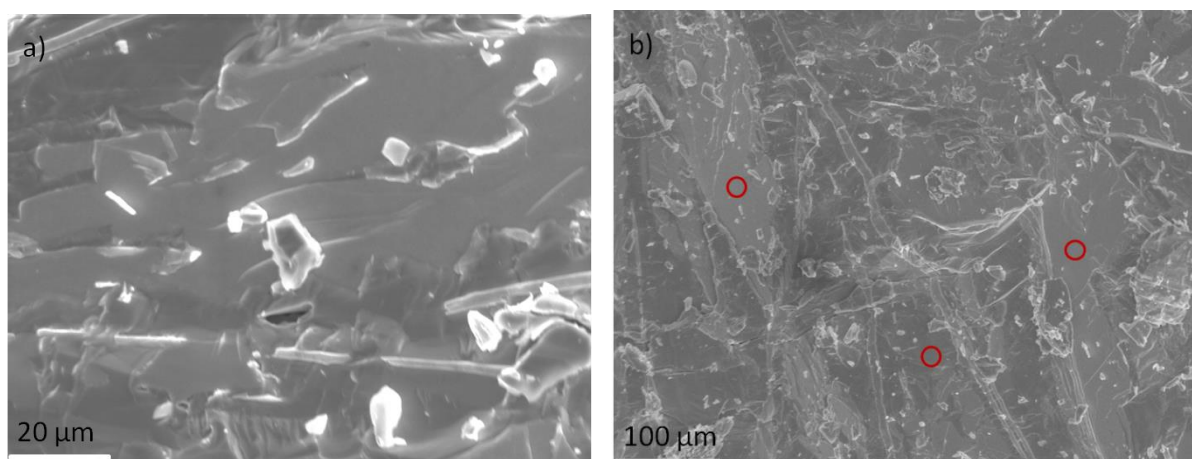


Fig. 7.2.4 SEM images of  $\text{Ba}_7\text{Ga}_4\text{Sb}_9$  (red circles indicate the spots where EDS measurements were carried out).

Table 7.2.2 Atomic percentages of all elements in Ba<sub>7</sub>Ga<sub>4</sub>Sb<sub>9</sub> determined using EDS.

	Ba (%)	Ga (%)	Sb (%)
Spot 1	35.17	20.57	44.26
Spot 2	37.29	19.09	43.62
Spot 3	34.92	19.40	45.68
Average	35.75	19.69	44.52
Theoretical values	35.00	20.00	45.00

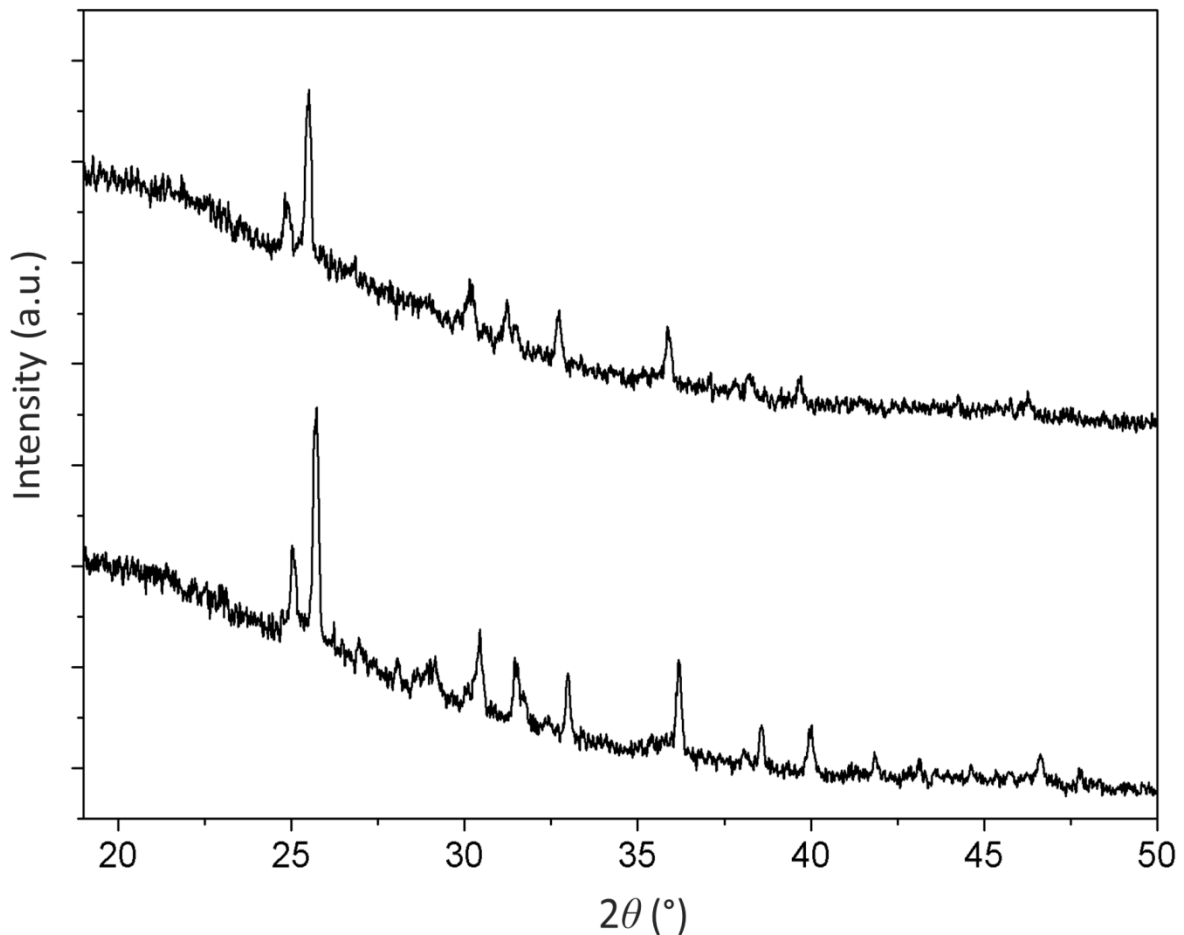


Fig. 7.2.5 Powder X-ray diffraction patterns before (bottom) and after SPS (top).

Ba<sub>7</sub>Ga<sub>4</sub>Sb<sub>9</sub> was compacted using the spark plasma technique as explained in the sec. 2.5. At 573 K the sample was compacted with an uniaxial pressure of 100 MPa. The heating and cooling rates were 25 K/min. The sample was sintered for one hour and then cooled down to the room temperature. Due to low decomposition temperature of

the compound the sample could not be treated at temperatures high enough for compaction. Due to the low sintering temperature sintering the sample broke before being investigated concerning its thermoelectric properties (fig. 7.2.6). The sintered sample was analyzed by powder X-ray diffraction. Fig. 7.2.5 shows the powder X-ray diffraction patterns of the starting material and the sintered sample. Both diffraction patterns are identical, so  $\text{Ba}_7\text{Ga}_4\text{Sb}_9$  did not undergo any changes during the sintering process. The density of the compacted sample of  $\text{Ba}_7\text{Ga}_4\text{Sb}_9$  was determined using a gas pycnometer. Volume and density values for all of the cycles are given in table 7.2.3. The average density was  $5.5566 \text{ g/cm}^3$ , so the compacted sample was 99.5 % dense compared to the theoretical value ( $5.58 \text{ g/cm}^3$ ) from X-ray diffraction.

Table 7.2.3 List of densities of compacted  $\text{Ba}_7\text{Ga}_4\text{Sb}_9$ .

Cycles	Volume ( $\text{cm}^3$ )	Density ( $\text{g/cm}^3$ )
1	0.1438	5.5475
2	0.1436	5.5571
3	0.1439	5.5435
4	0.1435	5.5602
5	0.1433	5.5675
6	0.1435	5.5600
7	0.1437	5.5524
8	0.1435	5.5592
9	0.1435	5.5598
10	0.1435	5.5588
Average	0.1436	5.5566



Fig. 7.2.6 Broken pellet of  $Ba_7Ga_4Sb_9$ .

### 7.2.2 Discussion of the results

Single crystals of  $Ba_7Ga_4Sb_9$  were synthesized in 1986 by Cordier et al. [113], but preparing monophasic powder samples of this compound was unknown. The compound appears as an impurity phase during the synthesis of  $Ba_3GaSb_3$ . Likewise, when  $Ba_7Ga_4Sb_9$  was attempted to prepare  $Ba_3GaSb_3$  appeared as an impurity phase.  $Ba_7Ga_4Sb_9$  was now prepared as bulk material using a different synthesis technique i.e- arc melting.  $Ba_7Ga_4Sb_9$  was not found to be stable above 600 K according to high temperature powder X-ray diffraction studies. Density functional theory studies showed no band gap and thus  $Ba_7Ga_4Sb_9$  was expected to show metallic properties. The sample was attempted to be compacted using spark plasma sintering. The sintering temperature (573 K) was not high enough due to the limitation of the low thermal stability of the compound. Thus, densification was not successful and the thermoelectric properties of  $Ba_7Ga_4Sb_9$  could not be studied.

---

## 7.3 BaGa<sub>2</sub>Sb<sub>2</sub>

---

### 7.3.1 Synthesis, characterization and compaction

Stoichiometric amounts of Ba (0.1320g, 0.96 mmol, Chempur, 99.3%), Ga (0.1340 g, 1.92 mmol, Degussa, 99.99%) and Sb (0.2340 g, 1.92 mmol, Chempur, Sb-Shots, 1-3 mm, 99.999%) were taken as purchased without any further purification. The elements were weighed inside the argon filled glove box with oxygen and moisture levels below 1 ppm then quickly transferred to the arc melting device that is connected to the vacuum line. The reactants were melted under a reduced pressure of argon. A current of 25 A was used to melt the sample over a period of 10-15 seconds. Melting the sample for longer periods led to the formation of secondary products such as binary Ba-Sb phases. Precise heating time and quick cooling yielded monophasic samples of BaGa<sub>2</sub>Sb<sub>2</sub>. When different synthetic routes such as heating in tantalum or graphite container were employed, side phases (Ba<sub>3</sub>GaSb<sub>3</sub> and binary phases) were found in large amounts. These observations led to the conclusion that arc melting is the most suitable method for the preparation of BaGa<sub>2</sub>Sb<sub>2</sub>.

Pure powder samples of BaGa<sub>2</sub>Sb<sub>2</sub> were prepared and analyzed by powder X-ray diffraction. The sample was found to be stable in air. The sample was finely ground and the powder was applied to a flat plate sample holder for the powder X-ray diffraction measurement. Fig. 7.3.1 shows the powder diffraction pattern of the sample, a powder diffraction pattern and the difference curve calculated based on the structure model from literature [114] after Rietveld refinement of the lattice parameters (table 7.3.1). The powder patterns are found to be similar and no secondary phases were identified in the powder pattern.

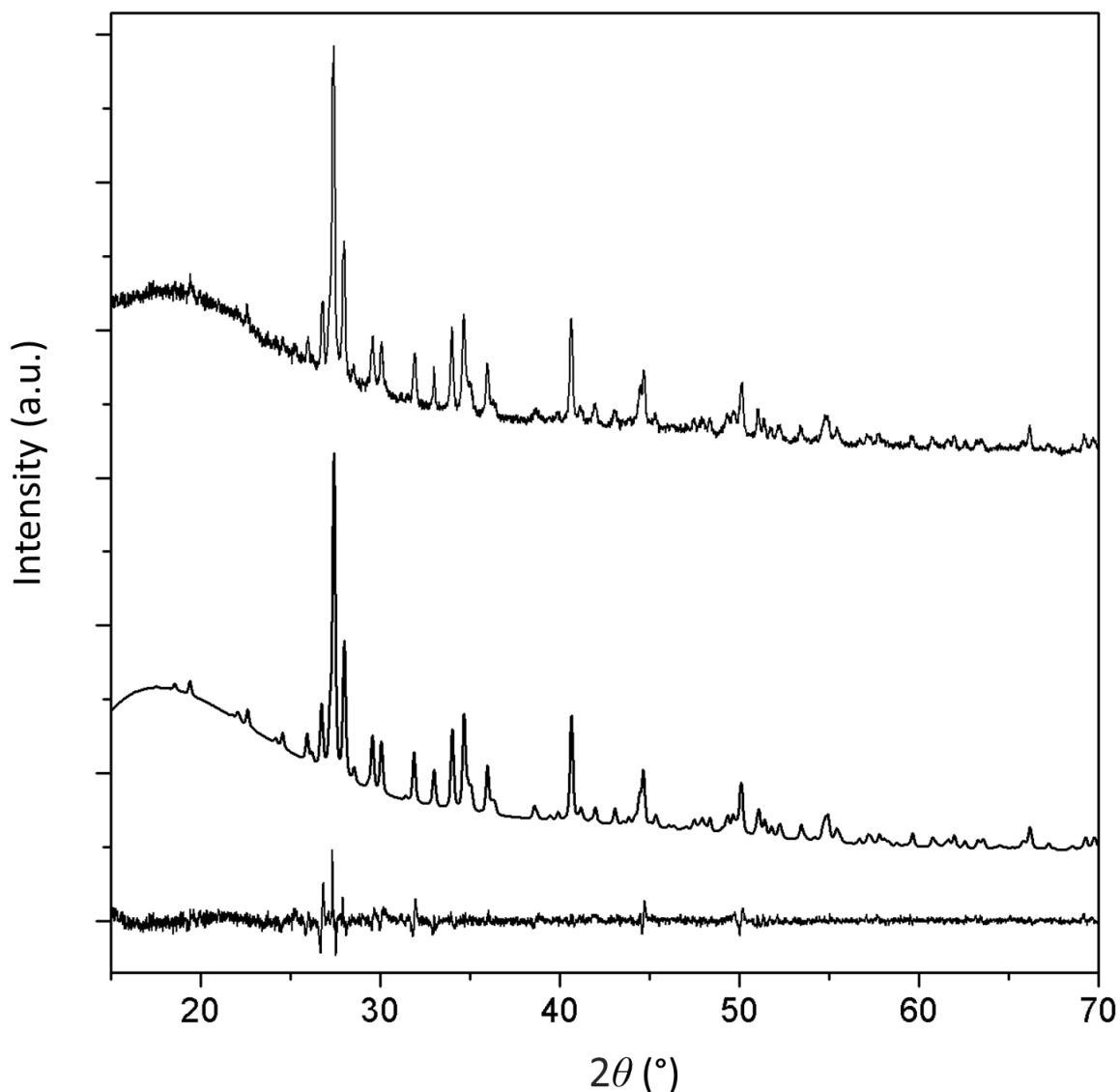


Fig. 7.3.1 Measured (top) and calculated (middle) powder X-ray diffraction diagrams of  $\text{BaGa}_2\text{Sb}_2$  along with difference curve (bottom).

Table 7.3.1 Lattice parameters of  $\text{BaGa}_2\text{Sb}_2$  from Rietveld refinement based on the structure model from literature [114].

	$a$	$b$	$c$
Literature	25.454 (5) Å	4.442 (9) Å	10.273 (2) Å
This work	25.425 (2) Å	4.432 (1) Å	10.263 (1) Å
$R_{\text{exp.}}$ : 4.50	$R_{\text{wp.}}$ : 5.36	$R_{\text{p.}}$ : 3.98	$GOF$ : 1.19

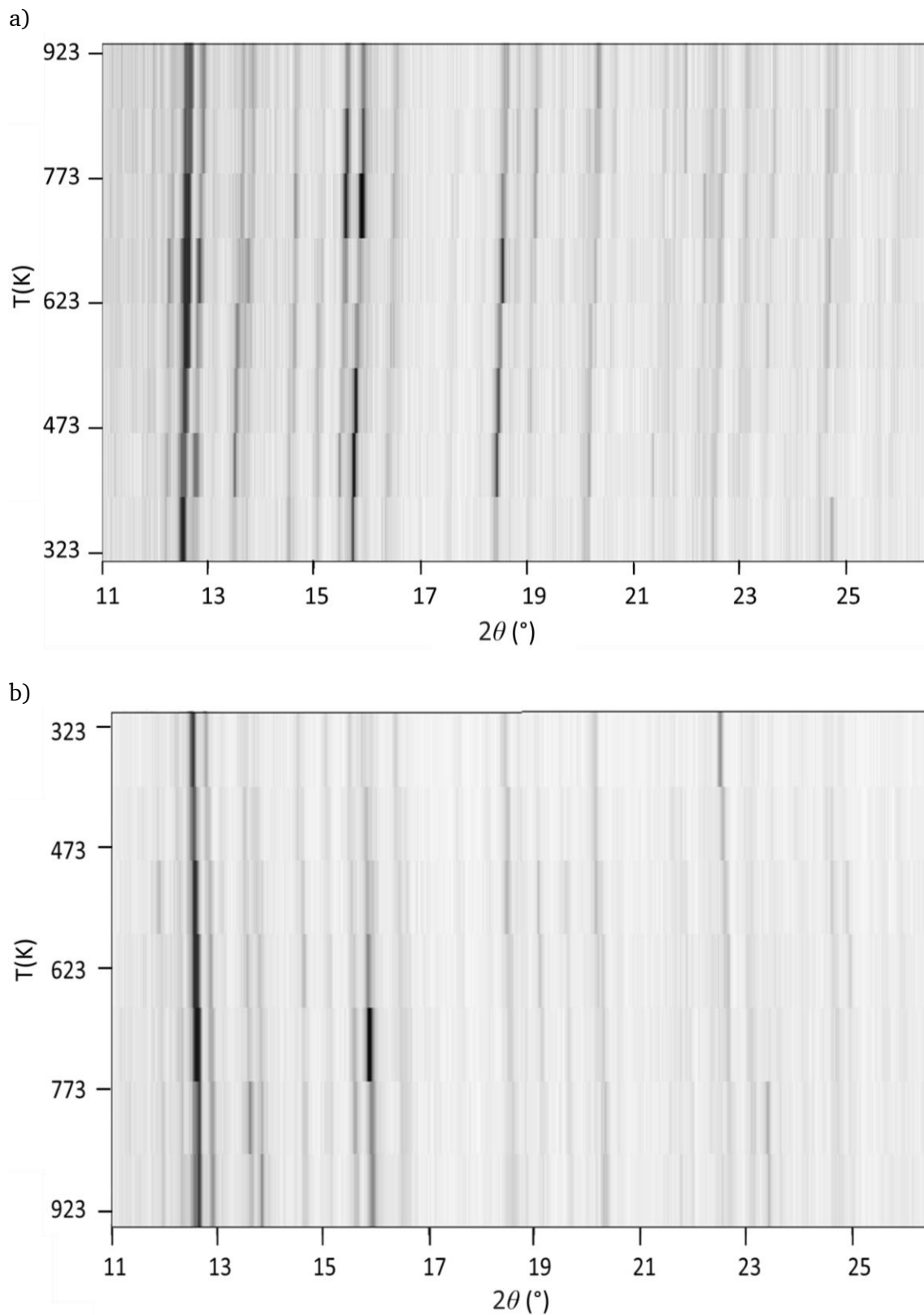


Fig. 7.3.2 a) Heating (top: 323 K-923 K) and cooling (bottom: 923 K-323 K) of  $\text{BaGa}_2\text{Sb}_2$ .

High temperature X-ray diffraction patterns were measured for  $\text{BaGa}_2\text{Sb}_2$ . The sample was loaded in sealed quartz capillary and heated from room temperature to 923 K and

then cooled down to the room temperature. Powder diffraction measurements were carried at steps of 100 K. Fig. 7.3.2 shows heating and cooling of the sample. At peak position of  $22.5^\circ$  the difference starts above 823 K. Thus,  $\text{BaGa}_2\text{Sb}_2$  seems to be stable up to 723 K.

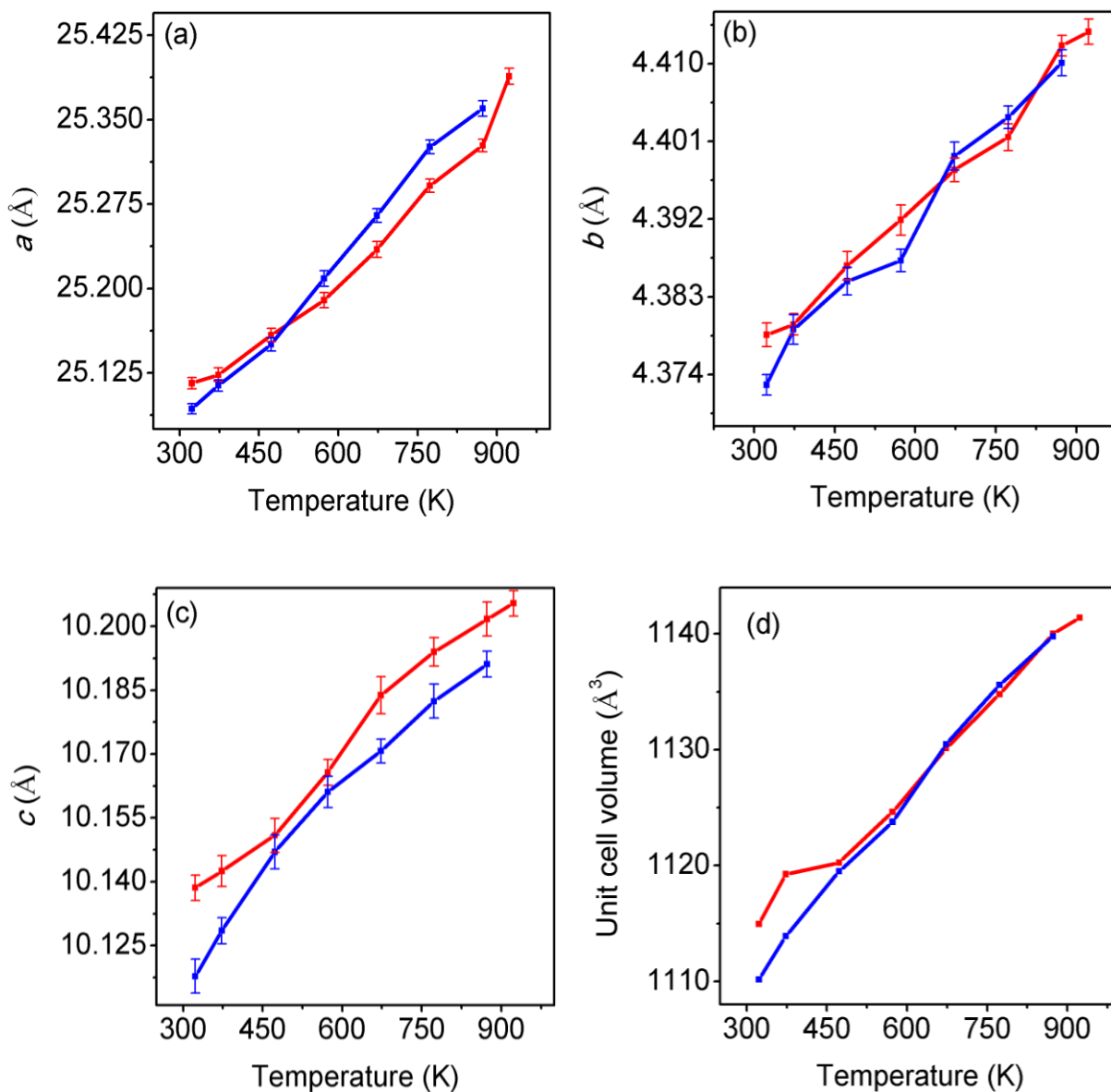


Fig. 7.3.3. a, b, c) Lattice parameters  $a$ ,  $b$  and  $c$  as functions of temperature, red lines indicate heating (323 K to 923 K) and blue lines indicate cooling (873 K to 323 K). Fig. 7.3.3. d) Unit cell volume as a function of temperature (standard deviations were smaller than the symbols).

There are some changes in the intensity of the reflections varying with temperature. All of the powder patterns measured at different temperatures were refined using the *TOPAS* program. The lattice parameters increase with temperature (fig.7.3.3 a, b and c). The relationship between unit cell volume and temperature is shown in fig. 7.3.3. d. As observed in other systems the lattice parameter values increase due to the expansion of unit cell at higher temperatures.

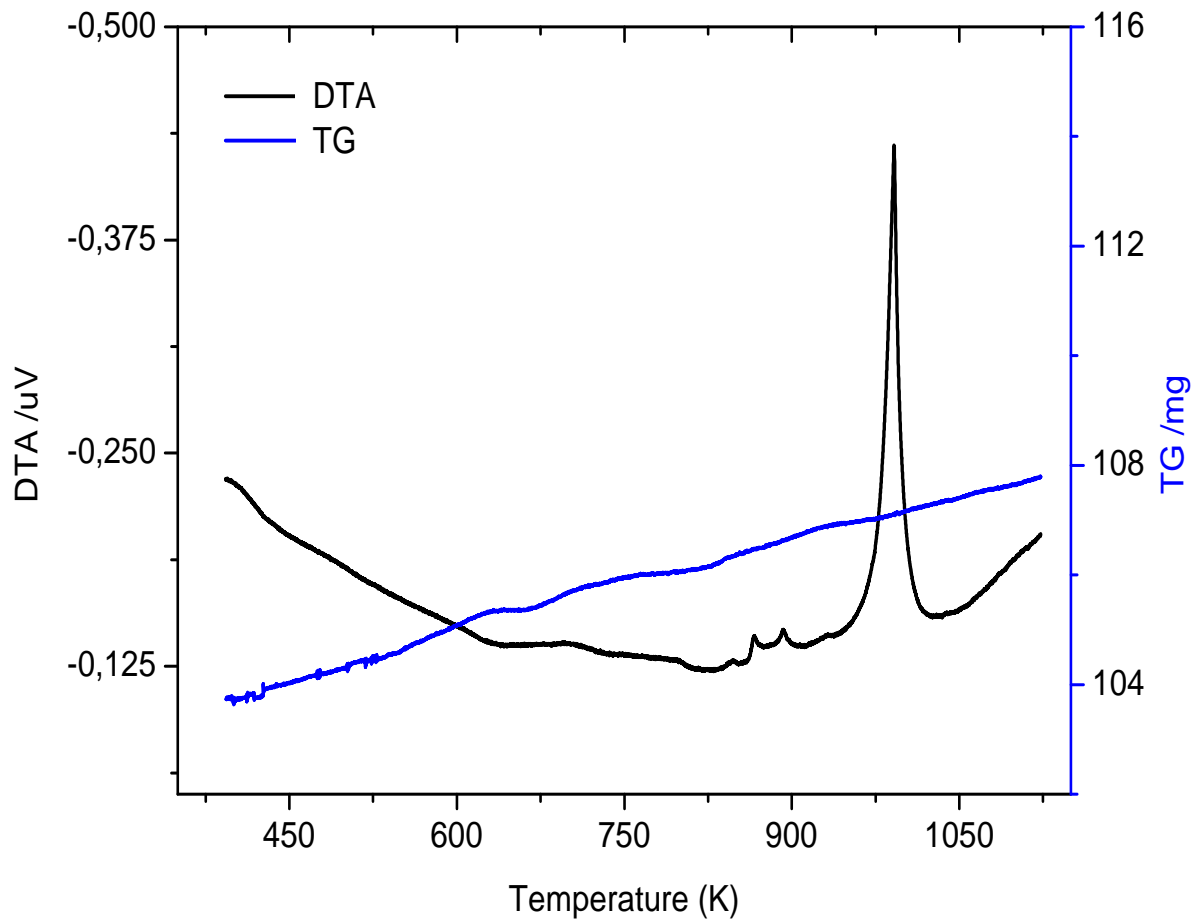


Fig. 7.3.4 Differential thermal analysis and thermal gravimetry measurements of BaGa<sub>2</sub>Sb<sub>2</sub>.

---

Differential thermal analysis and thermal gravimetric measurements were performed to investigate possible phase transitions, thermal stability and the melting point. Fig. 7.3.4 shows the results of differential thermal analysis and the thermal gravimetric curve for  $\text{BaGa}_2\text{Sb}_2$ . 20 mg of the sample were put in an alumina crucible and heated from room temperature to 1150 K with a heating rate of 10 K/minute, then cooled down to room temperature with the same rate. The compound was stable in air no oxidation was observed. No weight loss due to evaporation or decomposition was detected. Above 850 K two small peaks were observed at 864 K and 892 K in the DTA (may be due to the structural change above 823 K according to the high-temperature XRD) and then at 990 K there is a sharp peak that indicates the melting point of the compound.

Spark plasma technique was employed to compact  $\text{BaGa}_2\text{Sb}_2$  (fig. 7.3.5). The finely ground powder was sintered at 773 K with an uniaxial pressure of 100 MPa. The heating and cooling rates were 25 K/min. The sample was sintered for 20 minutes and then cooled down to room temperature. The compacted disk was analyzed by powder X-ray diffraction using a small piece from the compacted sample. Fig. 7.3.6 shows the powder diffraction patterns of the starting material and the compacted sample. Both diffraction patterns are similar. No impurity reflections or phase transitions were observed, so  $\text{BaGa}_2\text{Sb}_2$  was considered to be stable. The lower intensity of some of the reflections indicates a loss of crystallinity of the sample.



Fig. 7.3.5 Compacted sample of  $\text{BaGa}_2\text{Sb}_2$ .

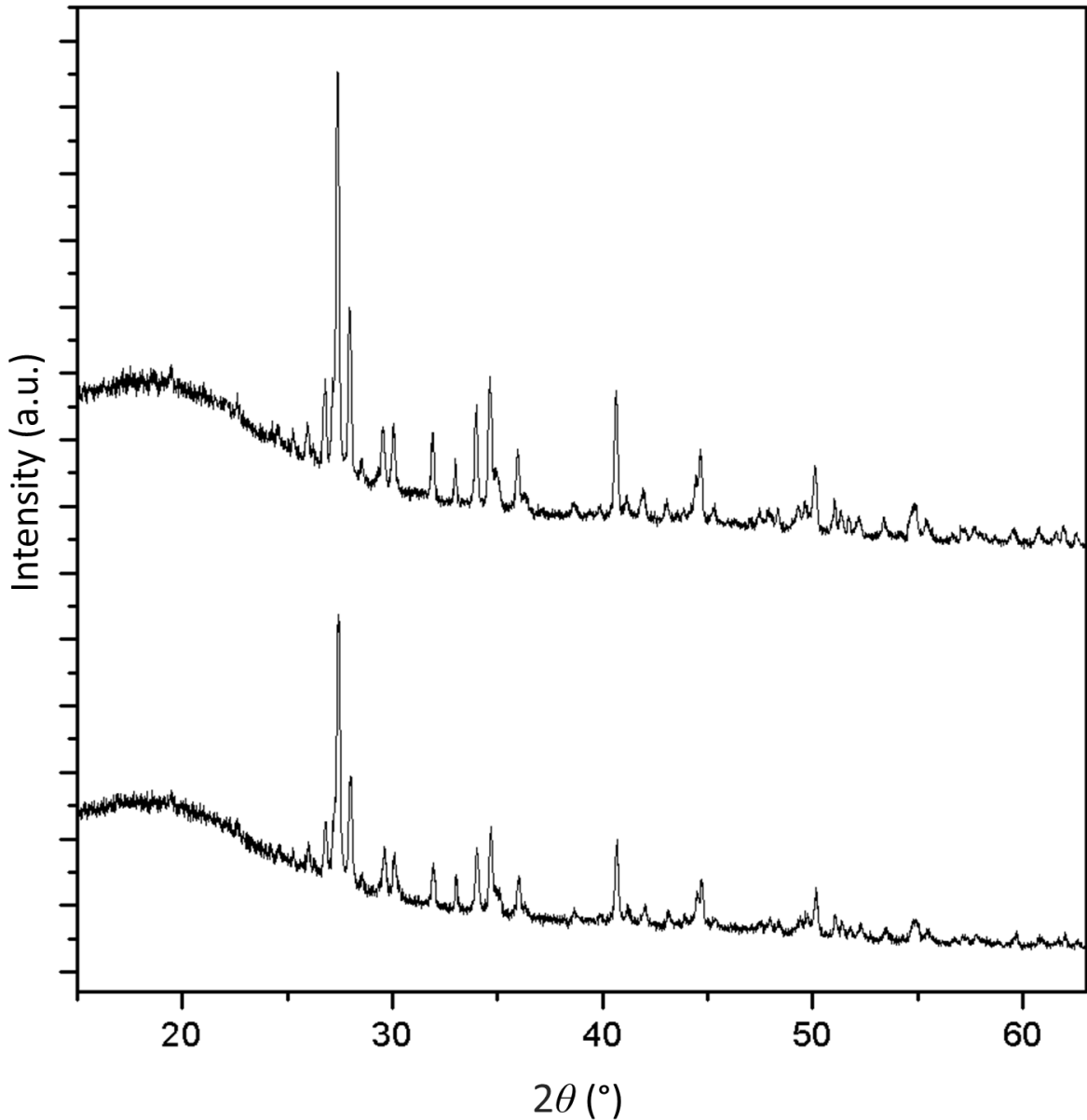


Fig. 7.3.6 Powder X-ray diffraction patterns of  $\text{BaGa}_2\text{Sb}_2$  before (top) and after SPS (bottom).

Using a gas pycnometer, the density of a compacted sample of  $\text{BaGa}_2\text{Sb}_2$  was calculated. Density values for ten cycles are given in table 7.3.2. The average density was calculated to be  $5.9312 \text{ g/cm}^3$ , so the compacted sample was 99.6 % dense compared to the theoretical value ( $5.95 \text{ g/cm}^3$ ) from X-ray diffraction.

Table 7.3.2 List of densities of compacted  $\text{BaGa}_2\text{Sb}_2$ .

Cycles	Volume ( $\text{cm}^3$ )	Density ( $\text{g/cm}^3$ )
1	0.1366	5.9289
2	0.1366	5.9297
3	0.1365	5.9339

4	0.1366	5.9311
5	0.1365	5.9331
6	0.1366	5.9315
7	0.1366	5.9299
8	0.1365	5.9327
9	0.1366	5.9303
10	0.1366	5.9311
Average	0.1366	5.9312

Fig. 7.3.7 shows scanning electron microscopy images of  $\text{BaGa}_2\text{Sb}_2$ . Energy dispersive spectroscopy was also carried out for this compound. The measurements were done at three different spots. The atomic percentages are given in table 7.3.3. These observations prove that the samples were homogeneous and there were no traces of tantalum in the samples.

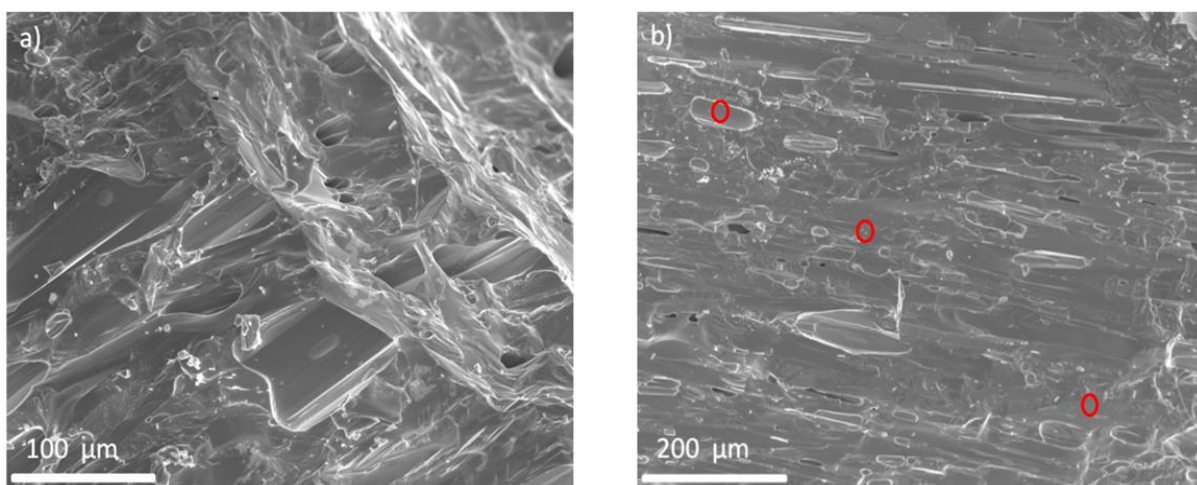


Fig. 7.3.7. a) SEM image of  $\text{BaGa}_2\text{Sb}_2$  (100  $\mu\text{m}$ ) b) red circles indicate the spots where EDS measurements were done.

Table 7.3.3 Atomic percentages of all elements in BaGa<sub>2</sub>Sb<sub>2</sub> determined using EDS.

	Ba (%)	Ga (%)	Sb (%)
Spot 1	21.98	38.85	39.17
Spot 2	21.74	39.32	38.94
Spot 3	19.08	40.91	40.01
Average	20.93	39.69	39.37
Theoretical values	20.00	40.00	40.00

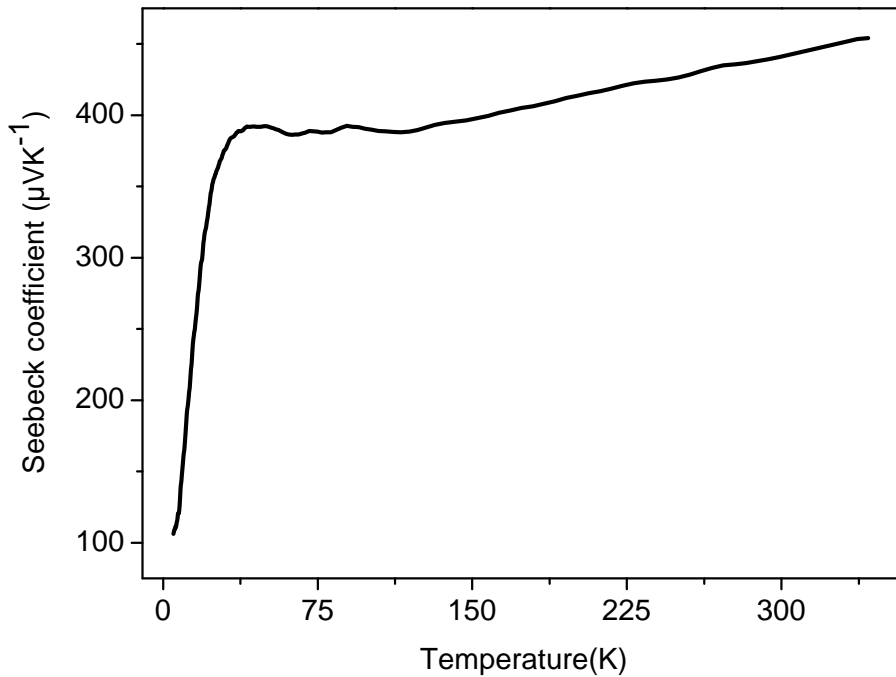
### 7.3.2 Thermoelectric studies

Low temperature thermoelectric properties were measured from 0 K to 350 K using the compacted piece of sample made by spark plasma sintering (Max Planck Institute for Chemical Physics of Solids, Dresden). Seebeck coefficients were measured from 0 K to 350 K (fig. 7.3.8. a). They increase from 0 K to 35 K and reach  $386 \mu\text{VK}^{-1}$ . Then, they further increase slowly up to 350 K and reach a maximum of  $453 \mu\text{VK}^{-1}$  at 340 K. Electrical conductivities were also measured from 0 K to 350 K (fig. 7.3.8. b). They increase from 0 K to 150 K and reach a maximum value of  $1348 \text{Sm}^{-1}$  around 157 K. This behavior is due to the semiconducting nature of the sample that was predicted by the DFT calculations. Then, electrical conductivity values decrease slowly up to 350 K. BaGa<sub>2</sub>Sb<sub>2</sub> exhibits a very narrow band gap that is responsible for the increase in the electrical conductivity values at the beginning. At higher temperatures the charge carriers can cross the gap and metallic behavior is exhibited. Thermal conductivities were also measured for the same temperature range. Fig. 7.3.8. c shows the total thermal conductivity ( $\kappa$ ) of BaGa<sub>2</sub>Sb<sub>2</sub>. Thermal conductivity sharply rises near zero. Around 15 K it reaches a maximum of  $17 \text{Wm}^{-1}\text{K}^{-1}$ . Then, they start to decrease up to 80 K and above which they decrease slowly. Thermal conductivity reaches a minimum of  $1.6 \text{Wm}^{-1}\text{K}^{-1}$  around 350 K. The low values of thermal conductivity in a long range of temperature (80 – 350 K) make it suitable for thermoelectric applications nearby room temperature. The figure of merits were calculated using the formula explained in sec. 3.4.  $ZT$  values are almost zero up to 50 K, due to the very poor electrical conductivities and low Seebeck coefficients below this temperature. Then,  $ZT$

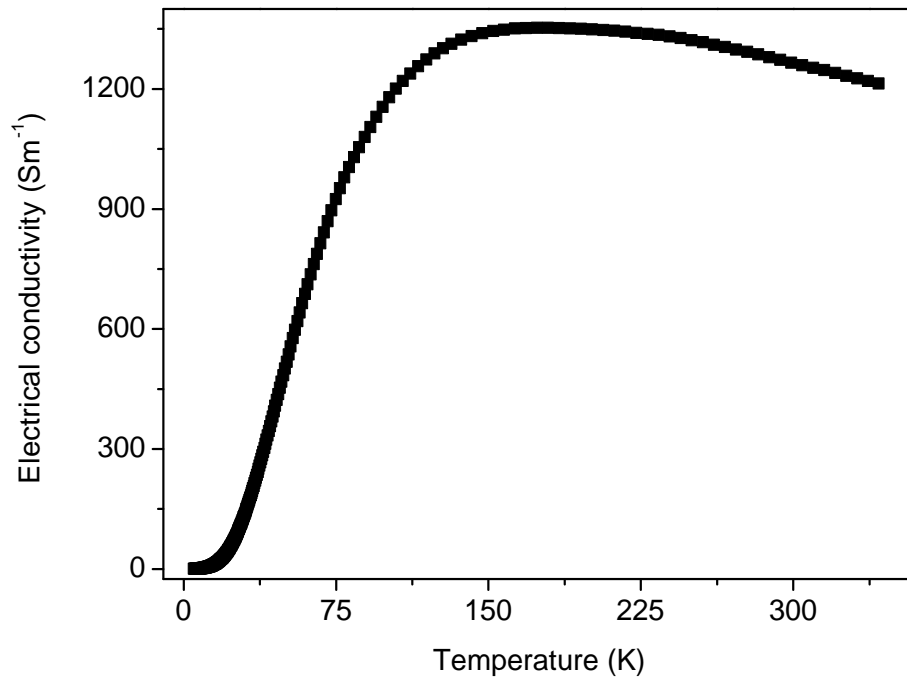
---

continuously increases with temperature up to 350 K. The value reaches a maximum of 0.055 around 350 K. BaGa<sub>2</sub>Sb<sub>2</sub> exhibits high Seebeck coefficients but its electrical conductivity values are too low to achieve high *ZT* values. Low thermal conductivities of this compound are an interesting feature for thermoelectric application. The nature of BaGa<sub>2</sub>Sb<sub>2</sub> (thermal and air stability) makes it suitable for the practical applications. Modified electrical properties of this system could yield an efficient thermoelectric material. Doping studies should be carried out to enhance the properties.

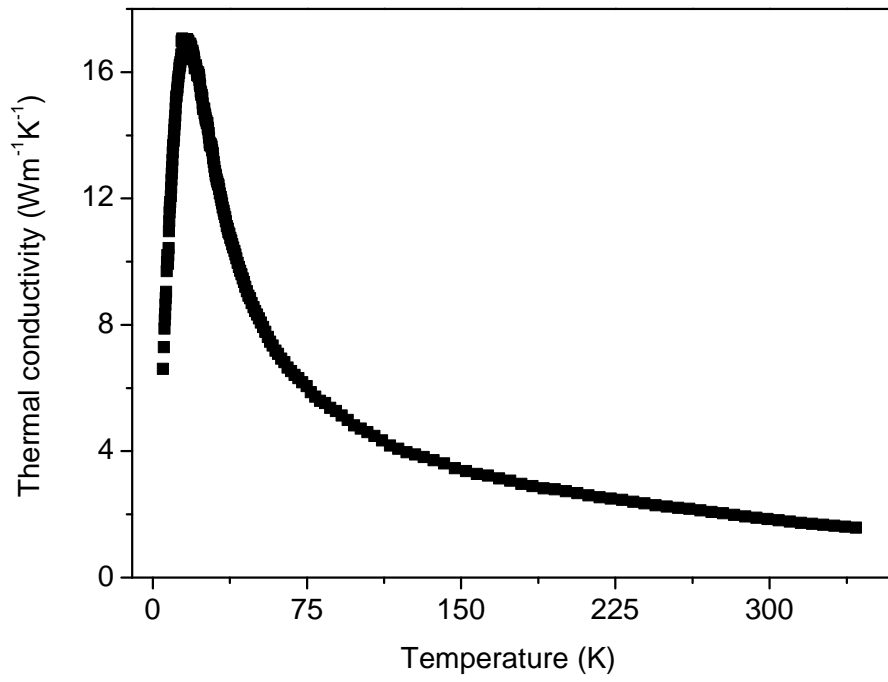
a)



b)



c)



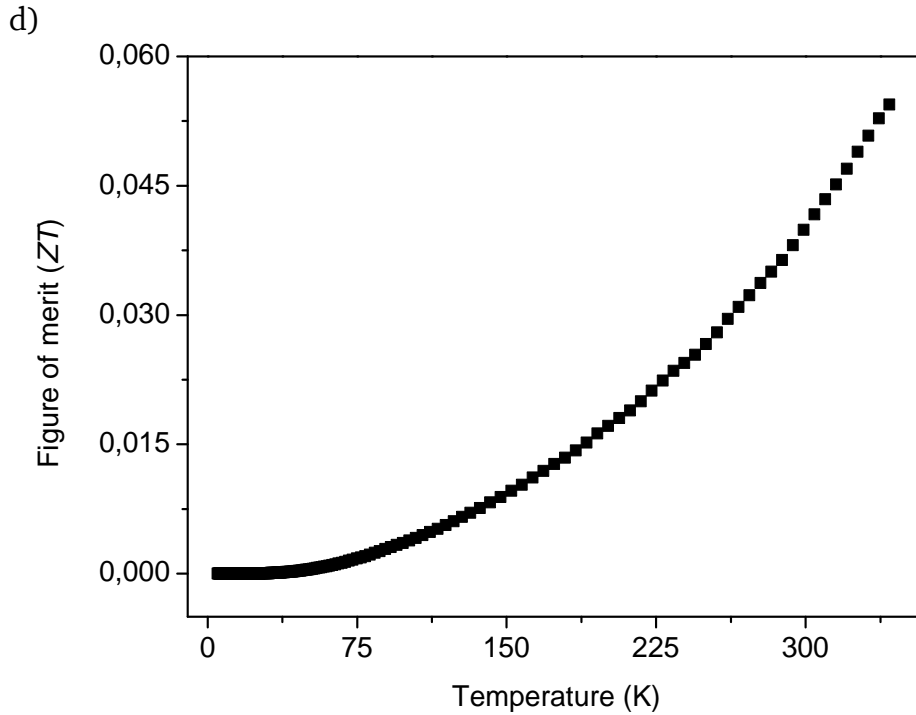


Fig. 7.3.8. (a) Seebeck coefficient of  $\text{BaGa}_2\text{Sb}_2$  as a function of temperature, (b) Electrical conductivity of  $\text{BaGa}_2\text{Sb}_2$  as a function of temperature. (c) Thermal conductivity of  $\text{BaGa}_2\text{Sb}_2$  as a function of temperature, (d) Figure of merit ( $ZT$ ) of  $\text{BaGa}_2\text{Sb}_2$  as a function of temperature.

### 7.3.3 Discussion of the results

$\text{BaGa}_2\text{Sb}_2$  was prepared as a monophasic product by arc melting. It was found to be stable in air which makes the study more interesting.  $\text{BaGa}_2\text{Sb}_2$  melts around 990 K. The compound was compacted using spark plasma sintering and the thermoelectric properties were studied. According to literature, Kanatzidis et al. [114] prepared this compound in a different synthetic route (sec. 4) and  $\text{BaGa}_2\text{Sb}_2$  was found to be a  $p$ -type semiconductor with a band gap of 0.35 eV that is similar to  $\text{Ba}_3\text{GaSb}_3$  (0.3 eV). Kanatzidis et al. reported the Seebeck coefficients and electrical conductivities in a temperature range of 290 to 450 K. At room temperature Seebeck coefficient was found to be  $+65 \mu\text{VK}^{-1}$  and electrical Conductivity was  $65 \text{ Scm}^{-1}$  [114]. In the current study, the low temperature thermoelectric properties from 0 to 350 K were measured. Like  $\text{Ba}_3\text{AlSb}_3$  and  $\text{Ba}_3\text{GaSb}_3$ , high Seebeck coefficients were observed for  $\text{BaGa}_2\text{Sb}_2$  and the maximum being  $453 \mu\text{VK}^{-1}$  around 340 K. Electrical conductivities increase continuously from 0 K which shows the typical behavior of a semiconductor and reaches maximum of  $1348 \text{ Sm}^{-1}$  around 157 K. Seebeck coefficients and electrical

---

conductivities observed in this work proved to be different from literature. This can be due to different synthesis procedures. Use of arc melting technique can lead to evaporation and loss of antimony to a small extent, bringing in a deficiency in the stoichiometry. Also, since BaGa<sub>2</sub>Sb<sub>2</sub> is a metastable phase and had to be cooled down quickly it might contain more defects that change the electronic properties of the compound. Very low thermal conductivities were observed for BaGa<sub>2</sub>Sb<sub>2</sub>, the minimum being 1.6 Wm<sup>-1</sup>K<sup>-1</sup> around 350 K. The temperature trend was similar to Ba<sub>3</sub>AlSb<sub>3</sub> and Ba<sub>3</sub>GaSb<sub>3</sub>. The values of figure of merit were not so high due to the low electrical conductivity values. Doping these compounds might improve the properties to produce an efficient thermoelectric material in future. This investigation brings interest to study other BaM<sub>2</sub>X<sub>2</sub>-type compounds such as BaGa<sub>2</sub>P<sub>2</sub>, BaGa<sub>2</sub>As<sub>2</sub> and BaMg<sub>2</sub>X<sub>2</sub> (X = Si, Ge, Sn, Pb) [134, 137].

---

## 8 $\text{Ba}_5\text{In}_2\text{Sb}_6$

---

### 8.1 Synthesis, characterization and compaction

Stoichiometric amounts of Ba (0.4169 g, 3.04 mmol, Chempur, 99.3%), In (0.1394 g, 1.21 mmol, Fluka AG, 99.995%) and Sb (0.4436 g, 3.64 mmol, Chempur, Sb-Shots, 1-3 mm, 99.999%) were loaded in a tantalum container and sealed in argon atmosphere. All manipulations were done inside the glove box filled with argon gas where the oxygen and moisture levels were below 1 ppm. Later the quartz ampoule was prepared as explained in the sec. 2.4. The sample was heated to 1400 K with a heating rate of 100 K/hour. The sample was kept at this temperature for six days and then cooled down to room temperature with the same cooling rate. This method yields a shiny, air-sensitive product of metallic grey color that was found to contain more than 90 % of the desired product. InSb was identified as one of the side phases. Other unidentified reflections were observed in the powder X-ray diffraction pattern. Fig. 8.1 shows the powder X-ray pattern of the sample prepared and the X-ray diffraction pattern calculated based on the structure model from literature [115]. When the duration of reaction was less than six days additional reflections from several binary phases ( $\text{Ba}_{11}\text{Sb}_{10}$ ,  $\text{Ba}_2\text{Sb}_3$ ,  $\text{Ba}_5\text{Sb}_3$  etc) were observed. Synthesis was possible between 1373 and 1473 K. Arc melting did not yield the expected product.

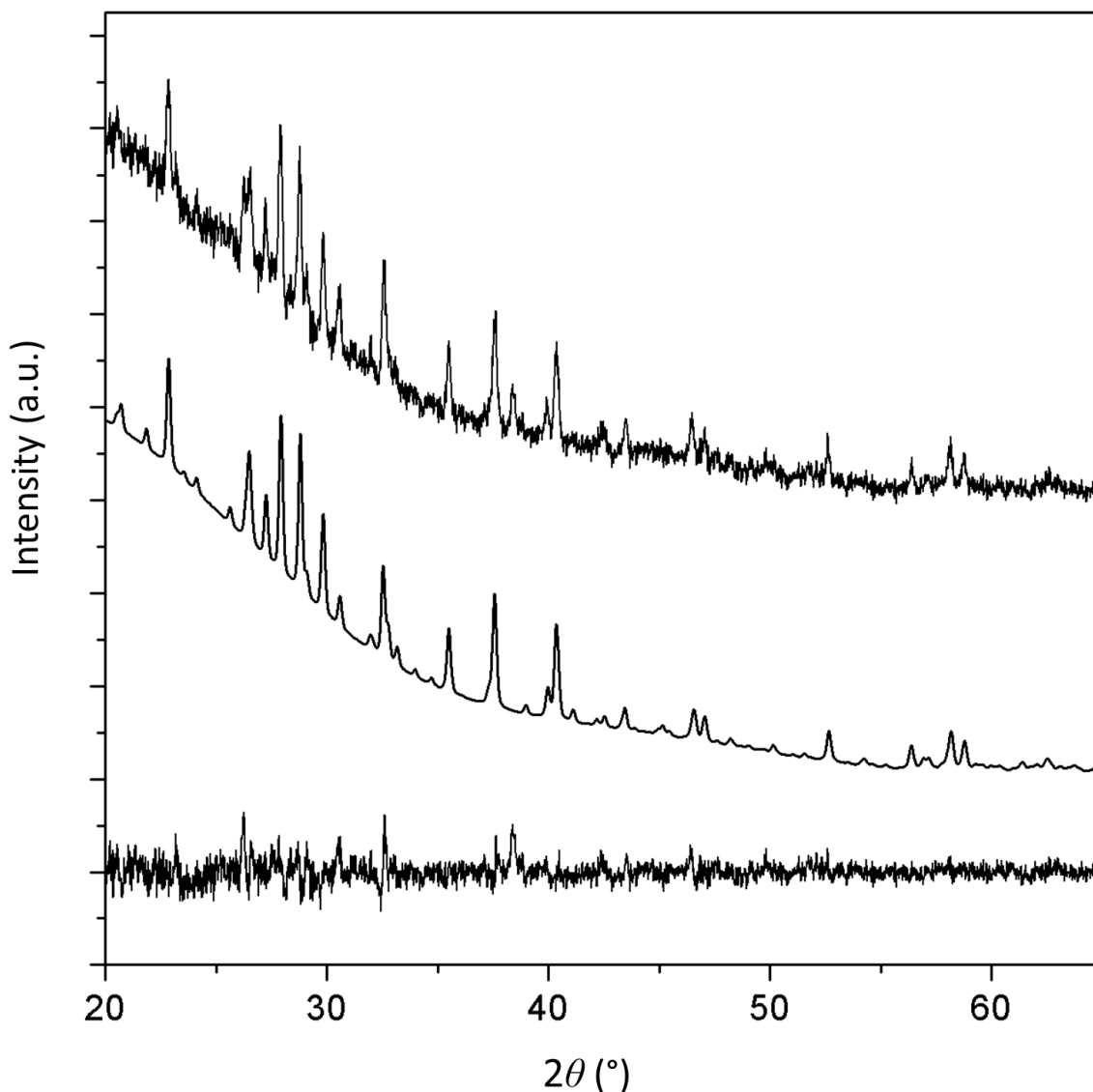


Fig. 8.1 Measured (top) and calculated (middle) powder X-ray diffraction diagrams of  $\text{Ba}_5\text{In}_2\text{Sb}_6$  along with difference curve (bottom).

The experimental powder X-ray pattern matches well with the calculated powder pattern of  $\text{Ba}_5\text{In}_2\text{Sb}_6$ , except for the reflections from the side phases. The reflections at  $26.14^\circ$  and  $38.25^\circ$  ( $2\theta$ ) belong to  $\text{InSb}$ . Table 8.1 gives the lattice parameters.

Table 8.1 Lattice parameters of  $\text{Ba}_5\text{In}_2\text{Sb}_6$  from Rietveld refinement based on the structure model from literature [115].

	$a$	$b$	$c$
Literature	15.307 (6) Å	13.358 (5) Å	4.686 (2) Å

This work	15.310 (3) Å	13.362 (2) Å	4.681 (5) Å
$R_{\text{exp.}}$ : 4.39	$R_{\text{wp.}}$ : 4.94	$R_{\text{p.}}$ : 3.76	$GOF$ : 1.13

In order to investigate the thermal stability and possible phase transitions of  $\text{Ba}_5\text{In}_2\text{Sb}_6$  high temperature X-ray diffraction studies were carried out. The sample was heated from room temperature to 1073 K. Powder X-ray diffraction patterns were recorded at steps of 100 K. Fig. 8.2 shows the high temperature powder X-ray patterns of  $\text{Ba}_5\text{In}_2\text{Sb}_6$ . There are no changes in the powder patterns of the sample in the temperature range of 323 K to 973 K. From fig. 8.2 it is evident that there are no phase transitions up to 973 K. Above this temperature the sample melts and there are no reflections at 1073 K. When the sample is cooled, peaks start to appear again at 973 K. This observation implies that the sample melts congruently around 973-1073 K and when it is cooled down the molten sample crystallizes.

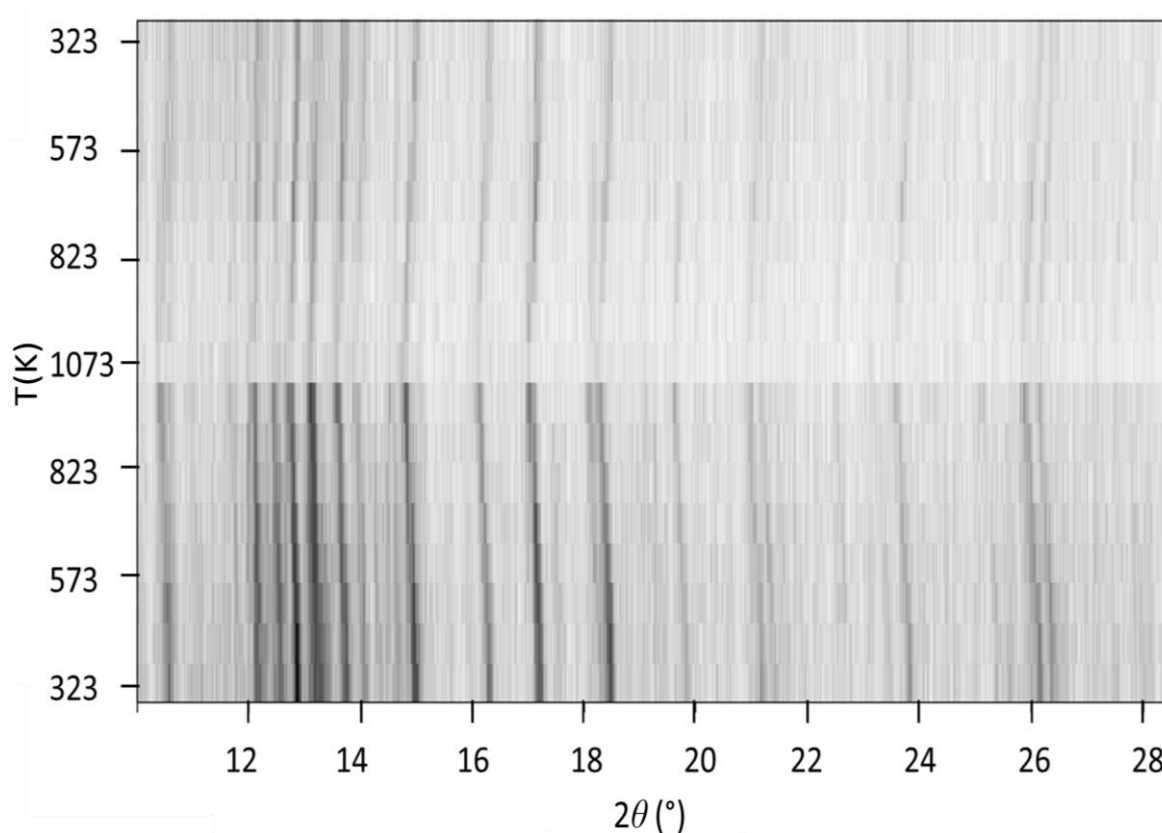


Fig. 8.2 High temperature powder X-ray diffraction of  $\text{Ba}_5\text{In}_2\text{Sb}_6$ , bottom: 323–1073 K and top: 923-323 K.

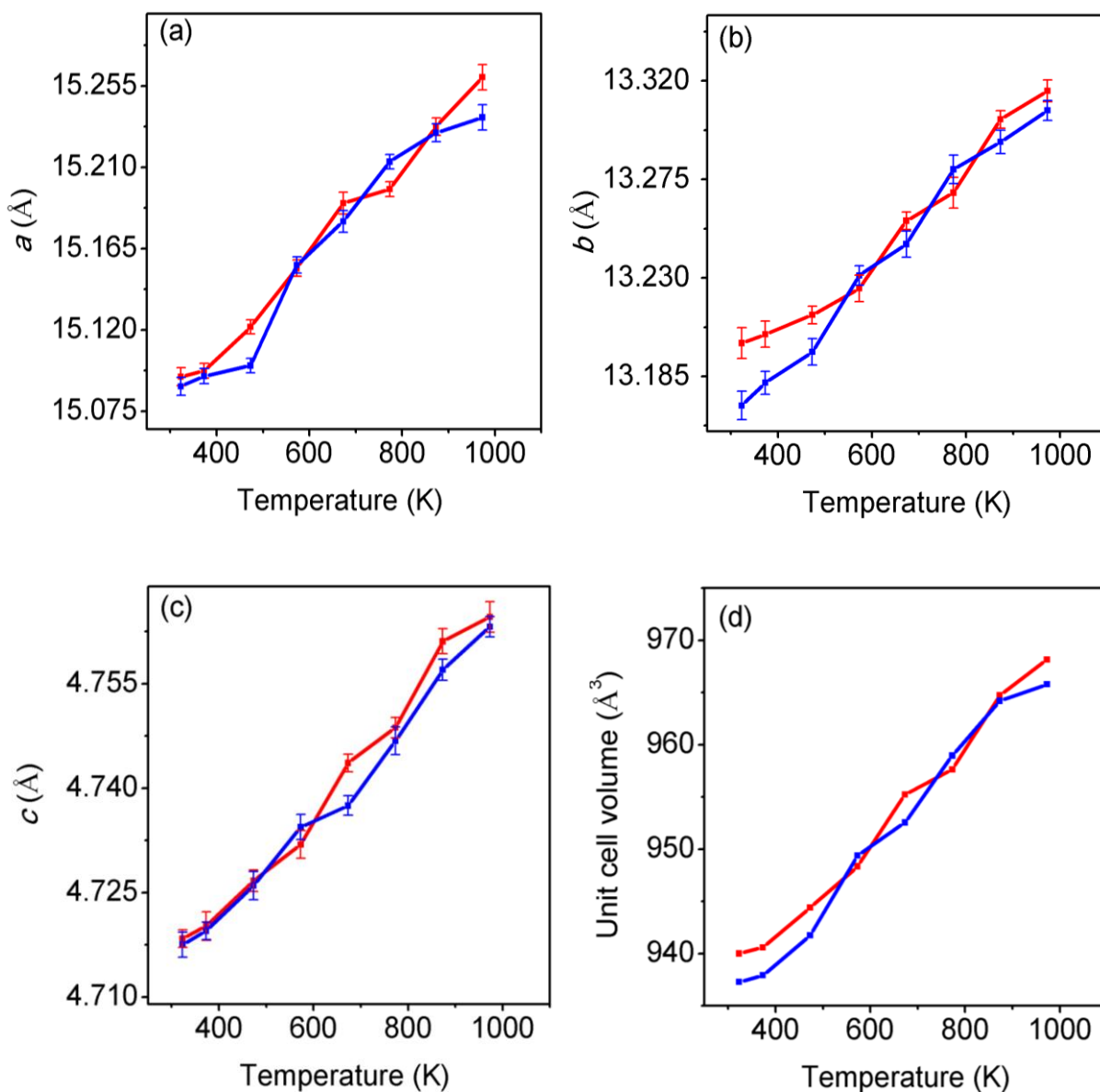


Fig. 8.3. a, b, c: Lattice parameters ( $a$ ,  $b$ ,  $c$ ) as function of temperature, red lines indicate heating (323 K to 973 K) and blue lines indicate cooling (973 K to 323 K). Fig. 8.3. d Unit cell volume as a function of temperature (standard deviations were smaller than the symbols).

Lattice parameters at different temperatures were refined using the *TOPAS* program. The results obtained from Rietveld refinement were used to plot the changes of the lattice parameters ( $a$ ,  $b$ ,  $c$ ) with temperature (fig. 8.3 a, b, c). Lattice parameters increase with the increasing temperature as expected. The same behavior is observed when the unit cell volume is plotted against the temperature which is shown in fig. 8.3. d.

$Ba_5In_2Sb_6$  was compacted using spark plasma sintering at 850 K with a pressure of 50 Mpa for 30 minutes, then the compound was cooled down to room temperature. Powder X-ray diffraction was employed to investigate the purity of the sintered sample. A small piece from the compacted sample was taken for powder X-ray diffraction. Fig. 8.4 shows the powder X-ray diffraction patterns of the starting material and the sintered sample. Both diffraction patterns are similar and neither additional impurity peaks nor any sort of phase transition are observed.  $Ba_5In_2Sb_6$  is stable and did not undergo any changes during the sintering process.

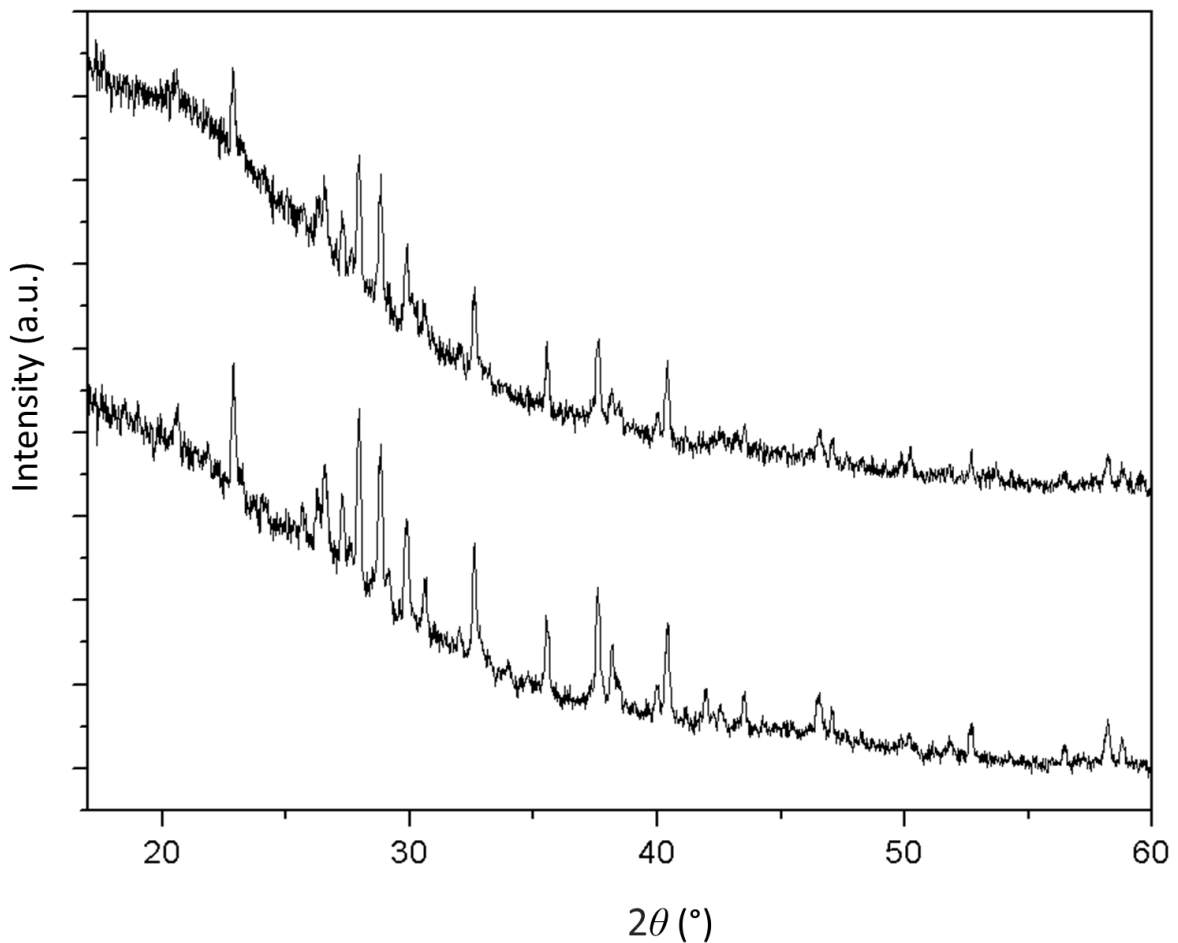


Fig. 8.4 Powder X-ray diffraction patterns of  $Ba_5In_2Sb_6$  before (bottom) and after SPS (top).

The density of the compacted sample of  $Ba_5In_2Sb_6$  was calculated using a gas pycnometer. Volume and density values for all the cycles are given in table 8.2. An average density was calculated to be  $5.2965 \text{ g/cm}^3$ . Thus, the compacted sample was 94.8 % dense compared to the theoretical value ( $5.59 \text{ g/cm}^3$ ) from X-ray diffraction.

Table. 8.2 List of densities of compacted Ba<sub>5</sub>In<sub>2</sub>Sb<sub>6</sub>.

Cycles	Volume (cm <sup>3</sup> )	Density (g/cm <sup>3</sup> )
1	0.1291	5.2977
2	0.1291	5.2981
3	0.1291	5.2965
4	0.1291	5.2981
5	0.1290	5.3005
6	0.1292	5.2946
7	0.1292	5.2949
8	0.1293	5.2907
9	0.1293	5.2917
10	0.1290	5.3025
Average	0.1291	5.2965

Fig. 8.5 shows scanning electron microscopy images of Ba<sub>5</sub>In<sub>2</sub>Sb<sub>6</sub>, red circles indicate the spots where EDS measurements were carried out to measure the atomic percentages of barium, indium and antimony in Ba<sub>5</sub>In<sub>2</sub>Sb<sub>6</sub>. The measurements were done in three different spots to ensure the homogenous nature of the sample. The calculated atomic percentages of all the elements are close to the theoretical values which indicate the homogeneous nature of the sample (table 8.3). Signals for tantalum were not observed anywhere in the sample, so there is no reaction between the container material and reactants.

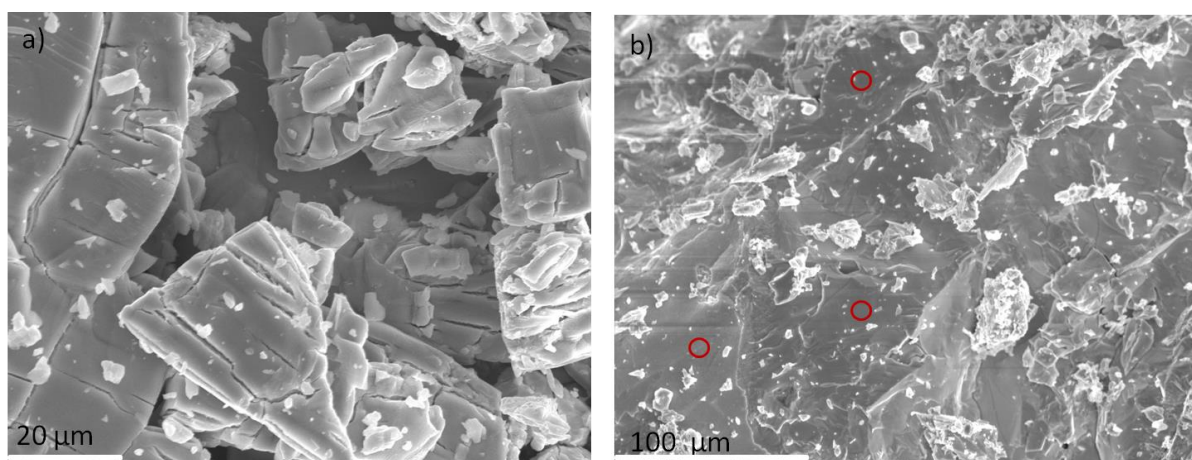


Fig. 8.5 SEM images of Ba<sub>5</sub>In<sub>2</sub>Sb<sub>6</sub> (red circles indicate the spots where EDS measurements have been done).

Table 8.3 Atomic percentages of the elements in Ba<sub>5</sub>In<sub>2</sub>Sb<sub>6</sub> determined using EDS.

	Ba (%)	In (%)	Sb (%)
Spot 1	39.93	14.38	45.69
Spot 2	40.01	14.76	45.23
Spot 3	37.68	15.93	46.39
Average	39.21	15.02	45.77
Theoretical values	38.46	15.39	46.15

## 8.2 Thermoelectric studies

A compacted pellet of Ba<sub>5</sub>In<sub>2</sub>Sb<sub>6</sub> prepared by spark plasma sintering was cut in to pieces of 14 mm x 3 mm x 3 mm for the measurement of the Seebeck coefficients and electrical conductivities. An automatic saw inside the glove box was used. The sides were not perfectly flat. The contact with the two thermocouples of the four-probe measurement instrument was difficult. As a consequence, there could be a small additional error in the measurement. Seebeck and electrical conductivity measurements were carried out between 323 K and 683 K. The Seebeck coefficients of Ba<sub>5</sub>In<sub>2</sub>Sb<sub>6</sub> are shown in fig. 8.6. a. The values initially decrease from  $-67 \mu\text{VK}^{-1}$  to a minimum Seebeck value of  $-74 \mu\text{VK}^{-1}$  around 473 K. Then, the values start to increase and reach  $-58 \mu\text{VK}^{-1}$  at 683 K. Negative Seebeck values confirm the *n*-type conducting nature of Ba<sub>5</sub>In<sub>2</sub>Sb<sub>6</sub>.

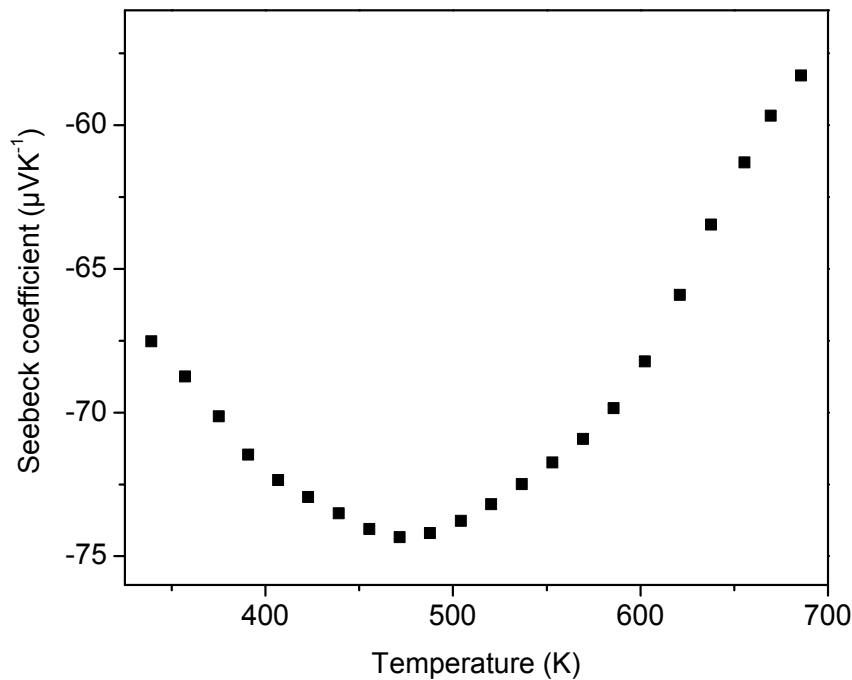
The electrical conductivities of Ba<sub>5</sub>In<sub>2</sub>Sb<sub>6</sub> were measured between 323 K and 683 K (fig. 8.6. b). The values increase with increasing temperature. This behavior is typical of a semiconductor but unexpected, since the DFT calculations suggested metallic behavior for Ba<sub>5</sub>In<sub>2</sub>Sb<sub>6</sub>. This is not unusual since DFT calculations usually underestimate the size of the band gap. In order to calculate the band gap the natural logarithm of the electrical conductivity ( $\text{Ln } \sigma$ ) was plotted against the reciprocal of  $kT$  ( $k = \text{Boltzmann constant}$ ) which is shown in fig. 8.6. e. The slope ( $dy/dx$ ) from the straight line (red line) gives the band gap. In the high temperature region ( $kT = 17$  to  $20$ ) the band gap was found to be 0.02 eV, corresponding to a narrow band gap semiconductor. Around 340 K the electrical conductivity is  $12136 \text{ Sm}^{-1}$  and slowly

---

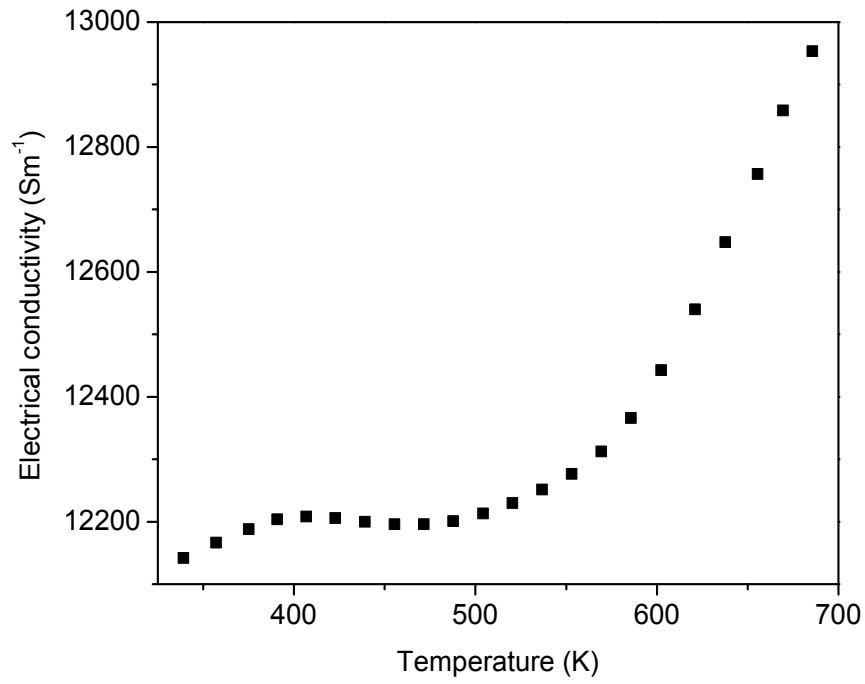
increases with temperature up to  $12210 \text{ Sm}^{-1}$ . Above 500 K the electrical conductivities increase and reach the maximum value of  $12955 \text{ Sm}^{-1}$ .

Thermal conductivity was measured using a compacted disk (10 mm in diameter and 2 mm thick) prepared by spark plasma sintering. The measurement was done between 323 K and 683 K (fig. 8.6. c). Thermal conductivity nearby room temperature is  $1.85 \text{ Wm}^{-1}\text{K}^{-1}$  and drops gradually to reach  $1.73 \text{ Wm}^{-1}\text{K}^{-1}$  at 520 K. Above this temperature the thermal conductivities increase to reach a maximum value of  $2.68 \text{ Wm}^{-1}\text{K}^{-1}$  at 604 K, then it drops to  $1.91 \text{ Wm}^{-1}\text{K}^{-1}$  at 680 K. The figure of merit ( $ZT$ ) was calculated and plotted as a function of temperature. At room temperature it was 0.011 and it slowly increases with increasing temperature. Fig. 8.6. d shows the calculated value of the figure of merit of  $\text{Ba}_5\text{In}_2\text{Sb}_6$ . The values increase up to 505 K and reach a maximum of 0.019. Then, they drop to 0.013 around 590 K and again increase slowly to 0.016 at 680 K.  $\text{Ba}_5\text{In}_2\text{Sb}_6$  exhibits low thermal conductivities, so it is a right candidate for thermoelectric applications. Doping can be useful to modify the properties to make this material an efficient thermoelectric material.

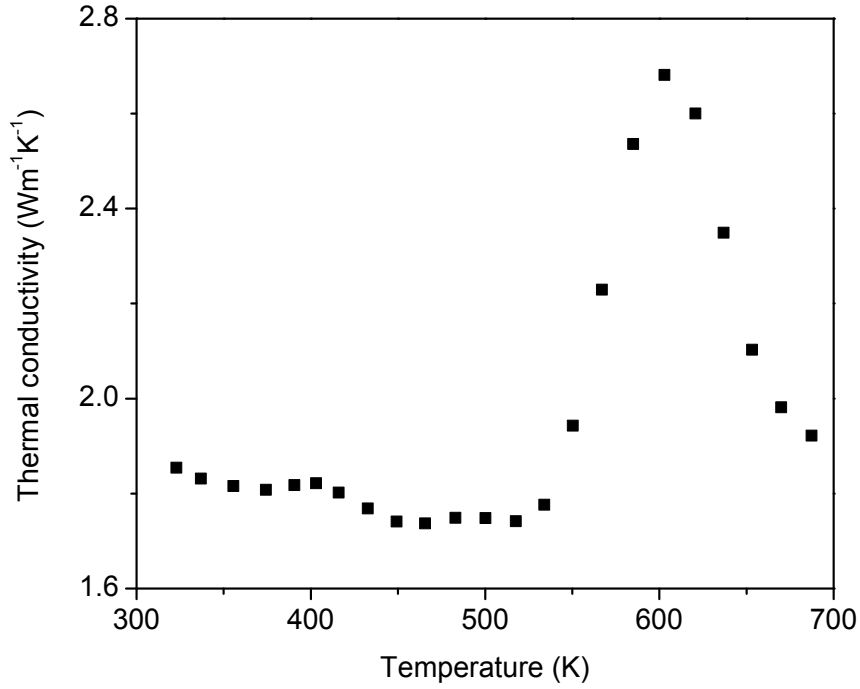
a)



b)



c)



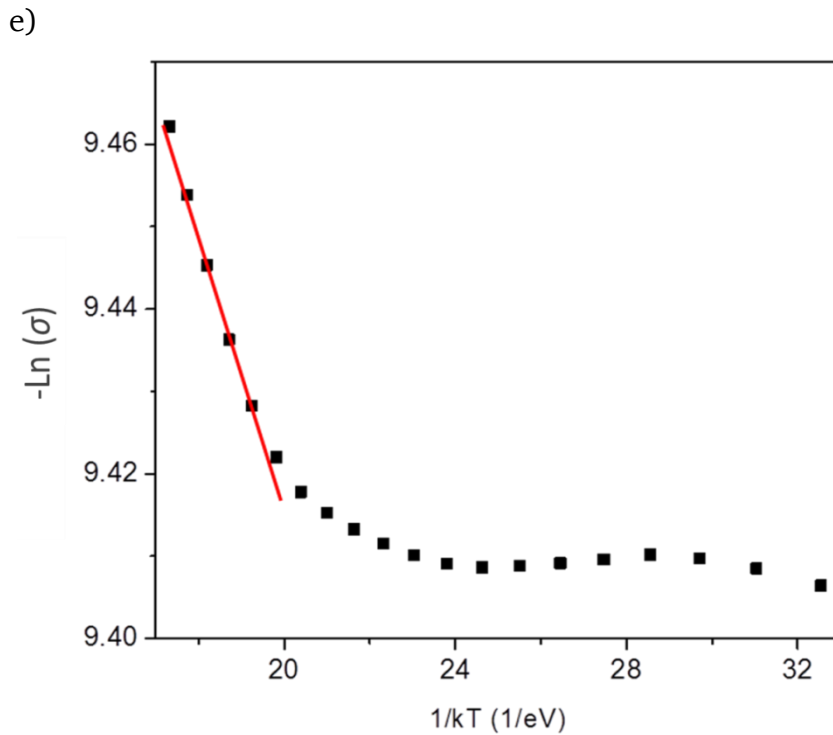
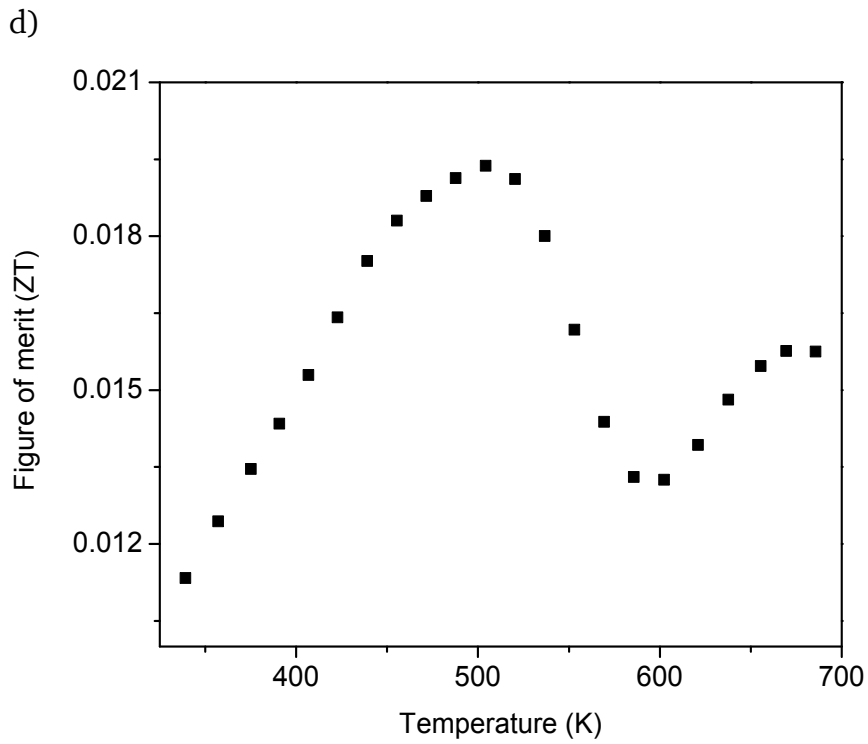


Fig. 8.6 Thermoelectric properties of  $\text{Ba}_5\text{In}_2\text{Sb}_6$  as function of temperature a) Seebeck coefficient, b) Electrical conductivity, c) Thermal conductivity, and d) Figure of merit ( $ZT$ ). e) Natural logarithm of electrical conductivity against reciprocal of  $kT$ .

---

### 8.3 Discussion of the results

$\text{Ba}_5\text{In}_2\text{Sb}_6$  was prepared successfully as the main phase in a product obtained by solid state reactions. This compound was expected to show metallic behavior according to the DFT calculations. From electrical conductivity studies it was found to be a narrow band gap semiconductor. It must be noted that according to literature, other phases in the  $\text{A}_5\text{In}_2\text{Sb}_6$  class of compounds such as  $\text{Ca}_5\text{In}_2\text{Sb}_6$ ,  $\text{Yb}_5\text{In}_2\text{Sb}_6$  and  $\text{Eu}_5\text{In}_2\text{Sb}_6$  are known to be narrow band gap semiconductors too [139, 77, 138].  $\text{Ba}_5\text{In}_2\text{Sb}_6$  was found to melt above 973 K without decomposition and to be stable under SPS conditions. The compacted sample was 94.8 % dense compared to the literature density. The measured Seebeck coefficients of  $\text{Ba}_5\text{In}_2\text{Sb}_6$  vary from  $-67 \mu\text{VK}^{-1}$  to  $-74 \mu\text{VK}^{-1}$  (323-683 K). In this work,  $\text{Ba}_5\text{In}_2\text{Sb}_6$  is the only compound exhibiting *n*-type behavior.  $\text{Yb}_5\text{In}_2\text{Sb}_6$  [77], a compound known from literature that exhibits *p*-type behavior and Seebeck coefficient of  $+30 \mu\text{VK}^{-1}$  at room temperature can be compared to  $\text{Ba}_5\text{In}_2\text{Sb}_6$ . Another interesting comparison is that with  $\text{Eu}_5\text{In}_2\text{Sb}_6$  [138] that is a *p*-type semiconductor and has a Seebeck coefficient of  $76 \mu\text{VK}^{-1}$  at room temperature.

The electrical conductivity of  $\text{Ba}_5\text{In}_2\text{Sb}_6$ , reaches a maximum of  $12136 \text{ Sm}^{-1}$  around 340 K. A plot of the negative natural logarithm of the electrical conductivities of  $\text{Ba}_5\text{In}_2\text{Sb}_6$  against reciprocal of  $kT$  allowed it to determine a band gap of 0.02 eV. The lowest thermal conductivity of  $\text{Ba}_5\text{In}_2\text{Sb}_6$  ( $1.73 \text{ Wm}^{-1}\text{K}^{-1}$  around 520 K) compares well to  $\text{Yb}_5\text{In}_2\text{Sb}_6$  ( $1.7 \text{ Wm}^{-1}\text{K}^{-1}$ ) [77] and  $\text{Ca}_5\text{In}_2\text{Sb}_6$  ( $1.1 \text{ Wm}^{-1}\text{K}^{-1}$ ) [139]. The *ZT* values of  $\text{Ba}_5\text{In}_2\text{Sb}_6$  were not high due to the low Seebeck and electrical conductivity values. This study encourages further research based on doping that can help to modify the electronic properties in future.

---

## 9 Summary and outlook

---

In this work bulk samples with high purity of known ternary Zintl phases have been synthesized. The band structure and band gaps were calculated using DFT. Characterization, densification and measurements of several physical properties were performed successfully. DFT suggests that  $\text{Ba}_3\text{AlSb}_3$  is a semiconductor. It was synthesized and found to be stable up to 1073 K.  $\text{Ba}_3\text{AlSb}_3$  shows high Seebeck coefficients ( $\alpha_{\text{max}} = 383 \mu\text{VK}^{-1}$  at 342 K), low electrical ( $\sigma_{\text{max}} = 18 \text{ Sm}^{-1}$  at 342 K) and thermal conductivities ( $K_{\text{min}} = 0.75 \text{ Wm}^{-1}\text{K}^{-1}$  at 350 K).  $ZT$  values were low due to poor electrical conductivities. Doping was attempted to modify the properties. Zinc atoms were substituted presumably at the sites of aluminium atoms ( $\text{Ba}_3\text{Al}_{1-x}\text{Zn}_x\text{Sb}_3$ ) and calcium atoms were substituted at the positions of barium atoms ( $\text{Ba}_{3-x}\text{Ca}_x\text{AlSb}_3$ ). Using atomic absorption spectroscopy (AAS) the presence of zinc in the doped samples was shown. EDS was used to identify the calcium content in the samples. The lattice parameters change according to Vegard's law. Hence, doping is possible in principle. As an example,  $\text{Ba}_3\text{Al}_{0.97}\text{Zn}_{0.03}\text{Sb}_3$  was compacted and the thermoelectric properties were studied (330-490 K). It shows different properties and higher  $ZT$  values compared to undoped  $\text{Ba}_3\text{AlSb}_3$  between 330 K and 345 K. A maximum figure of merit of 0.1081 was observed at 490 K for  $\text{Ba}_3\text{Al}_{0.97}\text{Zn}_{0.03}\text{Sb}_3$ . These observations show that doping is helpful to modify the thermoelectric properties.

$\text{Ba}_3\text{GaSb}_3$  was synthesized and found to be stable up to 1168 K. According to DFT,  $\text{Ba}_3\text{GaSb}_3$  was found to be a semiconductor with a band gap of 0.3 eV. It was compacted successfully and the thermoelectric properties were studied.  $\text{Ba}_3\text{GaSb}_3$  shows high Seebeck coefficients ( $\alpha_{\text{max}} = 425 \mu\text{VK}^{-1}$  at 340 K), low electrical ( $\sigma_{\text{max}} = 2050 \text{ Sm}^{-1}$  at 800 K) and thermal conductivities ( $K_{\text{min}} = 0.75 \text{ Wm}^{-1}\text{K}^{-1}$  at 340 K).  $ZT$  values were low due to very low electrical conductivities.  $\text{Ba}_3\text{GaSb}_3$  was attempted to be doped with zinc and strontium to yield  $\text{Ba}_3\text{Ga}_{1-x}\text{Zn}_x\text{Sb}_3$  and  $\text{Ba}_{3-x}\text{Sr}_x\text{GaSb}_3$ . Again using AAS the presence of zinc was shown in  $\text{Ba}_3\text{Ga}_{1-x}\text{Zn}_x\text{Sb}_3$  and EDS allowed it to identify the presence of strontium in  $\text{Ba}_{3-x}\text{Sr}_x\text{GaSb}_3$ .

---

$Ba_7Ga_4Sb_9$  was identified as a side phase during the preparation of  $Ba_3GaSb_3$  and was then synthesized successfully as an almost monophasic sample using arc melting. It proved to be expected to show metallic behaviour according to DFT calculations.  $Ba_7Ga_4Sb_9$  was stable only up to 623 K. This sample could not be compacted due to the lack of thermal stability. Hence, the thermoelectric properties of  $Ba_7Ga_4Sb_9$  could not be measured.  $BaGa_2Sb_2$  was also prepared using arc melting and that was found to be stable in air. It melts at 990 K and shows high Seebeck coefficients ( $\alpha_{max} = 453 \mu VK^{-1}$  at 340 K), low electrical ( $\sigma_{max} = 1348 Sm^{-1}$  at 157 K) and thermal conductivities ( $K_{min} = 1.6 Wm^{-1}K^{-1}$  at 350 K).  $ZT$  values were not high.

$Ba_5In_2Sb_6$  was prepared successfully and found to be stable up to 973 K.  $Ba_5In_2Sb_6$  melts above 973 K. It was expected to show metallic behavior according to the DFT calculations, but conductivity studies show that this compound is a semiconductor with a band gap of 0.02 eV.  $Ba_5In_2Sb_6$  shows negative Seebeck coefficients which is rare for Zintl compounds and a minimum of  $-74 \mu VK^{-1}$  was observed around 473 K.  $Ba_5In_2Sb_6$  shows low electrical ( $\sigma_{max} = 12,955 Sm^{-1}$  at 500 K) and thermal conductivities ( $K_{min} = 1.73 Wm^{-1}K^{-1}$  around 520 K) and as a result the  $ZT$  values were found to be very low. In conclusion, several ternary Ba-Al/Ga/In-Sb Zintl phases were synthesized and compacted successfully. Their thermoelectric properties have been successfully investigated. To modify their properties doping was found to be an effective method.

---

---

## 10 References

---

- [1] G. J. Snyder, E. S. Toberer, *Nat. Mater.*, 7 (2008) 105-114.
- [2] F. J. Disalvo, *Science*, 295 (1999) 703.
- [3] L. Bell, *Science*, 321 (2008) 1457-1461.
- [4] D. M. Rowe (ed.), *CRC Handbook of Thermoelectrics* (CRC, Boca Raton, 1995).
- [5] C. B. Vining, *Nat. Mater.*, 8 (2009) 83-85.
- [6] S. M. Kauzlarich, S. R. Brown, G. J. Snyder, *Dalton Trans.*, (2007) 2099-2107.
- [7] G. Chen, M. S. Dresselhaus, G. J. P. Fleurial, T. Caillat, *Int. Mater. Rev.*, 48 (2003) 45-66.
- [8] M. S. Dresselhaus, G. Chen, M. Y. Tang, R. G. Yang, H. Lee, D. Z. Wang, Z. F. Ren, J. P. Fleurial, P. Gogna, *Adv. Mater.*, 19 (2007) 1043-1053.
- [9] C. Uher, *Thermoelectric Materials Research I* (ed. T. Tritt), 139-253 (Semimetals and semimetals series 69, Elsevier, 2001).
- [10] G. S. Nolas, J. Poon, M. Kanatzidis, *Mat. Res. Soc. Bull.*, 31 (2006) 199-205.
- [11] G. J. Snyder, M. Christensen, E. Nishibori, T. Caillat, B. B. Iversen, *Nat. Mater.*, 3 (2004) 458-463.
- [12] F. Casper, T. Graf, S. Chadov, B. Balke, C. Felser, *Semicond. Sci. Technol.*, 27 (2012) 063001.
- [13] K. Koumoto, Y. Wang, R. Zhang, A. Kosuga, R. Funahashi, *Annu. Rev. Mater. Res.*, 40 (2010) 363-394.

- 
- [14] K. Koumoto, I. Terasaki, R. Funahashi, *Mater. Res. Soc. Bull.*, 31 (2006) 206-210.
- [15] S. M. Kauzlarich (ed.), *Chemistry, structure and bonding of Zintl phases and ions*, Wiley-VCH (1996).
- [16] E. S. Toberer, A. F. May, G. J. Snyder, *Chem. Mater.*, 22 (2010) 624-634.
- [17] W. Klemm, *Trab. Reun. Int. React. Solidos*, 3rd 1 (1956) 447.
- [18] W. Klemm, *Proc. Chem. Soc.*, London (1959) 329.
- [19] H. Schäfer, B. Eisenmann, W. Müller, *Angew. Chem. Int. Ed. Engl.*, 12 (1973) 694.
- [20] H. Schäfer, B. Eisenmann, *Rev. Inorg. Chem.*, 3 (1981) 29.
- [21] R. Nesper, *Prog. Solid State Chem.*, 20 (1990) 1.
- [22] W. B. Pearson, *The Crystal Chemistry and Physics of Metals and Alloys* (1973) Wiley-Interscience, New York.
- [23] N. W. Ashcroft, N. D. Mermin, *Solid State Physics*, Saunders College, Philadelphia, (1976) 304.
- [24] T. F. Fässler (ed.) *Zintl Phases: Principles and Recent Developments*, 139 (2011) Springer, Heidelberg.

- 
- [25] S.M. Kauzlarich, *Encyclopedia of Inorganic chemistry*, John Wiley & Sons (1994).
- [26] E. Zintl, G. Woltersdorf, *Z. Electrochem.*, 41 (1935) 876.
- [27] M. Panda, Ph.D. Thesis, *Synthesis and characterization of alkali metal borides and closo-hydroborates* (2006) Universität Hamburg.
- [28] D. Fofanov, Ph.D. Thesis, *Synthesis, characterization and physical properties of metal borides* (2006) Universität Hamburg.
- [29] F. Stober, Ph.D. Thesis, *Synthese, Charakterisierung und Untersuchung thermoelektrischer Eigenschaften ausgewählter Metallboride* (2012) Technische Universität Darmstadt.
- [30] D. M Young, S. M. Kauzlarich, *Chem. Mater.*, 7 (1995) 206-209.
- [31] R. Pöttgen, T. Gulden, A. Simon, *GIT Laborfachzeitschrift*, 43 (1999) 133.
- [32] M. Kayan, Ph.D. Thesis, *Transition metal borides: Synthesis, characterization and superconducting properties* (2013) Technische Universität Darmstadt.
- [33] C. Birkel, Ph.D. Thesis, *Wet Chemistry Synthesis towards Nanostructures of Thermoelectric Antimonides* (2010) Johannes Gutenberg Universität Mainz.
- [34] M. Suarez, A. Fernandez, J. L. Menendez, R. Torrecillas, H. U. Kessel, J. Hennicke, R. Kirchner, T. Kessel (ed. B. Ertug), *Sintering Applications*, INTECH (2013) 319-342.

- 
- [35] E. A. Olevsky, C. G. Cardona, W. L. Brabury, C. D. Haines, D. G. Martin, D. Kapoor, *J. Am. Ceram. Soc.*, 95, 8 (2012) 2414-2422.
- [36] K. Capelle, *Brazilian Journal of Physics*, 36, 4 A (2006) 1318-1343.
- [37] S. F. Sousa, P. A. Fernandes, M. J. Ramos, *J. Phys. Chem. A*, 111, 42 (2007) 10439-10452.
- [38] K. Koepernik, H. Eschrig, *Phys. Rev. B*, 59 (1999) 1743.
- [39] I. Opahle, K. Koepernik, H. Eschrig, *Phys. Rev. B*, 60 (1999) 14035.
- [40] A. R. West, *Solid State Chemistry and its Applications*, John Wiley & Sons (Asia) Pte. Ltd. (2003).
- [41] L. E. Smart, E. A. Moore, *Solid State Chemistry - An Introduction*, ed. 3, CRC Press (2005).
- [42] B. Albert, *Bunsen – Magazin*, 1 (2012) 4-15.
- [43] Stoe Stadi P, [www.stoe.com/pages/products/stadimp.html](http://www.stoe.com/pages/products/stadimp.html), 26-11-2013.
- [44] G. Bruhn, Ph.D. Thesis, *Farben von Titanaten des Freudenbergit-Strukturtyps* (2012) Technische Universität Darmstadt.
- [45] H. M. Rietveld, *J. Appl. Cryst.*, 2 (1969) 65-71.
- [46] H. M. Rietveld, *Acta Crystallogr.*, 22 (1967) 151-152.
- [47] Program *TOPAS 4.2*, Bruker AXS, Karlsruhe, Germany (2009).

---

[48] Joel USA, Inc., *www.joelusa.com=Default.aspx?tabid= 185*, 26-08-2008.

[49] S. Rades, Ph.D. Thesis, *Synthese und Charakterisierung von Nanopartikeln im System Eisen-Bor* (2012) Technische Universität Darmstadt.

[50] K. D. Vernon- Parry, *III Vs Review*, 13, 4 (2000) 40-44.

[51] S. Ponou, Ph.D. Thesis, *Germanides, Germanide-Tungstate Double Salts and Substitution Effects in Zintl Phases* (2006) Technische Universität München.

[52] C. Litterscheid, Ph.D. Thesis, *Synthesen, Kristallstrukturen und Eigenschaften quaternärer Ortho- und Pyrophosphate der zwei- und dreiwertigen 3d – Übergangsmetalle* (2009) Rheinischen Friedrich-Wilhelms-Universität Bonn.

[53] J. I. Goldstein, *Scanning electron microscopy and X-ray microanalysis*, Springer (2003).

[54] B. Piccolo, R. T. O'connor, *J. Am. Oil Chem. Soc.*, 45 (1968) 789-792.

[55] Micromeritics, <http://www.micromeritics.com>, 21-02-2014.

[56] T. M. Tritt, M. A. Subramanian, *Mater. Res. Soc. Bull Bulletin*, 31 (2006) 188-229.

[57] R. G. Chambers, *Phys. Educ.*, 12 (1977) 374- 380.

[58] D. M. Rowe (ed), *Thermoelectric handbook: Macro to nano*, CRC press (2010).

[59] M. Jonson, G. D. Mahan, *Phys. Rev. B*, 21 (1980) 4223-4229.

- 
- [60] J. P. Heremans, V. Jovovic, E. S. Toberer, A. Saramat, K. Kurosaki, A. Charoenphakdee, S. Yamanaka, G. J. Snyder, *Science*, 321 (2008) 554-557.
- [61] A. I. Hochbaum, R. Chen, R. D. Delgado, W. Liang, E. C. Garnett, M. Najarian, A. Majumdar, P. Yang, *Nature*, 451 (2008) 163-165.
- [62] B. Poudel, Q. Hao, Y. Ma, Y. Lan, A. Minnich, B. Yu, X. Yan, D. Wang, A. Muto, D. Vashaee, X. Chen, J. Liu, M. Dresselhaus, G. Chen, Z. Ren, *Science*, 320 (2008) 634-638.
- [63] J. S. Rhyee, K. H. Lee, S. M. Lee, E. Cho, S. Ilkim, E. Lee, Y. S. Kwon, J. H. Shim, G. Kotliar, *Nature*, 459 (2009) 965-968.
- [64] R. R. Heikes, R. W. Ure, *Thermoelectricity: Science and engineering*, Interscience, New York (1961).
- [65] F. D. Rosi, *Solid State Electron*, 11 (1968) 833-848.
- [66] C. Wood, *Rep. Prog. Phys.*, 51 (1988) 459-539.
- [67] H. J. Goldsmid, R. W. Douglas, *Britt. J. Appl. Phys.*, 5 (1954) 386-390.
- [68] F. D. Rosi, E. F. Hockings, N. E. Lindenbald, *RCA Rev.*, 22 (1961) 82-121.
- [69] Y. Gelbstein, Z. Dashevsky, M. P. Dariel, *Physica B*, 363 (2005) 196-205.
- [70] R. W. Fritts, *Thermoelectric materials and devices* (ed. I. B. Cadoff & E. Miller), Reinhold, New York (1960) 143-162.
- [71] K. F. Hsu, S. Loo, F. Guo, W. Chen, J. S. Dyck, C. Uher, T. Hogan, E. K. Polychroniadis, M. G. Kanatzidis, *Science*, 303 (2004) 818-821.

- 
- [72] N. A. Sidorenko, L. D. Ivenova, *Inorg. Mater.*, 37 (2001) 331-335.
- [73] H. Fleischmann, H. Luy, J. Rupprecht, *Zeitschrift für Naturforschung A*, 18 (1963) 646-649.
- [74] W. M. Yim, A. Amith, *Solid State Electron*, 15 (1972) 1141.
- [75] H. Fleischmann, *Zeitschrift für Naturforschung A*, 16 (1961) 765-780.
- [76] S. R. Brown, S. M. Kauzlarich, F. Gascoin, G. J. Snyder, *J. Sol. State. Chem.*, 180 (2007) 1414.
- [77] E. S. Toberer, C. A. Cox, S. R. Brown, T. Ikeda, A. F. May, S. M. Kauzlarich, G. J. Snyder, *Adv. Funct. Mater.*, 18 (2008) 2795-2800.
- [78] C. A. Cox, E. S. Toberer, A. A. Levchenko, S. R. Brown, G. J. Snyder, A. Navrotsky, S. M. Kauzlarich, *Chem. Mater.*, 21 (2009) 13541360.
- [79] H. Anno, M. Hokazono, M. Kawamura, J. Nagao, K. Matsubara, *Prcoodings of the Twenty First International Conference on Thermoelectrics* (2002) 77-80.
- [80] Y. I. Ravich, B. A. Efimova, I. A. Smirnov, *Semiconducting Lead Chalcogenides*, Plenum, New York (1970).
- [81] G. J. Snyder, T. Caillat, J. P. Fleurial, *Phys. Rev. B*, 62 (2000) 10185.
- [82] G. A. Slack, V. G. Tsoukala, *J. Appl. Phys.*, 76 (1994) 1665-1671.
- [83] H. Anno, M. Hokazono, H. Takakura, K. Matsubara, *International Conference on Thermoelectrics* (2005) 102.

- 
- [84] S. Johnsen, A. Bentien, G. K. H. Madsen, M. Nygren, B. B. Iversen, *Phys. Rev. B*, 76 (2007) 245126.
- [85] M. Hokazono, M. Kawamura, H. Anno, K. Matsubara, *Trans. Mater. Res. Soc. Jpn.*, 29 (2004) 2793.
- [86] H. Anno, M. Kawamura, M. Hokazono, J. Nagao, K. Matsubara, *Twenty Second International Conference on Thermoelectrics* (2003) 121-126.
- [87] T. Eto, K. Kishimoto, K. Koga, K. Akai, T. Koyanagi, H. Anno, T. Tanaka, H. Kurisu, S. Yamamoto, M. Matsuura, *Mater. Trans.*, 50 (2009) 631-639.
- [88] G. A. Slack, (ed.) *Solid State Physics* (Academic Press, New York, 1979).
- [89] D. M. Rowe, G. Min, *J. Mater. Sci. Lett.*, 14 (1995) 617-619.
- [90] V. Keppens, D. Mandrus, B. Sales, B. Chakoumakos, P. Dai, R. Coldea, M. Maple, D. Gajewski, E. freeman, S. Bennington, *Nature*, 395 (1998) 876-878.
- [91] D. T. Moreli, G. P. Meisner, *J. Appl. Phys.*, 77 (1995) 3777-3781.
- [92] G. S. Nolas, J. L. Cohn, G. A. Slack, S. B. Schujman, *Appl. Phys. Lett.*, 73 (1998) 178.
- [93] B. C. Sales, D. Mandrus, R. K. Williams, *Science*, 272 (1996) 1325.
- [94] M. M. Koza, M. R. Johnson, R. Viennois, H. Mutka, L. Girard, D. Ravot, *Nat. Mater.*, 7 (2008) 805-810.
- [95] E.S. Toberer, M. Christensen, B.B. Iversen, G.J. Snyder, *Phys. Rev. B* 77 (2008) 075203.

- 
- [96] S. R. Culp, S. J. Poon, N. Hickman, T. M. Tritt, J. Blumm, *Appl. Phys. Lett.*, 88 (2006) 042106.
- [97] C. B. Vining, W. Laskow, J. O. Hanson, R. R. Wanderbeck, P. D. Gorsuch, *J. Appl. Phys.*, 69 (1991) 4333-4340.
- [98] S.R. Brown, S.M. Kauzlarich, F. Gascoin, G.J. Snyder, *Chem. Mater.* 18 (2006) 1873- 1877.
- [99] J. P. Fleurial, T. Caillat, A. Borshchevsky, in Proc. ICT'97 16<sup>th</sup> Int. Conf. *Thermoelectrics* 1-11 (IEEE Piscataway, New Jersey, 1997).
- [100] K. Kurosaki, A. Kosuga, H. Muta, M. Uno, S. Yamanaka, *Appl. Phys. Lett.*, 87 (2005) 061919.
- [101] T. Caillat, J. P. Fleurial, A. Borshchevsky, *J. Phys. Chem. Solids*, 58 (1997) 1119-1125.
- [102] B. Wolfing, C. Kloc, J. Teuber, E. Bucher, *Phys. Rev. Lett.*, 86 (2001) 4350-4353.
- [103] T. Yi, E. S. Toberer, C. A. Cox, S. M. Kauzlarich, G. J. Snyder, *Chem. Mater.*, 22 (2010) 935-941.
- [104] S.-J. Kim, J.R. Ireland, C.R. Kannewurf, M.G. Kanatzidis, *J. Solid State Chem.* 155 (2000) 55-61.
- [105] A. F. May, E. S. Toberer, G. J. Snyder, *J. Appl. Phys.*, 106 (2009) 013706.

- 
- [106] S. J. Kim, S. Hu, C. Uher, M. G. Kanatzidis, *Chem. Mater.*, 11 (1999) 3154-3159.
- [107] X. J. Wang, M. B. Tang, J. T. Zhao, H. H. Chen, X. X. Yang, *Appl. Phys. Lett.*, 90 (2007) 232107.
- [108] G. K. H. Madsen, *J. Am. Chem. Soc.*, 128 (2006) 12140-12146.
- [109] C. L. Condron, S. M. Kauzlarich, F. Gascoin, G. J. Snyder, *J. Solid State Chem.*, 179 (2006) 2252.
- [110] Linseis Thermal Analysis, <http://www.linseis.com/en/our-products>, 26-11-2013.
- [111] G. Cordier, G. Savelsberg, H. Schäfer, *Z. Naturforsch. B*, 37 (1982) 975–980.
- [112] G. Cordier, H. Schäfer, M. Stelter, *Z. Naturforsch. B*, 40 (1985) 1100-1104.
- [113] G. Cordier, H. Schäfer, M. Stelter, *Z. Anorg. Allg. Chem.*, 534 (1986) 137.
- [114] S. J. Kim, M. G. Kanatzidis, *Inorg. Chem.*, 40, 15 (2001) 3781-3785.
- [115] G. Cordier, M. Stelter, *Z. Naturforsch. B*, 43, 4 (1988) 463-466.
- [116] S. Bobev, J. Hullmann, T. Harmening, R. Pöttgen, *Dalton Trans.*, 39, 26 (2010) 6049-6055.

---

[117] F. Emmerling, N. Laengin, F. Pickhard, M. Wendorff, C. Roehr, *Z. Naturforsch. B*, 59, 1(2004) 7-16.

[118] K. Deller, B. Eisenmann, *Z. Naturforsch. B*, 33 B, 6 (1978) 676-81.

[119] E. Brechtel, G. Cordier, H. Schaefer, *Z. Naturforsch. B*, 36 B, 10 (1981) 1341-1342.

[120] B. Eisenmann, K. Deller, *Z. Naturforsch. B*, 30 B, 1-2 (1975) 66-72.

[121] B. Eisenmann, C. Gieck, U. Rossler, *Z. Kristallogr.*, 216, 1 (2001) 36.

[122] B. Eisenmann, H. Jordan, H. Schäfer, *Z. Naturforsch. B*, 40 B, 12 (1985) 1603-1606.

[123] W. G. Zeier, A. Zevalkink, E. Schechtel, W. Tremel, G. J. Snyder, *J. Mater. Chem.*, 22, 19 (2012) 9826-9830.

[124] A. Zevalkink, J. Swallow, G. J. Snyder, *J. Electron. Mater.*, 41, 5 (2012) 813-818.

[125] A. Zevalkink, G. Pomrehn, Y. Takagiwa, J. Swallow, G. J. Snyder, *Chemsuschem.*, 6, (2013) 2316-2321.

[126] N. Nishiyama, J. Lin, A. Okazaki, M. Iwasaka, K. Hirakawa, *Jap. J. Appl. Phys.*, 29 (1990) 369-371.

[127] L. Vegard, *Z. Phys.*, 5 (1921) 17.

- 
- [128] L. Vegard, *Z. Cryst.*, 67 (1928) 239.
- [129] A. Zevalkink, W. G. Zeier, G. Pomrehn, E. Schechtel, W. Tremel, G. J. Snyder, *Energy Environ. Sci.*, 5, 10 (2012) 9121-9128.
- [130] E. S. Toberer, A. Zevalkink, N. Crisosto, G. J. Snyder, *Adv. Funct. Mater.*, 20, 24 (2010) 4375-4380.
- [131] A. Zevalkink, G. S. Pomrehn, S. Johnson, J. Swallow, Z. M. Gibbs, G. J. Snyder, *Chem. Mater.*, 24,11 (2012) 2091-2098.
- [132] S. Q. Xia, S. Bobev, J. Hullmann, *J. Solid state Chem.*, 181, 8 (2008) 1909-1914.
- [133] S. M. Park, S. J. Kim, M. G. Kanatzidis, *J. Solid state Chem.*, 175, 2 (2003) 310-315.
- [134] H. He, R. Stearrett, R. Nowak, S. Bobev, *Inorg. Chem.*, 49, 17 (2010) 7935-7940.
- [135] H. F. Wang, K. F. Cai, S. Chen, *J. Mater. Sci. Mater. Electron.*, 23 (2012) 2289-2292.
- [136] A. Zevalkink, E. S. Toberer, W. G. Zeier, E. F. Larsen, G. J. Snyder, *Energy Environ. Sci.*, 4 (2011) 510-518.
- [137] B. Eisenmann, H. Schäfer, *Z. Anorg. Allg. Chem.*, 403 (1974) 163-172.
- [138] S. M. Park, E. S. Choi, W. Kang, S. J. Kim, *J. Mater. Chem.*, 12 (2002) 1839-1843.
- [139] A. Zevalkink, J. Swallow, G. J. Snyder, *Dalton Trans.*, 42 (2013) 9713-9719.

---

[140] P. Alemany, S. Alvarez, R. Hoffmann, *Inorg. Chem.*, 29 (1990) 3070-3073.

[141] P. Alemany, M. Llunell, E. Canadell, *Inorg. Chem.*, 45 (2006) 7235-7241.

---

---

## 11 List of figures

---

2.1	Schlenk/vacuum line set up to handle air sensitive materials	5
2.2	Metal distillation setup with cylindrical steel apparatus	6
2.3	Evacuated quartz ampoule with sealed tantalum container	7
2.4	Schematic of Arc melting device	8
2.5	Schematic of high frequency induction furnace	9
2.6	Schematic representation of spark plasma sintering	11
2.7	<i>SPS – 211 Lx, Dr. Sinter LAB, FUJI electronics (Japan)</i> used for Spark plasma sintering	11
3.1	<i>STOE STADI P</i> diffractometer	13
3.2	Heating furnace used in HTXRD measurements	13
3.3	Schematic diagram of SEM	15
3.4	Schematic diagram of Energy Dispersive Spectroscopy	16
3.5	Schematic of atomic absorption spectroscopy	17
3.6	Schematic of gas pycnometer used for density measurements that works with helium	19
3.7	Schematic of a thermoelectric generator with hot and cold	

	ends	20
3.8	<i>Linseis LSR-3</i> used for Seebeck / resistivity measurement	23
3.9	<i>Linseis LFA 1000</i> used for Thermal conductivity / thermal diffusivity measurement	24
4.1	Figure of merit ( <i>ZT</i> ) of <i>n</i> -type materials and <i>p</i> -type materials	25
4.2	Effect of carrier concentration on thermoelectric properties and <i>ZT</i>	27
4.3	Relationship between thermal conductivity and carrier concentration in enhancing <i>ZT</i>	29
4.4	Low thermal conductivities found in various thermoelectric materials	30
4.5	Lattice thermal conductivities of variety of Zintl antimonides at 300 K	31
4.6	Unit cell of $\text{Ba}_3\text{AlSb}_3$ and dimer $(\text{Al}_2\text{Sb}_6)^{12-}$ of $\text{Ba}_3\text{AlSb}_3$	34
4.7	Unit cell and $(\text{Ga}_2\text{Sb}_6)^{12-}$ dimer unit of $\text{Ba}_3\text{GaSb}_3$	37
4.8	Unit cell and Ga-Sb anionic network of $\text{Ba}_7\text{Ga}_4\text{Sb}_9$	40
4.9	Crystal structure and $[\text{Ga}_2\text{Sb}_2]^{2-}$ framework of $\text{BaGa}_2\text{Sb}_2$	44
4.10	Unit cell and $[\text{In}_2\text{Sb}_6]^{10-}$ network of $\text{Ba}_5\text{In}_2\text{Sb}_6$	47

---

5.1	Band structure and Density of states (DOS) of $\text{Ba}_3\text{AlSb}_3$	51
5.2	Band structure and Density of states (DOS) of $\text{Ba}_3\text{GaSb}_3$	52
5.3	Band structure and Density of states (DOS) of $\text{Ba}_7\text{Ga}_4\text{Sb}_9$	53
5.4	Band structure and Density of states (DOS) of $\text{BaGa}_2\text{Sb}_2$	54
5.5	Band structure and Density of states (DOS) of $\text{Ba}_5\text{In}_2\text{Sb}_6$	56
6.1	Measured and calculated powder X-ray diffractions of $\text{Ba}_3\text{AlSb}_3$ along with difference curve	58
6.2	High temperature powder X-ray diffraction of $\text{Ba}_3\text{AlSb}_3$	60
6.3	Lattice parameters ( $\text{\AA}$ ) and unit cell volume with temperature	61
6.4	Powder X-ray diffraction patterns of $\text{Ba}_3\text{AlSb}_3$ before and after SPS	62
6.5	SEM images of $\text{Ba}_3\text{AlSb}_3$	63
6.6	Seebeck coefficient, Electrical conductivity, Thermal conductivity and Figure of merit as the functions of temperature of $\text{Ba}_3\text{AlSb}_3$	65
6.7	Powder X-ray diffraction patterns of doped and undoped $\text{Ba}_3\text{Al}_{1-x}\text{Zn}_x\text{Sb}_3$	67
6.8	Powder X-ray diffraction patterns of doped and undoped	

---

	$\text{Ba}_{3-x}\text{Ca}_x\text{AlSb}_3$	68
6.9	SEM images of $\text{Ba}_3\text{Al}_{1-x}\text{Zn}_x\text{Sb}_3$	70
6.10	SEM images of $\text{Ba}_{3-x}\text{Ca}_x\text{AlSb}_3$	71
6.11	EDS mapping of $\text{Ba}_{2.79}\text{Ca}_{0.21}\text{GaSb}_3$	72
6.12	Variation in lattice parameter $b$ (Å) as a function of dopant concentration (Zn) in $\text{Ba}_3\text{Al}_{1-x}\text{Zn}_x\text{Sb}_3$	73
6.13	Variation in lattice parameter $b$ (Å) as a function of dopant concentration (Ca) in $\text{Ba}_{3-x}\text{Ca}_x\text{AlSb}_3$	74
6.14	Seebeck coefficient, Electrical conductivity, Thermal conductivity and $ZT$ as the functions of temperature of $\text{Ba}_3\text{Al}_{0.97}\text{Zn}_{0.03}\text{Sb}_3$ in comparison to undoped $\text{Ba}_3\text{AlSb}_3$	75
7.1.1	Ternary phase diagram of well-known Ba-Ga-Sb compounds	80
7.1.2	Measured and calculated powder X-ray diffractions of $\text{Ba}_3\text{GaSb}_3$ along with difference curve	81
7.1.3	High temperature powder XRD of $\text{Ba}_3\text{GaSb}_3$	83
7.1.4	Lattice constants (Å) and unit cell with temperature	84
7.1.5	Differential thermal analysis (DTA) and thermal gravimetry (TG) measurements of $\text{Ba}_3\text{GaSb}_3$	85
7.1.6	Powder X-ray diffraction patterns of $\text{Ba}_3\text{GaSb}_3$ before and after sintering	86

7.1.7	SEM image of $\text{Ba}_3\text{GaSb}_3$	87
7.1.8	Seebeck coefficient, Electrical conductivity, Thermal conductivity and Figure of merit as the functions of temperature of $\text{Ba}_3\text{GaSb}_3$	89
7.1.9	Comparison of Thermoelectric properties of samples with different impurity compositions ( $\text{Ba}_3\text{GaSb}_3$ )	91
7.1.10	Powder X-ray diffraction patterns of doped and undoped $\text{Ba}_3\text{Ga}_{1-x}\text{Zn}_x\text{Sb}_3$	94
7.1.11	Powder X-ray diffraction patterns of doped and undoped $\text{Ba}_{3-x}\text{Sr}_x\text{GaSb}_3$	95
7.1.12	SEM images of $\text{Ba}_3\text{Ga}_{1-x}\text{Zn}_x\text{Sb}_3$	97
7.1.13	SEM images of $\text{Ba}_{3-x}\text{Sr}_x\text{GaSb}_3$	98
7.1.14	EDS mapping of $\text{Ba}_{2.79}\text{Sr}_{0.21}\text{GaSb}_3$	99
7.1.15	Variation in lattice parameter $b$ (Å) as a function of dopant concentration (Zn) in $\text{Ba}_3\text{Ga}_{1-x}\text{Zn}_x\text{Sb}_3$	100
7.1.16	Variation in lattice parameter $b$ (Å) as a function of dopant concentration (Sr) in $\text{Ba}_{3-x}\text{Sr}_x\text{GaSb}_3$	101
7.2.1	Measured and calculated powder X-ray diffraction diagrams of $\text{Ba}_7\text{Ga}_4\text{Sb}_9$ along with difference curve	104
7.2.2	High temperature X-ray diffraction measurement for	

---

	Ba <sub>7</sub> Ga <sub>4</sub> Sb <sub>9</sub>	105
7.2.3	Lattice constants and unit cell volume as the functions of temperature of Ba <sub>7</sub> Ga <sub>4</sub> Sb <sub>9</sub>	106
7.2.4	SEM images of Ba <sub>7</sub> Ga <sub>4</sub> Sb <sub>9</sub>	107
7.2.5	Powder X-ray diffraction patterns before and after SPS of Ba <sub>7</sub> Ga <sub>4</sub> Sb <sub>9</sub>	108
7.2.6	Broken pellet of Ba <sub>7</sub> Ga <sub>4</sub> Sb <sub>9</sub>	110
7.3.1	Experimental and calculated powder X-ray diffraction diagrams of BaGa <sub>2</sub> Sb <sub>2</sub>	112
7.3.2	High temperature powder X-ray diffraction of BaGa <sub>2</sub> Sb <sub>2</sub>	113
7.3.3	Lattice constants and unit cell volume as the functions of temperature of BaGa <sub>2</sub> Sb <sub>2</sub>	114
7.3.4	Differential thermal analysis (DTA) and thermal gravimerty (TG) measurements of BaGa <sub>2</sub> Sb <sub>2</sub>	115
7.3.5	Compacted sample of BaGa <sub>2</sub> Sb <sub>2</sub>	116
7.3.6	Powder X-ray diffraction patterns of BaGa <sub>2</sub> Sb <sub>2</sub> before and after SPS	117
7.3.7	SEM image of BaGa <sub>2</sub> Sb <sub>2</sub>	118
7.3.8	Seebeck coefficient, Electrical conductivity, Thermal conductivity and Figure of merit as the function of	

---

	Temperature of BaGa <sub>2</sub> Sb <sub>2</sub>	120
8.1	Measured and calculated powder X-ray diffraction diagrams of Ba <sub>5</sub> In <sub>2</sub> Sb <sub>6</sub> along with difference curve	125
8.2	High temperature powder X-ray diffraction of Ba <sub>5</sub> In <sub>2</sub> Sb <sub>6</sub>	126
8.3	Lattice constants and unit cell volume as the functions of temperature of Ba <sub>5</sub> In <sub>2</sub> Sb <sub>6</sub>	127
8.4	Powder X-ray diffraction patterns of Ba <sub>5</sub> In <sub>2</sub> Sb <sub>6</sub> before and after SPS	128
8.5	SEM images of Ba <sub>5</sub> In <sub>2</sub> Sb <sub>6</sub>	129
8.6	Thermoelectric properties of Ba <sub>5</sub> In <sub>2</sub> Sb <sub>6</sub> and plot of Natural logarithm of electrical conductivity along with reciprocal of kT	131

---

---

## 12 List of tables

---

2.1	Starting materials	4
4.1	Crystallographic data of $\text{Ba}_3\text{AlSb}_3$	32
4.2	Atomic coordinates and Wyckoff positions of $\text{Ba}_3\text{AlSb}_3$	33
4.3	Crystallographic data of $\text{Ba}_3\text{GaSb}_3$	35
4.4	Atomic coordinates and Wyckoff positions of $\text{Ba}_3\text{GaSb}_3$	36
4.5	Crystallographic data of $\text{Ba}_7\text{Ga}_4\text{Sb}_9$	39
4.6	Atomic coordinates and Wyckoff positions of $\text{Ba}_7\text{Ga}_4\text{Sb}_9$	39
4.7	Crystallographic data of $\text{BaGa}_2\text{Sb}_2$	42
4.8	Atomic coordinates and Wyckoff positions of $\text{BaGa}_2\text{Sb}_2$	43
4.9	Crystallographic data of $\text{Ba}_5\text{In}_2\text{Sb}_6$	46
4.10	Atomic coordinates and Wyckoff positions of $\text{Ba}_5\text{In}_2\text{Sb}_6$	46
6.1	Lattice parameters of $\text{Ba}_3\text{AlSb}_3$ from Rietveld refinement based on the structure model from literature [111]	59
6.2	Atomic percentages of all elements in $\text{Ba}_3\text{AlSb}_3$ determined using EDS	63
6.3	Average atomic percentages of doped samples of $\text{Ba}_{3-x}\text{Ca}_x\text{AlSb}_3$	71
7.1.1	Lattice parameters of $\text{Ba}_3\text{GaSb}_3$ calculated from Rietveld	

---

	refinement based on the structure model from literature [112]	82
7.1.2	Atomic percentages of all elements in $\text{Ba}_3\text{GaSb}_3$ determined using EDS	87
7.1.3	Average atomic percentages of doped samples of $\text{Ba}_{3-x}\text{Sr}_x\text{GaSb}_3$	99
7.2.1	Lattice parameters of $\text{Ba}_7\text{Ga}_4\text{Sb}_9$ calculated from Rietveld refinement based on the structure model from literature [113]	104
7.2.2	Atomic percentages of all elements in $\text{Ba}_7\text{Ga}_4\text{Sb}_9$ determined using EDS	108
7.2.3	List of densities of compacted $\text{Ba}_7\text{Ga}_4\text{Sb}_9$	109
7.3.1	Lattice parameters of $\text{BaGa}_2\text{Sb}_2$ calculated from Rietveld refinement based on the structure model from literature [114]	112
7.3.2	List of densities of compacted $\text{BaGa}_2\text{Sb}_2$	117
7.3.3	Atomic percentages of all elements in $\text{BaGa}_2\text{Sb}_2$ determined using EDS	119
8.1	Lattice parameters of $\text{Ba}_5\text{In}_2\text{Sb}_6$ calculated from Rietveld refinement based on the structure model from literature [115]	125
8.2	List of densities of compacted $\text{Ba}_5\text{In}_2\text{Sb}_6$	129
8.3	Atomic percentages of all elements in $\text{Ba}_5\text{In}_2\text{Sb}_6$ determined using EDS	130

---

Manikanda Prabu Nagu  
Kasino-Str. 27  
64293 Darmstadt

**Eidesstattliche Erklärung**

Hiermit erkläre ich an Eides Statt, dass ich die vorliegende Dissertation selbstständig und nur mit den angegebenen Hilfsmitteln ausgeführt habe.

Darmstadt, den

.....

Unterschrift

---

Manikanda Prabu Nagu  
Kasino-Str. 27  
64293 Darmstadt

**Erklärung**

Ich erkläre hiermit, noch keinen Promotionsversuch unternommen zu haben.

Darmstadt, den

.....

Unterschrift

---

---

## Curriculum vitae

---

### Manikanda Prabu Nagu

Eduard Zintl Institute of Inorganic and Physical  
Chemistry  
Technische Universität Darmstadt  
Alarich-Weiss-Strasse 12  
64287 Darmstadt, Germany.

Phone : +49-157-88400831

E-mail: manikandaprabu11@gmail.com



---

### Research experience:

**Pursuing Ph.D. from Technical University of Darmstadt under the supervision of Prof. Dr. Barbara Albert (working since December, 2009).**

This work focused on synthesis, characterization, compaction and thermoelectric studies of alkaline earth metal based Zintl compounds. Highly air sensitive phases were prepared and handled using glove box and Schlenk (or vacuum) lines.

**Worked as a research associate in the research group of Prof. Dr. S. Natarajan, SSCU, Indian Institute of Science, India (August 2007 to November 2009).**

This work focused on the preparation of metal-organic framework (MOF) materials and the complete characterization of them. Photocatalytic activities of these materials were also studied for the application of waste water treatment.

### Research interest:

Thermoelectric studies, Material chemistry, Synthetic Inorganic chemistry, Catalysis, Metal -organic frameworks etc.

### Selected Publications:

- Role of Temperature and Time in the formation of infinite M-O-M linkages and isolated clusters in MOFs: A few illustrative examples, Partha Mahata, Manikanda Prabu, Srinivasan Natarajan\*, *Inorg. Chem.*, 2008, 47(19), 8451-8463.

- 
- Time and Temperature dependent study in the three component Zn-Triazolate-Oxybis (benzoate) system: Stabilization of new topologies, Partha Mahata, Manikanda Prabu, Srinivasan Natarajan\*, *Cryst. Growth Des.* 2009, 9(8), 3683-3691.

**Educational qualifications:**

- Completed M.sc chemistry degree (2005-07) with 66%, The American College, Madurai, India.
- Completed B.sc chemistry degree (2002-05) with 73.3%, The American College, Madurai, India.
- Passed in Higher secondary education (2001-02) with 91.25%, St.Mary's HSC School, Madurai, India.
- Passed in SSLC (1999-2000) with 92%, St.Mary's HSC School, Madurai, India.
- Cleared National eligibility test (NET) conducted by Council of Scientific & Industrial Research, India in 2007.
- Cleared Graduate Attitude Test for Engineering (GATE) with 94.2 % in 2007.

**Personal details:**

Date of birth : 06-08-1984  
Nationality : Indian  
Marital status : Single  
Languages known : English, Tamil, Hindi (fluent), German (beginner)  
Hobbies : Playing cricket, cooking, travelling etc.  
Address : Kasinostrasse 27, 64293-Darmstadt, Germany